Spectroscopische detectie van glucose
met een op silicium gebaseerd optisch circuit

Spectroscopic Detection of Glucose
with a Silicon Photonic Integrated Circuit

Eva Ryckeboer

Promotor: prof. dr. ir. R. Baets
Proefschrift ingediend tot het behalen van de graad van
Doctor in de Ingenieurswetenschappen: Fotonica

Vakgroep Informatietechnologie
Voorzitter: prof. dr. ir. D. De Zutter
Faculteit Ingenieurswetenschappen en Architectuur
Academiejaar 2013 - 2014

UNIVERSITEIT
GENT

ISBN 978-90-8578-688-7
NUR 959, 954
Wettelijk depot: D/2014/10.500/34

Promotor:

Prof. Dr. Ir. Roel Baets

Examencommissie:

Prof. Dr. Ir. Rik Van de Walle (voorzitter)	Universiteit Gent, ELIS
Prof. Dr. Ir. Roel Baets (promotor)	Universiteit Gent, INTEC
Prof. Dr. Ir. Ronny Bockstaele	Universiteit Gent, INTEC
Prof. Dr. Ir. Wim Bogaerts	Universiteit Gent, INTEC
Prof. Dr. Ir. Danae Delbeke	Universiteit Gent, INTEC
Prof. Dr. Dirk Poelman	Universiteit Gent, LumiLab
Prof. Dr. Ir. Robert Puers	Katholieke Universiteit Leuven, ESAT-MICAS
Prof. Dr. Ir. Gunther Roelkens (secretaris)	Universiteit Gent, INTEC
Prof. Dr. Ir. Wouter Saeys	Katholieke Universiteit Leuven, MeBioS

Universiteit Gent
Faculteit Ingenieurswetenschappen en Architectuur

Vakgroep Informatietechnologie
Sint-Pietersnieuwstraat 41, B-9000 Gent, België

Tel.: +32-9-264.33.39
Fax.: +32-9-331.35.93

Dit werk kwam tot stand in het kader van het IWT-SBO GlucoSens project van het IWT-Vlaanderen (Instituut voor de aanmoediging van Innovatie door Wetenschap en Technologie in Vlaanderen).

Dankwoord

Wat geeft het een goed gevoel om op dit punt te zijn aangekomen! Enerzijds sluit dit een unieke periode af en anderzijds krijg ik nu de kans om iedereen eens goed te bedanken. Zo'n vijf jaar geleden, hadden prof. Roel Baets en Danaë het lumineuze idee dat een implanteerbare glucosemeter op basis van SOI wel eens onderzocht moest worden. Ik was hierover enthousiast, en ja ietwat naïef, en zo begon mijn doctoraat in de fotonica onderzoeksgroep met Roel als promotor. Als eerste in dit dankwoord wil ik dan ook graag Roel bedanken. Ik heb enorm veel van je bijgeleerd en ben blij dat je me zo regelmatig aanspoorde om verder te kijken dan mijn neus lang is.
Ik wil ook graag het hele GlucoSens team bedanken. Bedankt dat ik in al die verschillende labo's mocht rondneuzen! Al merkten we vrij snel dat een implanteerbare glucosemeter zich niet op een gouden schoteltje aanbiedt, de motivatie om er keihard tegenaan te gaan, heeft vruchten afgeworpen. De project managers Geert en Ronny hebben hierin onmiskenbaar een grote rol gespeeld. Ronny, jouw 'hoe de industrie het zou doen'-aanpak werkte echt aanstekelijk, bedankt daarvoor!
Verder wil ik ook graag de jury-leden van mijn examencommissie bedanken voor hun waardevolle feedback op dit doctoraat. Aussi, merci beaucoup à Alban pour notre collaboration sur les spectromètres! Thanks Agnes, Sam and prof. Jan Vierendeels for the collaboration on ring resonators for diffusion measurements.
Wat een geluk dat doctoreren geen eenzame taak is. Ik heb dan ook erg veel plezier beleefd in de fotonica-groep, tijdens en naast de uren. Om te beginnen met mijn bureaugenoten, Thijs, Raphael, Amin, Peter, Martijn, Thomas, Andreas, Pijush, Haolan, bureau-tegenover-genoten Bart, Pieter, Yannick en alle ex-bureaugenoten. Echt een gezellige bende! Samen brainstormen, elkaar een hart onder de riem steken als het wat moeilijker gaat of gewoon de laatste nieuwtjes (of ja roddels) uitwisselen, ik ging nooit met tegenzin werken! Ik heb in deze groep ook erg veel straffe persoonlijkheden leren kennen: Karel, de meest efficiënte mens ooit, eigenzinnige Elewout, sweet Chen, super-friendly Shahram, sunshine Nannicha, energetic Ananth, ... the list is so much longer! Echt een inspirerende omgeving! I want to thank the epixfab team, the post-docs, all the PhD students and people who left the group recently. You have helped me in many ways! Thanks for creating such a good atmosphere!

Ik wil ook graag het geweldige ondersteunende team van de fotonica-groep bedanken: de Ilses, Kristien, Bert, Mike, Jeroen en Eddy! Bedankt voor jullie hulp met de glimlach! Verder wil ik ook het indrukwekkende proffenteam Peter, Dries, Geert, Gunther, Wim en Nicolas bedanken voor hun toegankelijkheid en kennis van zake!
Mijn doctoraat was van alles wat: simuleren, ontwerpen, meten en fabriceren. Voor het ontwerp-gedeelte, was Manu van onschatbare waarde. Weg met picazzo 1, leve picazzo 2! En die lange dagen in de meetkamer gingen toch net iets vlotter dankzij de hulp van Michael en Peter Guns, met zijn stoffige maar magische werkplaats! Ook een welgemeende dankuwel aan Steven en Liesbet. Jullie houden in de CR de moraal hoog en zijn werkelijk onvervangbaar.
Bedankt ook Mathieu, Len, Pieter, Laura, Christophe en Thomas voor de gezellige koffietjes om het brug-eten te verteren!
Door die vele lange dagen in het technicum, was het goed om af en toe wat stoom te kunnen afblazen. Merci mede-atleten en trainer Koen voor de fijne trainingen. Merci Sofie, Kristin, Harlinde en Machteld voor de gezellige ladies nights, merci aan de Fre's, Julie's, Maartje, Lies, Adriaan en Jeroen voor de lawaaierige etentjes en super-deluxe BBQs, merci Derek, Mayte en Vincent voor de openhartige avonden in Gent en Brussel.
Dat ik tot op dit punt ben geraakt, heb ik ook te danken aan mijn familie, schoon-familie en vooral mijn ouders. Jullie zorg, liefde en steun zijn van onschatbare waarde!
Tenslotte wil ik zeker Jeroen bedanken! Echt onvoorstelbaar hoe jij me stimuleert, steunt en voor me zorgt! Je maakt me erg gelukkig!

Gent, 4 May 2014
Eva Ryckeboer

Table of Contents

Lijst van figuren

Lijst van tabellen

List of Acronyms

A

AWG	Arrayed Waveguide Grating

C

CAMFR	CAvity Modelling FRamework
CB	Combination Band
CGM	Continuous Glucose Monitoring
CMOS	Complementary Metal Oxide Semiconductor
CT	Cross Talk

D

DBR	Distributed Bragg Gratings
DR	Dynamic Range

F

FO	First Overtone
FPR	Free Propagation Region
FSR	Free Spectral Range
FTIR	Fourier Transform InfraRed spectrometer
FWHM	Full Width at Half Minimum

G

GaSb	Gallium Antimonide

I

IC	Integrated Circuit
IL	Insertion Loss
InP	Indium Phosphide
ISF	InterStitial Fluid
IR	Infra Red
IWT-SBO	Agentschap voor Innovatie door Wetenschap en Technologie - Strategisch Basisch Onderzoek

L

LD	Linear Dispersion

M

MARD	Mean Absolute Relative Distance
MFD	Mode Field Diameter
MMI	Multimode Interferometer
MWCO	Molecular Weight Cut-Off
MZI	Mach-Zehnder Interferometer

N

NEP	Noise Equivalent Power
NIR	Near Infra Red

O

OSA	Optical Spectrum Analyzer

P

PCG	Planar Concave Grating
PDMS	Poly DiMethylSiloxane
PEG	Poly Ethylene Glycol
PIC	Photonic Integrated Circuit
PLSR	Partial Least Squares Regression
PMF	Polarization Maintaining Fiber
PMMA	Poly MethylMethAcrylate

R

RIU	Refractive Index Unit
RMSEC	Root Mean Square Error of Calibration
RMSECV	Root Mean Square Error of Cross-Validation
RMSEP	Root Mean Square Error of Prediction

S

SIG	Signal
SLED	Superluminescent Light Emitting Diode
SMF	Single Mode Fiber
SNR	Signal to Noise Ratio
SOI	Silicon On Insulator

T

TE	Transverse-electric
TIR	Total Internal Reflection
TM	Transverse-magnetic

U

UV-VIS	Ultra-Violet-VISible

V

VCSEL	Vertical Cavity Surface Emitting Lasers

Nederlandse samenvatting –Summary in Dutch–

Diabetes is een ernstige ziekte die wereldwijd meer dan 348 miljoen mensen treft. Deze patiënten hebben een te hoge hoeveelheid aan bloedsuiker (glucose). Deze ziekte is ongeneeslijk en leidt tot vele gezondheidsproblemen doordat het de bloedvaten aantast. Wanneer grote bloedvaten worden aangetast is er een grotere kans op een hartinfarct, hersentrombose en slechte bloedcirculatie in de benen. Aantasting van de kleinere bloedvaten zorgt dan weer voor ernstige oog- en nierproblemen. Het mag duidelijk zijn dat deze ziekte de gezondheid van de patiënt sterk beinvloedt.
Om mogelijke verwikkelingen te voorkomen, wordt de patiënt aangeraden om regelmatig het bloedsuikerniveau op te meten en deze indien nodig deze bij te sturen met behulp van medicatie en/of insuline injecties. De meest gebruikte manier om het bloedsuikerniveau op te meten, is een teststrip waarop een klein druppeltje bloed wordt aangebracht. Deze test-strip wordt dan uitgelezen door een elektronisch toestel dat tevens de gemeten waarde weergeeft. Wanneer men echter het bloedsuikerniveau meerdere keren per dag wil opmeten, is deze techniek onpraktisch en pijnlijk, aangezien telkens in de vinger geprikt moet worden voor de nodige bloeddruppel. Nochtans kan de behandeling van diabetes beter op de patiënt afgestemd worden, wanneer het glucosepatroon gedurende de dag gekend is.
Om hieraan een oplossing te bieden, werden er toestellen ontwikkeld die de patiënt kan gebruiken om continu het glucoseniveau op te meten. In plaats van het bloedsuikerniveau, wordt glucose in het interstitieel vocht (het vocht tussen de cellen) opgemeten. Hierdoor moeten er geen bloedvaten doorprikt worden, wat de risico's op infecties vermindert. Via een kleine naald die de huid doorprikt, wordt de glucose in het interstitieel vocht bereikt en opgemeten. Deze glucosemeters kunnen gedurende een week op het lichaam gedragen worden en geven een alarm wanneer er te veel of te weinig glucose in het interstitieel vocht zit. Deze toestellen hebben echter nog last van enkele kinderziektes en een (te) hoge kostprijs. Daarom wordt er wereldwijd veel onderzoek gedaan naar alternatieve continue glucosemeters (CGM).

Het ontwerpen van een alternatieve glucosemeter is ook het onderwerp

Figuur 1: (a) Test-strip om het glucoseniveau in bloed op te meten. (b) Continue glucosemeter die op de huid gedragen wordt en glucose opmeet in het interstitieel vocht. (figuren overgenomen van (a) Bayer® en (b) Dexcom ®)

van dit doctoraat. De manier waarop we glucose willen detecteren is gebaseerd op de specifieke interactie van glucose deeltjes en lichtdeeltjes (fotonen). Wanneer een foton invalt op een glucose molecule, kan de molecule dit licht absorberen en de energie omzetten in een mechanische trilling. Dit gebeurt echter slechts bij welbepaalde golflengtes en niet altijd even efficient. Dit mechanisme uit zich in een uniek absorptiespectrum dat voor alle golflengtes, de verzwakking door absorberende deeltjes weergeeft. Om een absorptiespectrum op te meten maken we gebruik van een spectrometer. Eerder onderzoek toonde aan dat spectrometers zeer geschikt zijn om glucose op te meten. Een voordeel van deze techniek is dat er geen chemische reagentia nodig zijn die de meetbetrouwbaarheid op lange termijn negatief kunnen beinvloeden. Verder kunnen we op basis van het absorptiespectrum van interstitieel vocht niet alleen het glucoseniveau bepalen, maar ook de concentratie van andere absorberende biomolecules.

Terwijl de huidige CGM slechts een korte periode werkzaam zijn, stellen wij een implanteerbare CGM voor, die voor minstens een jaar betrouwbare glucose metingen oplevert. Dit betekent echter dat we een duurzame miniatuurspectrometer moeten ontwikkelen. De technologie die we hiervoor willen gebruiken is de zogenaamde silicon-on-insulator technologie. Deze technologie laat toe om miniscule optische componenten (lichtbron, detector, golfgeleider enz...) te integreren op een kleine optische chip gemaakt uit silicium, met dezelfde fabricageprocessen die gebruikt worden om (quasi alle) elektronica-chips te maken. Deze technologie laat toe om de kosten per glucosemeter sterk te drukken, terwijl we toch een hoge kwaliteit kunnen garanderen. Een voorbeeld van een geïntegreerde optische chip ziet u in figuur 2(a).

Er bestaan veel verschillende soorten spectrometers met elk hun voor- en nadelen. Hierdoor onderzochten we eerst welk type het meest geschikt is om te implanteren. Hierbij identificeerden we een spectrometer waar-

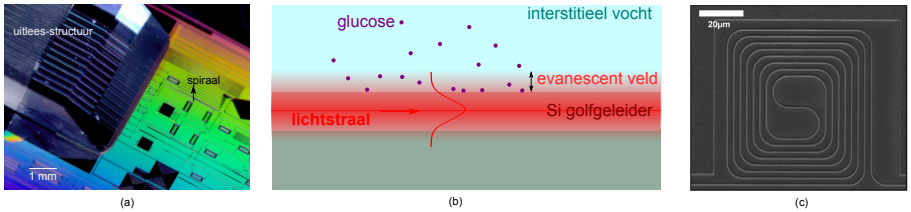

Figuur 2: (a) Geïntegreerde optische siliciumchip met uitleesstructuur om licht in en uit de optische chip te koppelen (verkregen door imec) (b) Evanescent veld van een golfgeleider, fotonen in het evanescente veld kunnen geabsorbeerd worden door de glucose deeltjes (c) Silicium golfgeleider opgekruld tot een spiraal met zeer kleine voetafdruk. Deze structuur kan gebruikt worden om glucose deeltjes te detecteren.

bij het evanescente veld van een lichtstraal, die propageert in een silicium golfgeleider, gebruikt wordt om te interageren met de glucose deeltjes. Dit evanescente veld, bestaat uit fotonen die net buiten de omtrek van de golfgeleider meepropageren met de lichtstraal (zie figuur 2(b)). Zodra een glucose deeltje in dit evanescente veld terechtkomt, kan het de evanescente fotonen absorberen en zodoende een meetbaar signaal genereren. Het onderdeel van de spectrometer waar deze evanescente interactie plaatsvindt, is een lange golfgeleider die opgekruld is tot een spiraal die minder dan een mm^2 beslaat op de optische chip (zie figuur 2(c)).
Door een druppel water met enkele glucose deeltjes op deze spiraal te leggen, kunnen we de *in vivo* context nabootsen. Het grootste verschil tussen deze *in vitro* en de *in vivo* situatie is dat een waterige glucose oplossing veel minder complex is qua samenstelling dan het interstitieel vocht in het lichaam.

Er is een grote uitdaging verbonden aan het meten van glucose op basis van het absorptiespectrum. Deze uitdaging ligt in het feit dat de fysiologische glucose concentratie zeer klein is in vergelijking met de hoeveelheid water in het interstitieel vocht. Voor elk glucose deeltje, zijn er ongeveer 10000 waterdeeltjes. Doordat al deze waterdeeltjes ook fotonen absorberen met gelijkaardige golflengtes als glucose, is het moeilijk om het absorptiesignaal van glucose te onderscheiden van dat van water. Toch is dit mogelijk, maar dan moet je wel het absorptiespectrum van interstitieel vocht opmeten met een foutenmarge van slechts 0.01% (dus correct tot op 4 cijfers na de komma!).

Een groot deel van dit onderzoek was dan ook het uitwerken van de meetopstelling en spectrometer configuratie, totdat de experimentele stabiliteit goed genoeg was om glucose op te meten.

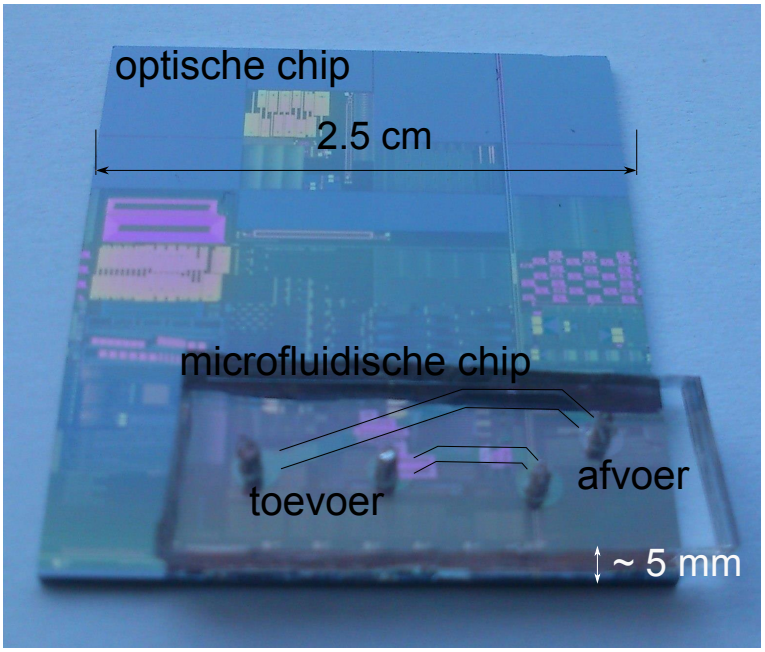

Figuur 3: Optofluidische chip bestaande uit een silicium-op-isolator chip met evanescente sensoren en een microfluidische chip gemaakt uit de polymeer PDMS. De twee microfluidische kanalen zijn aangeduid met zwarte lijnen. Het langste kanaal is het referentie-kanaal en het korste kanaal is het signaal-kanaal waardoor waterige glucose-oplossingen gepompt worden.

De glucose metingen werden uitgevoerd met een zogenaamde optofluidische chip. Dit is de combinatie van een optische siliciumchip, die de glucose sensor bevat, met erboven een microfluidische chip gemaakt uit de polymeer PDMS. Deze microfluidische chip bevat onderaan kleine kanaaltjes waarin we de verschillende glucose oplossingen kunnen aanbrengen. Een foto van deze optofluidische chip is getoond in figuur 3.

Door afwisselend water en een glucose oplossing met telkens lagere concentratie aan te leggen en het absorptiespectrum op te meten, konden we de nauwkeurigheid van onze glucosemeter bepalen. Het resultaat van deze meting is weergegeven in figuur 4(a,b).

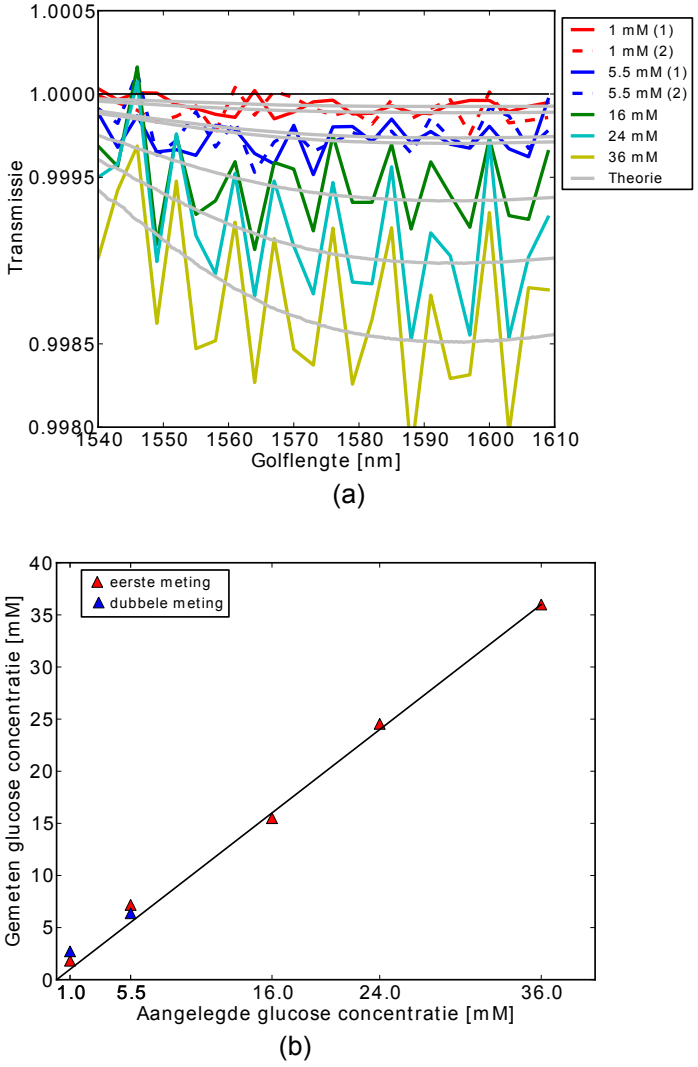

Figuur 4: (a) Glucose absorptiespectra die opgemeten werden met de optofluidische chip met de theoretisch verwachte absorptiespectra. Die laatste werden afgeleid door een lineair regressiemodel te ontwikkelen dat de gemeten absorptiespectra een glucoseconcentratie toekent. De theoretisch verwachte absorptiespectra (licht grijze curves) zijn op basis van deze afgeleide glucoseconcentraties berekend. (b) Grafische weergave van het lineaire regressiemodel dat de glucose concentraties toont die afgeleid werden uit de spectrale metingen versus de opgelegde glucose concentraties.

We behaalden een pasfout van 1.14 mM en een 95% betrouwbaarheidsinterval van 0.86 mM $\pm$ 0.86 mM, wat net voldoende is voor de continue glucosemeter toepassing. Aangezien dit resultaat enkel voor een waterige glucose oplossing geldt, hebben we ook verschillende serum stalen opgemeten met de optofluidische chip. Deze zijn meer representatief voor de geïmplanteerde glucosemeter. Uit deze serum metingen konden we afleiden dat het hoge zoutgehalte een probleem vormt voor onze sensor. We kunnen glucose nog steeds opmeten, maar de nauwkeurigheid ligt beduidend lager dan bij de eenvoudige waterige glucose stalen.

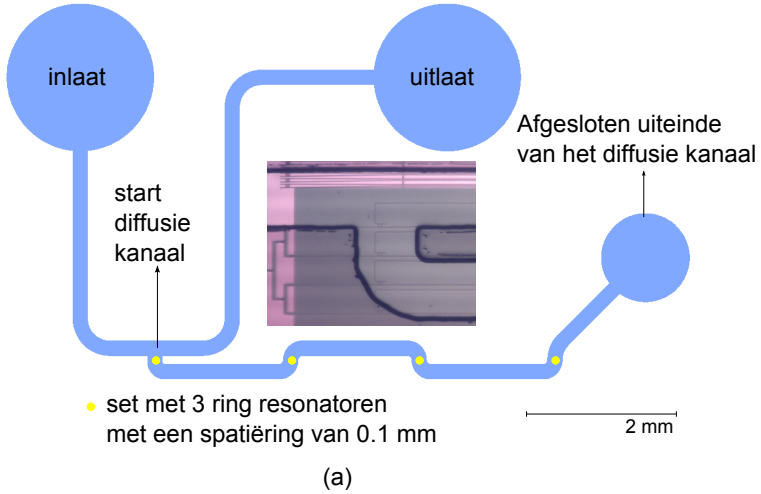

Figuur 5: Ontwerp van de optofluidische chip om glucose diffusie te bestuderen. Er is een stromingskanaal dat een lange aftakking, het zogenaamde diffusiekanaal, heeft waarin glucose via diffusie zich kan verplaatsen. Er zijn vier sets van telkens drie ring resonatoren die gebruikt kunnen worden om lokaal de tijds-evolutie van de glucose concentratie op te meten. Deze concentratiecurves worden gebruikt om de diffusiecoefficiënt van glucose nauwkeurig op te meten

Doordat de glucose deeltjes zich dicht tegen het oppervlak van de spiraalvormige golfgeleider moeten bevinden vooraleer we ze kunnen opmeten, hebben we het massatransport van glucose in water bestudeerd. Het is zo dat glucose zich verplaatst via diffusie. In dit doctoraat hebben we een nieuwe optofluidische chip ontwikkeld die toelaat om met hoge nauwkeurigheid het diffusieproces van kleine moleculen te bestuderen. Door de verandering in de glucose concentratie in de tijd en ruimte op te meten, kan de diffusie snelheid bepaald worden. Het ontwerp van deze optofluidische chip, samen met de voornaamste meetresultaten worden getoond

in respectievelijk figuur 5 en figuur 6.

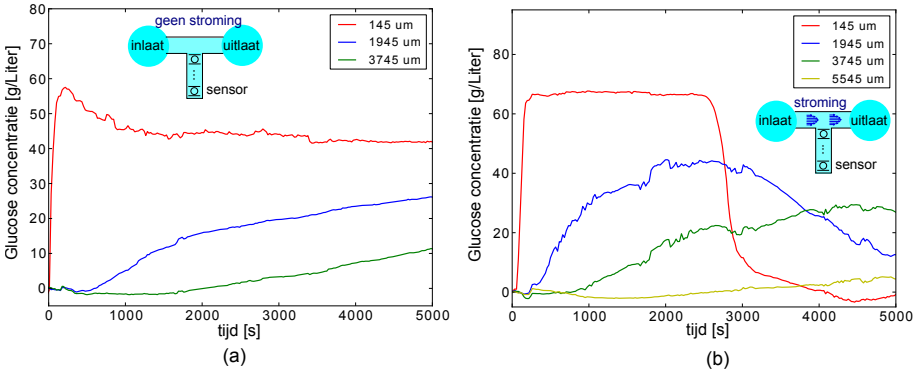

Figuur 6: Invloed van stroming in het hoofdkanaal op het massatransport van glucose in het diffusie kanaal: De concentratiegradient in geval (a) waarin er geen stroming in het hoofdkanaal is, is lager dan in geval (b) waar er een continue stroming in het hoofdkanaal is. Uit deze curves kunnen we de glucose diffusiecoefficiënt afleiden.

Verder ontwikkelden we een nieuwe techniek, die handig gebruik maakt van dit (trage) diffusieproces, om het glucosesignaal beter te kunnen opmeten met de implanteerbare glucosemeter.

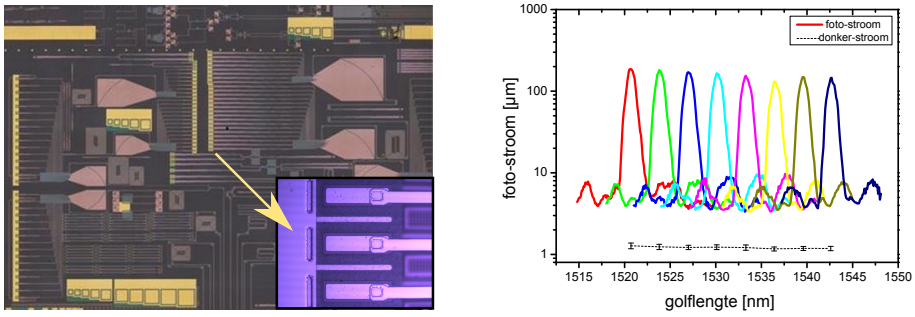

Figuur 7: (a) Microscoop beeld van de optische chip met geïntegreerde spectrometers. Onderaan worden de gebruikte lichtdetectoren getoond. (b) De fotostroom per golflengtekanaal is getoond voor een invallend vermogen van 1 mW aan de ingang van een van de geïntegreerde spectrometers.

Door het besef dat een spectrometer niet alleen als glucosemeter gebruikt kan worden, maar ook andere molecules meetbaar maakt, hebben we de spectrometer technologie zo breed mogelijk uitgewerkt (zie figuur 7 en figuur 8). Dit houdt o.a. het ontwerp in van spectrometers die een groot golflengtebereik hebben. Hoe breder het golflengtebereik, hoe meer unieke absorptie kenmerken van molecules boven komen drijven. Het resultaat van dit onderzoek was een optische chip met geïntegreerde spectrometers die werkzaam zijn in het golflengtebereik van van 1510 nm tot 2300 nm. Verder toonden we aan dat deze spectrometers nauwkeurige absorptiemetingen opleveren, ondanks dat we slechts een druppeltje staal nodig hebben.

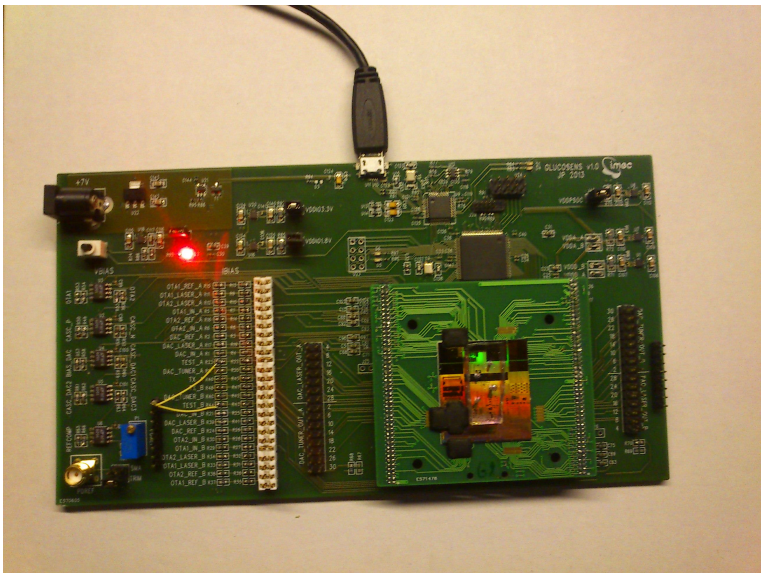

Figuur 8: Geïntegreerde spectrometer met uitleeselektronica die ontwikkeld werd tijdens het IWT-SBO GlucoSens project. De ontwikkelde spectrometer bevat evanescente sensoren, geïntegreerde fotodetectoren, microfluidische kanalen en een CMOS elektronica chip die via draadcontactering verbonden is met een printplaat.

English summary

Diabetes is a serious chronic disease that affects 347 million people worldwide. Diabetes patients have a too high blood sugar (glucose) level. This high amount of blood glucose leads to numerous health problems, as it deteriorates the blood vessels. When the larger blood vessels are affected, patients are at a larger risk for heart disease, stroke and can have blood circulation problems in the legs. In addition, when the smaller vessels are affected, serious eye problems (blindness!) and kidney disease can be expected. Diabetes clearly affects the life of patients in a detrimental way.
To avoid the aforementioned health complications, patients are advised to regularly measure their glucose level. When the glucose level is outside the healthy range, they should take medication or adjust their insulin level. The standard glucose meter is a test-strip to which a small droplet of blood is applied. This test-strip can be mounted into an electronic read-out device that will display the measured glucose concentration. Of course, patients will be reluctant to do this multiple times a day, as they have to prick their finger every time to deliver a small blood drop. Still, keeping a close eye on the glucose pattern throughout the day, allows to optimize the diabetes treatment and improves the health condition. Therefore, medical companies have invested heavily in the development of continuous glucose monitors (CGM) that patients can use for home-monitoring of their glucose level. Instead of the blood sugar level, the glucose is measured in the interstitial fluid (ISF). ISF is the fluid in between the cells. This way, it is not necessary to puncture blood vessels which reduces the risk for infections. By using a small sensor needle that is inserted into the skin, the glucose in the ISF can be accessed and measured. These CGM devices are worn onto the body for up to seven days and are set to give an alarm when the measured glucose level is too high or too low. Unfortunately, this relatively recent CGM technology still has accuracy problems, a short sensor lifespan and is not affordable for many diabetes patients. Therefore, huge research efforts are geared towards the development of alternative CGM devices.

The development of an alternative continuous glucose monitoring device is also the topic of this doctoral thesis. The measurement principle that we want to use to detect glucose relies on the specific interaction between

Figure 9: (a) test-strip to measure the blood glucose level (b) commercially available continuous glucose monitor that measures glucose in the interstitial fluid through a sensor needle that is inserted under the skin. ((a) adopted from Bayer® and (b) from Dexcom ®)

glucose and light (photons). When a photon is incident onto a glucose molecule, the latter can absorb the photon and convert the energy into a mechanical motion. This, however, happens only at a specific set of wavelengths and not all wavelengths are absorbed as efficiently. This absorption mechanism translates into a unique absorption spectrum that reflects for each wavelength by how much the light is attenuated due to absorption events. To measure an absorption spectrum we use a spectrometer. Earlier research has shown that it is possible to detect very low glucose levels based on the absorption spectrum of interstitial fluid. An important advantage of this technique is the prospect of long-term stability as it doesn't require chemical reagentia. In addition, when the transmission spectrum of ISF is measured, we can derive the concentration of other absorbing biomolecules as well.

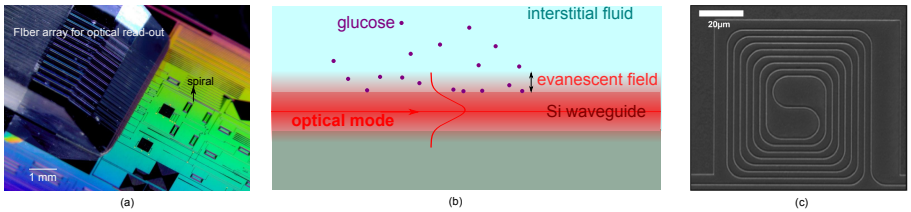

Figure 10: (a) Integrated optical silicon chip with attached fiber array for optical read-out (taken from imec) (b) Illustration of the evanescent field of an optical waveguide mode. The glucose molecules close to the waveguide surface can absorb the photons in the evanescent field (c) Silicon waveguide routed into a spiral with small footprint. This spiral is the evanescent sample interface for the implantable spectrometer.

In contrast to the present CGM devices that can only operate up to 7 days, we propose a reliable and implantable CGM device that is functional for at least one year. This, however, implies that we can develop a miniature implantable spectrometer. The technology that we will use for this miniaturized spectrometer is photonic integration using the silicon-on-insulator platform. This technology allows to integrate all optical components (light sources, detectors, waveguides etc) onto a small silicon chip with the same tools and processes that are used today to fabricate most of the electronic chips. This fabrication process opens the road to cheap, but reliable and high quality optical chips that can be implanted. An example of a silicon photonics integrated chip is shown in figure 10(a).

There is a wide variety of spectrometer concepts, each with its own benefits and disadvantages. Therefore, we started by selecting the spectrometer concept with the highest potential for the *in vivo* application. In this process, we identified a spectrometer with an evanescent sample interface. In this spectrometer configuration, glucose molecules interact with the evanescent field of an optical waveguide mode. The photons in the evanescent field propagate just outside the waveguide surface and can be absorbed by glucose molecules when they are near ($< 100nm$) to the surface. This is shown in figure 10(b). The evanescent sample interface is a long waveguide that is routed into a spiral with a total footprint smaller than 1 mm^2 (see figure 10(c)).
By applying a droplet of an aqueous glucose solution on top of this spiral, we mimic the *in vivo* situation. The main difference between this *in vitro* and the *in vivo* situation is the reduced complexity of the aqueous glucose solution, with respect to the composition of interstitial fluid.

The measurement of glucose using the absorption spectrum of ISF poses one main challenge. The physiological glucose concentration is very small compared to the water content of ISF. For every glucose molecule there are about 10000 water molecules. Because all these water molecules also absorb in the same wavelength range as glucose, it becomes difficult to differentiate the glucose signal from the water absorption. Yet the glucose signal can be retrieved, as long as the absorption spectrum is measured with an accuracy of 0.01% (thus, correct up to four digits).

A large part of the research efforts were, thus, geared towards setting up a measurement configuration with extremely good stability. Once this was achieved, we could start with sensitive glucose measurements.

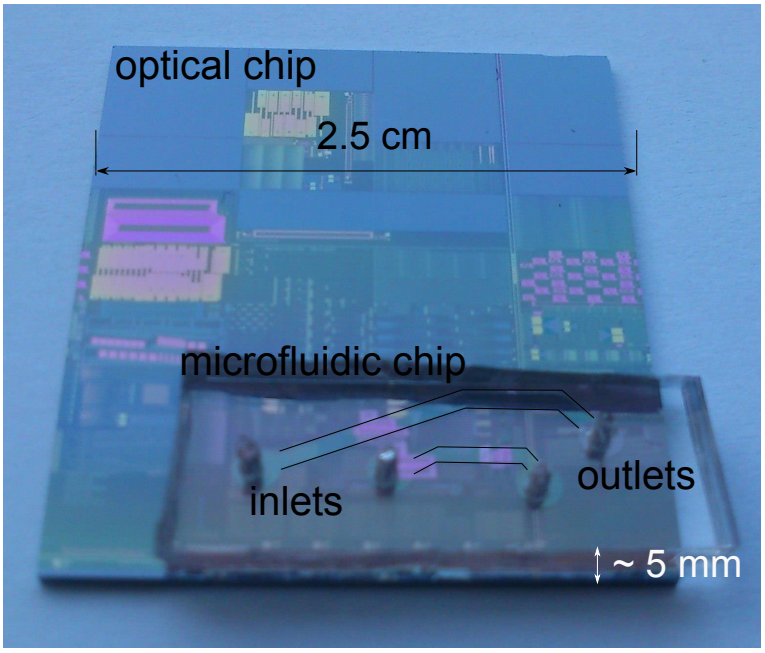

Figure 11: Opto-fluidic chip for glucose absorption spectroscopy. This optofluidic chip comprises an silicon-on-insulator optical chip with evanescent sensors and a silicone-based microfluidics chip. The latter contains a signal and reference channels which are indicated by the black lines. The signal channel is the shortest channel and is immersed with different glucose solutions.

The glucose measurements were performed with an opto-fluidic chip. This is the combination of an optical silicon chip comprising the glucose sensor with a microfluidic chip made out of PDMS. The microfluidic chip has little flow channels that can be filled with various glucose solutions. A picture of this opto-fluidic chip is shown in figure 11.

By applying pure water alternated with different glucose solutions and by acquiring the corresponding absorption spectrum, we could determine the accuracy of our glucose sensor. The result of this measurement is given in figure 12(a,b).

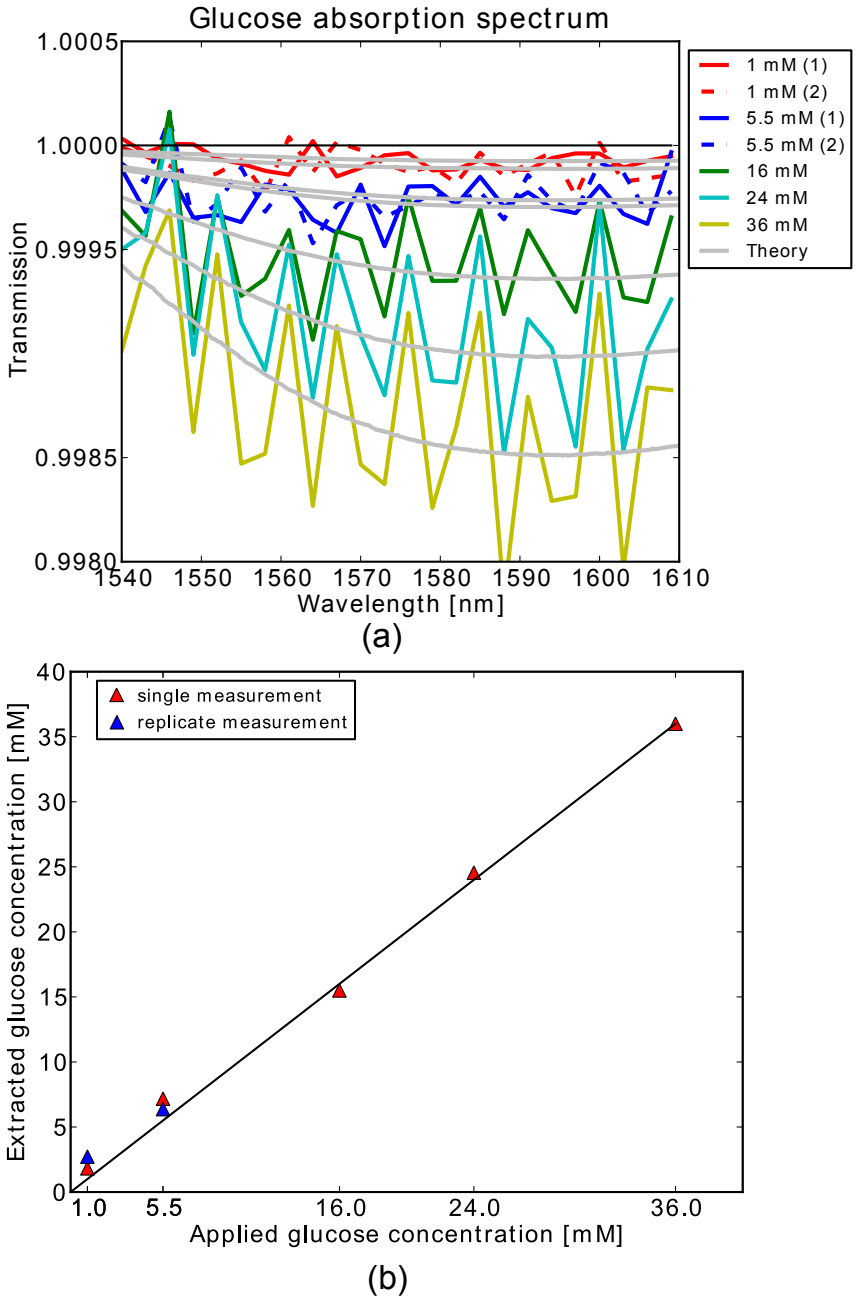

Figure 12: (a) Measured glucose absorption spectra together with the theoretically expected curves. The latter are obtained by using a linear regression model that assigns a glucose concentration for each measured spectrum. Based on these glucose concentrations, the theoretically expected curves (grey) are calculated. (b) Graphical representation of the linear regression model that shows the extracted glucose concentration compared to the glucose concentration that is applied to the opto-fluidic chip.

We achieved an error-of-fitting of 1.14 mM and 95% confidence interval of 0.86 $\pm$ 0.86 mM, which is on par with the requirements for a continuous glucose monitoring device. As this result only holds for simple aqueous glucose solutions, we also tried to measure glucose in human serum. These serum samples are more representative for the complexity of bodily fluids. From these serum measurements, we could conclude that the high salt content in serum is problematic. Although the exact cause was not identified, we found that the glucose detection accuracy drops significantly and the sensor becomes unstable due to salt.

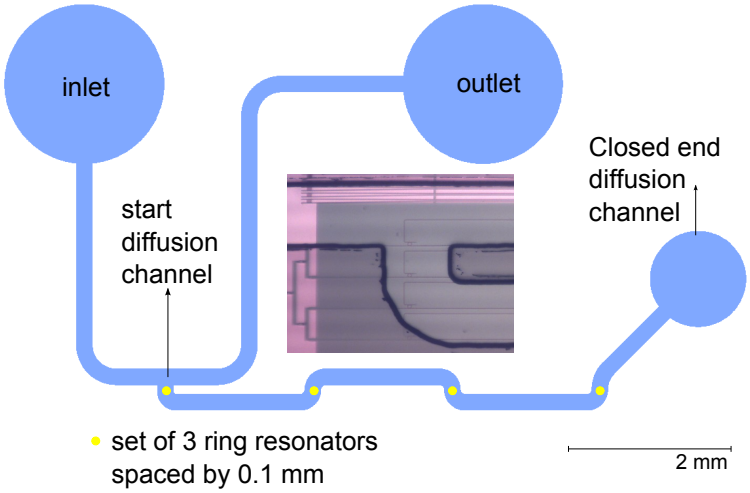

Figure 13: Design of the opto-fluidic chip that was used to study the diffusion process of small molecules in microfluidic channels. A primary channel has a branch, the so-called diffusion channel, in which glucose can diffuse. The diffusion channel comprises four sets of three ring resonators that measure locally the time-varying glucose concentration. These concentration curves are used to accurately derive the glucose concentration coefficient.

The evanescent sensing principle only works when the glucose molecules are close to the surface of the silicon waveguide. Glucose molecules can only reach this sensor surface through the process of diffusion. In this work, we developed a new opto-fluidic chip that allows to study the diffusion process of small molecules with high accuracy. By measuring the evolution in both time and space of the glucose concentration in a microfluidic channel, we can determine the diffusion speed. The design of this opto-fluidic chip, together with some important measurements are shown in figure 13 and 14.

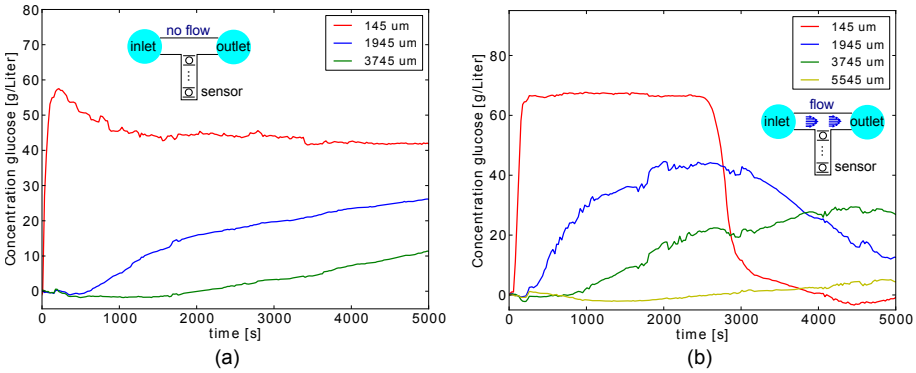

Figure 14: Influence of flow in the main channel on the glucose mass transport in the diffusion channel: The concentration gradient in case (a) when there is no flow in the main channel is larger than in case (b) when there is a continuous flow in the main channel. From these curves we accurately derive the glucose diffusion coefficient.

In addition, we show that we can use the (slow) diffusion process of glucose to more accurately measure the glucose signal in an implantable glucose sensor.

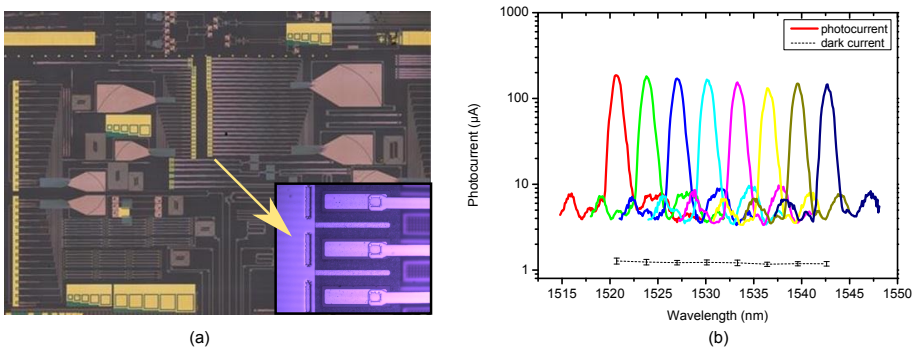

Figure 15: (a) Microscope image of the fabricated optical chip with integrated spectrometers. The used GaSb photodiodes are highlighted. (b) photocurrent for all wavelength channels for an input power of 1 mW at the entrance of one of the integrated spectrometers

Given that a spectrometer can as well be used to detect other bio-molecules apart from glucose, we targeted a generic spectrometer platform for a wide application range (see figure 15 and figure 16). This includes the development of spectrometers operating over a wide wavelength range. When the wavelength range is increased, we can access more molecule-specific absorption features which improves the detection limit. We succeeded in the design and fabrication of an optical silicon chip with integrated spectrometers that are operational from 1510 nm up to 2300 nm. In addition, we demonstrated that these integrated spectrometers can be used for sensitive absorption analysis of only a small sample droplet.

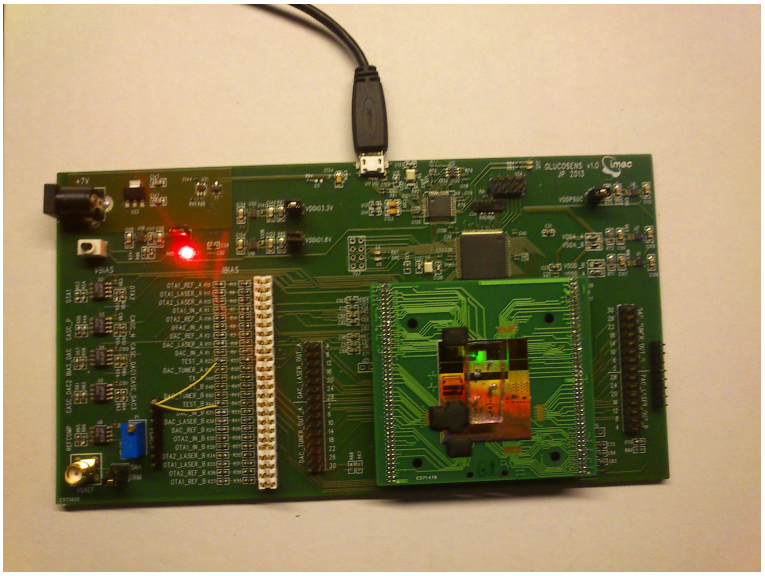

Figure 16: Integrated spectrometer with electronic read-out that was developed during the SBO-IWT GlucoSens project. The developed spectrometer comprises evanescent spiral sensors, integrated photodiodes, microfluidics and a CMOS electronics chip that is wire-bonded to a printed circuit board (PCB).

1 Introduction

1.1 Continuous Glucose Monitoring

Diabetes is a serious chronic disease that affects 347 million people worldwide. Typical symptoms of diabetes include frequent urination, strong thirstiness, blurry vision, extreme fatigue and so on. Patients with diabetes have a too high blood sugar level. This causes a myriad of health problems such as kidney disease, eye problems (glaucoma, cataract etc), nerve damage, high risk for heart disease and stroke. The high blood glucose level can be caused by a malfunction of the pancreas to produce enough insulin (type 1 diabetes) or when the body is insulin-resistant (type 2). Without insulin, cells do not take up glucose from the blood, leading to the increased blood glucose level.

Major clinical trials have demonstrated that tight control of the blood glucose level reduces the health complications and reduces the overall cost of treatment [1, 2, 3]. Continuous glucose monitoring (CGM) is crucial for this glycemic control. CGM is the regular measurement of the glucose concentration in either blood or the interstitial fluid (ISF), the fluid in between cells. These measurements can give insight in the patient-specific glucose pattern throughout the day. In addition, by providing trend information, CGM can predict the onset of unwanted periods with very low (hypo-glycemia) or very high (hyper-glycemia) blood glucose levels. This way, continuous monitoring gives the necessary information to optimize the diabetes treatment.

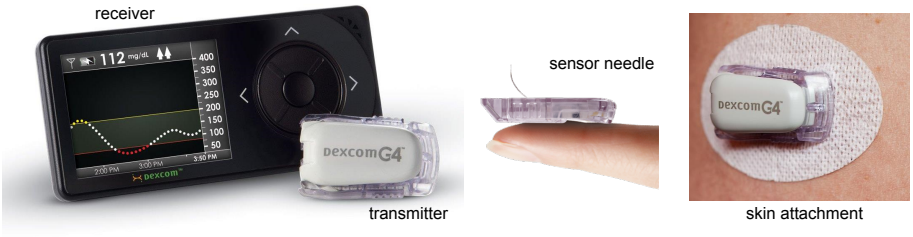

Figure 1.1: Illustration of a commercially available CGM device (adapted from Dexcom®)

Current status of CGM devices

Given the huge number of diabetes patients worldwide, the development of CGM devices attracts a lot of attention by research labs and medical companies. A CGM device typically consists of a sensor, a transmitter and a receiver that stores and/or displays the glucose measurements. When the patient nears a set upper or lower glucose level, a safety alarm signal is given by the CGM device. An example CGM device is shown in figure 1.1. Currently, only three companies (Dexcom, Abbott and Medtronic) market a CGM device for home monitoring. In all these CGM devices, a needle is used to insert the glucose sensor subcutaneously (under the skin). The actual glucose sensor is a thin, flexible wire that detects glucose in the interstitial fluid instead of in blood. The operation of the sensor is based on an electro-chemical reaction with the enzyme glucose-oxidase[4]. These CGM devices are termed minimally invasive as only the skin but no blood vessels are punctured.

Although CGM improves the diabetes treatment, there is a limited uptake of the continuous glucose monitors by diabetes patients. This is attributed to a few key disadvantages of the present CGM devices:

- The CGM system doesn't replace the traditional blood glucose meter based on test-strip technology. The suppliers clearly state that the continuous sensors readings may not be used for direct treatment decisions[5]. Moreover, the CGM system needs a calibration with a blood glucose meter every 12 hours, as it cannot provide absolute glucose readings.
- The limited sensor accuracy (average difference of 10-20% with blood glucose reference sensors), leads to false alarms and distrust in the CGM system[6, 7].
- The sensor lifespan is limited to 3 to 7 days. This is attributed to the

complex in vivo setting with biofouling, foreign body response and enzyme degradation. These effects render the sensor insensitive over time[8, 9, 10].

- The present cost of a CGM system is a major disadvantage. The price per person-year is 2.5 times higher compared to test-strip technology [11].

Moreover, there are additional problems, although patient-specific, with respect to the size of the CGM system, the pain and or irritation with the sensor insertion needle, discomfort and or reliability issues during physical activity etc.

Proposed solutions for future CGM devices

Many companies and research labs are developing new strategies to overcome the current limitations of continuous glucose monitoring devices. In the review paper [10], existing but non-commercial CGM technologies are compared with respect to their detection mechanism, invasiveness and prospects for future diabetes management. These sensor technologies can be classified as shown in figure 1.2. It is clear that a wide variety of transducer mechanisms can be used to measure glucose. Although it is impossible to argue which of these technologies will be the most successful, general risks for each of them can be stated.
Electrochemical sensors are very sensitive and glucose-specific, but the need for chemical reagents is a large risk for long-term operation. A similar argument holds for fluorescence based methods, but now the background fluorescence of interfering molecules adds to the complexity of a reliable glucose sensor. The methods listed as 'combinatorial' in figure 1.2 have problems with good specificity for glucose, unless chemical reagents are used. The direct optical methods offer the best prospects for long-term stability of the sensor. On the other hand, demonstration of high sensitivity and specificity becomes a greater challenge for these sensors. Next to the effectiveness of the transducer mechanism and long-term operation, the prospect for future miniaturization plays a key role. A smaller sensor will lead to better acceptance by the body and maximizes the patients' comfort.

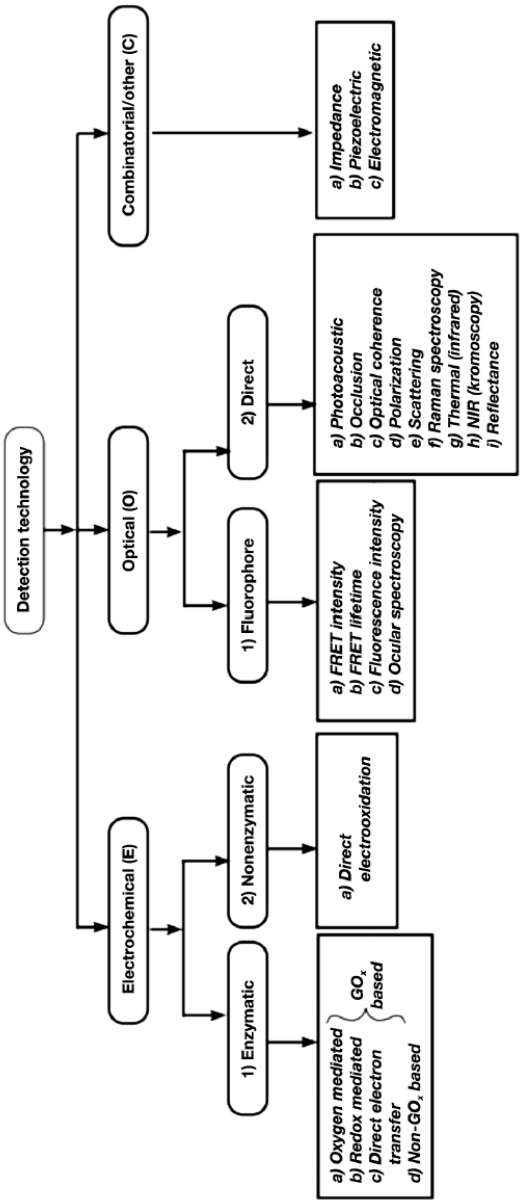

Figure 1.2: Overview of transducer mechanisms to detect physiological glucose levels (taken from [10])

1.2 Glucose detection using near-infrared absorption spectroscopy

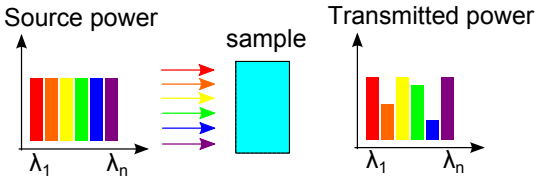

Figure 1.3: Principle of absorption spectroscopy

One promising direct optical detection method is near-infrared (NIR) absorption spectroscopy (see figure 1.3). In this method, a NIR light source illuminates a sample containing glucose and the transmission of the light is spectrally analyzed. When glucose is present, the transmission spectrum shows dips at specific wavelengths. These dips occur because the glucose molecules have absorbed photons with these wavelengths and converted the photon energy into mechanical motion. This technique doesn't require chemical reagents and obtains glucose specificity through its unique absorption spectrum. Moreover, it offers the prospects of long-term operation and the simultaneous detection of other bio-molecules.

Using this technique, reliable and specific glucose measurements are possible *in vitro* in both serum[12], whole blood[13, 14, 15, 16] and ISF solutions[17, 18, 19]. Driven by this success, researchers tried to measure glucose *in vivo* by measuring the spectrum of NIR light reflected of the human skin [20, 21, 22]. It was found that glucose could still be measured, but with a smaller accuracy due to the skin barrier that induces strong light scattering and unwanted variations in the optical signal[23, 24]. In addition, the location and contact pressure of the sensor onto the skin impacted the measurement results[25, 26]

It became a research question whether these problems could be solved by measuring inside the body, rather than from outside. This, however, requires an implantable sensor comprising a miniature absorption spectrometer. In addition, the implant should contain the electronic transmitter to send and receive data from outside. Luckily, the miniaturization of the transmitter is a more generic problem that has been successfully solved before [27, 28]. Nonetheless, only a few technologies can be used to realize a spectrometer that is small enough to be implanted. Integrated photonics (optics) is one of them. Similar to integrated electronics, the incredible small size of the individual components and reliable, self-aligned fabrication process, opens the road to complex optical functionalities on a

single semi-conductor chip. This means that using integrated optics, the complete miniature spectrometer can be integrated onto a thin, flat piece of semi-conductor material, small enough for implantation. In this work, we investigated if a miniature spectrometer integrated onto a silicon chip is suitable for an implantable continuous glucose monitoring device that measures glucose in the interstitial fluid.

1.3 Implantable glucose sensor based on silicon photonics

1.3.1 Silicon photonics

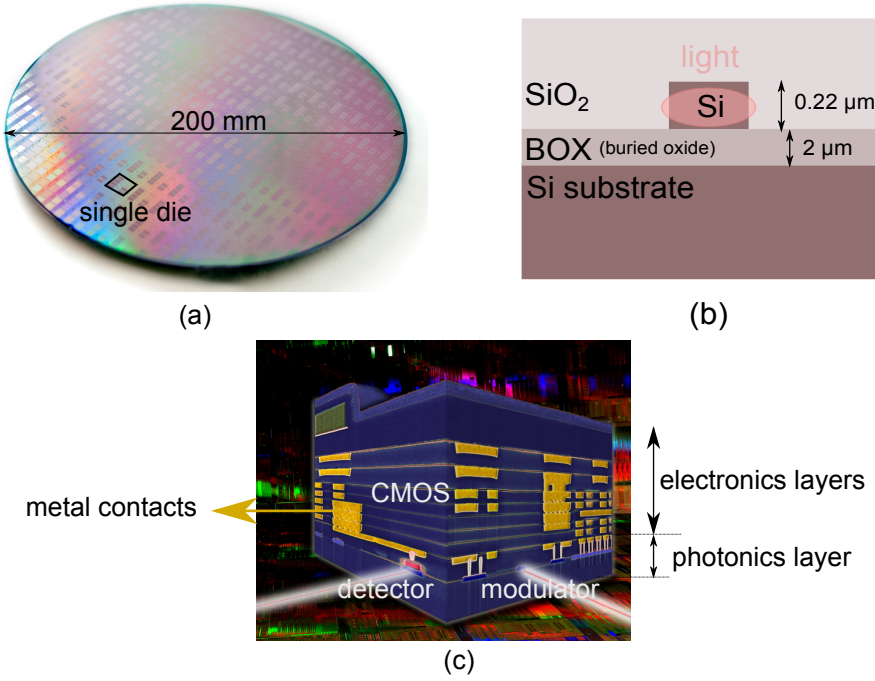

Figure 1.4: Silicon Photonics technology: (a) SOI wafer (b) SOI waveguide (c) co-integration with CMOS electronics ((a) adapted from website imec and (c) from IBM®)

The semi-conductor silicon is widely adopted as the standard base material for electronic integrated circuits (IC). This material can also be used for integrated photonics and this technology is commonly referred to as silicon photonics. The silicon photonics platform allows to fabricate pho-

tonic integrated circuits (PIC) with the same excellent tools and materials that the electronics industry has developed over the course of fifty years. Due to this high yield mass-fabrication process, the price per silicon chip is minimal.

In silicon photonics, the silicon-on-insulator (SOI) material system is used, in which the light-guiding layer consists of a thin layer of silicon that lies on top of a thick layer of silica. This material system is transparent for a wide wavelength range from 1.1 to 3.5 μm. The basic optical component is an optical waveguide that guides light based on the principle of total internal reflection (TIR). Due to the high (refractive) index contrast between silicon and silica, the TIR principle still holds for waveguides with submicron dimensions. This ensures that we can dramatically reduce the PIC footprint compared to other integrated photonics technologies that use a different base material system. Moreover, given the similar fabrication process of both the photonics and electronics circuits, it is possible to fabricate them together on a single silicon chip. This high level of integration has been demonstrated by e.g. the company IBM (see figure 1.4). This offers prospects for the co-integration of the transmitter of the glucose sensor with the miniature spectrometer. The benefits of a low cost, reliable, small optical chip with co-integrated electronics, make the silicon photonics platform very attractive for this glucose sensing application.

1.3.2 Sensor configuration

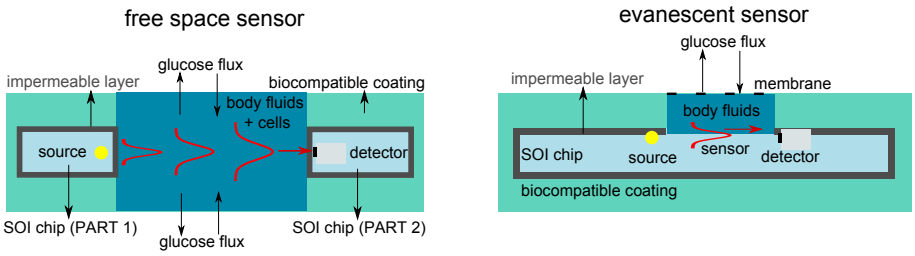

Figure 1.5: Cross-section of an implantable free space sensor and evanescent sensor

For the glucose monitoring application, the miniature absorption spectrometer can exist in two distinct optical configurations. The first is called the 'free-space' configuration and the second is the 'evanescent' configuration. Both are shown in figure 1.5. In a free-space sensor, the NIR light is coupled out of the silicon chip into a slab of tissue with glucose molecules and captured back into the chip for spectral analysis. In the evanescent sensor, the light never leaves the photonic chip. The interaction between the

light and the glucose molecules happens through the evanescent field of a waveguide mode. This evanescent field is the fraction of the optical mode that extends out of the waveguide core. Due to the typical waveguide dimensions and the high index contrast of the silicon photonics platform, the evanescent field of the waveguide mode is very sensitive to changes that take place close ($<$ 100 nm) to the waveguide's surface. If a glucose molecule is present close to the waveguide's surface, it will absorb the evanescent field photons of specific wavelengths.

1.3.3 Challenges

In order to demonstrate a miniature spectrometer for continuous glucose monitoring on a silicon chip, we face a number of challenges. These challenges can be divided into three main categories. The first type of challenges is related to the sensing principle itself. Can we measure glucose accurately enough in vivo? The main difficulty is the dominant NIR absorption due to water molecules, which make up the largest part of the interstitial fluid (ISF). If we compare the pure water concentration at 37°C (55138 mM [29]), with the typical glucose concentration (5.5 mM), we immediately understand that, although glucose has 10 times more absorbing bonds, the contribution of the glucose molecules to the ISF transmission spectrum is minimal. Thus, a very sensitive spectrometer is needed to extract the glucose signal from a large background. In addition, ISF is a complex fluid with a varying content of other absorbing bio-molecules such as proteins. These interferents also contribute to the ISF transmission spectrum. Therefore, careful data analysis is needed to separate the contribution from glucose and these interferents.

The second type of challenges relate to the integration of a spectrometer onto a silicon chip. While the silicon photonics platform offers many benefits, the indirect band gap of silicon makes the material unfit for light generation and detection beyond 1.1 μm. This means that additional materials have to be integrated on top of the silicon chip to serve as a light source and detector for the miniature spectrometer. Given the stringent sensitivity requirements of the spectrometer, these sources and detectors need to be of high quality. In addition, they have to be processed in a cheap and reliable way to serve in an implant for CGM.

A final category of challenges originates from the interaction of the miniature sensor with the human body. As for all implants, special care needs to be taken to guarantee the glucose supply to our sensor. If our sensor induces an inflammatory response, it will quickly be encapsulated with a dense tissue type that limits the glucose entry. In addition, as we measure glucose in the ISF instead of blood, a delay in glucose level can be expected between both. As the blood glucose concentration is used for therapeutic

decisions, this delay can be perceived as sensor inaccuracy. Care should thus be taken to optimize the sensor design such that the delay is minimized.

1.4 Thesis objectives

The overall goal of this work was to develop a spectroscopic sensor that can detect changes in the physiological concentrations of glucose and that can be fabricated using Silicon photonics technology. This research goal was strongly linked to the IWT-SBO GlucoSens project in which the different building blocks for an implantable continuous glucose monitoring device were developed. More about this project can be found in the appendix A.

Three main objectives are targeted:

- Extension of the operating wavelength range of SOI spectrometers to cover the first overtone band (1500-1850 nm) and combination band (2000-2500 nm).
- Development of a glucose sensor with an operating range from 3-20 mM and accuracy of 1 mM.
- Realization of a spectroscopic sensor configuration suitable for implantation.

The first objective consists of two parts. Firstly, we target the development of passive spectrometer components for longer wavelengths than typically addressed with Si photonics technology (1450-1600 nm). Secondly, the combination of passive with active spectrometer components is covered in this work to investigate the potential of this technology for spectroscopic applications. The development and fabrication of active spectrometer components itself (source, detectors) was the research subject of Dr. Nannicha Hattasan. The second objective targets the accurate measurement of small changes in the physiological glucose concentrations which are relevant for diabetes patients. The last objective comprises the analysis of the impact of the dynamic *in vivo* setting on the spectroscopic sensor design. This translates into the need for a power budget analysis, a solution for potential sensor delay due to slow diffusion of glucose to the sensor and a solution for an *in vivo* reference arm to reduce the impact of physiological variations in temperature and interfering bio-molecules.

1.5 Thesis outline

This doctoral thesis is outlined as follows: We start in chapter 2 with an introduction to absorption spectroscopy and explain the challenges involved for the spectral detection of glucose. In chapter 3 we discuss the possible spectroscopic sensor configurations, given the constraints of an *in vivo* implant with a special focus on the power budget. Given that an evanescent spectroscopic sensor was pursued, we introduce the theory of evanescent sensing in chapter 4. This is followed by chapter 5 with a description of the spectrometers that are developed in this work. In addition, chapter 5 contains the results of our non-glucose related detection experiments, showing the general potential of the miniature spectrometers for sensing applications. The glucose absorption spectroscopy experiments are divided over the two next chapters 6 and 7. In chapter 6, the focus is on the experimental configuration that allowed reliable glucose detection. We then proceed to chapter 7, that focuses on the transfer of this configuration to the *in vivo* situation. Finally, in chapter 8 we discuss a newly developed measurement technique to study glucose diffusion. Finally, we conclude this work in chapter 9.

1.6 Own Contributions

The work listed in this doctoral thesis covers the research that was conducted over a period of 4,5 year, during which the author was part of the Photonics Research Group (PRG) and the GlucoSens project consortium. This means that this work strongly depended on the research knowledge, infrastructure and discussions with members of both teams. In terms of software infrastructure, the author used the available ipkiss and pymeasure framework developed by the PRG for all optical and microfluidic designs and measurement scripts. This framework is based on the open source programming language Python. This way, the author could easily implement custom functions and scripts for this research.

In what follows, for each chapter is listed what was specifically done by other people and how the author contributed.

The content of the introductory chapter 2, combines information both from literature and results from the GlucoSens project. The latter include a short summary of the research results on multivariate calibration from the GlucoSens partner Mebios (section 2.4). Discussions with them shaped the classification of the listed bio-molecules (e.g. proteins) as interferents and listed temperature as an important parameter. The absorptivity spectrum of the various bio-molecules, used to discuss SNR requirements, was measured by Mebios. The other listed GlucoSens results are deduced by the

author.
In chapter 3, the free-space and evanescent sensor configurations are discussed in terms of their *in vivo* potential. The free-space configurations were in the original GlucoSens proposal, while the modified free-space (with membrane) and the evanescent configuration are first proposed in this work after valuable input from prof. Joris Delanghe. The exploration of these new configurations was done by the author. All the listed work on the biocompatible materials PMMA, PDMS and membrane integration was done by the GlucoSens partners except for the optical transparency measurements of these PMMA, PDMS materials and the agarose hydrogel samples.
Chapter 4 gives a theoretical and practical overview of evanescent sensing using SOI waveguides. The given theoretical derivation is based on a literature study. All listed simulations and measurements are performed by the author.
In chapter 5, planar concave grating (PCG) based spectrometers are discussed. The simulation and design framework for PCGs was developed by former PhD student Joost Brouckaert. The author used his simulation code and adapted the ipkiss design code to develop PCG's in the combination band. The development of other passive photonic components for the combination band was a joint effort of the mid-IR team of the PRG. The largest contribution of the author to this effort, was the development of three different grating coupler designs that can be fabricated in a standard passives process. These designs were the result of many discussions with former PhD student Diedrik Vermeulen. All simulations and passive characterizations listed in this chapter are done by the author, except for the advanced passive grating coupler results and wire waveguide loss measurements. The photodiode design and fabrication was done by PRG members Alban Gassenq, Nannicha Hattasan (both GaSb-based photodiodes) and Steven Verstuyft (InP-based photodiodes). The contact mask design, development of the measurement set-up and electro-optical characterization of the photodiodes were done by the author. The TIA design of the probe-card that was used to measure multiple photodiodes in parallel was done by Jeroen Allaert. The read-out of the probe-card required the incorporation of a data acquisition card in the pymeasure framework. This was programmed by PRG member Michael Vanslembrouck. All measurements with the probe-card and subsequent data analysis are performed by the author. The development of GlucoSens demo 4, the combination of an optical chip with microfluidics and integrated photodiodes with electronics, was a joint GlucoSens effort. The author designed the passive optical chip and microfluidics, performed the electro-optical characterization and fabricated the microfluidics.
In chapter 6, the fully automated glucose measurement set-up and detection results is discussed. All fabrication steps, measurements and data analysis are performed by the author. The author achieved remote con-

trol of the temperature controller, microfluidics pump and valve, thanks to efforts of both Ronny Bockstaele and Michael Vanslembrouck. Ronny Bockstaele also introduced the concept of the virtual water elimination. The algorithm and implementation of the virtual water procedure in software for data analysis, was developed by the author.
In chapter 7, a dual-beam sensor configuration with suitable reference arm for *in vivo* glucose detection is introduced. The theoretical work described in this chapter was the result of intensive discussions with PRG prof. Roel Baets. All fabrication steps, measurements and data analysis are performed by the author.
Finally, chapter 8 reports on a new method to measure the diffusion of small molecules using an opto-fluidic chip. The measurement concept was first explored experimentally by Agnes Lee, a master thesis student of prof. Roel Baets and the author. The author performed additional experiments with an improved microfluidics design and implemented the data analysis procedure to extract the diffusion coefficient. This data analysis procedure was the result of intensive discussions with prof. Jan Vierendeels from the department of Flow, Heat and Combustion Mechanics at Ghent University. He also performed 3D simulations of the complete opto-fluidic chip that were essential to gain insight in the experimental results. The used optical chip was originally designed by former PhD student Katrien De Vos for another application. The complete measurement set-up and data acquisition was previously developed by the bio-sensing team of the PRG and optimized by PhD student Sam Werquin.

1.7 Publications

The results obtained within this work have been published in various papers and presented at various conferences. This paragraph gives an overview of the publications. They can also be found in the publication section of the photonics research group website: `http://photonics.intec.ugent.be/publications`.

The following papers have been published in international peer reviewed journals or are submitted/accepted for publication:

1. E.M.P. Ryckeboer, R. Bockstaele, M. Vanslembrouck, R. Baets, "Glucose sensing by waveguide-based absorption spectroscopy on a silicon chip", Biomedical optics express, 5(5), p.16361648 (2013)

2. E.M.P. Ryckeboer, J. Vierendeels, A. Lee, S. Werquin, P. Bienstman, R. Baets, "Measurement of small molecule diffusion with an optofluidic silicon chip", Lab on a Chip, 13(22), p.4392 - 4399 (2013)
3. G. Roelkens, U.D. Dave, A. Gassenq, N. Hattasan, C. Hu, B. Kuyken, F. Leo, A. Malik, M. Muneeb, E.M.P. Ryckeboer, D. Sanchez, S. Uvin, Z. Hens, R. Baets, Y. Shimura, F. Gencarelli, B. Vincent, R. Loo, J. Van Campenhout, L. Cerutti, J.B. Rodriguez, E. Tournie, X. Chen, M. Nedeljkovic, "Silicon-based photonic integration beyond the telecommunication wavelength range", IEEE Journal of Selected Topics in Quantum Electronics (invited), 20(4), p.8201511 (2014).
4. G. Roelkens, U.D. Dave, A. Gassenq, N. Hattasan, C. Hu, B. Kuyken, F. Leo, A. Malik, M. Muneeb, E.M.P. Ryckeboer, S. Uvin, Z. Hens, R. Baets, "Silicon-based heterogeneous photonic integrated circuits for the mid-infrared", Optical Materials Express (invited), 3(9), p.1523-1536 (2013)
5. M. Muneeb, X. Chen, P. Verheyen, G. Lepage, S. Pathak, E.M.P. Ryckeboer, A. Malik, B. Kuyken, M. Nedeljkovic, J. Van Campenhout, G. Mashanovich, G. Roelkens, "Demonstration of silicon on insulator mid-infrared spectrometers operating at 3.8um", Optics Express, 21(10), p.11659-11669 (2013)
6. E.M.P. Ryckeboer, A. Gassenq, M. Muneeb, N. Hattasan, S. Pathak, L. Cerutti, J-B Rodriguez, E. Tournie, W. Bogaerts, R. Baets, G. Roelkens, "Silicon-on-insulator spectrometers with integrated GaInAsSb photodiodes for wide-band spectroscopy from 1510 to 2300 nm", Optics Express, 21(5),p.6101-6108 (2013)
7. N. Hattasan, B. Kuyken, F. Leo, E.M.P. Ryckeboer, D. Vermeulen, G. Roelkens, "High-efficiency SOI fiber-to-chip grating couplers and low-loss waveguides for the short-wave infrared", IEEE Photonics Technology Letters, 24(17), p.1536-1538 (2012)
8. K. Van Acoleyen, E.M.P. Ryckeboer, W. Bogaerts, R. Baets, "Efficient Light Collection and Direction-Of-Arrival Estimation using a Photonic Integrated Circuit", IEEE Photonics Technology Letters, 24(11), p.933-935 (2012)

The following papers have been presented at international conferences and are published in the conference proceedings:

9. R. Bockstaele, E.M.P. Ryckeboer, N. Hattasan, Y. De Koninck, M. Muneeb, S. Verstuyft, D. Delbeke, W. Bogaerts, G. Roelkens, R. Baets, "Glucose sensing by means of silicon photonics", accepted for publication in *Photonics West 2014*.

10. G. Roelkens, U.D. Dave, A. Gassenq, N. Hattasan, C. Hu, B. Kuyken, F. Leo, A. Malik, M. Muneeb, E.M.P. Ryckeboer, S. Uvin, Z. Hens, R. Baets, Y. Shimura, F. Gencarelli, B. Vincent, R. Loo, J. Van Campenhout, L. Cerutti, J. Rodriguez, E. Tournie, X. Chen, M. Nedeljkovic, G.Z. Mashanovich, L. Shen, N. Healy, A.C. Peacock, X. Liu, R. M. Osgood, W. Green, "Mid-IR heterogeneous silicon photonics", Photonics West 2014 (invited), 899316, (2013)
11. C. Hu, A. Gassenq, E.M.P. Ryckeboer, Yolanda Justo, Zeger Hens, G. Roelkens, "Colloidal PbS Quantum Dot Photodetectors for Short-wave Infrared applications", Proceedings of the 2013 Annual Symposium of the IEEE Photonics Society Belenux Chapter, Netherlands, p.41-44 (2013)
12. E.M.P. Ryckeboer, R. Bockstaele, R. Baets, "Absorption spectroscopy of glucose based on a silicon photonics evanescent sensor", IEEE photonics conference 2013 (IPC), United States, p.paper TuA2.4 (2013)
13. M. Muneeb, X. Chen, E.M.P. Ryckeboer, A. Malik, G. Mashanovich, G. Roelkens, "Silicon-o-insulator mid-infrared planar concave grating based (de)multiplexer", IEEE Photonic Conference 2013 (IPC), United States, p.paper MF 1.2 (2013)
14. N. Le Thomas, A. Dhakal, F. Peyskens, A. Subramanian, T. Claes, K. De Vos, E.M.P. Ryckeboer, R. Bockstaele, P. Bienstman, R. Baets, "Biological sensing with integrated silicon and silicon nitride photonics", The 2nd BioPhotonics Conference (invited), Taiwan, p.28-29 (2013)
15. G. Roelkens, B. Kuyken, F. Leo, N. Hattasan, E.M.P. Ryckeboer, M. Muneeb, C. Hu, A. Malik, Z. Hens, R. Baets, Y. Shimura, F. Gencarelli, B. Vincent, R. Loo, P. Verheyen, G. Lepage , J. Van Campenhout, L. Cerutti, J.B. Rodriguez, E. Tournie, X. Chen, M. Nedeljkovic, G. Mashanovich, X. Liu, W. Green, "Long-wavelength III-V/silicon photonic integrated circuits", Advanced Photonics - OSA Optics & Photonics Congress (invited), United States, p.paper IT2A.1 (2013)
16. E.M.P. Ryckeboer, A. Gassenq, N. Hattasan, Cerutti, Laurent, Rodriguez, J.B., Tournie, Eric, R. Baets, G. Roelkens, "Silicon-on-insulator spectrometers with integrated GaInAsSb photodiode array for wideband operation from 1500 to 2300 nm", CLEO, United States, p.paper JW2A.69.pdf (2013)
17. R. Baets, A. Subramanian, A. Dhakal, S. Selvaraja, K. Komorowska, F. Peyskens, E.M.P. Ryckeboer, N.A Yebo, G. Roelkens, N. Le Thomas, "Spectroscopy-on-chip applications of silicon photonics", Photonics West (invited), 8627(01), United States, p.86270I-1 - 86270I-10 (2013)

18. E.M.P. Ryckeboer, A. Lee, S. Werquin, J. Vierendeels, P. Bienstman, R. Baets, "Investigation of glucose diffusion using an optofluidic silicon chips", Proceedings of the 2012 Annual Symposium of the IEEE Photonics Society Belenux Chapter, Belgium, p.179-182 (2012)
19. E.M.P. Ryckeboer, A. Gassenq, N. Hattasan, B. Kuyken, Cerutti Laurent, Rodriguez Jean-Baptiste, Tournie Eric, G. Roelkens, W. Bogaerts, R. Baets, "Integrated spectrometer and integrated detectors on Silicon-on-Insulator for short-wave infrared applications", CLEO, United States, p.CTu1A.3 (2012)
20. E.M.P. Ryckeboer, W. Bogaerts, R. Baets, "Silicon photonics based evanescent sensor for absorption spectroscopy of glucose", XI Conference on Optical Chemical Sensors and biosensors (EUROPTRODE XI), Spain, p.37 (2012)
21. K. Van Acoleyen, E.M.P. Ryckeboer, K. Komorowska, R. Baets, "Light collection from scattering media in a silicon photonics integrated circuit", IEEE Photonics Conference 2011 (IPC11), United States, p.543-544 (2011)
22. E.M.P. Ryckeboer, N. Hattasan, G. Morren, D. Delbeke, W. Bogaerts, R. Baets, "Power budget considerations for in vivo continuous glucose monitoring using absorption spectroscopy", Proceedings of the 2010 Annual Symposium of the IEEE Photonics Benelux Chapter, Netherlands, p.253-256 (2010)
23. G. Roelkens, N. Hattasan, E.M.P. Ryckeboer, D. Delbeke, D. Van Thourhout, R. Baets, "Lab-on-a-chip approach based on heterogeneous III-V/silicon photonic integrated circuits for bio-medical applications", European Optical Society topical meeting on biophotonics, France, (2010)
24. G. Roelkens, N. Hattasan, E.M.P. Ryckeboer, D. Delbeke, D. Van Thourhout, R. Baets, "Integrated III-V semiconductor/silicon photonic integrated circuits for bio-medical applications", Optics within Life Sciences, Canada, p.S7-p4 (2010)

Parts of this work were the subject of a patent application.

- 'Implantable Sensor' European patent application number PCT/EP2010/063263 filed on 9 September 2010

- 'Implantable Sensor' US patent application number US13/415,392 filed on 8 March 2012

- 'Sensing of Components in Liquids' US patent application number US14/091.645 filed on 27 November 2013

References

[1] Irl B Hirsch, Dana Armstrong, Richard M Bergenstal, Bruce Buckingham, Belinda P Childs, William L Clarke, Anne Peters, and Howard Wolpert. *Clinical application of emerging sensor technologies in diabetes management: consensus guidelines for continuous glucose monitoring (CGM)*. Diabetes technology & therapeutics, 10(4):232–246, 2008.

[2] Robert A Vigersky, Stephanie J Fonda, Mary Chellappa, M Susan Walker, and Nicole M Ehrhardt. *Short-and long-term effects of real-time continuous glucose monitoring in patients with type 2 diabetes*. Diabetes Care, 35(1):32–38, 2012.

[3] Dorothee Deiss, Jan Bolinder, Jean-Pierre Riveline, Tadej Battelino, Emanuele Bosi, Nadia Tubiana-Rufi, David Kerr, and Moshe Phillip. *Improved glycemic control in poorly controlled patients with type 1 diabetes using real-time continuous glucose monitoring*. Diabetes care, 29(12):2730–2732, 2006.

[4] Joseph Wang. *Electrochemical glucose biosensors*. Chemical reviews, 108(2):814–825, 2008.

[5] Dexcom ®. *Dexcom G4 User's Guide*. Dexcom.

[6] Andrea Facchinetti, Giovanni Sparacino, Stefania Guerra, Yoeri M Luijf, J Hans DeVries, Julia K Mader, Martin Ellmerer, Carsten Benesch, Lutz Heinemann, Daniela Bruttomesso, et al. *Real-Time Improvement of Continuous Glucose Monitoring Accuracy The smart sensor concept*. Diabetes care, 36(4):793–800, 2013.

[7] Satish K Garg, James Smith, Christie Beatson, Benita Lopez-Baca, Mary Voelmle, and Peter A Gottlieb. *Comparison of accuracy and safety of the SEVEN and the Navigator continuous glucose monitoring systems*. Diabetes technology & therapeutics, 11(2):65–72, 2009.

[8] Natalie Wisniewski, Francis Moussy, and WM Reichert. *Characterization of implantable biosensor membrane biofouling*. Fresenius' journal of analytical chemistry, 366(6-7):611–621, 2000.

[9] Céline M Girardin, Céline Huot, Monique Gonthier, and Edgard Delvin. *Continuous glucose monitoring: A review of biochemical perspectives and clinical use in type 1 diabetes*. Clinical biochemistry, 42(3):136–142, 2009.

[10] Santhisagar Vaddiraju, Diane J Burgess, Ioannis Tomazos, Faquir C Jain, and Fotios Papadimitrakopoulos. *Technologies for continuous glucose monitoring: current problems and future promises*. Journal of diabetes science and technology, 4(6):1540–1562, 2010.

[11] Jeroen Hermanides, Moshe Phillip, and J Hans DeVries. *Current Application of Continuous Glucose Monitoring in the Treatment of Diabetes Pros and cons*. Diabetes care, 34(Supplement 2):S197–S201, 2011.

[12] S Kasemsumran, YP Du, K Murayama, M Huehne, and Y Ozaki. *Near-infrared spectroscopic determination of human serum albumin, γ-globulin, and glucose in a control serum solution with searching combination moving window partial least squares*. Analytica chimica acta, 512(2):223–230, 2004.

[13] David M Haaland, M Ries Robinson, Gary W Koepp, Edward V Thomas, and R Philip Eaton. *Reagentless near-infrared determination of glucose in whole blood using multivariate calibration*. Applied Spectroscopy, 46(10):1575–1578, 1992.

[14] YC Shen, AG Davies, EH Linfield, TS Elsey, PF Taday, and DD Arnone. *The use of Fourier-transform infrared spectroscopy for the quantitative determination of glucose concentration in whole blood*. Physics in medicine and biology, 48(13):2023, 2003.

[15] Yoen-Joo Kim and Gilwon Yoon. *Prediction of glucose in whole blood by near-infrared spectroscopy: influence of wavelength region, preprocessing, and hemoglobin concentration*. Journal of biomedical optics, 11(4):041128–041128, 2006.

[16] Airat K Amerov, Jun Chen, Gary W Small, and Mark A Arnold. *Scattering and absorption effects in the determination of glucose in whole blood by near-infrared spectroscopy*. Analytical chemistry, 77(14):4587–4594, 2005.

[17] Sandeep Sharma, Mohammad Goodarzi, Laure Wynants, Herman Ramon, and Wouter Saeys. *Efficient use of pure component and interferent spectra in multivariate calibration*. Analytica chimica acta, 778:15–23, 2013.

[18] Julie A. Stenken. *Membrane-Based Separations Applied to in Vivo Glucose SensingMicrodialysis and Ultrafiltration Sampling*, pages 157–190. John Wiley Sons, Inc., 2009.

[19] Lhoucine Ben Mohammadi, Thomas Klotzbuecher, Susanne Sigloch, Knut Welzel, Michael Göddel, Thomas R Pieber, and Lukas Schaupp. *In vivo evaluation of a chip based near infrared sensor for continuous glucose monitoring*. Biosensors and Bioelectronics, 53:99–104, 2014.

[20] Ilan Gabriely, Robert Wozniak, Michèle Mevorach, jonathan Kaplan, Yigal Aharon, and Harry Shamoon. *Transcutaneous glucose measurement using near-infrared spectroscopy during hypoglycemia.* Diabetes Care, 22(12):2026–2032, 1999.

[21] Katsuhiko Maruo, Mitsuhiro Tsurugi, Mamoru Tamura, and Yukihiro Ozaki. *In Vivo Noninvasive Measurement of Blood Glucose by Near-Infrared Diffuse-Reflectance Spectroscopy*. Applied spectroscopy, 57(10):1236–1244, 2003.

[22] Anke Sieg, Richard H Guy, and M Begoña Delgado-Charro. *Noninvasive and minimally invasive methods for transdermal glucose monitoring*. Diabetes technology & therapeutics, 7(1):174–197, 2005.

[23] Omar S Khalil. *Non-invasive glucose measurement technologies: an update from 1999 to the dawn of the new millennium*. Diabetes Technology & Therapeutics, 6(5):660–697, 2004.

[24] Jonathon T Olesberg, Lingzhi Liu, Valerie Van Zee, and Mark A Arnold. *In vivo near-infrared spectroscopy of rat skin tissue with varying blood glucose levels*. Analytical chemistry, 78(1):215–223, 2006.

[25] Wenliang Chen, Rong Liu, Kexin Xu, and Ruikang K Wang. *Influence of contact state on NIR diffuse reflectance spectroscopy in vivo*. Journal of Physics D: Applied Physics, 38(15):2691, 2005.

[26] Jason J Burmeister and Mark A Arnold. *Evaluation of measurement sites for noninvasive blood glucose sensing with near-infrared transmission spectroscopy*. clinical chemistry, 45(9):1621–1627, 1999.

[27] Tutku Karacolak, Arazon Z Hood, and Erdem Topsakal. *Design of a dual-band implantable antenna and development of skin mimicking gels for continuous glucose monitoring*. Microwave Theory and Techniques, IEEE Transactions on, 56(4):1001–1008, 2008.

[28] Marc C Shults, Rathbun K Rhodes, Stuart J Updike, Barbara J Gilligan, and William N Reining. *A telemetry-instrumentation system for monitoring multiple subcutaneously implanted glucose sensors*. Biomedical Engineering, IEEE Transactions on, 41(10):937–942, 1994.

[29] Airat K Amerov, Jun Chen, and Mark A Arnold. *Molar absorptivities of glucose and other biological molecules in aqueous solutions over the first overtone and combination regions of the near-infrared spectrum*. Applied spectroscopy, 58(10):1195–1204, 2004.

2

Spectroscopic detection of glucose

Glucose plays a vital role in a variety of biological processes. Therefore, we are not the first ones to measure glucose and definitely not the last. An enormous number of sensor technologies have been developed to measure glucose in both solutions, gases and fixed matter. Some researchers even succeeded in distinguishing glucose from other carbohydrates contained in a single protein, or detected glycolaldehyde, the base sugar that makes up glucose, in a cloud of gas and dust near the center of our own milky way galaxy. It is thus important to realize that a glucose sensor always operates given the constraints as determined individually for every application. In this work, we focus on the *in vivo* detection of glucose in interstitial fluid. Therefore, we can state that we detect glucose in an aqueous liquid with a possible glucose concentration range from 3 to 20 mM. Whereas this *in vivo* glucose concentration range can be detected in numerous ways, we focus in this chapter on optical sensors whose response to glucose depends on the wavelength of the light used. The underlying reasoning is that the interaction of radiation with molecules strictly depends on the energy levels that are present in the molecule. As the energy level distribution of molecules can serve as a fingerprint, it makes selective molecule identification possible.

2.1 Molecular absorption spectroscopy

When a photon is incident on a molecule it can either be scattered, absorbed or transmitted. In this section, we explain how a photon can be

absorbed by a molecule and how this depends on the energy level distribution within the molecule. Next, we introduce the important regions in the electromagnetic spectrum where absorption features can be found. We then show how to relate the molecular concentration to the transmission spectrum of an absorbing sample. Lastly, we briefly discuss Raman spectroscopy, a spectroscopic technique that exploits scattering events rather than absorption events for molecular detection.

2.1.1 Physical origin

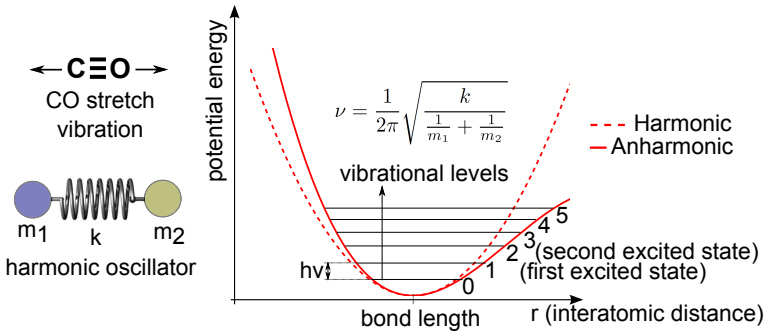

Figure 2.1: Vibrational energy level distribution based on the (an)harmonic oscillator model

An important result from the theory of quantum mechanics is that molecular energy is quantized. A molecule can only exist in a set of quantum states that have a specific associated amount of energy. The quantum state of a molecule depends on the rotational, vibrational and electronic modes it is currently in. For each molecule, a non-continuous set of rotational, vibrational and electronic modes exists. Every mode has a unique energy level associated to it. For most molecules, the energy spacing between two electronic levels is larger than the spacing between vibrational levels, which is larger than the spacing between rotational levels. A simple example of a vibrational mode of a carbon monoxide (CO) molecule is shown in fig 2.1. This oscillation can be described with a classic harmonic oscillator model in which the atoms are replaced by masses, separated by a spring with a certain stiffness.
It is possible for a molecule to change between two modes, whether they are rotational, vibrational or electronic modes. But, this requires a certain amount of energy. Because a photon with frequency ν is a small packet of energy E = hν, it can provide the right amount of energy that is required to make this transition between two modes. This feature creates the wavelength-dependence in absorption spectra of molecules. We can

conclude that the absorption features are narrow lines that represent the energy level distribution of the molecule under test. These lines can, however, be broadened under different circumstances such as high pressure or neighbouring molecules. This effect is called linewidth broadening. When we study glucose in interstitial fluid, the disorder inherent to fluids leads to numerous different solvent environments for glucose molecules. Each glucose molecule will, therefore, feel a different environment and this influences its absorption spectrum slightly. The observed absorption spectrum is the combination of all these slightly different absorption spectra and hence features broader absorption bands instead of individual lines.

2.1.2 Electromagnetic spectrum

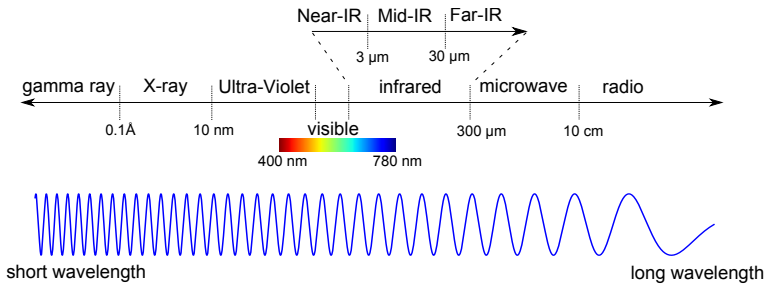

Figure 2.2: The electromagnetic spectrum

The electromagnetic spectrum is the set of all wavelengths that electromagnetic waves can have. It is typically subdivided in different regions as shown in fig 2.2. For molecular absorption spectroscopy, three regions are of importance. Firstly, the microwave region (0.3 mm - 10 cm) which corresponds to energies of rotational transitions in molecules. Secondly, infrared (IR) light (0.78 μm - 300 μm), which features the vibrational transitions and thirdly, the visible and ultra-violet (10 nm-780 nm) part of the electromagnetic spectrum, where the electronic transitions can be found. Two parts of the infrared light are of special importance: the near-infrared (NIR) (0.78-3 μm) and the mid-infrared (mid-IR) (3-30μm). The latter is the traditional region to probe fundamental molecular vibrations. Fundamental transitions take place between the ground level and first excited state of a vibrational mode. These fundamental transitions have the highest probability to occur, making them a good candidate for molecular detection. In figure 2.3, the location of fundamental transitions for absorbing molecules in the mid-IR is shown. There is, however, an incompatibility between mid-IR spectroscopy and our silicon-on-insulator technology. The silica layer of the photonic chip starts to heavily absorb wavelengths above 4 μm

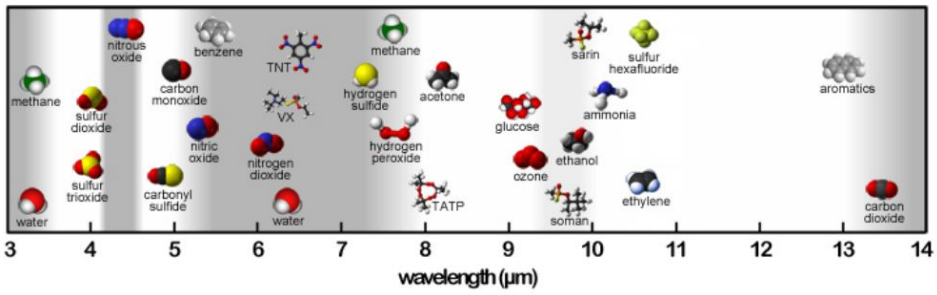

Figure 2.3: Absorbing molecules in the mid-IR. Taken from (daylightsolutions).

[1]. Therefore, we focus on the near-infrared which probes overtone vibrations. Overtone vibrations are transitions between the ground level and the second or higher excited states of a vibrational mode. These transitions are possible because the harmonic oscillator approximation doesn't strictly hold and anharmonic terms are present in the expression of the vibrational energy levels. Overtone transitions have, however, a lower probability to occur which results in a weaker signature of molecules in the NIR. The absorption strength typically decreases, compared to the fundamental transitions, by a factor of 10 to 20 for transitions between the ground level and each consecutive excited state level. Next to overtone transitions, so-called combination vibrational transitions are also possible in the NIR. These are observed when two or more fundamental vibrations are excited simultaneously. The absorption strength of combination transitions are also weaker compared to the fundamental transitions found in the mid-IR.

2.1.3 Beer-Lambert

Now we know that molecules can absorb light of specific wavelengths, we need to quantify how much the transmission of photons is altered by the presence of absorbing molecules. The law of Beer-Lambert is a straightforward expression that relates the decay in intensity I of light to the number of absorbing molecules it passes. It can be written as:

$$I = I_0 10^{-\epsilon c L} \tag{2.1}$$

in which I_0 is the incident light intensity, ϵ is the molecular absorptivity expressed in $mM^{-1}mm^{-1}$, c is the molecule concentration (mM) and L is the path length (mm) the light has traveled. The transmission spectrum can be acquired as $T = \frac{I}{I_0}$. The shape of the transmission spectrum is determined by the wavelength dependency of the molecular absorptivity. The molecular absorptivity is, therefore, the true molecular fingerprint and determines

the shape of the transmission spectrum. In absorption spectroscopy, typically the sample absorbance A is reported instead of the measured transmission T. By definition, both are related as follows:

$$T = 10^{-\epsilon c L} = 10^{-A} \tag{2.2}$$

The transmission through a sample can also be expressed in terms of the sample absorption coefficient α (also known as sample loss) as in:

$$T = e^{-\alpha L} \tag{2.3}$$

We can thus easily relate the sample loss α to the molecular absorptivity ϵ and concentration c as:

$$\alpha = \ln(10)\epsilon c \tag{2.4}$$

In figure 2.4 the absorption coefficient α [μm^{-1}] is shown for glucose and water over a wide wavelength range. As discussed in section 2.1.2, the absorption coefficient is larger at the longer wavelengths. From this figure we can derive that the wavelength region around 9μm is interesting, because there are strong and sharp glucose features compared to a weaker and relatively flat water absorption curve. Unfortunately this region cannot be accessed with our technology platform.

2.1.4 Raman Spectroscopy

Next to absorption events in which a photon is absorbed by a molecule, it is also possible for a photon to be scattered. This scattering can either be elastic (no change in wavelength after scattering) or inelastic. In the latter case, the photon can either gain or loose energy upon interaction with the molecule. As the exchanged energy is quantized according to the energy levels of the molecule, the shift in wavelength of the scattered photon (Raman shift) can be used to identify molecules. This inelastic scattering is exploited in the field of Raman spectroscopy (as opposed to absorption spectroscopy). One of the advantages of Raman spectroscopy is that the spectrum of Raman shifts features many sharp lines, which enables good molecular identification.

For most molecules, including glucose, the probability that a photon is inelastically scattered is much lower than that it is absorbed (typically 6 orders of magnitude lower!). Therefore, using Raman spectroscopy, care must be taken to boost the signal from the inelastically scattered photons. The intensity of the Raman scattered light scales with λ^{-4}, λ the wavelength of the light incident on the molecule. It is thus key to work with shorter wavelengths. Typically, in a Raman spectroscopy set-up one probes a biological sample with a laser diode emitting at λ=785 nm. This wavelength enables a relatively strong Raman signal, while limiting the background fluorescence of the biological sample under test [6]. This background fluorescence is problematic as it can overpower the Raman signal.

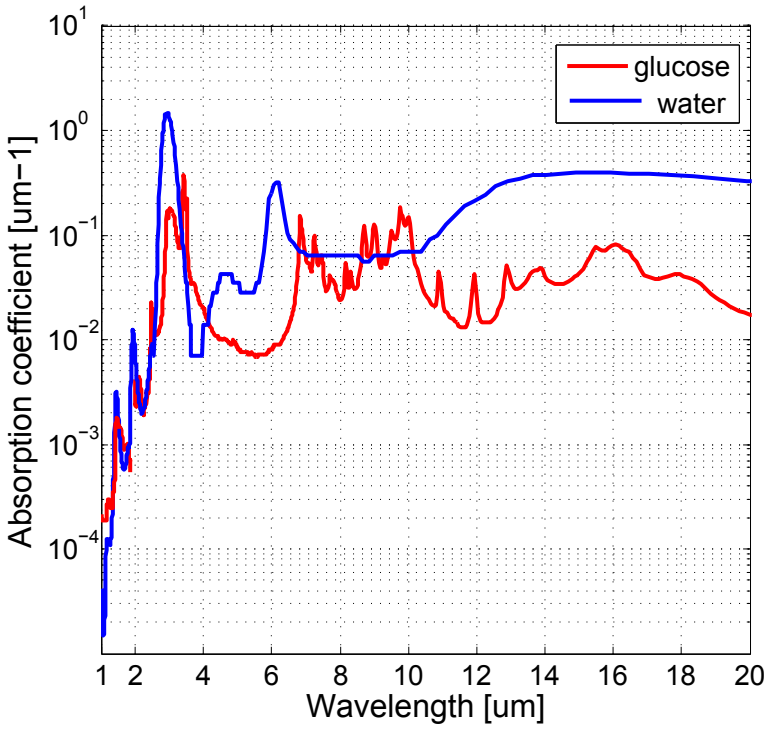

Figure 2.4: Absorption coefficient of water and glucose over a wide wavelength range. This graph is based on data from [2, 3, 4, 5]

The silicon-on-insulator material platform is no longer transparent for the shorter wavelengths (< 1.1 μm), hence a different material platform should be used to develop an implantable Raman spectrometer (such as Silicon Nitride Si_3N_4). In [7] a good overview of the current developments for *in vivo* Raman spectroscopy for the detection of glucose is given.

Despite various known enhancement techniques for Raman spectroscopy, the very low probability for inelastic scattering to occur in comparison with absorption events, gives this method an inherent disadvantage in terms of required source power. This leads to a strong disadvantage of Raman spectroscopy for the detection of glucose in an implantable device, as low power consumption is key. We, therefore, consider absorption spectroscopy a more promising detection principle for the development of an implantable glucose sensor.

2.2 Instrumentation

In this section we describe the typical instrumentation that is used for vibrational absorption spectroscopy. Two distinct types of spectrometers are widely used: dispersive spectrometers and fourier transform interferometers. The first type requires a dispersive element, whereas the latter incorporates an interferometer. Next to spectrometers, lasers also commonly used. A short introduction to these three different methods is given below.

2.2.1 Dispersive spectrometer

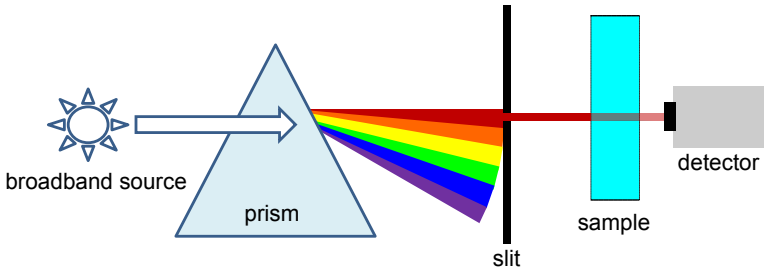

Figure 2.5: Basic implementation of a pre-dispersive spectrometer

A spectrometer needs to measure the transmission of electromagnetic radiation of different wavelengths after passing through a sample. To separate the different wavelengths, a dispersive element is used, hence the name. The dispersive element can separate the wavelengths in time or in space. The former case requires a fast photo-detector and is less often used. A dispersive spectrometer can be pre- or post-dispersive, depending on whether the wavelength demultiplexing happens before or after the sample. The most basic implementation of a dispersive spectrometer comprises a broadband source, a prism, a slit (or diaphragm) and a detector as shown in figure 2.5. In modern dispersive spectrometers, the dispersive element is a diffraction grating. The resolving power R of a grating is a measure for its ability to separate two closely spaced wavelengths λ and $\lambda + \Delta\lambda$. It is determined by the diffraction order m and the number of grooves N that are illuminated: $R = \frac{\lambda}{\Delta\lambda} = Nm$ (see figure 2.6). When two closely spaced absorption peaks need to be distinguished, resolution comes into play. The spectrometer resolution is not only defined by the resolving power of the grating, but also depends on the system configuration. We can divide the grating-based configurations in two main categories depending on whether a single photodetector or a photodetector array is used. In the former case, the resolution is strongly affected by the slit size. The slit size can affect the amount of illuminated grating grooves

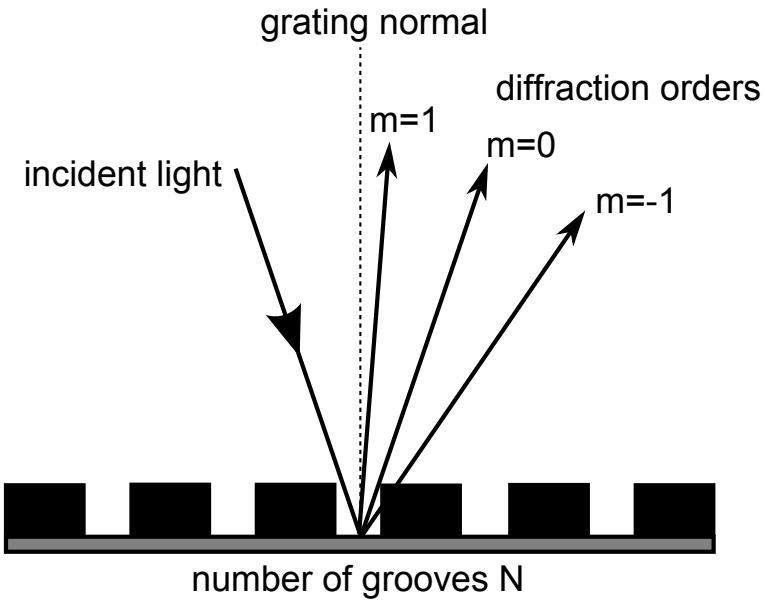

Figure 2.6: Schematic of a diffraction grating showing the first diffraction orders m=0,±1

and/or select the range of wavelengths that can reach the photodetector by blocking wavelengths that are already angularly dispersed by the grating. If the slit size is smaller, a higher resolution can be obtained. However, a smaller slit size also lowers the signal throughput. The latter influences the attainable signal-to-noise ratio (SNR). This trade-off between resolution and SNR is inherent for most dispersive spectrometers designs. When a photodetector array is used, the mimimal spacing between the different photodetectors limits the resolution. Although limited in resolution, designs with a photodetector array have a faster acquisition time and are considered more robust because no moving parts (such as a rotating grating) are present. The limiting resolution of commercially available dispersive spectrometers in the near-infrared varies typically between 0.2-3 nm.

2.2.2 Fourier transform infrared spectrometer

In a fourier transform infrared spectrometer, light from a broadband source first enters an interferometer to generate an interferogram. This interferogram is transmitted through the sample and acquired with a detector(see figure 2.7). After the acquisition of the interferogram, it can be converted into an absorption spectrum by means of the fourier transform. The amplitude accuracy of the measured absorption spectrum strongly depends on

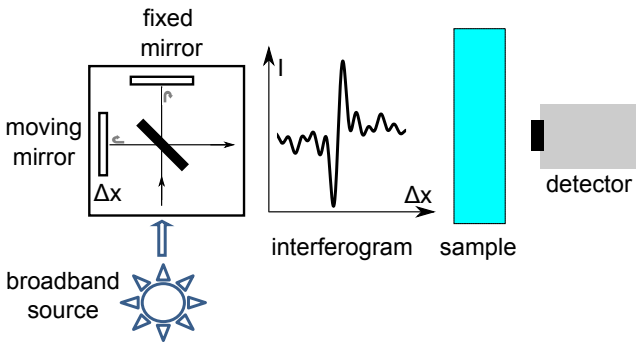

Figure 2.7: Basic implementation of a fourier transform infrared spectrometer

the linearity and (especially) the dynamic range of the photodetector that acquires the interferogram. The resolution of an FTIR is inversely proportional to the maximum optical path length difference, hence movement of the mirror. This way, high resolution is possible without limiting the signal throughput. Nowadays, commercial instruments can offer a spectral resolution of 0.07 $cm^{-}1$ ($\approx$ 0.03 nm at 2μm)[8]. A HeNe laser (633 nm) is used to monitor the moving mirror closely and serves as an internal calibration element. The nyquist theorem states that a sinusoid can be restored if it has been sampled at a frequency at least twice as high as its own frequency. The measured interferogram is sampled by the zero's in the reference interferogram of the HeNe laser, therefore the lowest wavelength that theoretically can be measured with an FTIR is about 2 times 633 nm. In practice, FTIR instruments and dispersive spectrometers are used side by side, with dispersive spectrometers dominating the UV-VIS spectroscopy market and FTIR instruments focusing on mid-IR applications.

2.2.3 Laser spectroscopy

The final type of spectroscopic instrumentation that we will briefly discuss is a laser-based spectrometer. In this case, light from a laser is transmitted through the sample and is directly incident on a detector as shown in figure 2.8(a). The laser emits monochromatic radiation, but the emitted wavelength can be tuned slightly. Due to the narrow emission line width of a laser, very fine features in the absorption spectrum can be sampled and resolved. This high-resolution method is mostly used for atoms and molecules in the gas phase as the absorption spectrum then comprises a set of very narrow lines as shown in figure 2.9(b). Although lasers offer high input power which can lead to high signal-to-noise measurements, the diluted nature of gases also requires a long ($>$ 1 m) interaction length between the gas and the laser light. This can be achieved when the sample

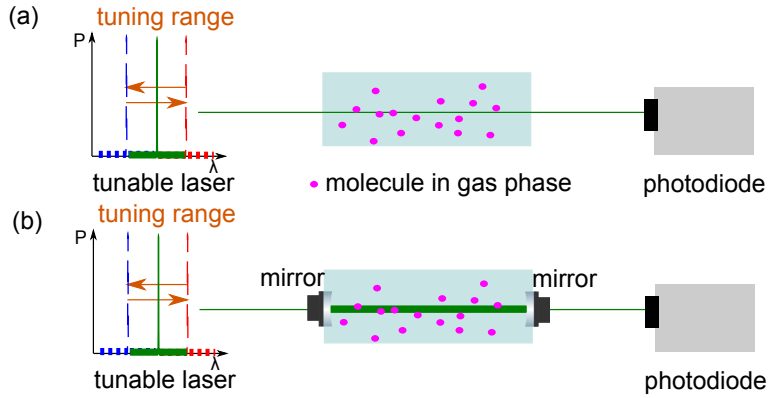

Figure 2.8: Basic implementation of (a) a direct laser based and (b) a cavity enhanced laser based spectroscopy set-up

cell is constructed as a cavity (see 2.8(b)), such that the light can interact with more molecules while bouncing back and forth in the cavity. This method is called cavity enhanced detection (see also section 4.4).

2.3 Absorption spectroscopy of glucose solutions

Absorption spectroscopy becomes more complex when no longer a single molecule is studied but a mixture. As often required in practice, one needs to measure the concentration of various molecules in a mixture. The absorption spectrum of this mixture then represents the combined absorption of all different molecules and atomic bonds present in the mixture. The relative magnitude of concentration of the different molecules and their absorptivities then determine which features are dominant. In this section, we start by introducing the glucose spectrum and identify which molecules are true interferents that can mask the glucose absorption features. We continue with a discussion on the optimal path length that has an important role in signal throughput, hence signal-to-noise ratio (SNR) of the spectroscopic measurements. Subsequently, the required SNR for glucose detection is derived and we end this section with a discussion of the metrics that are used for qualifying *in vivo* glucose sensors.

2.3.1 Glucose spectrum

The chemical formula of glucose is $C_6H_{12}O_6$, therefore there is a limited number of atoms and chemical bonds that can influence the absorption spectrum. In the near-infrared wavelength range, that we can easily access with SOI technology, the glucose absorptivity shows two regions with

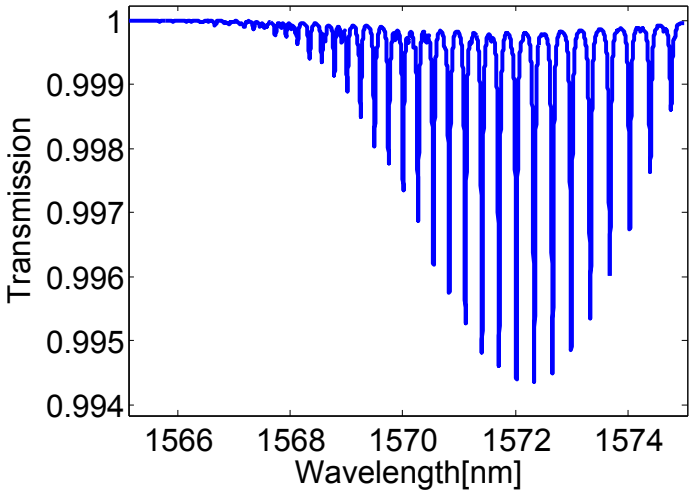

Figure 2.9: Example of the narrow line-features in the near-infrared absorption spectrum of CO_2 (based on data from the Hitran database)

characteristic features (see fig. 2.10)[2]. The first region is the so-called first overtone band that comprises the first overtone transitions of C-H stretching vibrations. The second region is the combination band that corresponds to the combination of stretching and bending vibrations for C-H and O-H bonds. When we compare both regions, we notice that glucose absorbs 4 to 5 times stronger in the combination band and that all features are broadband in nature. In the same figure (fig. 2.10), the absorptivity of other interfering bio-molecules is plotted. The influence of these interferents is explained in the next section.

2.3.2 Interfering molecules

If we take a look at the absorptivity spectra in figure 2.10, we can see that the absorption features are highly overlapping. The interfering bio-molecules have similar chemical bonds, hence features as glucose and need to be distinguished. Two factors determine the magnitude of the associated problems: the *in vivo* concentration of the interferent and the measured wavelength range. Water for example is omnipresent in interstitial fluid (ISF) and dominates the absorption spectrum. On the other hand, fructose has the same chemical formula as glucose ($C_6H_{12}O_6$), but its influence on the absorption spectrum is negligible, because its concentration in ISF is 3 orders of magnitude lower than glucose [9]. The *in vivo* concentration of urea and lactate is similar to glucose and they are therefore considered to be the two main interferents, next to water. Note, however, that each

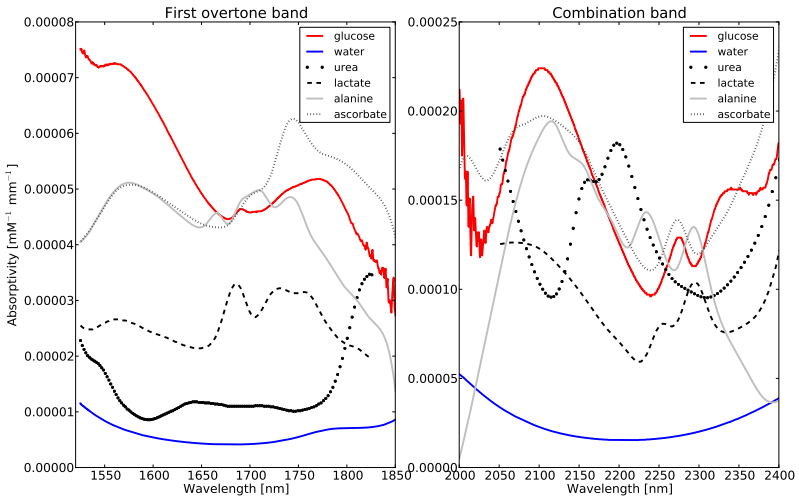

Figure 2.10: Absorptivity of glucose, water and interfering bio-molecules in the near-infrared. (based on data from [2]

person's metabolism is different, leading to a large variety of possible ISF compositions in which other bio-molecules can start to play an important role as well.
The measured wavelength range is also important to consider. If we can measure a wider range, the number of molecule-specific features increases and identification becomes easier. Still, the wavelength resolution of the measured spectrum needs to be high enough to resolve the finer absorption features. For glucose, this wavelength resolution is preferably 3 nm [10]. However, some parts of the wavelength range might not be accessible due to the unavailability of adequate sensor technology (e.g. lack of sources) or due to the heavy background absorption of the solvent.

Water

Water is a very strong interferent for *in vivo* glucose detection. Although the water absorptivity is of the same order of magnitude as glucose, the molar concentration of pure water at 37°C is 55138 mM [2], which is four orders of magnitude larger than the mean *in vivo* glucose concentration of 5.5 mM. In addition, the water absorption is so strong in the wavelength range from 1870-2000 nm and 2400-4000 nm, that the transmission drops to zero when the path length exceeds 1 mm (see figure 2.11). This effectively eliminates these regions for NIR absorption spectroscopy of weakly

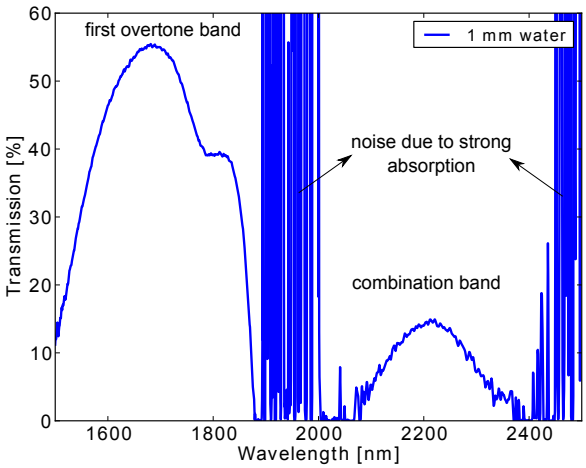

Figure 2.11: Measured water transmission in the near-infrared with a path length of 1 mm

absorbing solutes in aqueous solutions. Another important effect of water as a solvent is the presence of hydrogen bonds (see fig 2.12(a)). These bonds are sensitive to temperature and introduce a blue shift in the water absorptivity peak at 1411 nm with increasing temperature [11]. This effect is shown in figure 2.12(b). The first overtone features of glucose are located on the tail of this moving peak, so that the variable water background needs to be properly referenced for [12].

When one wants to eliminate the water spectrum from the spectrum of an aqueous glucose solution, the so-called water displacement effect also plays a role. The number of absorbing water molecules is smaller for a given measurement volume in a glucose solution compared to pure water. By introducing the water displacement factor f_w, a pure water reference can still be used for easy elimination of the water spectrum from a solution spectrum. The water displacement factor corresponds to the molar concentration change of water caused by the dissolution of a unit molar concentration of a solute ([2]). For glucose this factor is $f_w = 6.245$. When a pure water reference is used, the change in absorbance due to glucose A_g with a concentration c_g can then be written as:

$$A_g = \epsilon_g c_g L - f_w \epsilon_{H_2O} c_g L \tag{2.5}$$

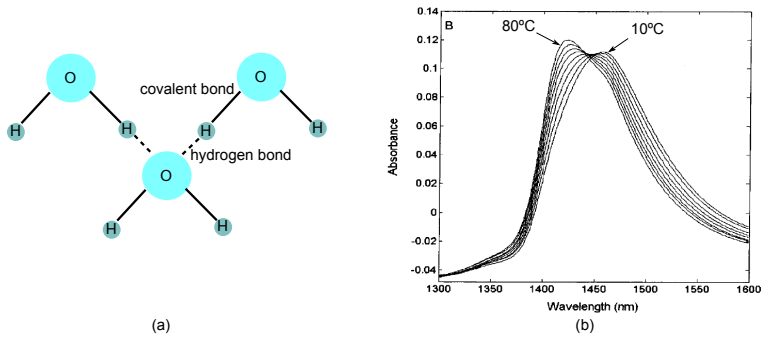

Figure 2.12: (a) formation of hydrogen bonds in liquid water and (b) the temperature dependence of the NIR water spectrum [11]

Glycated proteins

Another type of potential interfering signal comes from glycated proteins (see fig. 2.13). These are proteins that have glucose molecules covalently bound to them. The concentration of glycated proteins is typically higher in diabetic patients [13]. This is because the glucose is not effectively taken up by their cells, leading to an increased probability for glucose to (permanently) bind with proteins. When the sample under test also contains these glycated proteins, the bound glucose molecules might contribute to the NIR signal. Yet, only the freely floating glucose molecules should be measured. A preliminary investigation of this effect is described in the later section 2.4.3. For the used data set with serum samples, it was found that the present proteins lower the glucose estimation accuracy, but that the number of glycated proteins does not significantly impact this result.

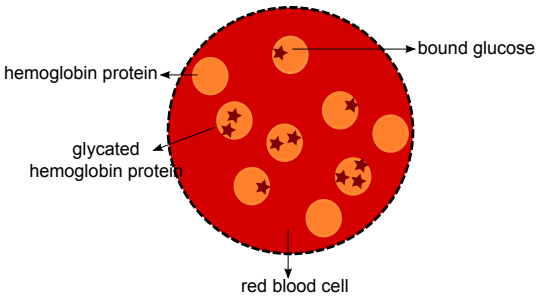

Figure 2.13: Example of a red blood cell with glycated hemoglobin proteins

2.3.3 Path length

By being such a strong absorber in the near-infrared, water plays an important role in the path length determination for the implantable spectrometer. To explain this, we start from the following (reasonable) assumptions: (1) the detector noise is ultimately limiting the attainable signal-to-noise ratio (SNR) of our sensor and (2) this noise can be considered constant and independent of the light intensity incident on the detector. Now, imagine the following two cases: In the first case, the path length is chosen very long such that the transmittance through the ISF sample is very low due to water absorption. Then, the signal becomes smaller relative to the noise, hence the SNR goes down. Secondly, imagine now a very short path length. The transmittance will be high but the signal due to glucose will be low due to the low number of molecules that the light beam has passed. It is, therefore, clear that there is an optimum in the path length. Now, we show how to relate this optimal path length with the water absorption. According to Beer-Lambert, the transmission T of a liquid mixture with n components and a path length of L can be written as:

$$T = 10^{-\sum_{i=1}^{n} \epsilon_i c_i L} \tag{2.6}$$

The sensitivity s_i of the transmission T for a variation in concentration c_i is:

$$s_i = \left| \frac{\delta T}{\delta c_i} \right| = T \cdot ln(10) \cdot \epsilon_i \cdot L \tag{2.7}$$

If we now take the derivative of s_i with respect to the path length and equal this to zero ($\frac{\delta s_i}{\delta L} = 0$), then the optimal sensitivity is found to be:

$$L_{opt} = \frac{1}{ln(10) \cdot \sum_{i=1}^{n} \epsilon_i c_i} \tag{2.8}$$

Given the above equation, the optimal length is mainly influenced by the water absorption as it dominates $\sum_{i=1}^{n} \epsilon_i c_i$. Due to the strong wavelength dependence of the water absorptivity, this optimal length also depends on the transmission wavelength that is measured. According to this equation 2.8, the optimal path length for the peak absorption wavelength of glucose in the first overtone band (1590 nm) is $L_{opt,1590nm} = 1.36$ mm and for the combination band (2110 nm) we get a length of $L_{opt,2110nm} = 0.37$ mm. Initial research has shown that the use of multiple path lengths can improve the detection limit [14, 15]. Given the small footprint of our spectroscopic sensor, we can thus envision a set of sensors with each a different sample path length. This way, we can optimize the SNR for a larger wavelength range.

2.3.4 Required signal-to-noise ratio

If we expect that the glucose detection accuracy scales directly with our sensor's performance and assume no significant improvement by spectral analysis techniques, we can derive a minimally required signal-to-noise ratio of our measurements. To derive the required SNR, we start by introducing the clinically relevant glucose concentration range and minimum change in glucose that should be measured. For healthy persons the normal concentration range of blood glucose is 4.4 to 6.1 mM. Shortly after a meal, the glucose level may rise shortly to 7.8 mM. For diabetes patients, the glucose level may rise up to 20 mM after a meal. This state of high glucose level (>9 mM) is called hyperglycemia. The opposite case is hypoglycemia and occurs when the glucose level drops below 3.9 mM. This is a serious condition and if left untreated, it may lead to unconsciousness. The glucose range that we target with our *in vivo* glucose sensor is thus 3-20 mM.
Next to this dynamic range, a sensor resolution can be determined. This is the minimal change in concentration that can be resolved by the sensor. The clinically required, absolute minimum resolution is 1 mM, which is especially critical when the patient is suffering from a hypoglycemia [16]. We will now determine the change in transmission that is associated to this minimum sensor resolution of 1 mM.
In the previous section, we calculated the optimal path length for the peak absorption wavelength of glucose in the first overtone band (1590 nm) and combination band (2110 nm) according to 2.8. We get a length of $L_{opt,1590nm} = 1.36$ mm and $L_{opt,2110nm} = 0.37$ mm. The theoretical transmission of aqueous glucose mixtures with different concentrations for both the first overtone and combination band for these calculated path lengths based on the absorptivity data from [2], is shown in figure 2.14. The left y-axis represents the change in transmission due to a glucose solution, calculated as $T = 10^{-A_g}$ with A_g as defined in formula 2.5. We can now derive the change in transmission δT at a wavelength of 1590 nm and 2100 nm, that is caused by a change in glucose concentration of 1 mM:

$$\delta T(\lambda = 1590nm) = 1 - T_{gluc=1mM} = 1 - 0.99990 = 0.01\% \tag{2.9}$$

and

$$\delta T(\lambda = 2110nm) = 1 - T_{gluc=1mM} = 1 - 0.99992 = 0.008\% \tag{2.10}$$

It is this very small change in transmission that we should be able to measure with our device. The required SNR associated with this δT can be calculated as: $\frac{1}{\delta T}$. This yields an SNR of 10000 at λ=1590 nm and SNR=12500 at λ=2110 nm. In comparison, commercially available FTIR spectrometers specify a SNR of 15000 [8]. The *in vivo* spectroscopic detection of glucose, thus, poses two important challenges: (1) development of a very high

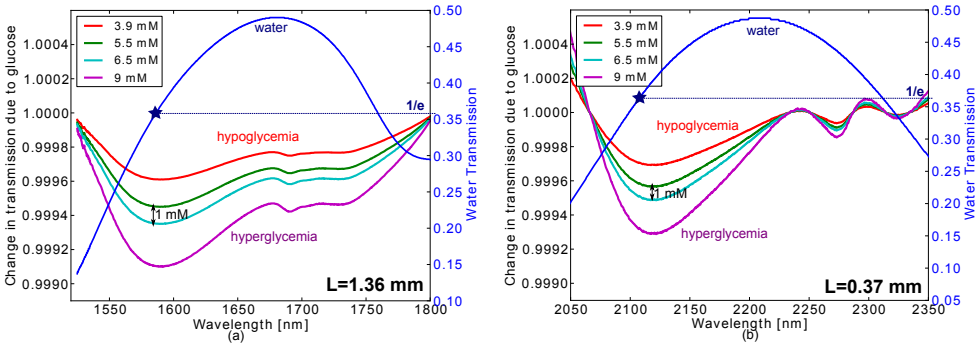

Figure 2.14: (Theoretical) change in transmission due to a glucose solution, taken into account the water displacement effect, in (a) the first overtone band and (b) the combination band for different glucose concentrations. The pure water transmission spectrum for the optimal path lengths is also shown.

SNR sensor and (2) the required specific detection given the variable background of water and interfering bio-molecules.

2.3.5 Requirements for *in vivo* glucose detection

Next to the sensor's concentration range and resolution, the overall accuracy of a continuous glucose monitoring (CGM) device must obey international clinical standards. The following standards are used: Clark error grid, ISO15197 and MARD.

Clarke error grid

The Clarke error grid is shown in fig. 2.15 [17]. The x-axis represents the actual blood glucose values as expressed in mg/dL. Use the conversion factor of 1/18.016 to convert from mg/dL to mM. The y-axis is the blood glucose value as measured with a CGM sensor. The error grid contains five different zone's, namely A,B,C,D,E. The CGM sensor should only give readings that fall within zone A and B. More information on the significance of these zones can be found in [17].

ISO15197

This is an ISO standard on "*Requirements for blood-glucose monitoring systems for self-testing in managing diabetes mellitus*" that provides a good reference for CGM. It states that at least 95% of all sensor readings should fall within ± 0.8 mM of an analytical reference method when the

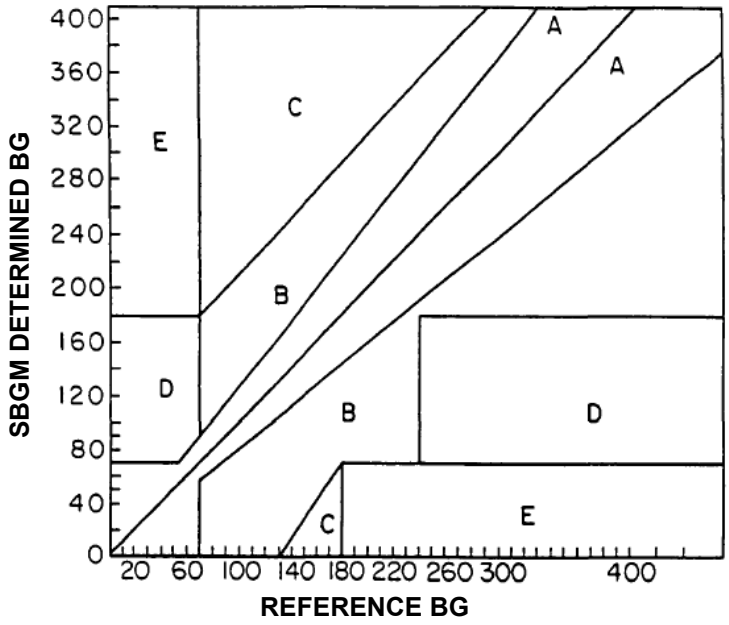

Figure 2.15: Clarke Error grid from [17]. SMBG stands for self-monitoring of blood glucose (BG) which is expressed in mg/dL

blood glucose level is below 4.2mM and within $\pm 20\%$ when the blood glucose level is above 4.2 mM.

Mean absolute relative distance

The last CGM performance measure is the Mean Absolute Relative Distance (MARD) that measures the average disparity (in percentage) between sensor and analytical reference method readings [18]. The MARD for n readings is calculated as:

$$MARD = \frac{100}{n} \sum_{i=0}^{n} \frac{|c_{CGM,i} - c_{ref,i}|}{c_{ref,i}} \tag{2.11}$$

The lower the MARD value, the more accurate the sensor. Typical values for commercial CGM devices are 10-15%.

A note of attention should also be given to the following issue: the diagnostic measures are derived for blood glucose levels but most CGM devices, also the GlucoSens implant, measure glucose in the interstitial fluid (ISF).

Research has shown that the blood and ISF glucose levels are closely related, but a delay of 10 to 20 minutes between the two is often present [19]. Future will tell if the diagnostic measures will shift to ISF values, but for now the delay should be minimized by implanting the CGM is a densily vascularized region.

2.4 Multivariate analysis

The previous section clearly indicated that the degree of overlap between the various absorption features in a mixture will make molecular identification more difficult. By monitoring the mixture in the mid-IR, thus the fundamental transitions, the degree of overlap can be minimized. In the near-infrared, however, the weak and broadband nature of overtone vibrations necessitates a different approach. One straightforward method is to increase the spectral range that is measured, because more features mean better identification. Another, but complimentary, approach is to use a priori knowledge of absorption spectra of the mixture components. The measured absorbance can then be written as a linear combination of the individual absorbance spectra for which the coefficients represent the concentration distribution. Actually, a whole field of science has been devoted to this problem of spectral analysis, namely multivariate analysis. In this section, we give a short introduction to the basic principles of multivariate calibration and discuss the relevant results that were obtained (in the GlucoSens project) for *in vivo* glucose sensing.

2.4.1 Introduction to multivariate calibration

In multivariate calibration of spectra, the goal is to establish a relationship between a measured spectrum and the content of the measured sample. By measuring multiple samples with varying, but known, concentration of various analytes, this relationship can be established. This relationship can then be used to find the content of an unknown sample whose absorption spectrum is measured.
In principle, the relationship can be derived by standard regression techniques. For example, we can derive the regression model $C = A\beta$ for the measured spectra (if the law of Beer-Lambert applies). In this model C is the multicomponent concentration matrix, A is the corresponding spectral absorbance matrix and β a matrix with the regression coefficients. Every row in A is a measured absorbance spectrum and is seen as a set of variables (one variable per measured wavelength). These variables can be highly correlated when they are part of the same broad absorption peaks. This makes it challenging to solve the above regression model, as the regression coefficients β are found by matrix inversion of the matrix product $A^T A$. Due to the high correlation of the variables, this matrix product is

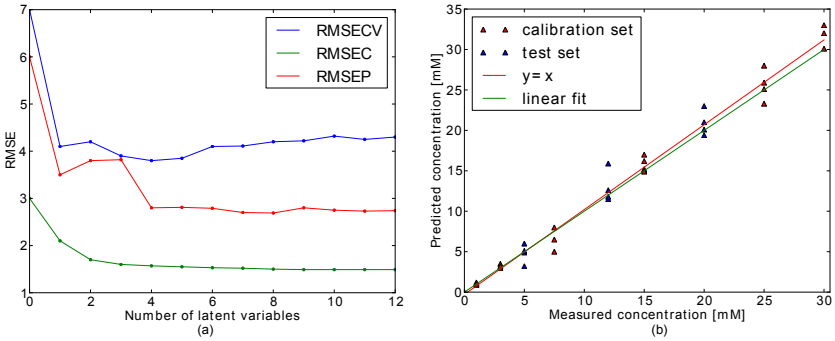

Figure 2.16: (a) Variation in the multivariate model performance in terms of the root mean squared error of cross validation (RMSECV), calibration (RMSEC) and predication (RMSEP) with the number of latent variables and (b) typical graphical representation of the multivariate modeling results.

not of full rank, hence inversion gives numerical problems [20]. A different approach is thus needed to establish the relation between a measured spectrum and it's sample content.
The most popular multivariate calibration technique is partial least squares regression (PLSR) [21] and is explained below as in [22]. This technique starts from the observation that the measured variables X can be written as $X = TP + E$ in which T are the so-called latent variable scores, P a matrix of loadings and E an error term that represents spectral residuals [22]. The dimensions of the individual matrices are n x p (X), n x a (T), p x a (P) and n x p (E) with n the number of measured spectra, p the number of wavelengths and a the number of latent variables. These latent variables are limited in number and represent the true underlying causes of variation in the observed spectra. They reduce the dimensionality of the spectral data by eliminating redundant information of the observed variables. The matrix of loadings P contains the coefficients used in the projection (by writing it as a linear combination) of the observed variables onto the latent variables.
The process of iteratively solving $X = TP + E$ for T, P and E, while minimizing E, is called data compression. The next step in PLSR is to solve the regression equation $c = Tq + e_c$, in which c is a n x 1 vector representing the concentrations, q is a a x 1 vector of regression coefficients and the n x 1 error vector e_c. Once both the data compression and regression step is finished, the multivariate calibration model can be tested with an unkown spectrum. A multivariate model thus has a calibration phase (data compression + regression) and a testing phase. The testing phase makes use of the matrix P and vector q to estimate the concentration of the unkown

sample. For PLSR this testing phase yields the estimated concentration $\hat{c}$ of a spectrum x using $\hat{c} = b_0 + xb$. In this equation b_0 is called the intercept and b is a p x 1 regression vector that is computed using P and q (from the calibration phase) as $b = W(PW)^{-1}q$. In this latter equation, W is a p x a matrix that represents (iteratively optimized) weighting factors for the latent variables to make sure they remain orthogonal, hence carry unique underlying information about the spectrum.
Without going further into detail, the result of the multivariate modeling is a set of estimated concentrations $\hat{c}$ that can be compared to the actual concentrations c. This data can then be used to define three evaluation measures for the model: the root mean squared error of calibration (RMSEC), cross-validation (RMSECV) and prediction (RMSEP). These values are dependent on the number of latent variables that are used in the modeling, and provide a way to optimize this number. Care must be taken to prevent a too high number of latent variables as this increases the risk of overfitting. All three measures are based on the calculation of the root mean squared error RMSE:

$$RMSE = \sqrt{\sum_{i=1}^{n} \frac{(c_i - \hat{c_i})^2}{n}} \tag{2.12}$$

To estimate the future performance of the model, RMSEP is the best measure. To calculate the RMSEP, the $\hat{c_i}$ in formula 2.12 are calculated for spectra that were not used in the calibration phase. These $\hat{c_i}$ are calculated with the calibration model for which the RMSECV is optimized. The RMSECV is typically calculated using leave-one-out cross-validation: for every spectrum in the calibration set, a calibration model is developed by leaving this spectrum out of the calibration set. This yields n-times a RMSE that can be averaged to yield the RMSECV. Other methods to calculate the RMSECV can be found in [20]. The RMSEC is calculated only with the spectra that were used in the calibration phase. This should give the lowest RMSE and represents the most optimistic estimation of the model performance. After optimization of the multivariate model, the model information can be represented as in fig. 2.16. The RMSECV, should be minimized, while limiting the number of latent variables to decrease the risk for overfitting. The number of latent variables is often determined as the number for which an additional latent variable does not result in a significant improvement of the RMSECV [23].

2.4.2 Multivariate modeling of aqueous glucose solutions

We now introduce the multivariate analysis results of our GlucoSens partner MeBios from KULeuven. They studied a set of ISF mimicking solutions that were measured with an FTIR at 37° [22]. The dataset was a full factorial design of aqueous solutions with 7 levels of glucose (1 mM, 3 mM, 7

mM, 12 mM, 15 mM, 22 mM and 30 mM), two levels of urea (5 mM, 6 mM) and two levels of lactate (1 mM, 5 mM). Each of the 28 different solutions was put into a cuvette with an optical path length of 1 mm and measured three times in the NIR wavelength range from 1333 to 2354 nm. The results are shown in table 5.1. It can be seen that the multivariate model performs best when the large wavelength range from 1333-1836 nm and 2173-2354 nm is used for modeling. This shows how the measured wavelength range influences the detection limit. Both the wavelength dependence of the instrumental noise and the deviation from the optimal path length attribute to this effect. It is not yet clear if this detection limit can be improved further by using other calibration strategies.

Table 2.1: PERFORMANCE OF PLSR MULTIVARIATE MODELING FOR THE PREDICTION OF GLUCOSE CONCENTRATION IN ISF-MIMICKING AQUEOUS SOLUTIONS

λ [nm]	2173-2354	1333-1836	1525-1825	1333-1836 2173-2354
RMSEC [mM]	3.39	0.95	0.88	0.73
RMSECV [mM]	4.00	1.03	1.08	0.86
RMSEP [mM]	4.36	1.00	1.08	0.79

2.4.3 Multivariate modeling of glucose in blood serum

A similar experiment was performed for blood serum [24]. The serum samples consists of 92 vol% water, 64-83g/L dissolved proteins and a variety of small molecules such as glucose. A total of 65 human blood serum spectra were measured in threefold in the 800-2500 nm wavelength range with an FTIR, using a 1 mm flow through cuvette. The samples were measured at a temperature of 37°. In the calibration phase of the multivariate modeling 150 spectra (50 samples x triplicates) were used and in the test phase another 45 spectra (15 samples x triplicates). Only the first overtone (1550-1810 nm) and combination band (2070-2375 nm) were considered for building the PLSR model. The resulting model used 13 latent variables and achieved a RMSECV of 1.41 mM and RMSEP of 1.16 mM. In figure 2.17, the results of the model are shown in a Clarke grid. The encircled datapoint correspond to three outlier samples that were identified by the model. Except for one outlier spectrum, all samples fall in zone A and B of the Clarke Grid, indicating a good performance of the PLSR model. This means that the multivariate model can handle the uncertainties generated by varying interferent and protein content in blood serum.

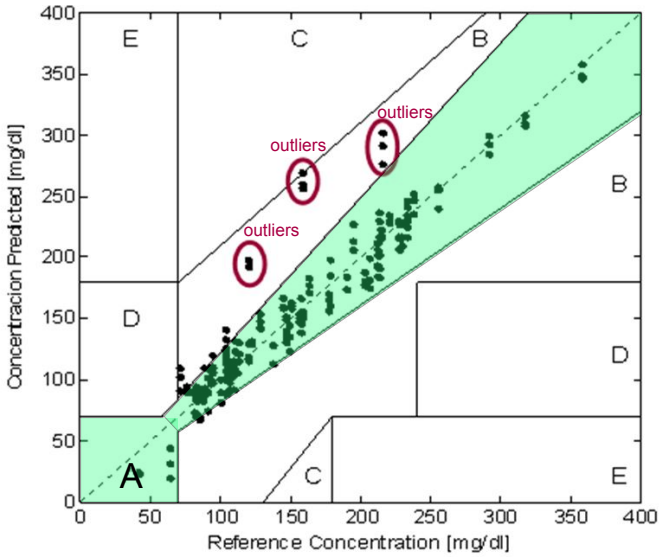

Figure 2.17: Clarke error grid analysis for human serum samples using PLSR modeling in the first overtone and combination band. The encircled outlier spectra were automatically detected in the multivariate modeling.[24]

Influence glycated proteins

As mentioned in section 2.3.2, the effect of glycated proteins on the glucose prediction had to be studied. This was investigated by our GlucoSens partner Mebios and is reported in [25]. It was found that proteins in general have a significant influence on the glucose prediction error. This can be attributed to the fact that proteins are very efficient light scatterers. This lowers the signal-to-noise ratio of the measurements as more light is lost upon scattering. In addition, even when the light is captured by the detector, it is difficult to estimate the traveled path length due to the scattering events. This yields uncertainty on the glucose concentration through the law of Beer-Lambert as the path length is a parameter in the equation 2.1.3. On the other hand, it was concluded from the study that the very nature of the HbA1C proteins itself does not have a significant effect on the glucose prediction.

2.4.4 Optimal wavelength band

One could ask how many wavelengths are needed to have a good glucose detection limit using absorption spectroscopy in the first overtone band and combination band. Our GlucoSens partner MeBios investigated this and found that it is possible to select a limited number of regions that carry

the most selective information about glucose. Using the human serum data-set a selection of 14 wavelengths was made. Using these 14 wavelengths a reasonable RMSEP of 1.64 mM is obtained. The wavelengths are located both in the first overtone band (mostly around 1690 nm) and around the broad absorption peak at 2110 nm in the combination band. It is, however, not yet clear by how much this set of 14 wavelengths depends on the specific spectral data set.

2.5 Conclusion

In this chapter, we showed how glucose can be detected by using near infrared absorption spectroscopy. This measurement method poses three important challenges for the *in vivo* detection of glucose.
Firstly, the required signal-to-noise ratio of our sensor must be at least 40 dB, given the required sensor resolution of 1 mM.
Secondly, the weak and broadband nature of glucose absorption features makes the absorption spectrum prone to interferents. Water is the main interferent, followed by urea and lactate and scattering proteins. The dominant water absorption can be eliminated from the glucose solution spectrum, using the water-displacement factor. Care, however, is needed to monitor the temperature as this influences the water spectrum. Multivariate analysis can help in the process of extracting the glucose concentration from the measured absorption spectrum. Promising results have been achieved with multivariate modeling in both simple aqueous solutions and complex serum samples. The RMSEP for serum samples is 1.16 mM, but requires the information from both the first overtone and combination band. The third challenge is related to this large spectral range that should be covered for sensitive glucose detection. Given the large technological challenges of light source integration on a Silicon photonic chip, we cannot cover every wavelength in this wide range. A selection thus has to be made taking into account the availability of light sources.

Although the nature of near-infrared spectroscopy for glucose detection is challenging, the advantages of this approach compared to other detection methods, are driving this research. Below the three main advantages are listed:

1. This method requires no reagents nor labeling. This is beneficial for both the bio-compatibility and long term stability of the sensor

2. The absorption spectrum serves as a molecular fingerprint due to the direct link with the molecule's energy level diagram. This ensures high specificity.

3. By using multivariate modeling of the measured absorption spectra, multiple molecules can be monitored at once.

These advantages also hold for mid-IR absorption spectroscopy and Raman spectroscopy. Still, it is technologically much more challenging to integrate these alternative detection methods onto an implantable optical silicon chip. In addition, the high required source power for Raman spectroscopy most likely leads to a device too power-hungry for implantation.

References

[1] Richard Soref. *Mid-infrared photonics in silicon and germanium*. Nature Photonics, 4(8):495–497, 2010.

[2] Airat K Amerov, Jun Chen, and Mark A Arnold. *Molar absorptivities of glucose and other biological molecules in aqueous solutions over the first overtone and combination regions of the near-infrared spectrum*. Applied spectroscopy, 58(10):1195–1204, 2004.

[3] Yizhong Yu, Katherine D Crothall, LG Jahn, and Mark A DeStefano. *Laser diode applications in a continuous blood glucose sensor*. In Integrated Optoelectronics Devices, pages 268–274. International Society for Optics and Photonics, 2003.

[4] Ken-ichi Izutsu, Yukio Hiyama, Chikako Yomota, and Toru Kawanishi. *Near-infrared analysis of hydrogen-bonding in glass-and rubber-state amorphous saccharide solids*. AAPS PharmSciTech, 10(2):524–529, 2009.

[5] Kent F Palmer and Dudley Williams. *Optical properties of water in the near infrared*. JOSA, 64(8):1107–1110, 1974.

[6] Olga Lyandres, Jonathan M Yuen, Nilam C Shah, Richard P Van-Duyne, Joseph T Walsh Jr, and Matthew R Glucksberg. *Progress toward an in vivo surface-enhanced Raman spectroscopy glucose sensor*. Diabetes technology & therapeutics, 10(4):257–265, 2008.

[7] Jonathan M Yuen, Nilam C Shah, Joseph T Walsh Jr, Matthew R Glucksberg, and Richard P Van Duyne. *Transcutaneous glucose sensing by surface-enhanced spatially offset Raman spectroscopy in a rat model*. Analytical chemistry, 82(20):8382–8385, 2010.

[8] Varian. *660/670/680-IR FTIR spectroscopy solutions*. Brochure, 2013.

[9] Takahiro Kawasaki, Hiroshi Akanuma, and Toshikazu Yamanouchi. *Increased fructose concentrations in blood and urine in patients with diabetes*. Diabetes Care, 25(2):353–357, 2002.

[10] Qing Ding, Gary W Small, and Mark A Arnold. *Genetic algorithm-based wavelength selection for the near-infrared determination of glucose in biological matrixes: initialization strategies and effects of spectral resolution*. Analytical chemistry, 70(21):4472–4479, 1998.

[11] Vegard H Segtnan, Š Šašic, Tomas Isaksson, and Y Ozaki. *Studies on the structure of water using two-dimensional near-infrared correlation spectroscopy and principal component analysis*. Analytical chemistry, 73(13):3153–3161, 2001.

[12] Peter Snoer Jensen, Jimmy Bak, and Stefan Andersson-Engels. *Influence of temperature on water and aqueous glucose absorption spectra in the near-and mid-infrared regions at physiologically relevant temperatures*. Applied spectroscopy, 57(1):28–36, 2003.

[13] Simon P Wolff, Zhen Y Jiang, and James V Hunt. *Protein glycation and oxidative stress in diabetes mellitus and ageing*. Free Radical Biology and Medicine, 10(5):339–352, 1991.

[14] Rong Liu, Kexin Xu, Yanhui Lu, and Huili Sun. *Combined optimal-pathlengths method for near-infrared spectroscopy analysis*. Physics in medicine and biology, 49(7):1217, 2004.

[15] Kexin Xu, Yanhui Lu, Qingbo Li, and Yan Wang. *Path length selection method for quantitative analysis with near-infrared spectroscopy*. In ALT'03 International Conference on Advanced Laser Technologies: Biomedical Optics, pages 100–106. International Society for Optics and Photonics, 2004.

[16] Annette Rebel, Mark A Rice, and Brenda G Fahy. *The Accuracy of Point-of-Care Glucose Measurements*. Journal of diabetes science and technology, 6(2):396–411, 2012.

[17] William L Clarke, Daniel Cox, Linda A Gonder-Frederick, William Carter, and Stephen L Pohl. *Evaluating clinical accuracy of systems for self-monitoring of blood glucose*. Diabetes care, 10(5):622–628, 1987.

[18] Karin Obermaier, Günther Schmelzeisen-Redeker, Michael Schoemaker, Hans-Martin Klötzer, Harald Kirchsteiger, Heino Eikmeier, and Luigi del Re. *Performance evaluations of continuous glucose monitoring systems: precision absolute relative deviation is part of the assessment*. J Diabetes Sci Technol, 7(4):824–832, 2013.

[19] Eda Cengiz and William V Tamborlane. *A tale of two compartments: interstitial versus blood glucose monitoring*. Diabetes technology & therapeutics, 11(S1):S–11, 2009.

[20] Tormod Næs, Tomas Isaksson, Tom Fearn, and Tony Davies. *A user-friendly guide to multivariate calibration and classification*, volume 6. NIR publications Chichester, 2002.

[21] Sijmen de Jong and Aloke Phatak. *Partial least squares regression*. Recent advances in total least squares techniques and errors-in-variables modeling, pages 311–338, 1997.

[22] Sandeep Sharma, Mohammad Goodarzi, Laure Wynants, Herman Ramon, and Wouter Saeys. *Efficient use of pure component and interferent spectra in multivariate calibration*. Analytica chimica acta, 778:15–23, 2013.

[23] Sandeep Sharma. *Exploiting expert information in multivariate calibration of an implantable glucose sensor*. PhD thesis, Biosystems department (Mebios), KULeuven, 2014.

[24] Sandeep Sharma, Mohammad Goodarzi, Joris Delanghe, Herman Ramon, and Wouter Saeys. *Using experimental data designs and multivariate modelling to assess the effect of glycated serum protein concentration on glucose prediction from near infrared spectra of human serum*. Applied spectroscopy, 2014.

[25] Sandeep Sharma, Mohammad Goodarzi, Joris Delanghe, Herman Ramon, and Wouter Saeys. *Using Experimental Data Designs and Multivariate Modeling to Assess the Effect of Glycated Serum Protein Concentration on Glucose Prediction from Near-Infrared Spectra of Human Serum*. Appl. Spectrosc., 68(4):398–405, Apr 2014.

3

Implantable spectrometer configurations

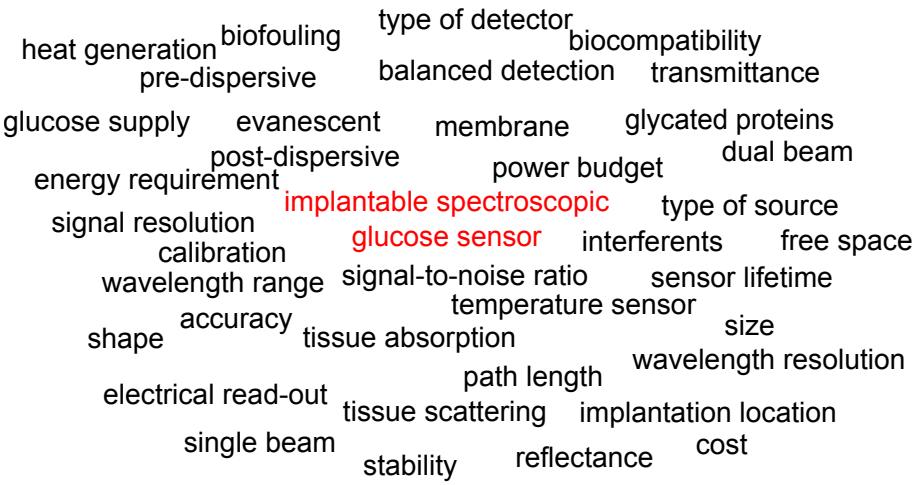

Figure 3.1: Design considerations for an implantable spectroscopic glucose sensor

To highlight the complexity of the development of an implantable spectroscopic glucose sensor, a condensed list of the design considerations is given in figure 3.1. The goal of this chapter is to discuss the possible spectrometer

configurations, given the constraints of the in vivo glucose detection application. At the start of the project, little experience was available in terms of the integration of a fourier transform interferometric spectrometer (FTIR). The first demonstration of an on-chip FTIR was e.g. not yet published. Therefore, the focus of miniaturization was on dispersive spectrometers. However, most of the work is applicable to FTIR spectrometers as well. We start this chapter with the basic classification of dispersive spectrometers: pre- versus post dispersive and single versus dual-beam. Afterwards, we discuss the different types of sources that can be used for absorption spectroscopy. We then shortly touch upon modulation techniques for spectroscopy. Next, we discuss the sample interface of the spectrometer. This interface can be either free-space or evanescent. Both will be compared in terms of power budget and biocompatibility. This chapter ends with the discussion of two general features of implants, namely the electrical power budget and associated heat generation.

3.1 Classification of spectrometers

3.1.1 Pre-dispersive vs Post-dispersive

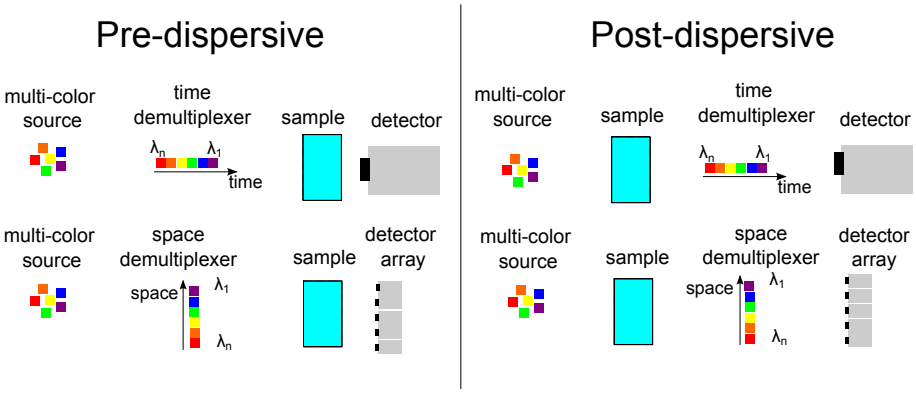

Figure 3.2: Schematic of a pre- and post-dispersive spectrometer

For dispersive spectrometers, essentially two configurations exist: either the wavelength demultiplexing is done before the sample, or after. This wavelength demultiplexing can be done in time or in space. The power incident on the sample in both cases (pre- vs post) can differ significantly. Therefore, the thermal loading of the sample may also differ substantially. The choice between pre- or post-dispersive, however, depends mostly on how efficient the light can be coupled to the wavelength demultiplexer. In the case of an integrated wavelength demultiplexer, the coupling efficiency

is determined by the overlap integral between the field at the entrance of the demultiplexer and the fundamental optical mode of the demultiplexer. Any mode mismatch between both, will lead to a smaller coupling efficiency, hence power loss. In a post-dispersive spectrometer, substantial mode mismatching can be induced by scattering or beam spreading upon propagation through the sample. Therefore, special care must be taken in most post-dispersive spectrometers to optimize the coupling to the wavelength demultiplexer.

3.1.2 Single-beam vs Dual-beam

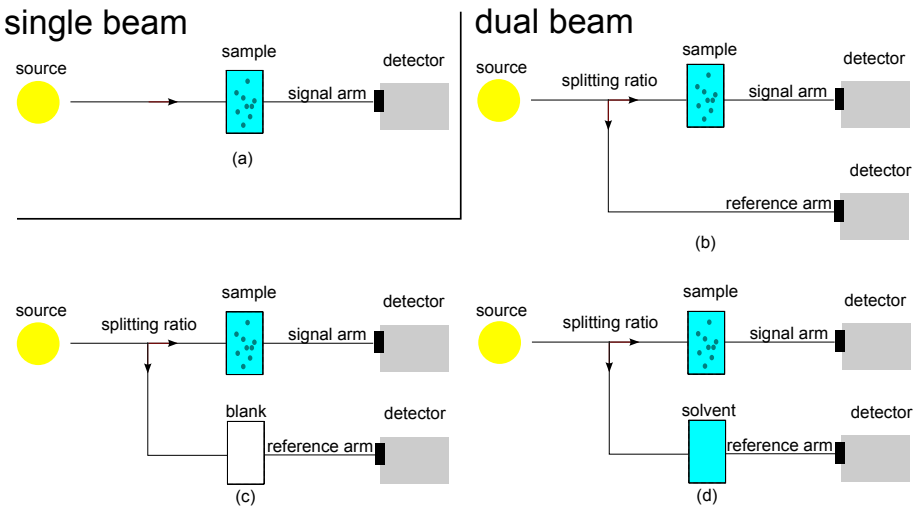

Figure 3.3: Schematic of (a) single and (b,c,d) dual beam configurations

The easiest implementation of a spectroscopic sensor is a single-beam configuration as shown in figure 3.3(a). The important drawback of this system is the fact that any variation in light intensity originating outside the sample, is also measured. It is thus impossible to distinguish for example between absorption in the sample and source fluctuations. To eliminate this type of noise, a dual beam configuration can be employed. In figure 3.3(b-d), the most commonly used dual-beam options are shown. In the first case (b), only the source intensity variations are monitored. In case (c) also variations in the sample interface can be canceled. In the last case (d), next to source and interface variations, the large background absorption of the solvent can be eliminated. A few practicalities are important to make a dual-beam system work properly: (1) the splitting ratio must remain constant, (2) the detectors must be similar in performance and noise

and (3) variations in the non-common path need to be minimized. In addition, these non-common variations need to be at least smaller than the common-path variations. It is necessary to carefully analyze the complete optical set-up with respect to the above listed requirements to obtain a dual-beam system that obtains a high SNR (>40 dB) over a long period in the order of hours to days. For example: it may look straightforward to design a fixed splitting ratio, but this ratio can be affected by indirect parameters such as the incident light polarization, next to direct environmental changes such as temperature, mechanical drift etc. In a dual-beam configuration as in figure 3.3(d), we obtain the transmission due to glucose as the ratio between the signal and reference detector values:

$$\frac{P_{sig}}{P_{ref}}(\lambda) = \frac{T_{H_2O+Gluc}T_{common}P_{in}}{T_{H_2O}T_{common}P_{in}} = T_{gluc}(\lambda) \tag{3.1}$$

In this equation P symbols an optical power, while T symbols transmission. Using Beer-Lambert's law, this transmission spectrum can then be used to calculate the glucose concentration.

Balanced detection

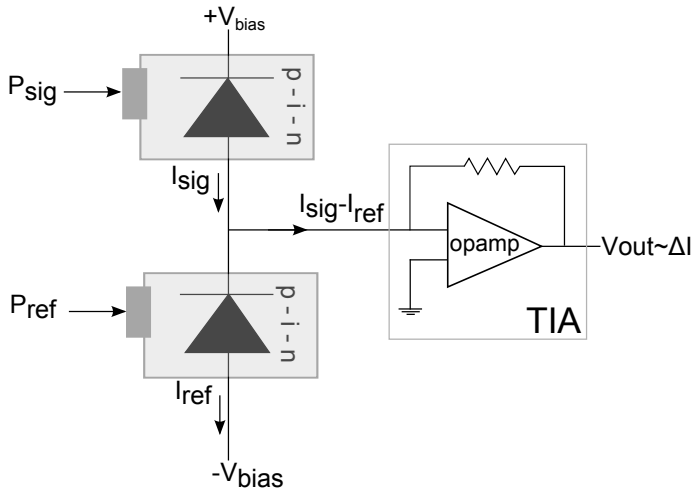

Figure 3.4: Schematic of balanced detection

In a special form of dual beam sensors, the direct difference between two detector is used as signal. By connecting the anode of the signal photodiode with the cathode of the reference photo-diode, the difference current is readily obtained. This is shown in figure 3.4. Mathematically, the operation of a balanced detector system, not taking into account noise, can be written as:

$$\Delta P = P_{sig} - P_{ref} = P_{common}(1 - T_g) \cong P_{common}(1 - (1 - \alpha_g c_g))$$

$$\Downarrow$$

$$\Delta P \sim c_g \tag{3.2}$$

with T_g the transmission due to glucose, which is linearly proportional to glucose c_g for physiologically relevant concentrations. The detected power difference is thus directly proportional to the glucose concentration. But, the glucose transmission spectrum can no longer be directly obtained from the balanced detection measurement. The use of balanced detection has the distinct advantage that the full dynamic range of the read-out system is used to measure the useful signal due to glucose. In addition, all the electronic components of the read-out circuit after the photodetectors is common, which reduces the electrical noise[1]. The read-out circuit typically consists of a linear transimpedance amplifier (TIA) followed by an analog-to-digital convertor (ADC). The main drawback of balanced detection with this read-out circuitry is that any variation in the common path cannot be distinguished from the glucose signal. To circumvent this, one can also use a logarithmic amplifier for both signals which yields $\log(I_{sig})$ and $\log(I_{ref})$. By subtracting both and by sending this difference to a common ADC, the useful information (I_{sig}/I_{ref}) can be retrieved, while eliminating unwanted variations in the common path.

3.2 Optical sources for absorption spectroscopy

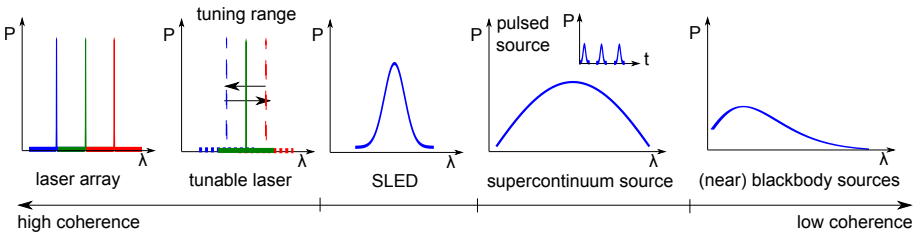

Figure 3.5: Sources for near infrared absorption spectroscopy

In figure 3.5, we list the different sources that can be used for near-infrared absorption spectroscopy. We can classify these sources in terms of their coherence length. Sources with a short coherence length, have a spectrally broad emission spectrum and vice versa. For a source with a lorentzian-like emission spectrum, this coherence length is proportional to $\frac{\lambda^2}{\Delta\lambda}$ with λ the center wavelength and $\Delta\lambda$ the full width half max (FWHM) of the

lorentzian spectrum. In both dispersive and FTIR spectrometers, a broadband, low coherent source is used. These sources have the advantage that a large number of spectral features can be sampled. Still, the minimum resolution of the spectrometers can be insufficient to resolve fine absorption features. Lasers on the other hand, have a very narrow linewidth that can be used to scan along sharp absorption features. In addition, lasers have the highest spectral power density. Therefore, tunable lasers are often used for the spectral analysis of gaseous samples that show very sharp but weak features in the absorption spectrum. When tunable lasers are used, only a narrow wavelength range can be measured due to the limited wavelength tuning range. Still, on an integrated platform, a laser array can be implemented to cover a broad wavelength range. When a laser source is used, the spectrometer configuration is by definition pre-dispersive.
The high coherence of laser sources can lead to unwanted effects such as speckle and interference fringes in the optical transmission spectrum. To reduce the impact of these coherence effects, unwanted Fresnel reflections and scatter points along the optical path need to be avoided.

The choice between the different sources is application-specific and depends on a large number of parameters: the required output power stability, operating wavelength range, spectral power density, (electrical) power efficiency, coherence length, size and cost. In addition, the fabrication yield and tolerance to fabrication imperfections are very important if the source is to be integrated on a silicon chip.

3.3 Modulation techniques for spectroscopy

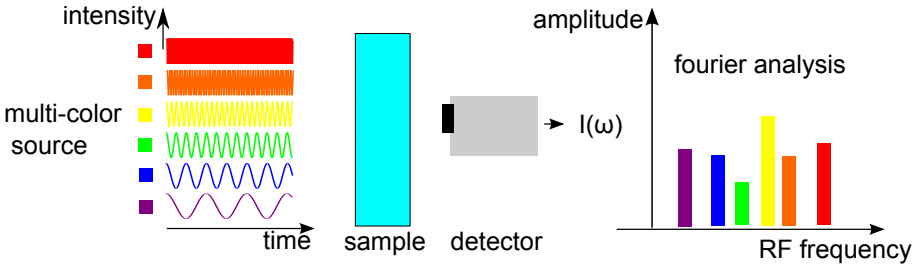

Figure 3.6: Conceptual drawing of wavelength demultiplexing using an intensity modulation scheme

In absorption spectroscopy, one very often uses modulation schemes to enhance the detection limit. The main reasoning is that if the signal is modulated, one can select the least noisy frequency range to detect the

signal. For example, the system's 1/f noise can be minimized by measuring at a higher frequency instead of DC. A wide range of modulation techniques have been developed: wavelength modulation [2], frequency modulation [3], derivative spectroscopy [4] etc. In figure 3.6 we show an example wavelength demultiplexing scheme based on modulation, that can be integrated on-chip. By modulating each wavelength with a different frequency followed by spectral fourier analysis of the detector signal, the transmission spectrum can be obtained. This has the advantage that all wavelengths can be measured at once, instead of sequentially, while using a single photo-detector. In this case, a larger number of spectra can be obtained given a certain measurement time, which can increase the signal to noise ratio by averaging and fourier noise filtering techniques.

When the source is a laser array, modulation wavelength multiplexing is easily obtained by direct modulation of the driving current. When using a broadband light source such as an SLED, modulation wavelength demultiplexing can also be used, but more design effort is needed. One first has to demultiplex the spectrum into thin slices that each have a separate modulator after which the spectrum needs to be reconstructed. The total footprint, insertion loss and modulator energy consumption has to be minimized to keep this option open for an implantable sensor.

3.4 Free space sensor

In figure 3.7, we show two free space configurations that can be used as an implantable glucose sensor. These configurations originate from the GlucoSens project proposal. The first configuration contains a laser array as the source and has a single detector (pre-dispersive). The second configuration has a single broadband source and a spectrometer with photodetector array (post-dispersive). In this free-space approach, the glucose molecules are accessed by sending the light from the source through tissue, and after transmission the light is captured back into the photonic chip. The sensor is encapsulated in a donut shaped biocompatible coating as shown in figure 3.7. This approach has clear advantages over existing glucose sensors: the tissue only sees the biocompatible coating, minimizing the risk of heavy body reactions. In addition, when the sensor is fully encapsulated, the risk of sensor failure due to water insertion is minimized. This is especially critical for the incorporated CMOS electronics. Unfortunately, these advantages do not weigh up to the disadvantages that are discussed in the following subsections.

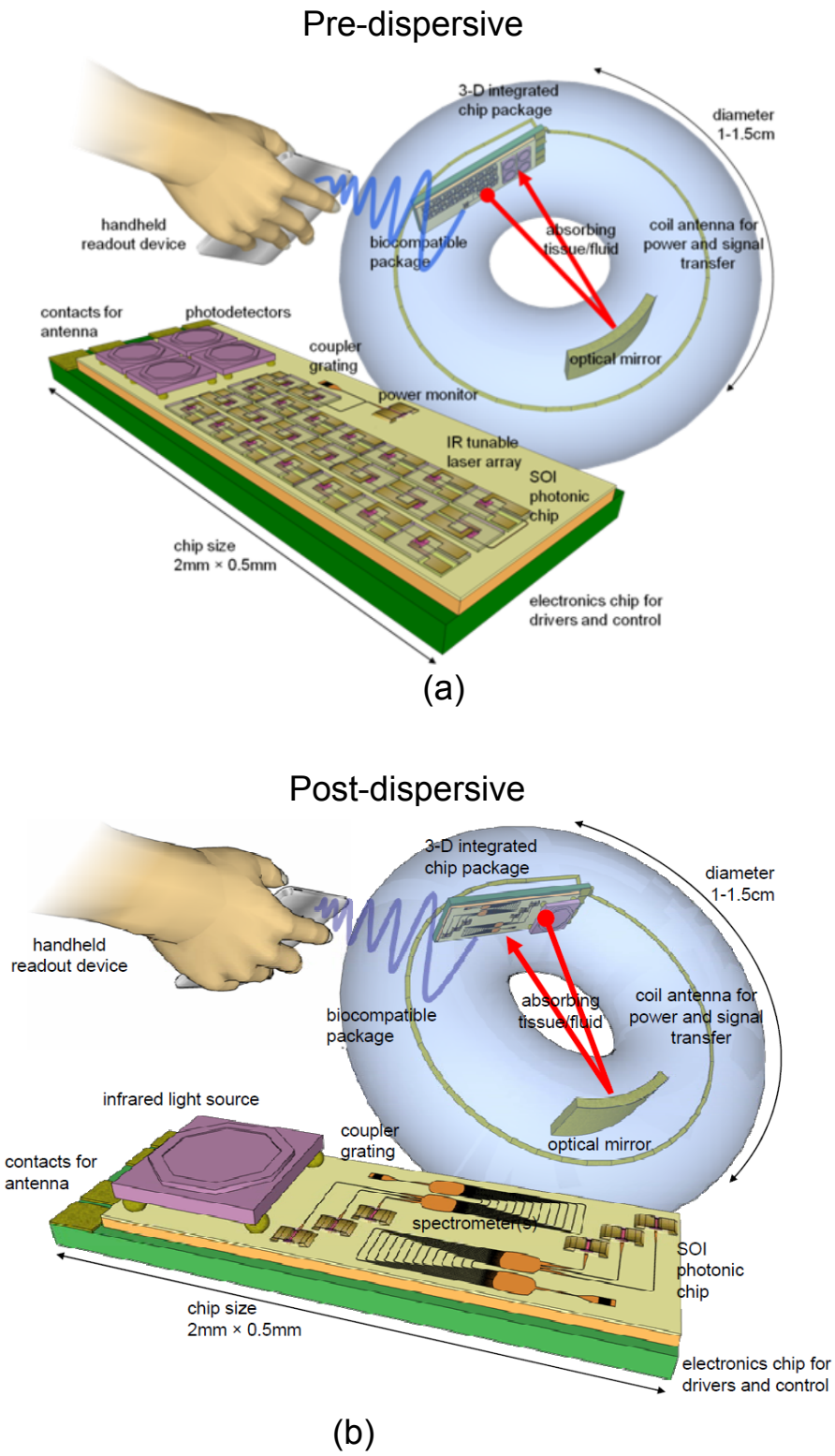

Figure 3.7: Free space glucose sensor (graphics design by Wim Bogaerts)

3.4.1 Biocompatible materials

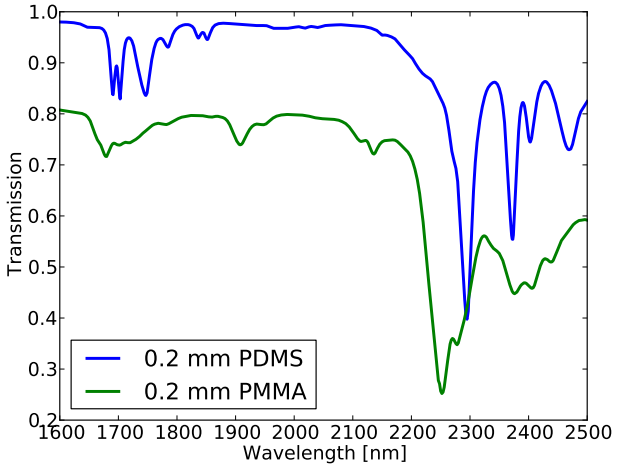

Figure 3.8: Transmission through 0.2 mm thin slices of PDMS and PMMA, showing the strong absorption features in the combination band

In this text, we adhere to the following definition of biocompatibility [5]: "the ability of a material to perform its desired function with respect to a medical therapy, without eliciting any undesirable local or systemic effects in the recipient or beneficiary of that therapy, but generating the most appropriate beneficial cellular or tissue response in that specific situation, and optimizing the clinically relevant performance of that therapy."

Two materials were studied by the Polymer chemistry and biomaterials research group (see appendix A) for the biocompatible coating: (poly) methyl methacrylate (PMMA) and (poly)dimethyl siloxane (PDMS). These materials were selected for their proven biocompatibility in medical applications such as soft lenses (PDMS), hard lenses (PMMA), hearing aids (PDMS) and as a coating for fiber optic sensors (PMMA and PDMS). For the implantable glucose sensor application, these materials should be surface-functionalized for two reasons:

- reduction of dense tissue ingrowth in the opening of the donut-shaped implant
- enhancement of glucose supply by attracting small blood vessels

Unfortunately, tissue ingrowth cannot be completely avoided, but one can hinder dense tissue types that limit the light transmission. The growth of

dense tissue is the end-stage of an inflammation response to the implant [6]. It starts by the adherence of plasma proteins onto the surface of the implant. These proteins promote the adherence of macrophages that signal the start of tissue inflammation. The macrophages secrete inflammation mediators that stimulate the growth of foreign body giant cells (FBGCs) which in their turn attract fibroblasts. These fibroblasts deposit a fibrous layer onto which collagen is deposited. Finally, the surface is covered with dense fibrous tissue. It is, thus, essential that the surface-treatment minimizes the adsorption of plasma proteins.

Next to biocompatibility, the optical properties of these materials were studied. Given that the probing light will traverse the coating, the materials have to be sufficiently transparent. The transmission spectra of a 0.2 mm thin slice of PMMA and PDMS are shown in figure 3.8. Although part of the losses were caused by small airbubbles in the materials, it is clear that both materials have a very strong absorption above 2200 nm. This limits the use of these materials for glucose spectroscopy in the combination band, as two out of three glucose features in the combination band (at 2.1 μm, 2.27 μm and 2.32 μm) cannot be accessed.

3.4.2 Tissue scattering

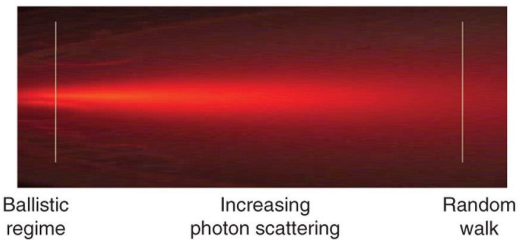

Figure 3.9: Illustration of tissue scattering (from [7])

In the proposed free space implant, the transmitted power is limited by losses due to tissue absorption and scattering. Given the typical sizes of biological structures, tissue appears as very inhomogeneous for the NIR wavelengths that we use [8]. This leads to strong light scattering effects such that the photon zig-zags rather than to follow a straight line. This way, many photons do not make it to the detector, resulting in a decrease in transmission. It is not straightforward to distinguish this decrease from power loss due to absorption. Therefore, if there is tissue ingrowth in the opening of the free-space implant and this tissue changes considerably over time, it becomes difficult to predict glucose reliably. It is important

to note that even when the tissue structurally doesn't change, the refractive index of the surrounding interstitial fluid fluctuates and can alter the scattering properties. This refractive index fluctuation of the ISF depends on the time-varying concentration of small molecules and proteins.
The scattering inside a given type of tissue can be described by a phase function $p(\mathbf{s}\cdot\mathbf{s}^{'})$ and μ_s [9]. The latter parameter is the scattering coefficient that represents the probability for a photon to be scattered when propagating a length unit in tissue. The scattering coefficient μ_s and the attenuation coefficient due to absorption μ_a combine to a single total attenuation coefficient μ_{total} (wavelength-dependent!). This way, the transmission of ballistic photons (non-scattered, non-absorbed) in tissue over a distance L is described with following modified version of Beer-Lambert's law [9].

$$T = \frac{I}{I_0} = e^{-\mu_{total}L} = e^{-(\mu_s+\mu_a)L} \tag{3.3}$$

The phase function is the angular distribution that is used to calculate the probability $p(\mathbf{s}\cdot\mathbf{s}^{'})d\omega$ that a photon with direction $\mathbf{s}$ (vector!) is scattered into a unit of solid angle $d\omega$ of the direction $\mathbf{s}^{'}$, when it encounters a scattering particle [9]. Every particle has, for each wavelength, its own phase function that depends on its shape, size and refractive index. For particles with a simple shape, such as a sphere, the phase function can be calculated analytically (Mie theory [10]). Most often, it is assumed that a given tissue type is an isotropic medium in terms of scatterers. This results in a single phase function for a given tissue. Using the phase function $p(\mathbf{s}\cdot\mathbf{s}^{'})$, a coefficient of anisotropy g can be defined as:

$$g = \int_{4\pi} p(\mathbf{s}\cdot\mathbf{s}^{'})(\mathbf{s}\cdot\mathbf{s}^{'})d\omega \tag{3.4}$$

This anisotropy parameter g can range between -1 (completely backward scattering) and +1 (completely forward scattering). When $g = 0$ the scattering is isotropic and the phase function is simply $\frac{1}{4\pi}$.

Effective path length estimation

Even when scattered photons do make it to the detector, a large fraction of them is causing actual noise. All scattered photons have traveled a different path length before reaching the detector. The path length, however, needs to be known to extract the glucose concentration. Any fluctuation on the mean path length, results in uncertainty in the glucose concentration estimation. By using Monte Carlo simulations with the appropriate tissue parameters μ_s, μ_a, g, the number of photons that reach the detector for a given sensor configuration can be estimated, as well as the mean effective path length[11].

Glucose-empty cells

A final, but important limitation of the free-space implant is the spatial inhomogeneity of glucose in tissue. A key observation in diabetes patients is that the glucose content in cells is strongly reduced, as the molecules can no longer enter the cells efficiently. Thus, when the photons travel from source to detector, the larger the amount of cells they pass, the lower the amount of glucose molecules they encounter. This weakens the glucose signal. In addition, the diagnostically relevant glucose concentration is the blood glucose level and the strongly related ISF. By measuring the concentration average over ISF and cells, we thus do not measure the relevant concentration to take corrective actions.

3.4.3 Power budget considerations

Here we will calculate the power budget for three free-space configurations that can be integrated onto a silicon photonic chip. As shown in figure 3.7, either a pre- or post-dispersive free-space implant can be developed. In the pre-dispersive free space spectrometer, the light source can be either a laser array or a broadband SLED. In the case of a laser array, the light from the different lasers is first multiplexed into one waveguide before it is coupled out to the tissue. After transmission through tissue, the light is captured with a large photo-detector. When a broadband SLED is used, the light first passes a tunable wavelength filter, before it passes the tissue. The transmitted light is also captured by a large photo-detector.
In the post-dispersive free space configuration, a broadband SLED is used as a source. This source light is directly incident onto the tissue. The transmitted light first has to be collected into a waveguide, before it can be spectrally analyzed with an integrated wavelength demultiplexer and integrated photodetectors. Coupling the transmitted light into a waveguide is not straightforward as this light beam is no longer diffraction-limited due to the high number of scattering events in tissue. The highest coupling efficiency is obtained for ballistic photons and these photons also travel a known path length (needed to accurately derive the glucose concentration). Therefore, we only take these photons into account for the post-dispersive configuration.
In all three free-space configurations, we assume a 3 dB loss when coupling from the light source to the silicon guiding layer of the chip. The component losses are based on the typical losses of components integrated onto a silicon photonic chip as reported in [12, 13, 14]. In addition, we assume that the tunable filter has the same losses as the wavelength demultiplexer. We assume that the implant is inserted subcutaneously, therefore the optical properties of adipose tissue (body fat) is used to calculate the absorption and scattering losses [8]. The calculations are performed in the first overtone (@ 1590 nm) and combination band (@ 2110 nm), while we assume a

wavelength demultiplexer with 14 channels (see section 2.4.4). The optical path length L is the optimal length in aqueous solutions (1.36 mm in first overtone band and 0.37 mm in combination band) times 10, as we consider the glucose content in cells negligible and there is about 10% of ISF in adipose tissue [15].
Eventually, the power budget calculation yields the required power such that a change in transmitted power due to 1 mM is three times larger than the noise produced in the photodiode and the transimpedance amplifier. The minimal input power P_N at the detector can then be written as:

$$P_N = 3\sqrt{(NEP \cdot \sqrt{\frac{1}{2t_s}})^2 + (\frac{i_{n,TIA}}{\Re} \cdot \sqrt{\frac{1}{2t_s}})^2} \tag{3.5}$$

in which $\Re$ [A/W] is the responsivity of the photodiode, NEP [W/$\sqrt{Hz}$] the noise-equivalent power of the photodiode, t_s [s] the integration time and $i_{n,TIA}$ [A/$\sqrt{Hz}$] the input-referred noise of the transimpendance amplifier. We do not consider additional noise produced by the electronic read-out circuitry, but limit the power budget here to the optical link and first amplifier stage. The detector NEP is calculated using the normalized detectivity $D^*$of highly performant InGaAs photodetectors with a surface area S and frequency bandwidth Δf by using following formula:

$$NEP = \frac{\sqrt{S\Delta f}}{D^*} \tag{3.6}$$

In the pre-dispersive case, the surface of the detector needs to be chosen to accommodate at least the size of the diffracted beam. This detector will capture scattered photons as well. In adipose tissue, where scattering dominates over absorption ($\mu_s >> \mu_a$), the inverse of the reduced scattering coefficient $\mu_s^{'} = \mu_s(1-g)$ represents the distance d (= $\frac{1}{\mu_s^{'}}$) after which the photons have isotropically distributed directions each with $\frac{1}{4\pi}$ probability [7]. This distance d is shorter than the optimal path length for our free-space sensor. Therefore, we capture only non-absorbed photons, uniformly distributed in a solid angle $\Omega = \frac{S}{L^2}$. The transmission from the entrance of the tissue to the detector, thus, equals the absorption losses $\exp -\mu_a L$ times the fraction of captured photons.
When the detector surface area is chosen larger, more light can be captured, leading to a better power budget. This, however, has a trade-off with the prediction accuracy that lowers with an increased amount of scattered photons versus ballistic photons.
In the post-dispersive case, we consider that we capture only ballistic photons, therefore the transmission equals $\exp -(\mu_a + \mu s)L$. The detector surface area in the post-dispersive case is based on the dimensions of grating-assisted integrated photodiodes. Given the directionality of the grating coupler, maximally 50% is coupled to the photodiode, introducing a loss

factor of 3 dB.
The resulting power budget (see table 3.10) shows that a laser array based system is the most attractive option. In the first overtone band, the required power of 0.42 mW is reasonable, but for the combination band a laser power of 6.03 mW is not feasible in an implant. A strong improvement is possible by optimizing the grating coupler. By using more advanced processing using a silicon overlay (see further section 5.2.3), the losses can be reduced to 2 dB instead of 6 dB. The pre-dispersive configuration with SLED needs the same source power per wavelength channel, thus the total SLED power scales with the number of channels. A post-dispersive configuration is completely impossible due to strong tissue scattering.

3.4.4 Modified free space implant

A modified version of the free space implant can overcome most of the above listed problems related to light propagation in tissue. By using a membrane above the openings of the donut-shaped implant, tissue ingrowth can be avoided. In addition, the molecular weight cut-off of the membrane can be chosen to block interferents such as (glycated) proteins. This way, we can decrease the complexity of the sampled fluid, leading to a better glucose prediction. A schematic of the modified version is shown in figure 3.11.
Important to note is that, by using membranes, we create a small cavity without blood vessels. Glucose can only move within this cavity by the slow process of diffusion. This can lead to small differences and a time-delay in the glucose level as compared to the physiologically relevant concentration outside this cavity. This compromises the direct relation between the sensor response and the patient's actual blood glucose level. Therefore, the dimensions, location and glucose transfer coefficient of the membranes should be adequately chosen to minimize this effect. By opting for an implant with membranes, an alternative glucose sensor configuration was identified, namely evanescent sensors. Both are compared in figure 3.12

In evanescent sensors, the light never leaves the photonic chip. This offers a large design flexibility that can lead to e.g. multiplexing of the sensor or the use of multiple path lengths for better glucose prediction. The surface of the evanescent sensor is in direct contact with the sample fluid to be able to probe glucose. When cells or proteins adhere to the evanescent sensor surface, the sensor can no longer measure glucose. Therefore, a membrane is needed to avoid this adhesion. The success of evanescent sensors strongly depends on the quality of the membrane that is used. The same holds for the modified free space implant. Therefore, the modified free space implant is still a justified choice if the direct contact with the silicon surface would lead to body reactions. But if not, the evanescent sensor

Transmission losses		F.O. Band	C.B. Band	unit
	wavelength	1590	2110	nm
optimal path length	path length	1.36	0.37	cm
Losses adipose tissue	absorption μ_a	1.00	2.00	cm^{-1}
	anisotropy (g)	0.80	0.90	
	reduced scattering ($\mu_s^{'}$)	8.00	9.00	cm^{-1}
	scattering (μ_s)	40.0	90.0	cm^{-1}
Sensor resolution	concentration	1.0	1.0	mM
	absorptivity H_2O	5.77E-06	2.12E-05	$\frac{1}{mMmm}$
	water displacement	6.25	6.25	
	absorptivity glucose	6.79E-05	2.23E-04	$\frac{1}{mMmm}$
	absorbance glucose	4.33E-04	3.35E-04	
Minimum SNR	SNR=10*log10(1/ΔT)	-30.01	-31.13	dB
	ΔT due to glucose	9.99E-01	9.99E-01	
Transmission to detector	T (PRE)	-39.37	-49.86	dB
	T (POST)	-242.1	-147.8	dB
Photodetector		F.O. Band	C.B. Band	unit
Area needed due to diffraction	refractive index (H_2O)	1.31	1.29	
	gaussian start width	4.50E-06	6.00E-05	m
	rayleigh range	5.38E-05	6.91E-03	m
	gaussian end width	1.15E-03	6.89E-05	m
	surface area (PRE)	1.05E-06	3.73E-09	m^2
	surface area (POST)	3.00E-10	3.60E-10	m^2
Detector specs	normalized detectivity	4.90E+11	6.30E+10	$\frac{cm\sqrt{Hz}}{W}$
	integration time	1.0	1.0	s
	responsivity	0.7	0.7	$\frac{A}{W}$
	input referred noise	1.0E-12	1.0E-12	$\frac{A}{\sqrt{Hz}}$
	minimal input power (PRE)	-85.16	-85.18	dBm
	minimal input power (POST)	-85.19	-85.18	dBm
Component loss	demultiplexer loss	-3.0	-3.0	dB
	grating coupler loss	-6.0	-6.0	dB
	SLED/laser to chip coupling	-3.0	-3.0	dB
	coupling to photodiode	-3.0	-3.0	dB
Power division	number of λ channels	14	14	
	10*log10(channels)	11.46	11.46	dB
Required source power	Configuration	F.O. Band	C.B. Band	unit
	laser array (per λ)	0.42	6.03	mW
	SLED + PRE	5.86	84.40	mW
	SLED + POST	1.11E+21	5.29E+11	mW

Figure 3.10: Power budget calculation for the 3 free-space configurations

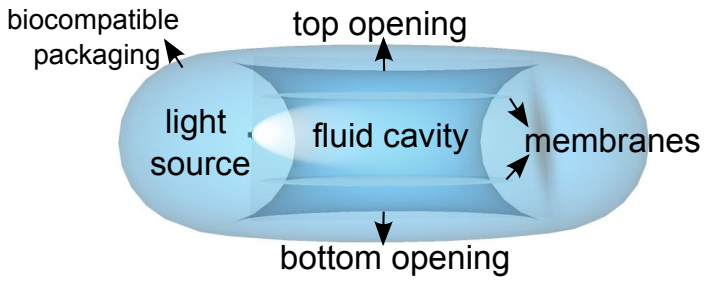

Figure 3.11: Modified free space implant with membranes to prevent tissue ingrowth

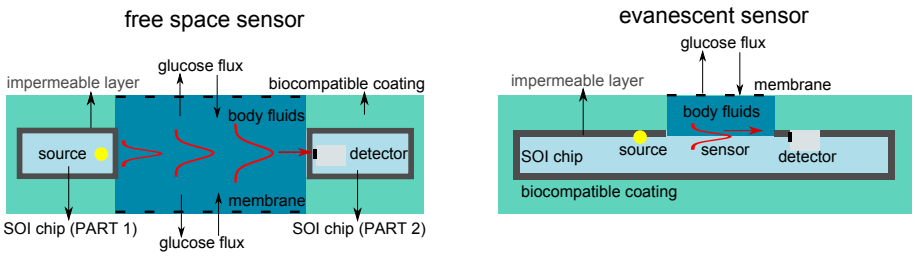

Figure 3.12: Cross-section of an implantable free space sensor and evanescent sensor

approach, that is discussed in the next section, is the preferred option due to its large design flexibility and potential SNR improvements. In addition, the evanescent sensor can minimize the sensor delay, as the distance between the membrane and the sensor surface can be minimized.

3.5 Evanescent sensor

As mentioned above, the light stays on-chip in an evanescent sensor. This means that the light propagates as a guided mode in an integrated waveguide. In the silicon-on-insulator platform, this waveguide is formed by a silicon layer on top of a layer of oxide. The E-field of the propagating waveguide mode stretches slightly outside the physical dimensions of the silicon waveguide. The fraction of the E-field that extends outside the waveguide is called the evanescent field (see figure 3.13(a)). This evanescent field is directly affected by the optical properties of the materials around the waveguide. Therefore, when the waveguide is immersed in ISF, the photons in the evanescent field can be absorbed by molecules

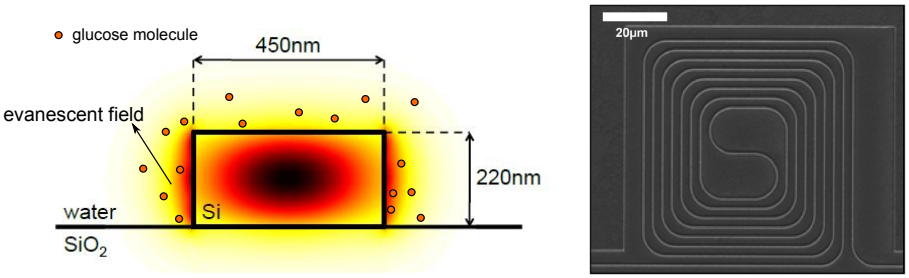

Figure 3.13: (a) evanescent field of a silicon waveguide (b) microscope picture of a waveguide spiral ((a) taken from [16])

in the ISF. This situation is similar to attenuated total reflectance, an absorption spectroscopy configuration well-known in literature [17]. In the next chapter, theoretical derivations and simulations are used to elaborate on the evanescent sensing principle using optical waveguides. By routing the waveguide into a spiral, the sensor footprint is strongly reduced, such that multiple spiral waveguides can be used on a single chip (see figure 3.13(b)).
In the remainder of this section, we describe the biocompatibility issues related to an evanescent implant and how evanescent sensing offers us more design freedom to multiplex the sensor. In addition, we will show with power budget calculations that, in contrast to the free-space implant, a post-dispersive configuration is again a feasible option.

3.5.1 Biocompatibility

Biocompatibility plays an even more important role in evanescent sensors as the sensor surface is directly exposed to the human fluids. Moreover, this sensor surface should stay 'clean'. Permanent adhesion of biological material to the sensor surface is to be avoided as it will decrease the sensor's sensitivity. Even a thin adhered layer (< 100 nm) will strongly reduce the region of overlap between analytes and the evanescent field, hence limits the absorption signal. Surface chemistry can be used to avoid adhesion of biological material, but also this surface chemistry should be biocompatible. In addition, glucose molecules need to reach the silicon chip surface in order to be sensed. As glucose molecules travel by diffusion in the absence of flow in the ISF, this also means that the diffusion time needs to be small to minimize the concentration difference with the ISF glucose level. When the body reacts to the implant by covering it with dense tissue or by clogging the membrane, the glucose molecules cannot enter the implant

efficiently and the diffusion time becomes intolerably long [18, 19].

Membrane

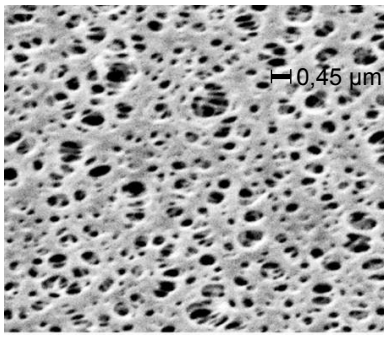

Figure 3.14: Microscope image of a polyethersulfone membrane showing the pore size distribution (taken from sartorius®)

The selection of a suitable membrane depends on the following important properties:

- ease of fabrication in combination with the biocompatible coating materials
- molecular weight cut-off (MWCO) to allow glucose diffusion but blocking of larger proteins and cells
- mechanical strength for a given thickness that allows fast glucose diffusion
- resistance to accumulation of bio-material that can clog the membrane

The last item is of key importance and a lot of research is devoted to this problem alone. Most of the knowledge is well-protected by patents and in the hands of the medical industry. The molecular weight (MW) provides an approximate measure for the size of small molecules and is expressed in the Dalton unit (1 dalton=one-twelfth the weight of an atom of 12C). Glucose for example has a molecular weight of 180 Da. The molecular weight cut-off of a membrane is directly related to the membrane pore size. Mostly, a membrane has a distribution of pore sizes (see figure 3.14) and thus the MWCO is not a sharp line. By choosing a small MWCO, we can reduce the complexity of the fluid that resides above the evanescent sensor.

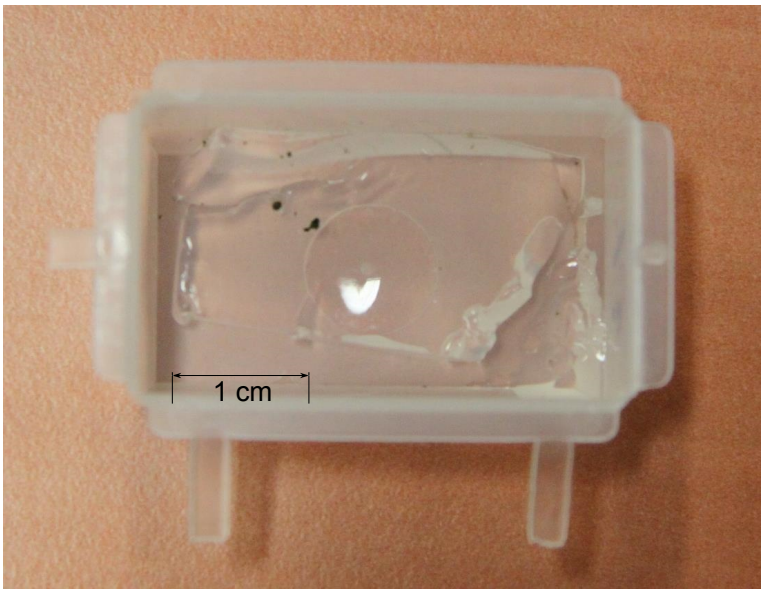

Figure 3.15: Picture of an agarose hydrogel. The black spots are bacteria, showing that it is a good environment to grow in.

Hydrogel

Instead of a membrane, a hydrogel can also be considered to allow glucose to the sensor surface, while blocking the adherence of proteins and cells. A hydrogel consists of a hydrophilic polymer matrix filled with hydrogen-bonded water molecules. The flexibility and pore size of the hydrogel can easily be tuned during fabrication. Most hydrogels are biocompatible and are often used as a porous environment in which cells can grow. In addition, glucose sensors have been invented that optically monitor the swelling of hydrogels in response to glucose. In figure 3.15 an agarose hydrogel is shown. As the hydrogel is in direct contact with the sensor, the high water content and polymer matrix introduce optical losses due to absorption and scattering. In the case of agarose, we measured a 30% inrease in optical losses compared to a pure water cladding.

Silicon-on-insulator

In the proposed evanescent sensor, the body fluids are in contact to both silicon and its native oxide SiO_2. The biocompatibility of SiO_2 has been proven in literature [5]. It is for example commonly used in dental implants. However, most reports on the biocompatibility of silicon are negative. In figure 3.16 from [6], it is shown for example how the number

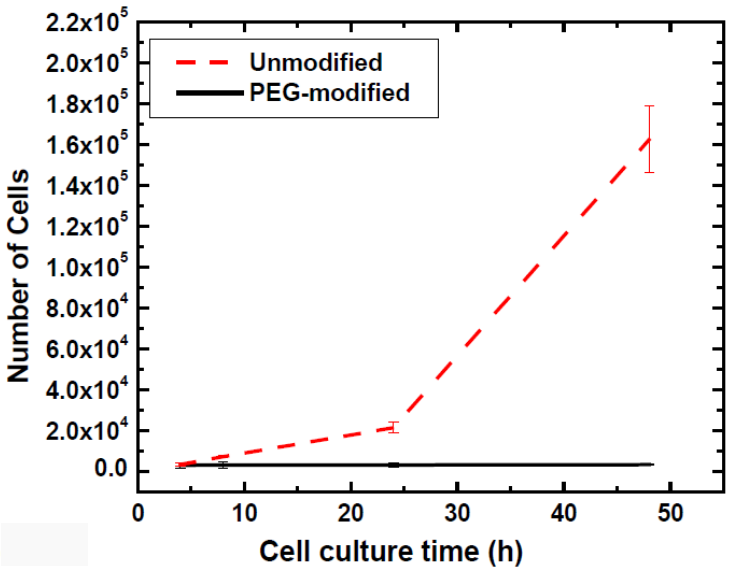

Figure 3.16: Growth of fibroblasts on top of silicon in cell culture as a hostile reaction to its presence. Surface treatment of the silicon with PEG reduces the inflammatory response [6]

of fibroblast cells steadily increases on top of bare silicon in a cell culture medium. These fibroblasts are responsible for dense tissue growth and a sign that the body wants to isolate itself from the silicon. By coating the silicon with a poly-ethylene glycol (PEG) monolayer this evolution is stopped, suggesting that silicon can benefit from a surface treatment. When using a membrane, it is only tissue fluid that is in contact with the silicon and it remains a research question whether this will invoke an inflammatory response around the implant.

3.5.2 Sensor multiplexing

The main advantage of an evanescent sensor is the design freedom that it offers us. By using on-chip power splitters, we can easily send the light from the source to multiple sensing spirals, wavelength demultiplexers and detectors. This multiplexing would not be possible in a free-space implant. In addition, for an evanescent implant, we can choose different spiral lengths, which is equivalent to different optical path lengths for spectroscopy. This can enhance the glucose detection limit, as explained in section 2.3.3. As the spiral length should be optimized for a given wavelength range, each spiral can be interrogated by a wavelength demultiplexer specifically designed for these wavelengths. Moreover, it is pos-

sible to monitor extra parameters such as temperature and pH, by integrating other sensors (e.g. ring resonators, Mach-Zehnder) next to the absorption-sensitive spiral waveguides. This multi-parameter sensing approach would exploit the key assets of the silicon photonics platform. Sensor multiplexing, however, has a trade-off with the optical power budget as every splitting action introduces a loss penalty.

In vivo evanescent dual-beam sensing

The simplest case of sensor multiplexing is to employ a signal and a reference spiral to create an on-chip dual-beam spectrometer. By integrating all components on a small single chip, a very high common-noise reduction can be achieved. Indeed, all environmental parameters (mechanical, thermal, electrical) can be matched for both the signal and reference optical path. An interesting question pops up when we consider how to create a proper reference arm in vivo. In the ideal measurement setting, the signal spiral and reference spiral see exactly the same sample fluid except for the number of glucose molecules. The glucose molecules are, however, very small and cannot be isolated easily. Thus, how can we ensure a high glucose concentration at the signal spiral, while minimizing the amount of glucose molecules at the (otherwise identical) reference spiral? The solution to this problem is the subject of chapter 7. We will show there how the diffusion process can be used to create a glucose concentration gradient such that the signal spiral sees a high concentration and the reference spiral a minimal glucose concentration.

3.5.3 Power budget

In this section, we will calculate the power budget for both a pre- and post-dispersive dual-beam evanescent configuration that can be integrated onto a silicon chip. A schematic of both configurations is shown in figure 3.17. In the pre-dispersive configuration, the light from a laser array is combined into one waveguide. This can be achieved with either a wavelength demultiplexer (not shown in figure 3.17(a)) or by using one bus waveguide that evanescently couples the light from all lasers (as shown in figure3.17(a)). This light is then splitted into a signal and a reference path with an identical evanescent spiral and integrated photo-detector. In the post-dispersive configuration, a broadband SLED is used. The light from this SLED is split into a signal and reference channel. Both channels have an identical evanescent spiral and wavelength demultiplexer with photodetector array. As for the free space implant, we assume that we need 14 wavelengths to specifically detect glucose and that either the first overtone band or combination band is probed. Secondly, we assume grating-assisted photodiodes to determine the surface area of the detector. In addition, we assume that

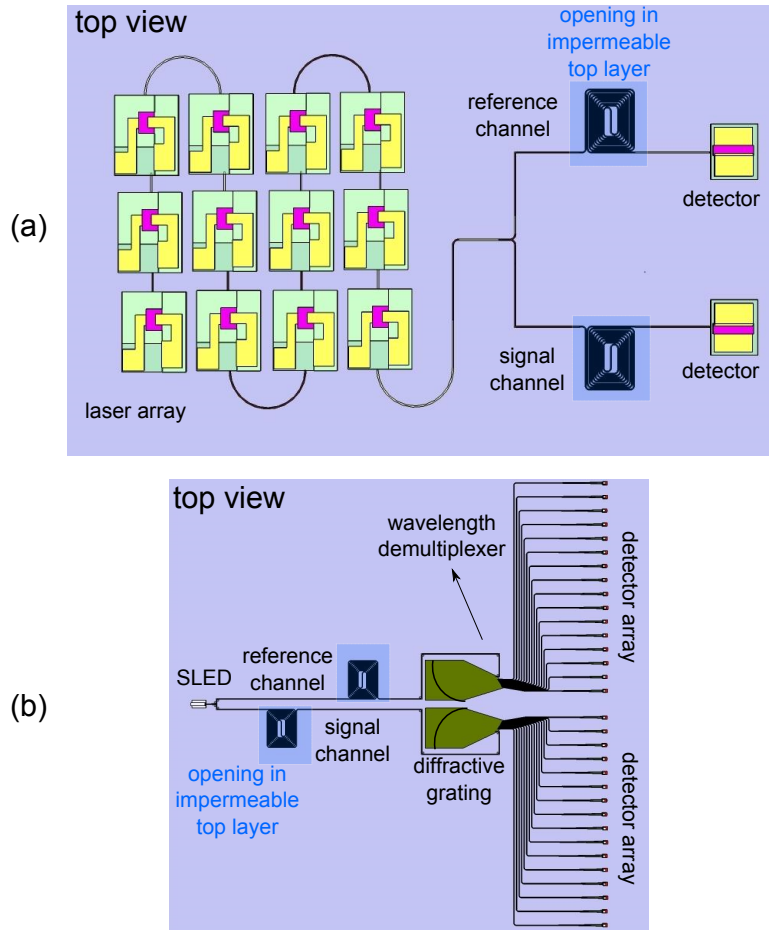

Figure 3.17: Schematic of (a) pre-dispersive dual-beam evanescent sensor configuration (b) post-dispersive dual-beam evanescent sensor configuration

the light from the individual lasers is combined using a wavelength demultiplexer as this is the most general configuration.
As in section 3.4.3, we limit the power budget to the optical link and the first transimpedance amplifier stage. Still, one extra noise source will be added to handle the dark current of the integrated photodiodes. In the case of the first overtone band, heterogeneously integrated InP photodiodes can be used, which have a low dark current on the order of 10 nA. In the case of the combination band, GaSb photodiodes need to be used, which have a much larger dark current of approximately 2.5 μA. We can offset this dark current by adding a current source opposite to the dark cur-

rent in front of the transimpedance amplifier, but this current source will generate shot noise. The minimal input power P_N needed at the detector should then be written as:

$$P_N = 3\sqrt{(NEP \cdot \sqrt{\frac{1}{2t_s}})^2 + (\frac{i_{n,TIA}}{\Re} \cdot \sqrt{\frac{1}{2t_s}})^2 + (\frac{1}{\Re}\sqrt{2qi_D\frac{1}{2t_s}})^2} \quad (3.7)$$

in which $\Re$ [A/W] is the responsivity of the photodiode, NEP [W/$\sqrt{Hz}$] the noise-equivalent power of the photodiode, t_s [s] the integration time and $i_{n,TIA}$ [A/$\sqrt{Hz}$] the input-referred noise of the transimpendance amplifier, q the elementary charge and i_D [A] the detector dark current.
The result of the power budget calculation is presented in table 3.18. We can derive that the total required power stays below 1 mW for all evanescent configurations. This is clearly advantageous compared to the free space configurations. Still, it is important to realize that the presented calculation is for the basic dual-beam system configuration. Any additional integrated sensor, next to the signal and reference evanescent sensor, will require more power, but can in turn increase the signal-to-noise ratio.

Transmission losses		F.O. Band	C.B. Band	unit
spiral waveguide	transmission	3.68E-01	3.68E-01	
detector specs	surface detector	3.00E-10	3.60E-10	m^2
	normalized detectivity	4.90E+11	6.30E+10	$\frac{cm\sqrt{Hz}}{W}$
	integration time	1.0	1.0	s
	responsivity	0.7	0.7	$\frac{A}{W}$
	dark current	1E-8	2.5E-6	A
	input referred noise	1.0E-12	1.0E-12	$\frac{A}{\sqrt{Hz}}$
	minimal input power	-85.18	-83.91	dBm
component losses	demultiplexer loss	3.0	3.0	dB
	SLED/laser to chip coupling	3.0	3.0	dB
	coupling to photodiode	3.0	3.0	dB
Power division	number of λ channels	14	14	
	10*log10(channels)	11.5	11.5	dB
Sensor multiplexing	number of sensors	2	2	
	splitting	3.0	3.0	dB
Required SNR	SNR	40	40	dB
Required source power				
	laser array per λ	1.31	1.75	μW
	SLED (14 channels)	18.3	24.5	mW

Figure 3.18: Power budget calculation for the evanescent configurations

3.6 Electrical power consumption and heat generation

The electronic chip that is implanted next to the photonic chip has two important tasks: firstly, driving the light source and secondly, providing the photodetector read-out. Here, we shortly discuss the electrical power that is needed to drive the light source. Commercially available SLEDs typically require a drive current of 250 mA to yield 1 mW of optical power [20]. Commercially available laser sources, such as a vertical cavity surface emitting lasers (VCSEL), however, only require 2-8 mA for the same optical power [21]. Heterogeneously integrated laser sources that can deliver up to 1 mW of output power, often have a higher threshold current in the order of 30 mA [22]. In contrast, heterogeneously integrated laser sources with smaller output power ($< 1mW$), such as micro-disk lasers, only require a few mA driving current. With a forward voltage between 1 and 2 V for the above listed sources, the needed electrical power is on the order of 10 mW (laser) to 100 mW (SLED). This required power can be transmitted wirelessly to the implant using magnetic inductive powering. Next to wireless powering of the implant, a wireless communication scheme can be set up to send (calibration!) and receive (the measured signal) information.

3.6.1 Heat transfer model

For implantable sensors it is important to know that the energy dissipation in the implant doesn't cause substantial heating in the surrounding tissue. In this section, we calculate the temperature distribution around the implant with the software comsol®. We assume that the sensor is implanted subcutaneously, 1 cm under the skin. We use a 2D axisymetric heat transfer model with cylindrical coordinates z and r. The software solves the following steady-state heat transfer equation:

$$\nabla \cdot (-\vec{k}\nabla T) = Q_{metabolism} + Q_{driver} \tag{3.8}$$

in which $Q_{metabolism}$, the heat generated due to our metabolism and Q_{driver} the heat generated by the electronics driver circuitry. We assume that the full electrical power is dissipated as heat in the tissue and a uniform initial temperature distribution of $37°$C. The simulation parameters and boundary conditions are shown in figure 3.19. The internal heat can escape through the skin to the outside air. When we simulate a laser source with $P_{driver} = 10$ mW, see figure 3.20(a), we have a negligible temperature rise in the tissue around the sensor. However, when we employ a SLED source with $P_{driver} = 100$ mW, see figure 3.20(b), the temperature in the immediate vicinity of the sensor rises to $40°$C. This is a substantial rise compared to the body temperature of $37°$C and might cause detrimental effects such

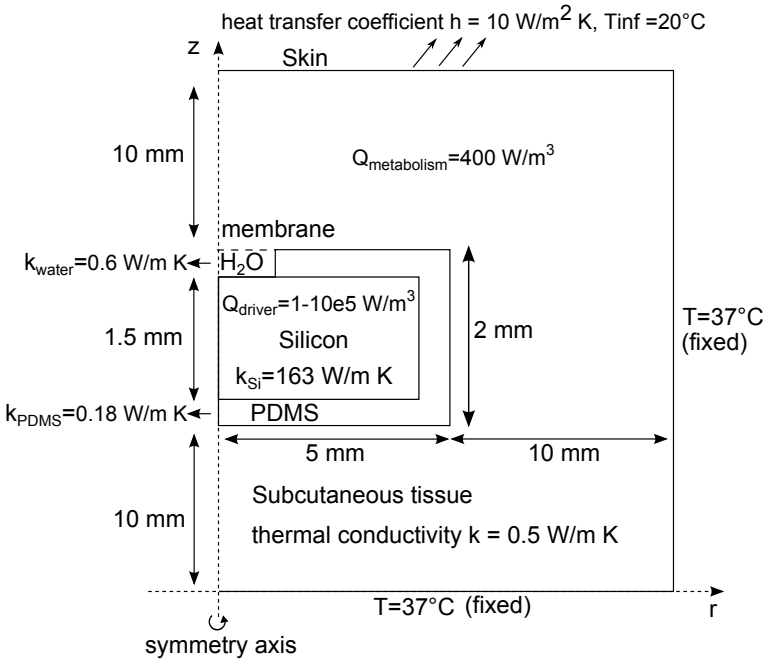

Figure 3.19: Heat transfer model settings

as reduced cell regeneration etc. [23]. However, this is the steady-state result, so we can still minimize the build-up of heat in tissue by reducing the measurement time.

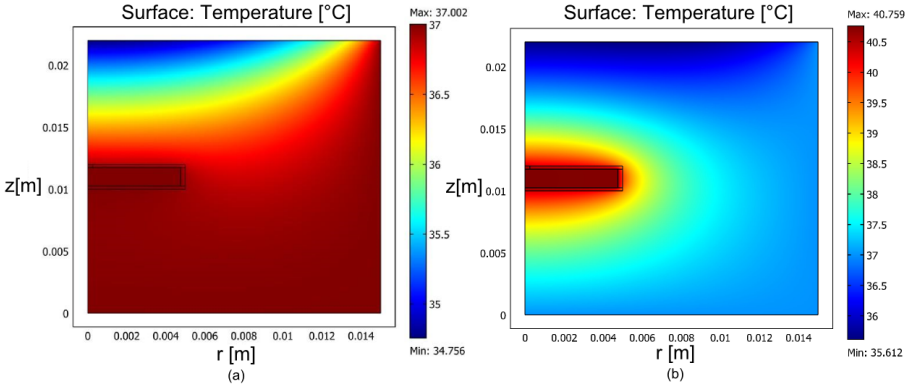

Figure 3.20: (a) temperature distribution around sensor with 10 mW dissipation and (b) 100 mW dissipation inside the sensor (mind the color scale)

3.7 Conclusion

In this chapter, we gave an overview of the key aspects of an implantable dispersive spectrometer: the system configuration, bio-compatibility of the used materials and the electrical and optical power budget. To design a complete spectrometer system, the following minimal set of design questions need to be answered, while keeping the power budget in mind:

- Do we use a pre- or post-dispersive configuration?
- How many sensors and what type of sensors do we use?
- Which sample interface do we use?
- How do we guarantee the glucose supply to our sensor?
- Can we implement an energy- and footprint efficient modulation scheme?

We have shown that the presence of tissue in the light path poses important problems. First of all, due to strong scattering we have large optical losses. Secondly, the tissue will introduce a distribution of path lengths that, through Beer-Lambert's law, can only yield an approximate glucose value. Finally, when tissue is probed, we also measure the (limited) glucose content in cells, whereas only the ISF glucose level is relevant for the glucose sensing application. This has led to the conclusion that a membrane is needed to eliminate the cells from the light path. The membrane needs to be carefully selected to ensure good bio-compatibility and a steady glucose supply, while blocking large interferents. The membrane is not only necessary in the case of a free space sample interface, but also to keep the surface of an evanescent sensor accessible for glucose molecules. It was decided to pursue an evanescent sensor because of the superior sensor multiplexing capabilities and the minimal risk for sensor delay due to slow glucose diffusion. This way, not only a dual-beam system can easily be implemented, but additional environmental parameters can be monitored as well. This multi-parameter sensing can benefit the glucose detection limit by tracking e.g. the interfering water spectrum in response to temperature variations. In this thesis, we haven't exploited this multi-parameter sensing yet, but we demonstrate in the following chapters the potential of both single and dual-beam pre- and post-dispersive evanescent sensors for near infrared absorption spectroscopy.

References

[1] David M Sonnenfroh, W Terry Rawlins, Mark G Allen, Claire Gmachl, Federico Capasso, Albert L Hutchinson, Deborah L Sivco, James N Baillargeon, and Alfred Y Cho. *Application of balanced detection to*

absorption measurements of trace gases with room-temperature, quasi-cw quantum-cascade lasers. Applied optics, 40(6):812–820, 2001.

[2] Pawel Kluczynski, Jörgen Gustafsson, Åsa M Lindberg, and Ove Axner. *Wavelength modulation absorption spectrometryan extensive scrutiny of the generation of signals*. Spectrochimica Acta Part B: Atomic Spectroscopy, 56(8):1277–1354, 2001.

[3] James M Supplee, Edward A Whittaker, and Wilfried Lenth. *Theoretical description of frequency modulation and wavelength modulation spectroscopy*. Applied optics, 33(27):6294–6302, 1994.

[4] Gerhard Talsky and John Wiley. *Derivative spectrophotometry: low and high order*. VCH Weinheim, 1994.

[5] David F Williams. *On the mechanisms of biocompatibility*. Biomaterials, 29(20):2941–2953, 2008.

[6] Sheeny Lan, Mandana Veiseh, and Miqin Zhang. *Surface modification of silicon and gold-patterned silicon surfaces for improved biocompatibility and cell patterning selectivity*. Biosensors and bioelectronics, 20(9):1697–1708, 2005.

[7] Vasilis Ntziachristos. *Going deeper than microscopy: the optical imaging frontier in biology*. Nature methods, 7(8):603–614, 2010.

[8] AN Bashkatov, EA Genina, VI Kochubey, and VV Tuchin. *Optical properties of human skin, subcutaneous and mucous tissues in the wavelength range from 400 to 2000 nm*. Journal of Physics D: Applied Physics, 38(15):2543, 2005.

[9] Gilberto Branco. *chapter 2: Fundamentals of tissue optics*. PhD thesis, UCL department of medical physics and bioengineering, 2007.

[10] Gustav Mie. *Beiträge zur Optik trüber Medien, speziell kolloidaler Metallösungen*. Annalen der physik, 330(3):377–445, 1908.

[11] Lihong Wang, Steven L Jacques, and Liqiong Zheng. *MCMLMonte Carlo modeling of light transport in multi-layered tissues*. Computer methods and programs in biomedicine, 47(2):131–146, 1995.

[12] Shankar Kumar Selvaraja, Patrick Jaenen, Wim Bogaerts, Dries Van Thourhout, Pieter Dumon, and Roel Baets. *Fabrication of photonic wire and crystal circuits in silicon-on-insulator using 193-nm optical lithography*. Lightwave Technology, Journal of, 27(18):4076–4083, 2009.

[13] Frederik Van Laere, Tom Claes, Jonathan Schrauwen, Stijn Scheerlinck, Wim Bogaerts, Dirk Taillaert, Liam O'Faolain, Dries Van Thourhout, and Roel Baets. *Compact focusing grating couplers for*

silicon-on-insulator integrated circuits. Photonics Technology Letters, IEEE, 19(23):1919–1921, 2007.

[14] Wim Bogaerts, Shankar Kumar Selvaraja, Pieter Dumon, Joost Brouckaert, Katrien De Vos, Dries Van Thourhout, and Roel Baets. *Silicon-on-insulator spectral filters fabricated with CMOS technology*. IEEE Journal of Selected Topics in Quantum Electronics, 16(1):33–44, 2010.

[15] Poul-Erik Paulev. *Textbook in Medical Physiology and Pathophysiology: Essentials and clinical problems*. Copenhagen Medical Publishers, 1999.

[16] Tom Claes. *Advanced Silicon Photonic Ring Resonator Label-free Biosensors*. PhD thesis, Photonics Research Group, University of Ghent, 2012.

[17] HM Heise and A Bittner. *Investigation of experimental errors in the quantitative analysis of glucose in human blood plasma by ATR-IR spectroscopy*. Journal of molecular structure, 348:21–24, 1995.

[18] Natalie Wisniewski, Francis Moussy, and WM Reichert. *Characterization of implantable biosensor membrane biofouling*. Fresenius' journal of analytical chemistry, 366(6-7):611–621, 2000.

[19] N Wisniewski, B Klitzman, B Miller, and WM Reichert. *Decreased analyte transport through implanted membranes: differentiation of biofouling from tissue effects*. Journal of biomedical materials research, 57(4):513–521, 2001.

[20] QPhotonics ®. *QSDM-1550-2 Fiber coupled superluminsecent diode 1 mW at 1550 nm*. data sheet, 2014.

[21] Vertilas ®. *VL-1550-1 nm VCSEL 1 mW at 1550 nm*. data sheet, 2014.

[22] M Lamponi, Shahram Keyvaninia, C Jany, F Poingt, F Lelarge, G De Valicourt, Günther Roelkens, Dries Van Thourhout, S Messaoudene, J-M Fedeli, et al. *Low-threshold heterogeneously integrated InP/SOI lasers with a double adiabatic taper coupler*. Photonics Technology Letters, IEEE, 24(1):76–78, 2012.

[23] Caroline Jolly and Richard I Morimoto. *Role of the heat shock response and molecular chaperones in oncogenesis and cell death*. Journal of the National Cancer Institute, 92(19):1564–1572, 2000.

4
Evanescent Sensing

Evanescent sensing is the general term for the detection of changes in the environment of a waveguide, by extraction of the information carried by the evanescent field of a waveguide mode. These environmental changes can always be translated into a variation in the complex refractive index of the waveguide cladding. As the evanescent field of the waveguide mode extends into the cladding, refractive index alterations are picked up and influence the propagation constant of the waveguide mode. Changes in the real part of the propagation constant impact the phase velocity of the mode, whereas changes in the imaginary part represent modal losses (or gain). As we are interested in absorption spectroscopy, only the variations in the imaginary part of the propagation constant due to molecular absorption in the cladding are of interest.
The variations in the refractive index of the cladding can be described as a perturbation $\delta n(x, y)$ to the refractive index profile of the waveguide $n_0(x, y)$. This perturbation is complex as the cladding can introduce losses. To describe the relation between (small) changes δn and the resulting changes in the propagation constant β of the waveguide mode, perturbation analysis can be used [1]. For a waveguide with geometrical cross-section S, this perturbation analysis yields the explicit expression[1]:

$$\delta\beta = \omega\epsilon_0 \frac{\iint_S n_0 \delta n \left|\mathbf{e}_0\right|^2 dxdy}{\iint_S (\mathbf{e}_0 \times \mathbf{h}_0) \cdot \mathbf{u}_z dxdy} \tag{4.1}$$

The cross-section S of the waveguide is taken perpendicularly to the waveguide propagation direction z (S $\perp$ z). In this equation 4.1, x and y are the

transverse dimensions, $\mathbf{u}_z$ the propagation direction vector, ω the angular frequency, ϵ_0 the vacuum permittivity, $n_0(x, y)$ the (real) refractive index profile of the waveguide and $\mathbf{e}_0$, $\mathbf{h}_0$ are the modal fields. When the perturbation in refractive index δn only takes place in the cladding, the integral in the numerator of this equation reduces to the cladding area as $\delta n(x, y) = 0$ in the rest of the waveguide cross-section S.
The expression 4.1, however, needs to be incorporated into Beer-Lambert's law, which is customary for absorption spectroscopy. Hence, to initiate this chapter, we will show how we can modify Beer-Lambert's law to suit evanescent absorption spectroscopy. Next, we study the influence of the waveguide design on the sensitivity of this method. We then investigate how sensitive this method is for changes in the waveguide's refractive index profile which aren't related to glucose absorption. We continue this chapter with a short discussion on the use of optical cavities for evanescent sensing and present a set of measurement results that clearly demonstrate the potential of evanescent detection.

4.1 Beer-Lambert law for evanescent sensing

We have seen in section 2.1.3 that the transmission of a light beam through a uniform medium can be expressed through Beer-Lambert's law. The light beam is uniformly subjected to the absorption events in the medium. For a waveguide mode, however, only the photons in the evanescent field can be absorbed. In addition, the waveguide mode has propagation losses due to the waveguide's structure and core materials. The latter losses are generally termed waveguide losses. The total loss for a waveguide mode is thus the sum of both absorption (α_s) and waveguide losses (α_{wg}). The Beer-Lambert's law (see section 2.1.3) for a waveguide of length L should thus be modified to:

$$I = I_0 e^{-\alpha_s L} e^{-\alpha_{wg} L} \tag{4.2}$$

In this notation, the modal absorption loss α_s is purely caused by absorption in the cladding and all other modal losses are part of α_{wg}. We now need to find an expression that relates α_s to the imaginary part of the cladding's refractive index. To start this derivation, we assume a waveguide with a purely real refractive index profile n_0, with a cladding with complex refractive index n_{clad}. We consider the waveguide mode with effective mode index n_{eff} for evanescent sensing. The imaginary part $\Im(n_{eff})$ is non-zero due to losses in the cladding. This becomes evident when we rewrite equation 4.1 using $\delta\beta = k_0 \delta n_{eff} = k_0 \Im(n_{eff})$, $k_0 = \frac{\omega}{\sqrt{\epsilon_0 \mu_0}}$ and $\delta n = \Im(n_{clad})$:

$$\Im(n_{eff}) = \sqrt{\frac{\epsilon_0}{\mu_0}} \frac{\iint_{clad} n_0 \Im(n_{clad}) \left|\mathbf{e}_0\right|^2 dxdy}{\iint_S (\mathbf{e}_0 \times \mathbf{h}_0) \cdot \mathbf{u}_z dxdy} \tag{4.3}$$

To simplify this expression, we introduce the concept of a confinement factor Γ, that is defined as:

$$\Im(n_{eff}) = \Gamma \Im(n_{clad}) \tag{4.4}$$

It is clear that we can calculate the confinement factor as:

$$\Gamma = \sqrt{\frac{\epsilon_0}{\mu_0}} \Re(n_{clad}) \frac{\iint_{clad} |\mathbf{e}_0|^2 \, dxdy}{\iint_S (\mathbf{e}_0 \times \mathbf{h}_0) \cdot \mathbf{u}_z dxdy} \tag{4.5}$$

Note that the integral in the numerator is limited to the cladding area as only here $\delta n = \Im(n_{clad}) \neq 0$. The denominator is the power flow through the geometrical cross section S of the waveguide.
Now that we have defined this confinement factor, we can easily rewrite the modal losses α_s in function of $\Im(n_{clad})$ or (equally) the cladding loss α_{clad}.

$$\alpha_s = \frac{4\pi}{\lambda} \Im(n_{eff}) = \frac{4\pi}{\lambda} \Gamma \Im(n_{clad}) = \Gamma \alpha_{clad} \tag{4.6}$$

When we assume that the cladding has no scatter points such that the losses are purely caused by absorption events, we can rewrite α_{clad} in terms of the molecular content of the cladding:

$$\alpha_{clad} = \ln(10) \sum_i \epsilon_i c_i \tag{4.7}$$

Finally, the Beer-Lambert law for evanescent absorption spectroscopy can be stated as:

$$I = I_0 e^{-\Gamma \ln(10) \sum_i \epsilon_i c_i L} e^{-\alpha_{wg} L} \tag{4.8}$$

It is important to know that both the confinement factor and waveguide losses are wavelength dependent. Therefore, the measured transmission spectrum is shaped both by the molecular absorption features and the wavelength-dependence of Γ and α_{wg}.

4.1.1 Spiral length

A similar derivation as presented in section 2.3.3, yields an optimal interaction length for evanescent sensing. This optimal waveguide length is calculated as:

$$L_{opt} = \frac{1}{\Gamma \ln(10) \cdot \sum_i \epsilon_i c_i + \alpha_{wg}} \tag{4.9}$$

For a typical confinement factor Γ=0.1, an aqueous cladding and waveguide losses of 2 dB/cm, the waveguide length is on the order of 1 cm for a wavelength of 1590 nm. This is a considerable length given the small size of a silicon-on-insulator chip. Therefore, the waveguide is routed into a spiral to reduce the footprint.

4.1.2 Sensitivity of evanescent absorption spectroscopy

It is insightful to discuss the two physical mechanisms that determine the sensitivity of an evanescent sensor. To start this discussion, we rewrite the denominator in the expression of $\Im(n_{eff})$ 4.3 as in [2]:

$$\iint_S (\mathbf{e}_0 \times \mathbf{h}_0) \cdot \mathbf{u}_z dxdy = v_g \iint_S n_0^2 |\mathbf{e}_0|^2 dxdy \tag{4.10}$$

in which v_g is the group velocity and n_0, the (real) refractive index profile of the waveguide. This formula does not take into account material dispersion. The change in the effective index of the mode due to a change in absorption in the cladding can then be written as:

$$\Im(n_{eff}) = n_g \cdot \frac{\iint_{clad} n_0 \Im(n_{clad}) |\mathbf{e}_0|^2 dxdy}{\iint_S n_0^2 |\mathbf{e}_0|^2 dxdy} \tag{4.11}$$

We note that this is the product of two terms: the first term is the group index n_g, related to the group velocity of the light $v_g = c/n_g$. If light can be temporally confined (e.g. bouncing back and forth in a cavity), leading to a lower v_g, this will enhance the light attenuation for a given structural sensor length (as opposed to the complete path that the light has traveled). Researchers have used this temporal confinement effect in e.g. photonic crystals to reduce the footprint of evanescent sensors [3]. The second term is related to the spatial confinement of the electric field energy density in the cladding. This spatial confinement can be stimulated by an increase of the electric field in the cladding.

The normal component of the electric displacement field must be continuous at the core cladding interface. This means that the normal component of the electric field at the cladding side ($\mathbf{e}_{clad}$) must obey: $\mathbf{e}_{clad} = \frac{n_{core}^2}{n_{clad}^2} \mathbf{e}_{core}$ in which $\mathbf{e}_{core}$ is the normal component of the electric field at the core side. For a waveguide integrated on SOI and immersed in water, this results in a seven-fold enhancement of $\mathbf{e}_{clad}$ compared to $\mathbf{e}_{core}$ ($\frac{n_{core}^2}{n_{clad}^2} = \frac{3.47^2}{1.31^2} = 7.01$)! It is thus beneficial for evanescent sensors to work with a high index contrast material platform.

Note that the confinement factor Γ is a measure for both the temporal and spatial confinement and should be maximized to enhance the evanescent sensitivity. In the next section we will, therefore, compare evanescent sensor designs in terms of their confinement factor and waveguide losses.

4.2 Evanescent sensor design

In this section, we introduce some basic properties of the evanescent field itself which influence the sensor design. In addition, we evaluate which waveguide design and choice of optical mode is best suited for evanescent absorption spectroscopy. We will limit ourselves to the design space that is allowed by the fabrication process at imec [4]. This process is in line with CMOS industry standards and therefore allows reproducible, low-cost mass manufacturing of high quality optical chips. In addition, we limit ourselves to single-mode waveguides in which we excite either the quasi-TE or quasi-TM mode.

4.2.1 Evanescent field

The evanescent field of a waveguide mode is an exponentially decaying field with distance d from the core surface. A small part of the evanescent field is located below the core and cannot be used for sensing. The evanescent field in the cladding E_{clad} can be described as follows:

$$|E_{clad}| = |E_0| \cdot exp(-\kappa d) \tag{4.12}$$

in which, $|E_0|$ is the E-field at the core/cladding interface and κ is the decay constant, which can be calculated as [5]:

$$\kappa = \frac{2\pi}{\lambda} \cdot \sqrt{n_{eff}^2 - n_{clad}^2} \tag{4.13}$$

The evanescent field intensity thus has a certain penetration depth $d = \frac{1}{2\kappa}$ in the cladding. The waveguide mode is effectively isolated from changes beyond this depth. The larger the refractive index contrast between core and cladding, the smaller the penetration depth. When we calculate this penetration depth for the TE-mode of a standard 450 nm wide x 220 nm high SOI waveguide with water cladding, we obtain d=62 nm at a wavelength of 1590 nm. This small penetration depth has two consequences: firstly, only a very small sample volume is needed for sensitive detection. For a straight 1 cm long standard waveguide, the strictly needed volume is only 1 pL. Researchers therefore like to quote the number of molecules or equivalent mass that they can measure with evanescent sensors rather than the concentration. Secondly, the silicon surface has to remain accessible. Any thin layer of adherents will reduce the sensitivity of the sensor as molecules need to be within the penetration depth in order to be sensed.

4.2.2 Simulation settings

We use the eigenmode expansion tool CAMFR (CAvity Modelling FRamework) for simulations of both the effective mode index n_{eff} and the confinement factor Γ [6]. All simulations use following refractive indices for

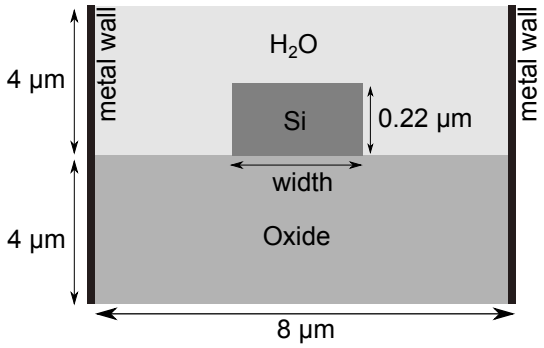

Figure 4.1: Simulation settings for the calculation of the confinement factor

the waveguide stack: n_{ox}=1.444, n_{si}=3.477 and $n_{clad} = n_{H_2O}$=1.315+$\Im n_{clad}$, unless stated otherwise. The confinement factor is calculated according to equation 4.4 with $\Im n_{clad} = -1.23e^{-8}$ (quite arbitrarily). The simulation settings are shown in figure 4.1 and tested for convergence. The bottom silicon layer is not incorporated, as this will influence $\Im n_{eff}$ through substrate leakage. We limit the wavelength range for which we simulate the confinement factor to the range that we have addressed in the glucose sensing experiments that are detailed in chapters 6,7. This wavelength range was mainly limited by the emission window of the available stable light sources.

4.2.3 Waveguide width

The fabrication process at imec offers a fixed waveguide height of 220 nm, but a user-definable waveguide width. Therefore, we will simulate the confinement factor in function of the waveguide width. This simulation is performed for the fundamental quasi-TE mode at three wavelengths: 1.55 μm (the traditional telecom-wavelength), 1.59 μm (the peak absorption wavelength of glucose) and 1.65 μm (interesting for biodiesel detection) and the fundamental quasi-TM mode at 1.59 μm. To ensure single-mode behavior the waveguide width is varied between 0.45 μm and 0.65 μm. At wider waveguide widths, the first order TE mode can propagate as well. The result of the simulation is presented in figure 4.2. We can see that the confinement factor decreases with increasing waveguide width as the mode gets stronger confined to the core of the waveguide. In addition, the confinement factor increases with increasing wavelength, as the mode expands more at these larger wavelengths.

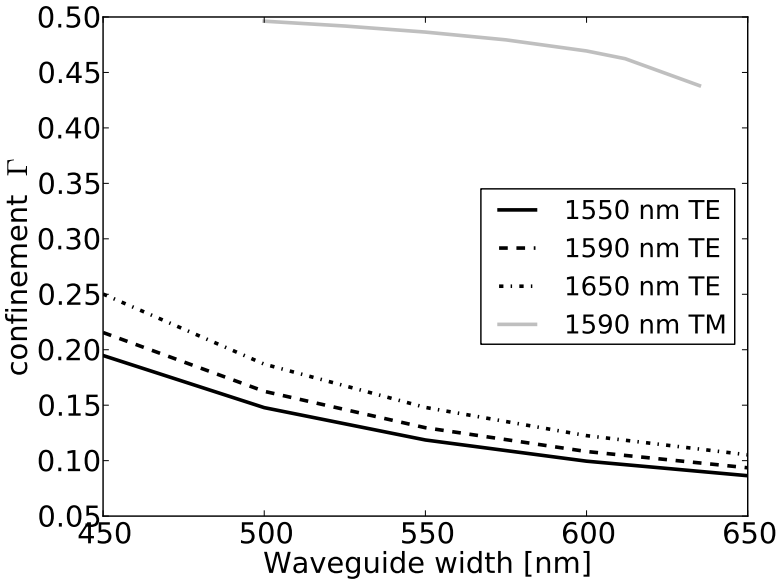

Figure 4.2: Variation of the confinement factor with waveguide width for the quasi-TE mode at three wavelengths:1.55 μm, 1.59 μm and 1.65 μm and for the quasi-TM mode at 1.59 μm.

4.2.4 Optimal waveguide mode

In integrated rectangular waveguides, two fundamental modes exists: the quasi-TE and the quasi-TM mode. To illustrate the difference between the quasi-TE and quasi-TM mode, we plot the countour lines of the dominant field components for a 500 nm wide waveguide immersed in water in figure 4.3. It is clear that the TM mode is more sensitive to the top surface of the waveguide whereas the TE mode is more sensitive to the sides of the waveguide. To compare both modes, we simulate the confinement factor in function of wavelength for a given waveguide width of 500 nm, 550 nm and 600 nm. The result is shown in figure 4.4.

It shows that the confinement factor for the quasi-TM mode is high for all wavelengths, but reaches an optimum point. This is a different trend than the steady increase with wavelength for the quasi-TE mode in figure 4.4. In addition, in figure 4.2 is shown that the confinement factor for different waveguide widths for the quasi-TM mode at a wavelength of 1590 nm is higher than for the quasi-TE mode in the identical setting. It is thus beneficial for evanescent sensing to excite the quasi-TM waveguide mode.

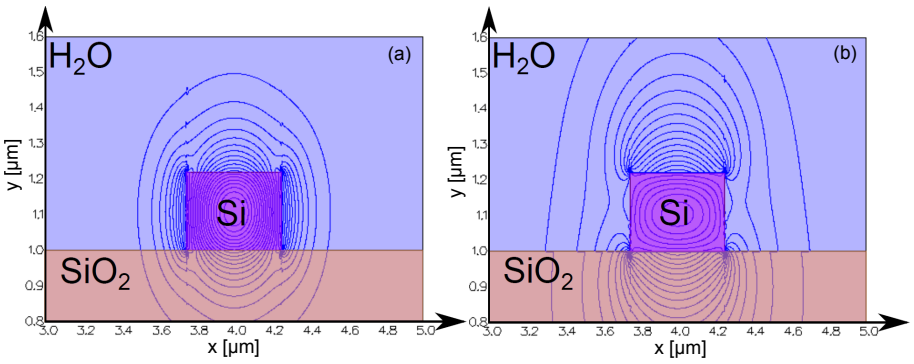

Figure 4.3: Contour plot of the dominant (a) Ex component of the quasi TE mode and (b) Ey component of the quasi TM mode in a 500 nm wide waveguide immersed in water.

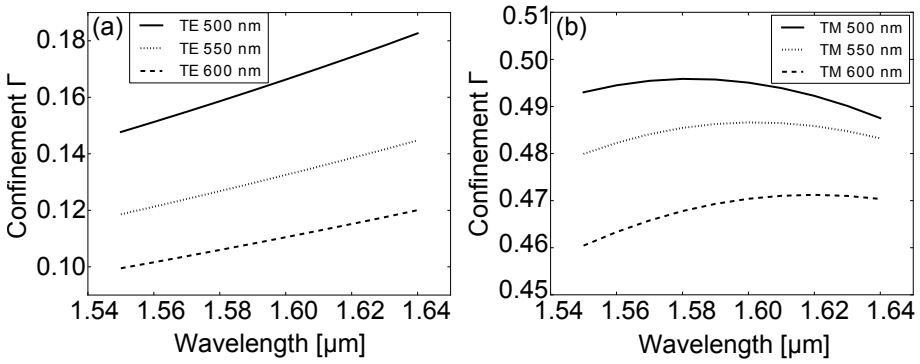

Figure 4.4: Confinement factor for the (a) quasi-TE mode and (b) quasi-TM mode in function of wavelength for 500 nm, 550 nm and 600 nm wide wire waveguides immersed in water

Nonetheless, the wavelength demultiplexers that are used throughout this work have better performance for the quasi-TE mode. Due to its high confinement factor, the TM mode is much more sensitive to small thickness variations in the free propagation region of the wavelength demultiplexer, leading to phase errors. Given that the evanescent spiral needs to be incorporated with the TE-based wavelength demultiplexer, we have focused in this work on evanescent sensing with the quasi-TE mode.

4.2.5 Wire versus Rib waveguide

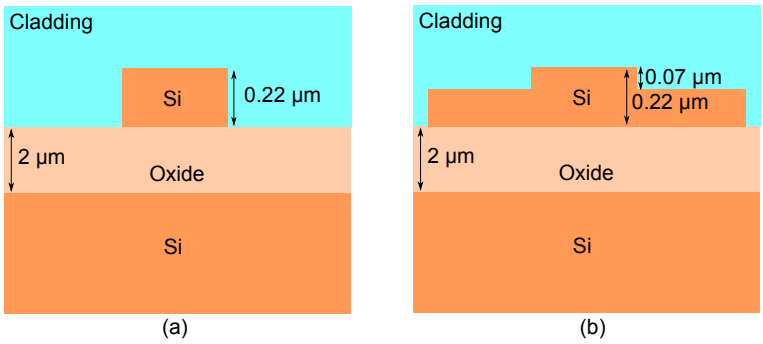

Figure 4.5: Silicon-on-insulator (a) wire waveguide and (b) rib waveguide and (c) linear taper (from [7])

Two waveguide types can be fabricated at imec: either wire waveguides or rib waveguides (also referred to as shallow waveguides). Both are depicted in figure 4.5. A linear taper, as shown in figure 4.6 can be used to con-

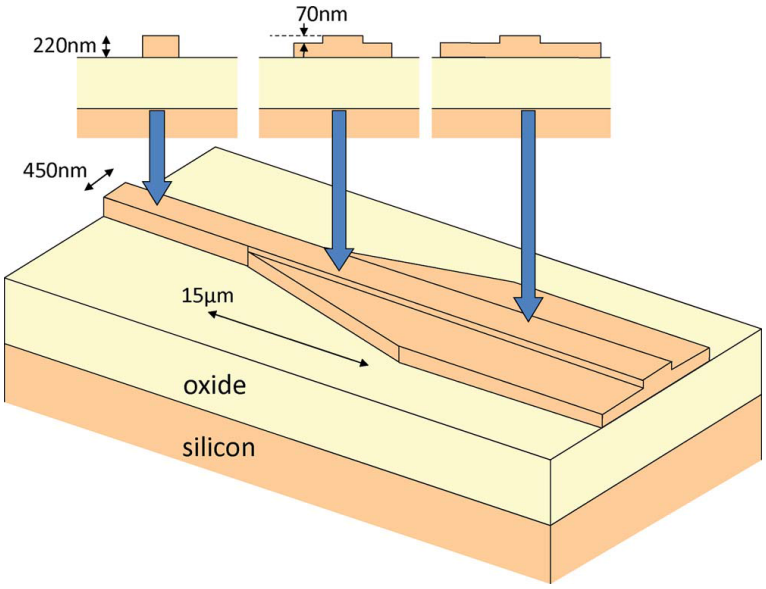

Figure 4.6: Linear taper to adiabatically convert the wire waveguide mode to a rib waveguide mode and vice versa(from [7])

vert between these two waveguide types. The performance of both types

for evanescent sensing is influenced by the following parameters: confinement factor, waveguide loss and sidewall roughness. The latter two are related as low loss waveguides typically have a lower sidewall roughness[8]. When the waveguide loss is low, while a reasonable confinement factor is present, the spiral length can be increased. This leads to a higher sensitivity due to the enhanced interaction with more glucose molecules.

The waveguide loss for 450 nm wide wire waveguides with air cladding varies from wafer to wafer, but is about 2.5 dB/cm [9]. For rib waveguides with the same width, the waveguide loss can be lower due to a reduced modal overlap with the side-walls of the waveguide [8]. The roughness of these side-walls have a strong impact on the propagation loss due to scattering losses. For the samples that we have used in this work, we measured an air-clad rib waveguide loss of 3 dB/cm. When a waveguide is immersed in water, the intrinsic waveguide loss will decrease due to the smaller index contrast between the core and cladding. This effect is clear when oxide-clad spiral waveguides losses are measured. In this case the (measured) propagation loss reduces to 2.2 dB/cm and 0.5 dB/cm for respectively 450 nm wide wire and rib waveguides.

The confinement factor for the quasi-TE mode of (water clad) wire and rib waveguides with a similar waveguide width for a wavelength of 1590 nm is compared in figure 4.7(a). In addition, we simulated the confinement factor for wire and rib waveguides for a fixed width of 500 nm and 600 nm and different wavelengths. The results are shown in figure 4.7(b).

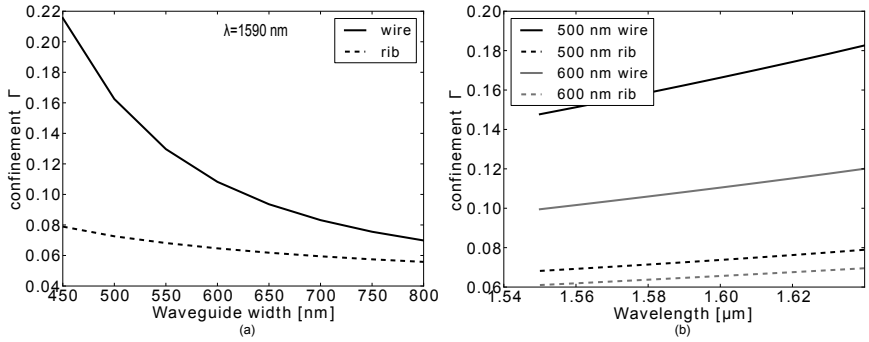

Figure 4.7: Confinement factor of the quasi-TE mode in function of (a) waveguide width and (b) wavelength for wire and rib waveguides immersed in water

The rib waveguides have a lower confinement factor, but allow a more tolerant design to waveguide width variations due to fabrication process imperfections. This is due to the smaller normalized derivative $\frac{\delta\Gamma}{\delta w}/\frac{\delta\Gamma_0}{\delta w_0}$,

with w the waveguide width, compared to wire waveguides. Based on the optimal spiral length for both a water-clad 450 nm wide wire and rib waveguide, we calculated the (evanescent) absorbance of 1 mM of glucose in both cases for a wavelength of 1590 nm. The wire waveguide only has a 0.4% higher absorbance value, giving it a small advantage in terms of evanescent sensitivity.

The last parameter, sidewall roughness, has proven to be critical for evanescent sensing. The experimental results, presented in chapter 6, show that the sidewall roughness introduces spurious reflections. These in turn translate into a very dense interference pattern in the transmission spectrum when measured with a coherent light source. As the sidewall roughness has less impact on rib waveguides, these are preferred for evanescent sensing.

4.2.6 Slotted waveguide

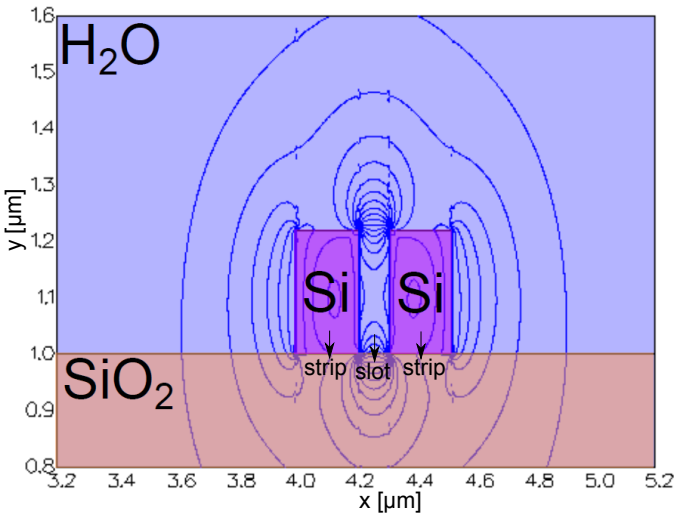

Figure 4.8: Contour plot of the dominant Ex field of the quasi-TE mode of a slotted waveguide

Slotted waveguides, as shown in figure 4.8 can also be considered for evanescent sensing. This type of waveguide has the advantage of a very high electric field density in the slot, which enhances the evanescent sensitivity. In the PhD of Tom Claes [10], slotted waveguides with a slot of 100 nm and 210 nm strip width were investigated for evanescent (real) refractive index sensing. It reported a confinement factor of 0.77, but a waveguide loss of

oxide-clad waveguides of 12 dB/cm. In water-clad waveguides this loss should be even higher due to the higher index contrast.
If we calculate the optimal spiral length based on these parameters for a wavelength of 1590 nm, we obtain $L_{opt} = 1.2$ mm, compared to 4.85 mm for a standard 450 nm wide wire waveguide. Based on these lengths, we calculated the (evanescent) absorbance (see also equation 2.5) of 1 mM of glucose (=c_g) for both the slotted (A_{slot}) and standard wire waveguide (A_{wire}):

$$A = (\epsilon_g c_g L_{opt} - f_w \epsilon_{H_2O} c_g L_{opt}) \cdot \Gamma \tag{4.14}$$

The result is that the wire waveguide has a 14% higher absorbance value, illustrating that the high electric field density in the cladding is countered by the large propagation losses (shorter L_{opt}).

4.2.7 First overtone band versus Combination band

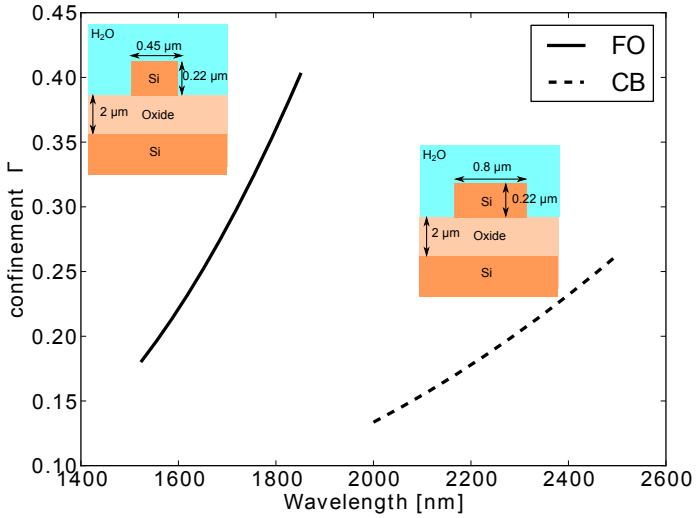

Figure 4.9: Confinement factor of the quasi-TE mode in wire waveguides in function of wavelength for the first overtone band (FO) and combination band (CB), (b) normalized 1 mM glucose evanescent transmission spectrum for the FO and CB.

As glucose has absorption features in both the first overtone band (FO, 1500-1850 nm) and the combination band (CB, 2050-2350 nm), it is interesting to compare both in terms of evanescent sensitivity. We will compare a standard 450 nm wide wire waveguide for the first overtone band with

a 800 nm wide wire waveguide for the combination band. Throughout this research 800 nm wide waveguides were used for sensing experiments and the design of wavelength demultiplexers for the combination band. More about waveguide design for the combination band can be found in the next chapter 5. A simulation is performed for the confinement factor of the quasi-TE mode of the wire waveguides in an aqueous environment. This time, the material dispersion is taken into account so that the refractive index of the oxide, silicon and water layer varies with wavelength. The result is shown in figure 4.9. It shows that, for the given waveguide dimensions, the confinement factor in the FO is slightly higher than in the CB.

The waveguide losses for an 800 nm wire waveguide with oxide cladding amount to 0.8 dB/cm for the combination band, whereas the 450 nm wire with oxide cladding has 2.1 dB/cm loss, for the lower part of the first overtone band ($\leq 1.65\mu$m). The combination band, thus, clearly has an advantage in terms of waveguide losses.

From the waveguide losses and the confinement factor, we calculate the

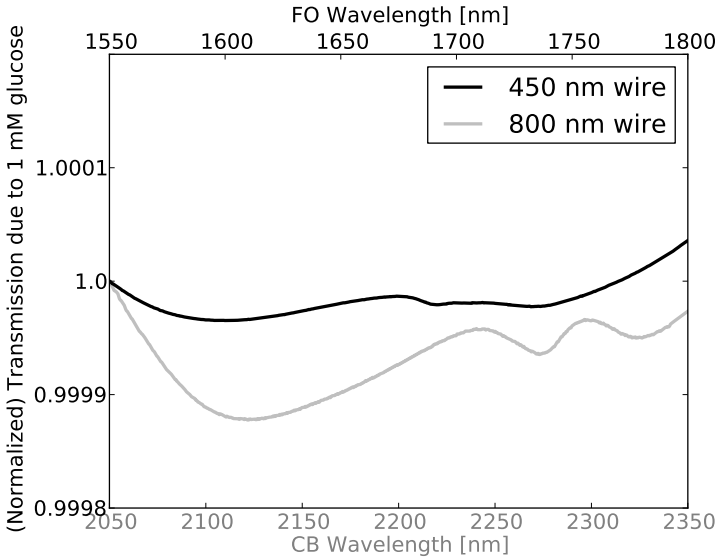

Figure 4.10: Normalized 1 mM glucose evanescent transmission spectrum for the FO and CB.

optimal spiral length using equation 4.9 for the peak glucose absorption wavelengths (1.59 μm and 2.11 μm). An optimal spiral length of 4.85 mm and 2.27 mm is obtained for the FO and CB respectively. Next, we calculate

the change in transmission due to a 1 mM glucose solution according to:

$$T_g = 10^{-A_g \cdot \Gamma} = 10^{-(\epsilon_g c_g L - f_w \epsilon_{H_2O} c_g L) \cdot \Gamma} \tag{4.15}$$

and normalize this 1 mM glucose transmission to the first wavelength, 1550 nm and 2050 nm, of the FO and CB respectively. The result is plotted in figure 4.10. It shows clearly that the combination band has an advantage in terms of evanescent sensitivity for glucose, as the absorption features are larger and more pronounced.

4.2.8 Nonlinear effects

To improve the signal-to-noise ratio of the evanescent sensor, the power in the waveguide can be increased, such that the change in detected power due to glucose absorption increases. The upper limit of power in the waveguide is given by the onset of nonlinear effects. For a standard 450 nm wide wire waveguide, the power limit is ≈50 mW [11]. At this power, a nonlinear waveguide loss of 3 dB/cm at 1550 nm is generated.

4.3 Influence of environmental changes

For our glucose sensor, it is important to know how the sensor reacts to variations that are not caused by glucose absorption. According to equation 4.8, the measured transmission spectrum can be influenced by variations in the confinement factor or waveguide losses. Both can be translated into a change in the waveguide refractive index profile n_0. In this section we will, therefore, investigate how n_0 is influenced by environmental changes. Two situations can be distinguished: either only the cladding is affected or the complete waveguide stack is affected. As an example for the first case, glucose can influence the (real) refractive index of the cladding, but doesn't change the refractive index profile of the SOI. Contrary, a change in temperature will affect both the cladding and the SOI through the thermo-optic effect. Both effects are investigated using simulations. These are performed for the quasi-TE mode of a 450 nm wide rib waveguide, as this is the waveguide that we have used for our glucose sensing experiments. Following refractive indices for the waveguide stack are used: n_{ox}=1.444, n_{si}=3.477 and $n_{clad} = n_{H_2O}$=1.315+$Re(\delta n)$.

4.3.1 Concentration changes

Based on the theory of electrostatics of dielectrics by L. Landau [12], the dielectric permittivity ϵ_{mix} of a diluted solution can be written as:

$$\epsilon_{mix} = \epsilon_{solvent}(1 + 3C\frac{\epsilon_{solute} - \epsilon_{solvent}}{\epsilon_{solute} + 2\epsilon_{solvent}}) \tag{4.16}$$

in which $\epsilon_{solvent}$ and ϵ_{solute} are the dielectric permittivity of respectively the solvent and solute molecules. This expression is correct to the first order of C, with C the concentration of the solute. The change in refractive index of a mixture, due to a change in solute concentration, can thus be written as $\Delta n = \frac{\delta n}{\delta C} \cdot \Delta C$. This implies that when more solute molecules are present, the confinement factor can change through a change in the effective index of the waveguide mode, which was influenced by the change in the cladding's index. Based on:

$$\frac{\Delta C}{C} = \frac{\Delta \Gamma}{\Gamma} \tag{4.17}$$

we can derive following expression for the error in the concentration estimation σ_C due to a change in the refractive index Δn caused by a shift in concentration ΔC:

$$\sigma_C = \frac{C}{\Gamma}\frac{\delta \Gamma}{\delta n}\Delta n = \frac{C}{\Gamma}\frac{\delta \Gamma}{\delta n}\frac{\delta n}{\delta C}\Delta C \tag{4.18}$$

The only parameter in this expression, next to Γ, that we can influence is $\frac{\delta \Gamma}{\delta n}$. Therefore, we simulated for small δn, how large this derivative is in function of wavelength. The result can be written as the linear relation:

$$\frac{\delta \Gamma}{\delta n} = 0.043\lambda(\mu m) - 0.001 \tag{4.19}$$

A small numerical example teaches us that this effect is negligible for glucose variations ($\frac{\delta n}{\delta C} = 2e^{-5}\frac{RIU}{mM}$), detected at a wavelength of 1.59 μm: for a variation in the glucose concentration of 20 mM (maximal change in vivo), we expect an error in the order of 1.5μM on the true glucose concentration of 5.5 mM.

4.3.2 Thermal changes

It is well-known that the refractive index of a material depends on the temperature ($\frac{\delta n}{\delta T} \neq 0$). In the case of silicon, this thermo-optic effect is rather strong with $\frac{\delta n}{\delta T} = 1.86 \times 10^{-4} K^{-1}$ [13]. Similar to equation 4.18, we can derive the following expression for a change in temperature ΔT:

$$\sigma_C = \frac{C}{\Gamma}\frac{\delta \Gamma}{\delta T}\Delta T \tag{4.20}$$

We have used information on $\frac{\delta n}{\delta T}$ for water, silicon and SiO_2 from references [14, 15, 16] to calculate $\frac{\delta \Gamma}{\delta T}$.

$$\frac{\delta \Gamma}{\delta T} = -8.64e^{-5}\lambda(\mu m) + 1.2035e^{-4} \tag{4.21}$$

As expected, $\frac{\delta\Gamma}{\delta T}$ is small as, in essence, it is a second order effect: $\frac{\delta\Gamma}{\delta T} = \frac{\delta\Gamma}{\delta n}\frac{\delta n}{\delta T}$. Given the expected change in temperature in the lab, its influence on the measured glucose concentration is negligible. In addition, for an implantable evanescent sensor, we have the advantage that the body temperature is well-regulated. The performance of other components in the implant, such as the source and wavelength demultiplexer, can be more dependent on temperature, but this is not further investigated in this work.

4.3.3 Flow speed

There is one experimental setting that might influence the sensor surface: a change in flow speed above the sensor. In the glucose sensing experiments, we use microfluidics for the glucose supply to the evanescent sensor. This can introduce noise as the flow/pressure in the microfluidic channels isn't necessarily stable throughout the whole experiment. We have tested with ring resonators (which are very sensitive to refractive index variations) that when the pump is switched on and off to a flow speed of 25 μL/min, that the effective index of the wire waveguide mode alters by 3.25e-5 RIU. This is a small value. In addition, we also tested with spiral waveguides what the influence is of a change in microfluidic pump speed on evanescent sensing. These experimental results can be found in chapter 6, section 6.4.2. Still, in vivo there won't be any substantial flow (in comparison to the 25 μL/min) above the sensor surface.

4.3.4 Dual-beam design

Typically, a dual-beam system is used to compensate for environmental changes. Key to optimal dual-beam performance, is the similarity between the refractive index profile of the signal and reference spiral. By putting the signal and reference spiral close together on the same chip, we can minimize differences caused by the fabrication process or temperature. This will also reduce the impact of spatially inhomogeneous environmental factors.

4.4 Cavity enhanced detection

Due to the high index contrast of the silicon photonics platform, optical cavities are easily created. It is possible to use these optical cavities for evanescent sensing. This is typically called cavity-enhanced sensing and is a popular technique for mid-IR gas sensing applications [17, 18]. This approach has the advantage that the sensor footprint is strongly reduced [19]. Indeed, in a high-quality cavity the light bounces back and forth such that the total interaction length with the sample is large, even for small cavity dimensions. The sample loss can be calculated by fitting the theoretical

transmission spectrum of the cavity to the measured spectrum [20].

Due to the cavity, we can only extract loss information for a set of wavelengths separated by the free spectral range ($FSR = \frac{\lambda^2}{n_g L}$) of the cavity with round trip length L. The measurement resolution $\delta\lambda$ thus equals the FSR. This introduces a design limitation, as the round trip length can then no longer be designed separately from the resolution. Still, the round trip length should be optimized, by equaling the total traveled path length ($L_{eff} = \Gamma \frac{Q\lambda_0}{2\pi n_{eff}}$) to the optimal interaction length (equation 4.9). Another concern is that, for glucose detection, this approach needs a widely scanning laser source. This type of source is still a challenge for the silicon photonics platform. Therefore, although promising results have been presented using this technique [21], we did not consider cavity sensing for glucose.

4.5 Measurement results

To demonstrate the evanescent sensing principle, we report here on our measurements of pure liquid poly-ethylene glycol (PEG) samples in the first overtone band (FO) and the combination band (CB). This liquid polymer has clear absorption features both in the FO and CB and is therefore a good test molecule. The structural formula is shown in figure 4.11. The encircled part is responsible for the strong absorption features.

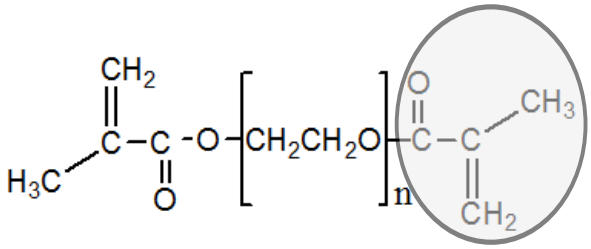

Figure 4.11: Structural formula of PEG

4.5.1 Measurement set-up

The measurement set-up was a single-beam configuration with a broadband light source and optical spectrum analyzer (OSA). In the case of the first overtone band, high signal-to-noise ratio (SNR) measurements could be achieved thanks to a strong and stable SLED source. In contrast, for the combination band, we had to use a laser source pumped below threshold. This, in combination with rather high on-chip losses, resulted in a

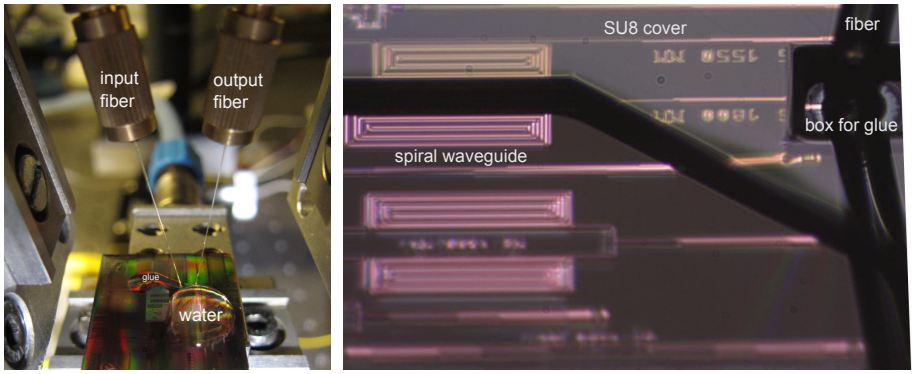

Figure 4.12: (a) measurement set-up for single-beam evanescent absorption spectroscopy (b) close-up of the fabricated evanescent sensor.

rather low SNR. The fabricated evanescent sensor and set-up is shown in 4.12. Grating couplers are used to couple light from a near-vertically optical fiber into the plane of the SOI chip. A thick cover layer of SU8 (50 μm) is used to create a container for the applied liquid. Two openings in the SU8 layer are created to serve as a container for glue. This way, the optical fibers can be glued easily to minimize their movement, which improves the SNR significantly.

4.5.2 PEG

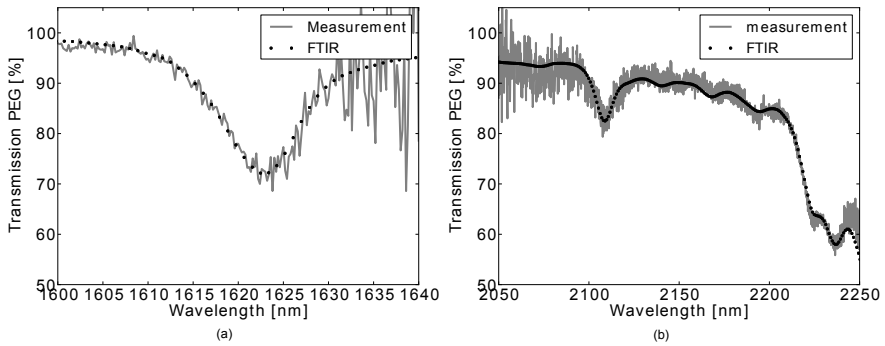

Figure 4.13: Measurement of (a) the first overtone band transmission spectrum of PEG and (b) combination band transmission spectrum of PEG

We have measured pure PEG with a 1 cm long 450 nm wide rib waveguide in the FO and a 1.28 mm long 800 nm wide wire waveguide in the CB. The result is shown in figure 4.13. What is plotted is the raw measurement data without any averaging. It is clear that we can resolve the absorption features nicely over a wide wavelength range. The strong transmission drop at 2.2 μm is typical for polymers and also visible in the absorption spectra of the biocompatible materials PDMS and PMMA. To compare the measured absorption features, we measured the same PEG sample with a high-performant FTIR (Agilent 680 Series). For these measurements, we used 1 mm and 2 mm glass cuvettes and subtracted both absorbance measurements to eliminate the influence of the glass. This yields the absorbance of 1 mm pure liquid $A_{FTIR} = -log_{10}(T_{1mm})$. We then calculated the expected evanescent transmission spectrum using the following formula:

$$T_{FTIR} = 10^{-\Gamma \cdot \frac{A_{FTIR}}{1mm} L_{spiral}(mm)} \tag{4.22}$$

in which Γ is the simulated confinement factor for the used waveguide type. It is clear from figure 4.13 that although our measurements are more noisy, we obtain a good match with the reference FTIR measurements.

4.6 Conclusion

In this chapter, we showed how the Beer-Lambert's law can be modified for evanescent absorption spectroscopy. This was possible by introducing the confinement factor Γ. This factor incorporates the two physical mechanisms that enhance the evanescent sensitivity: temporal and spatial confinement. Thanks to the high index contrast of the silicon photonics platform, the spatial confinement is high and can be tuned easily by changing the waveguide dimensions. We have studied which (single-mode) silicon-on-insulator waveguides with 220 nm thickness are optimal for evanescent sensing. This resulted in the following conclusions:

- narrower waveguides offer a higher confinement factor Γ due to the mode expansion into the cladding.
- ridge waveguides are preferred over wire and slot waveguides, thanks to the low propagation and scattering losses and reasonably high Γ.
- the quasi-TM mode is preferred over the quasi-TE mode thanks to the very high Γ.
- the combination band offers better prospects for glucose detection.

Based on these conclusions, we can select the optimal sensing configuration for glucose detection. Given that we do not have a stable source for the combination band, we need to design for the first overtone band. For this

wavelength range, the quasi-TE mode of a 450 nm wide ridge waveguide is then optimal for sensing, as the quasi-TM mode is not considered for future sensor integration with highly performant TE wavelength demultiplexers. For this quasi-TE mode, we investigated the sensitivity of the confinement factor to refractive index variations in the cladding and thermal variations. It was found that thermal variations can be neglected compared to the refractive index variations. We discussed shortly the use of optical cavities and ended this chapter with experimental results of a single-beam evanescent SOI sensor in both the first overtone band and combination band. These results show that evanescently measured transmission spectra are in good agreement with high SNR FTIR reference measurements and demonstrate the feasibility of evanescent molecular detection.

References

[1] Jan Haes, Bart Demeulenaere, Roel Baets, D Lenstra, TD Visser, and H Blok. *Difference between TE and TM modal gain in amplifying waveguides: analysis and assessment of two perturbation approaches*. Optical and Quantum Electronics, 29(2):263–273, 1997.

[2] Jacob T Robinson, Kyle Preston, Oskar Painter, and Michal Lipson. *First-principle derivation of gain in high-index-contrast waveguides*. Optics express, 16(21):16659–16669, 2008.

[3] Niels Asger Mortensen, Sanshui Xiao, and Jesper Pedersen. *Liquid-infiltrated photonic crystals: enhanced light-matter interactions for lab-on-a-chip applications*. Microfluidics and Nanofluidics, 4(1-2):117–127, 2008.

[4] Shankar Kumar Selvaraja, Patrick Jaenen, Wim Bogaerts, Dries Van Thourhout, Pieter Dumon, and Roel Baets. *Fabrication of photonic wire and crystal circuits in silicon-on-insulator using 193-nm optical lithography*. Lightwave Technology, Journal of, 27(18):4076–4083, 2009.

[5] Adam Densmore, D-X Xu, Philip Waldron, Siegfried Janz, Pavel Cheben, J Lapointe, André Delâge, Boris Lamontagne, JH Schmid, and Edith Post. *A silicon-on-insulator photonic wire based evanescent field sensor*. Photonics Technology Letters, IEEE, 18(23):2520–2522, 2006.

[6] P Bienstman, S Selleri, L Rosa, HP Uranus, WCL Hopman, R Costa, A Melloni, LC Andreani, JP Hugonin, P Lalanne, et al. *Modelling leaky photonic wires: A mode solver comparison*. Optical and Quantum Electronics, 38(9-11):731–759, 2006.

[7] Joost Brouckaert. *Integration of Photodetectors on Silicon Photonic Integrated Circuits (PICs) for Spectroscopic Applications*. PhD thesis, Photonics Research Group, University of Ghent, 2010.

[8] Wim Bogaerts et al. *Compact single-mode silicon hybrid rib/strip waveguide with adiabatic bends*. IEEE Photonics Journal, 3(3):422–432, 2011.

[9] Shankar Kumar Selvaraja. *Wafer-Scale Fabrication Technology for Silicon Photonic Integrated Circuits*. PhD thesis, Photonics Research Group, University of Ghent, 2011.

[10] Tom Claes. *Advanced Silicon Photonic Ring Resonator Label-free Biosensors*. PhD thesis, Photonics Research Group, University of Ghent, 2012.

[11] Bart Kuyken. *Four-Wave-Mixing in Dispersion-Engineered Silicon Nanophotonic Circuits for Telecommunication and Sensing Applications*. PhD thesis, Photonics Research Group, University of Ghent, 2013.

[12] Lev Davidovich Landau, Evgenij Mihajlovič Lifšic, John Bradbury Sykes, John Stewart Bell, MJ Kearsley, and Lev Petrovich Pitaevskii. *Electrodynamics of continuous media*, volume 364. Pergamon press Oxford, 1960.

[13] Sarvagya Dwivedi, Herbert Dheer, and Wim Bogaerts. *A compact all-silicon temperature insensitive filter for WDM and bio-sensing applications*. 25(22):2167–2170, 2013.

[14] Allan H Harvey, John S Gallagher, and JMH Levelt Sengers. *Revised formulation for the refractive index of water and steam as a function of wavelength, temperature and density*. Journal of Physical and Chemical Reference Data, 27(4):761–774, 1998.

[15] HH Li. *Refractive index of silicon and germanium and its wavelength and temperature derivatives*. Journal of physical and chemical reference data, 9(3):561–658, 1980.

[16] CZ Tan and J Arndt. *Temperature dependence of refractive index of glassy SiO¡ sub¿ 2¡/sub¿ in the infrared wavelength range*. Journal of Physics and Chemistry of Solids, 61(8):1315–1320, 2000.

[17] Juejun Hu, Nathan Carlie, Laeticia Petit, Anu Agarwal, Kathleen Richardson, and Lionel C Kimerling. *Cavity-enhanced IR absorption in planar chalcogenide glass Microdisk resonators: experiment and analysis*. Journal of Lightwave Technology, 27(23):5240–5245, 2009.

[18] Pao Tai Lin, Vivek Singh, Juejun Hu, Kathleen Richardson, J David Musgraves, Igor Luzinov, Joel Hensley, Lionel C Kimerling, and Anu Agarwal. *Chip-scale Mid-Infrared chemical sensors using air-clad pedestal silicon waveguides*. Lab on a Chip, 13(11):2161–2166, 2013.

[19] Timothy McGarvey, AndrÚ Conjusteau, and Hideo Mabuchi. *Finesse and sensitivity gain in cavity-enhanced absorption spectroscopy of biomolecules in solution*. Optics express, 14(22):10441–10451, 2006.

[20] Daniel Hofstetter and Robert L Thornton. *Theory of loss measurements of Fabry Perot resonators by Fourier analysis of the transmission spectra*. Optics letters, 22(24):1831–1833, 1997.

[21] Arthur Nitkowski, Long Chen, and Michal Lipson. *Cavity-enhanced on-chip absorption spectroscopy using microring resonators*. Optics express, 16(16):11930–11936, 2008.

5

Development of miniature silicon-based spectrometers

Whereas spectrometers are typically bulky and expensive devices, there is a very wide range of applications that require cheap, small-scale spectrometers. These miniature spectrometers can, for example, be applied for structural health monitoring of gas pipes, in food production or fuel analysis, or even medical diagnosis in remote areas. Nowadays, fully integrated spectrometers with the size of a standard USB-stick are already commercially available. One can thus ask, how and why should silicon photonics play a role in this demand for miniature spectrometers? In essence, the key assets and unique properties of the silicon platform have to make the difference. The chip fabrication process has a significant cost-advantage and offers high reliability, next to promising co-integration with electronics. Therefore, silicon photonics technology can be used to produce highly reliable spectrometers with a higher performance (e.g. higher resolution) at an even smaller scale and cost. The development of an implantable spectrometer for continuous glucose monitoring is the ultimate crystallization of this reasoning.

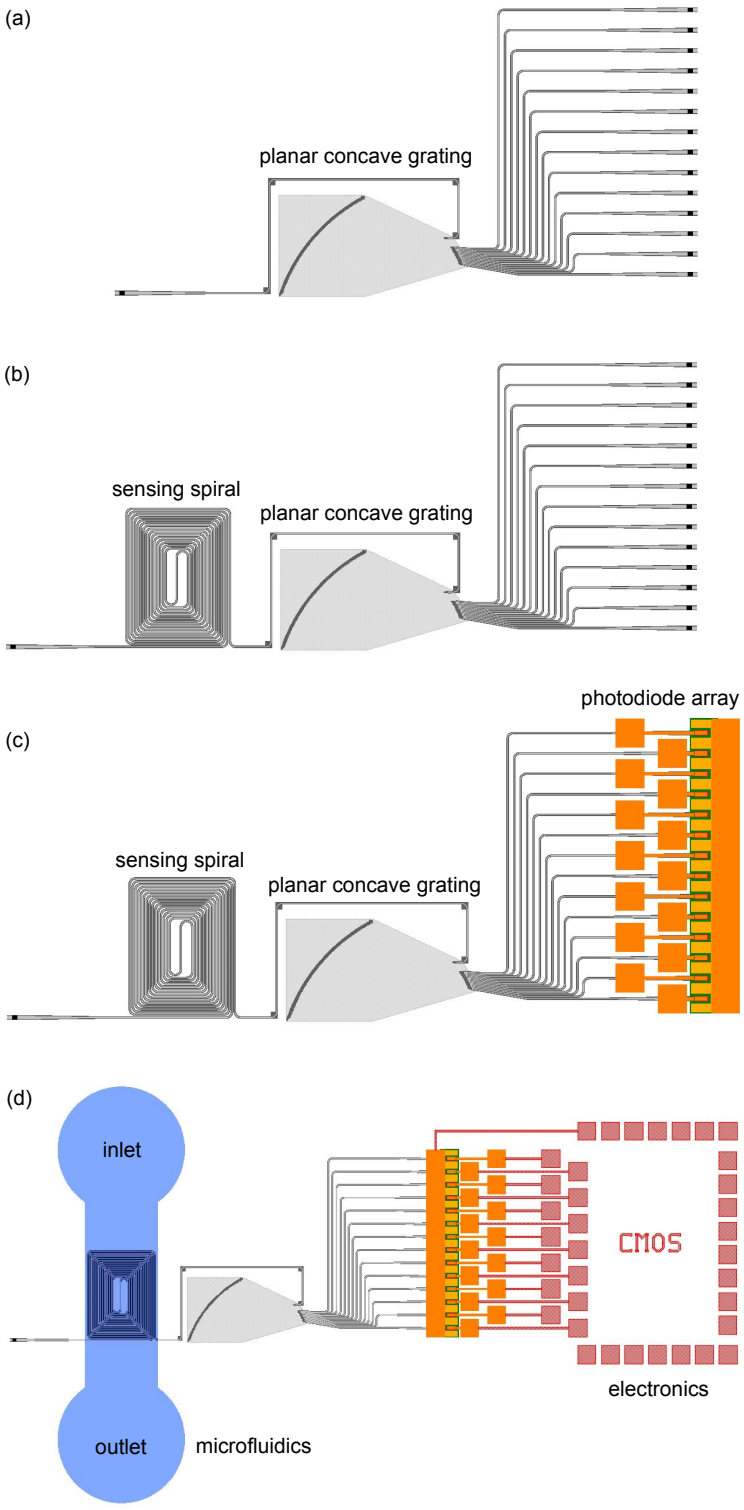

Figure 5.1: Development of a miniature spectrometer: (a) wavelength demultiplexer (b) evanescent sensor with wavelength demultiplexer (c) evanescent sensor with wavelength demultiplexer and photodiode array (d) fully integrated spectrometer with microfluidics and electronics

This chapter is devoted to the design and use of miniature silicon-based spectrometers for molecular detection. Two goals were targeted with this work:

- the development of a fully integrated spectrometer
- the extension of the SOI platform to the combination band (2-2.5 μm).

The latter goal stems from the fact that the molecular absorptivity in the near-infrared typically increases with increasing wavelength. Therefore, measuring at these longer wavelengths, should enhance the detection limit. To achieve this goal, we had to redesign all standard passive components such as grating couplers, waveguides and the wavelength demultiplexer for these longer wavelengths. However, only passive components do not get you a fully integrated miniature spectrometer. As shown in figure 5.1, different levels of miniaturization are possible. Whereas a lot of literature was available on the first level of miniaturization, the route to a fully integrated SOI spectrometer was still unknown. During the GlucoSens project, we have investigated all steps along the way and this up to the highest level of integration (see figure 5.1(d)). For this an integrated photodetector array was needed. To meet both of our goals, we needed performant photo-detectors that can cover a wide wavelength range including the combination band. This need was resolved by the heterogeneous integration of photodiodes based on GaSb epitaxial layers.

This chapter is structured as follows: firstly, we review the state-of-the-art in silicon-based passive wavelength demultiplexers. The developed spectrometers in this work use a planar concave grating (PCG) as the wavelength demultiplexer. These can offer high performance at a small footprint. Therefore, we continue the chapter with a discussion on the theory and design methodology for PCGs and discuss the developed passive components for the longer wavelengths. Next, we detail on the integration of GaSb- and InP-based photodiodes on top of a set of four different PCGs that cover the large wavelength range from 1510 to 2300 nm. Afterwards, we discuss the system that we developed for parallel read-out of the spectrometers with integrated photodiodes. This is followed by the results of our sensing experiments with these miniature spectrometers. Finally, we detail on our efforts to combine our spectrometer with electronics and micro-fluidics to obtain a truly integrated spectrometer.

5.1 State-of-the-art silicon-based spectrometers

There is a wide variety of silicon-based spectrometers with excellent performance. In this section, we selected the most prominent and 'future-proof' wavelength demultiplexers designs and discuss their attractive features.

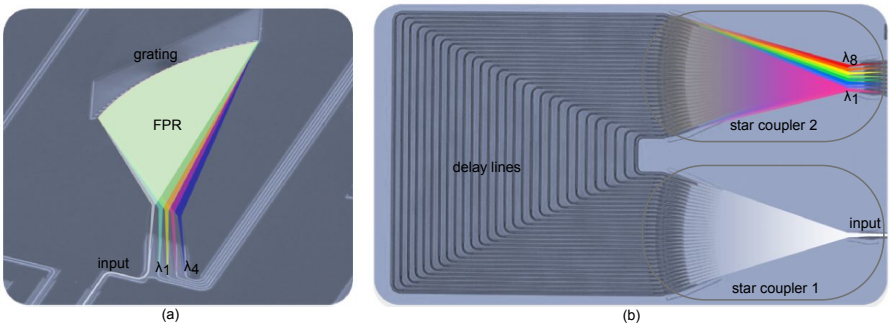

Figure 5.2: Microscope picture of a (a) planar concave grating and (b) arrayed waveguide grating integrated on a silicon-on-insulator chip. (adapted from [1])

5.1.1 Planar concave grating

The planar concave grating (PCG), also known as echelle grating, is the planar version of the classic diffraction grating spectrometer. An example is shown in figure 5.2(a). Light from an input waveguide (slit!) enters a free propagating region (FPR) and hits onto a curved diffraction grating that both focuses the light and angularly disperses the light with respect to the wavelength. The FPR is a slab waveguide and the grating teeth are etched into this slab. The PCG channels have a gaussian-like spectral response. The operation can be modeled using grating theory, which describes how the interference of multiple light contributions, each with a different phase delay, causes a spatially varying pattern that depends on the wavelength of the different light contributions. For grating spectrometers, a higher resolution can be obtained by decreasing the size of the aperture and by increasing the focal length, thus size of the FPR.

Pioneering work on PCGs using the SOI platform, was done by W.H. Wang [2], followed by Joost Brouckaert [3, 4] and others [5, 6, 7]. Thanks to the high index contrast and dimensions of the SOI platform, the typically high insertion losses due to the non-verticality of the grating teeth are avoided. The grating teeth are blazed to increase the reflection for the chosen grating order[8]. Currently, the performance of PCGs is limited by phase errors accumulated in the FPR. These originate in small thickness variations of the slab waveguide. Insertion losses on the order of 2 dB and crosstalk levels between -15 dB (footprint $\approx 1mm^2$) and -30 dB (footprint $\approx 0.01mm^2$) have been demonstrated[3, 4].

5.1.2 Arrayed waveguide grating

The most frequently used type of integrated wavelength demultiplexer is an arrayed waveguide grating (AWG), also known as phased array or waveguide grating router. An example of an AWG is shown in figure 5.2(b). It consists of two star couplers with a FPR and a set of delay lines with a constant length increment ΔL. The operation can also be described using grating theory. This device was invented by Meint Smit [9, 10] and transferred to SOI technology by T. Baba [11] and others [12, 13, 14]. For an overview of the design trade-offs, we refer to [15]. The insertion losses can be reduced up to 0.53 dB and the crosstalk level can be as low as -25 dB[16]. To obtain a flat-top spectral channel response, rather than a gaussian-like, the input aperture of the first star coupler can be replaced with a multi-mode interference coupler[17]. Similar to PCGs, the performance of SOI-based AWGs is limited by phase errors due to small dimensional changes in the delay lines. For larger devices, these phase errors become more problematic.

5.1.3 Slow light enhanced spectrometers

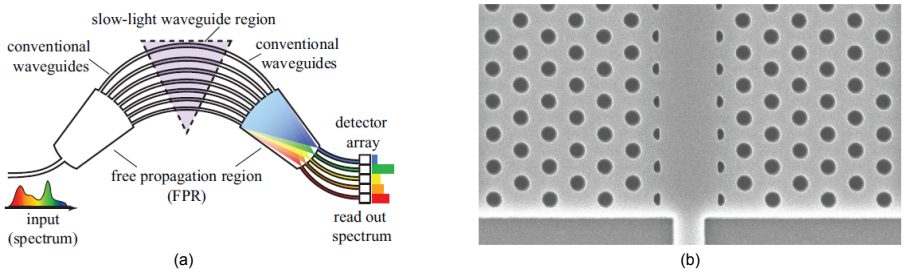

Figure 5.3: (a) conceptual drawing of a slow-light enhanced AWG and (b) a photonic crystal waveguide (both images from [18])

To reduce the size of integrated spectrometers, the slow light enhancement effect can be used[19, 20]. By increasing the wavelength dispersion (increase group index n_g) of the spectrometer, the light needs a smaller interaction length with the dispersive medium to obtain a given optical delay. For AWGs, whose footprint scales linearly with $\frac{1}{n_g}$, this slow-light concept can be implemented by using photonic crystal waveguides in the delay lines as shown in figure 5.3. Nonetheless, an experimental result of this elegant idea is yet to be demonstrated.

5.1.4 Fourier transform spectrometers

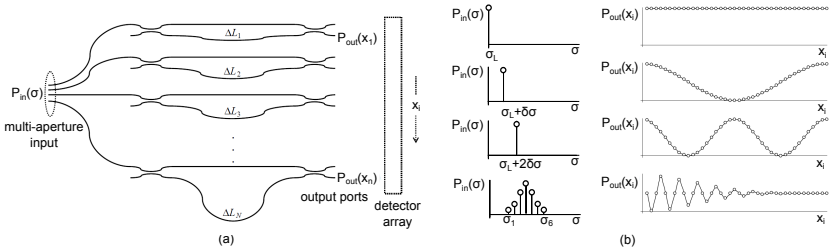

Figure 5.4: (a) Layout of an integrated FTIR and (b) operating principle (both images from [21])

Whereas standard FTIR spectrometers have a scanning mirror, this moving element can be replaced on an integrated platform by an array of interferometers, each with a different optical delay. These interferometers can e.g. be Fabry-Perot cavities [22] or Mach-Zehnder interferometers (MZI) [21, 23]. In the latter case, the integrated FTIR contains a $1 \times N$ splitter and an array of N non-balanced MZIs, each with an increasing arm length difference (see figure 5.4). The design is such that a monochromatic input will generate a sinusoidal spatial distribution along the array of the upper (or lower) MZI outputs. By extension of this principle, any input signal is mapped onto its Fourier-transform (the interferogram). The number of MZI's can be determined by the fourier sampling theorem as: $N = 2\frac{\Delta\lambda}{\delta\lambda}$, in which $\Delta\lambda$ is the spectral range of the spectrometer and $\delta\lambda$ the resolution. As only one output of the MZI is needed for the interferogram, the other can be used as a signal to calibrate the spectrometer. Literature on the theory and successful demonstrations of this principle on the SOI platform can be found in [23]. Unfortunately, the loss figure and cross-talk are not stated.

5.1.5 High resolution spectrometers

Typically, the size of integrated spectrometers grows quickly with required resolution. This, however, compromises the spectrometer performance as a larger size induces more losses and phase errors. To circumvent this issue, either a large set of high-Q resonators can be used or a cascade of spectrometers. A high-Q resonator has a transmission spectrum with very sharp peaks (or dips) located at the resonance wavelengths ($Q = \frac{\lambda_{res}}{FWHM}$), with $FWHM$ the full width half max of the resonance peak. When a limited wavelength range $\Delta\lambda$ is required, an array of these resonators can be used to sample the spectrum [24]. This is shown in figure 5.5. Given the

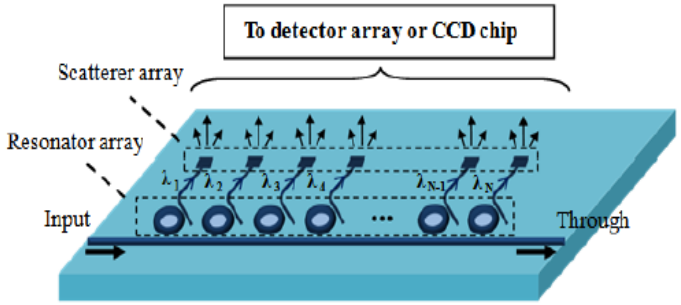

Figure 5.5: Solutions for high resolution spectrometers: array of optical cavities [24]

small footprint of standard SOI resonators, a high resolution but small-sized spectrometer can be achieved. However, the location of the resonances are very sensitive to fabrication imperfections and environmental changes. Post-fabrication trimming, encapsulation and calibration of the resonators can be used to reduce the impact of these problems. The other approach to enhance the resolution of integrated spectrometers, cascading, is suitable when a large spectral range needs to be analyzed. A number of configurations have been demonstrated: either coarse filtering is followed by consecutive stages of narrower filtering [25, 27] or a tunable narrow-band filter is used to scan along the pass-band of a coarse wavelength demultiplexer [26]. An example of the first approach in which a coarse filter is followed by a narrow filter is shown in figure 5.6(a). An example of the second approach in which a tunable filter is used is shown in figure 5.6(b). In this example, the FSR of the ring resonator, matches the channel spacing of the PCG. This way, a small footprint is possible but the spectrum is not acquired at once and additional energy is needed to tune the narrow-band filter. When spectrometers are cascaded, care should be taken to minimize the insertion losses of the individual filters. In addition, the filter characteristic of the in-coupling scheme (e.g. grating couplers) should be considered as well.

5.2 Spectrometer design

For our glucose monitoring application, we need to cover a large wavelength range with a fairly high resolution of 3-5 nm to allow specific detection. This implies a large number of spectral channels M. The size of AWG-based spectrometers scales with M, whereas for PCGs the size scales with xM with $x < 1$ [28]. As footprint is an important feature for implantable devices and often determines the performance of integrated devices due

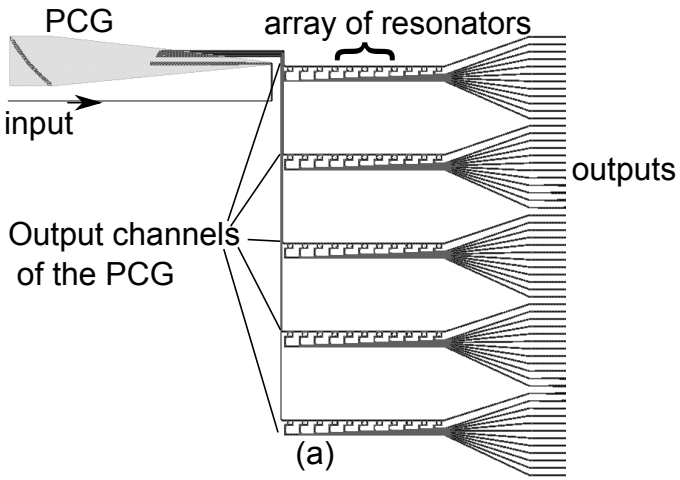

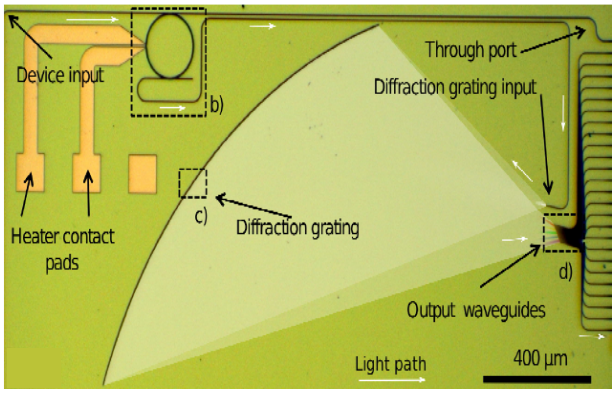

[h]

(b)

Figure 5.6: Solutions for high resolution spectrometers: (a) cascade of coarse and dense filters [25] (b) tunable ring filter cascaded with a PCG for coarse filtering [26]

to phase errors, we chose for PCG-based spectrometers. In addition, the very high resolution realized by optical cavities was not needed and the FTIR approach had to be developed from scratch while it doesn't offer a footprint advantage.
Multivariate analysis of glucose solutions typically gives a selection of important wavelengths that are not uniformly distributed across the first overtone band or combination band [29]. However, spectrometers have an equal channel spacing. Therefore, we decided at the start of the GlucoSens project to focus on the absorption peaks of glucose with a fixed channel spacing of minimally 3 nm. Next to the glucose sensing application, also the spectral analysis of bio-diesel was targeted. In this case, important absorption features are found at 1650 nm and 2125 nm, which can be resolved with a resolution of 7 nm [30, 31].

In this section, we shortly discuss the design methodology that was followed for the PCG design. We leveraged a great deal from the PhD thesis work from Joost Brouckaert [1]. For a more detailed explanation on the design and simulation framework for SOI PCGs, we refer the reader to the doctoral thesis of Joost Brouckaert[1]. Our main focus will be on the extension of his work in the telecom-wavelength range to the longer wavelengths up to 2.5 μm.

5.2.1 Theory of planar concave gratings

The PCG geometry is based on the Rowland configuration [32] with one stigmatic point correction [1]. In this particular configuration, the input and output apertures are located on a circle with radius R, whereas the grating has a curvature of 2R as shown in figure 5.7(b). The point where both circles meet is called the pole P. For this configuration, the grating equation determines the direction of the diffracted light θ_d, given the direction of the incoming light θ_i:

$$d(sin(\theta_i) + sin(\theta_d)) = m\frac{\lambda}{n_{eff}} \tag{5.1}$$

with m the diffraction order and n_{eff} the effective index of the slab mode in which the incoming light propagates. Typically, the angles θ_i and θ_d are chosen approximately the same (Eagle mounting [33]) to increase the diffraction efficiency. For the Rowland configuration, the facets further from the pole introduce aberrations[1], as the light reflected from a point P and P′ no longer arrive at the same output (see figure 5.7(a)). This can be reduced by introducing a one stigmatic point correction for the central operating wavelength as shown in figure 5.7(b) [1].
The linear dispersion LD= $\frac{\Delta\lambda}{\Delta s}$ determines the channel spacing $\Delta\lambda$ between two output apertures that are located at a distance Δs along the Rowland

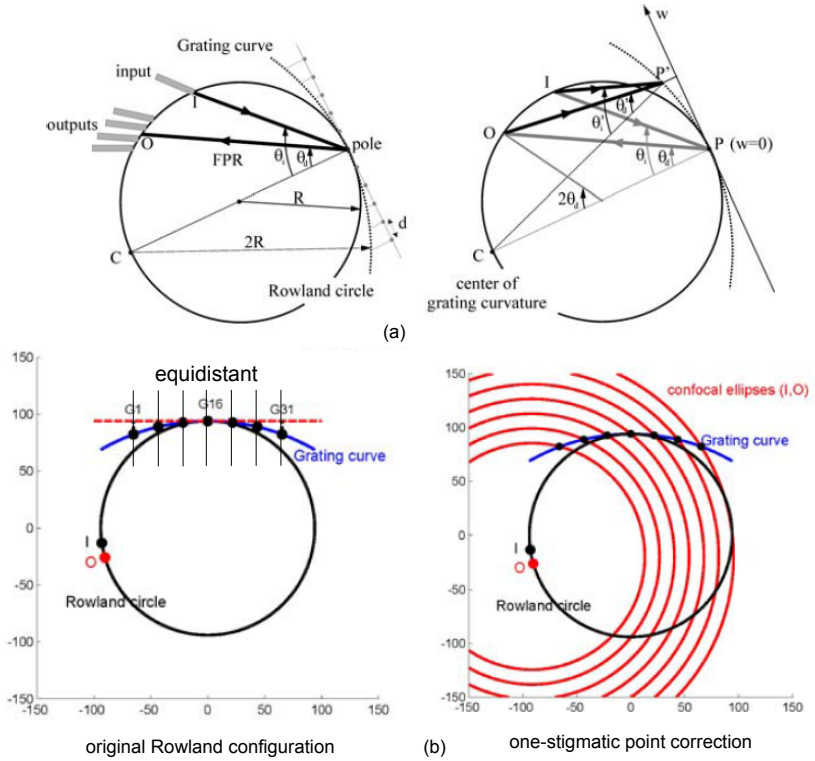

Figure 5.7: (a) Rowland geometry (b) Comparison of the original Rowland geometry with the one stigmatic point correction configuration (both from [1])

circle. It can be expressed in terms of the angular dispersion $\frac{\delta\theta_d}{\delta\lambda}$ times the Rowland diameter 2R:

$$LD = \frac{\Delta\lambda}{\Delta s} = 2R\frac{\delta\theta_d}{\delta\lambda} = \frac{2R \cdot m \cdot n_g}{d \cdot cos(\theta_d) \cdot n_{eff}^2} = \frac{2R \cdot (sin(\theta_i) + sin(\theta_d)) \cdot n_g}{\lambda \cdot cos(\theta_d) \cdot n_{eff}} \tag{5.2}$$

Because $\frac{n_g}{n_eff}$ is large for SOI waveguides, a much smaller device can be obtained for a given LD, in comparison with other material platforms.
The equation 5.2 can be used to design the PCG for a certain channel spacing, alias wavelength resolution, $\Delta\lambda$. The spectral operating range is limited by the free spectral range (FSR) of the PCG. Two wavelengths, separated by the FSR, will be imaged onto the same output aperture. The FSR is strongly dependent on the diffraction order m:

$$FSR = \frac{\lambda}{m}\left[1 - \frac{m+1}{m}(1 - \frac{n_g}{n_{eff}})\right]^{-1} \tag{5.3}$$

Increasing the diffraction order m, increases the linear dispersion and leads to a higher resolution but decreases the operation range.

5.2.2 PCGs for the combination band

As mentioned, performant SOI PCGs have been demonstrated in the telecom range. To expand the operating range to the longer wavelengths, we should scale all dimensions with the wavelength. However, the thickness of the silicon layer is fixed to 220 nm by the fabrication process. Therefore, perfect scaling is not possible and a number of elements should be changed to the design. The following set had to be optimized: waveguides, bend radius, DBR facets, in- and output apertures, linear tapers and grating couplers. These elements are highlighted in figure 5.8.

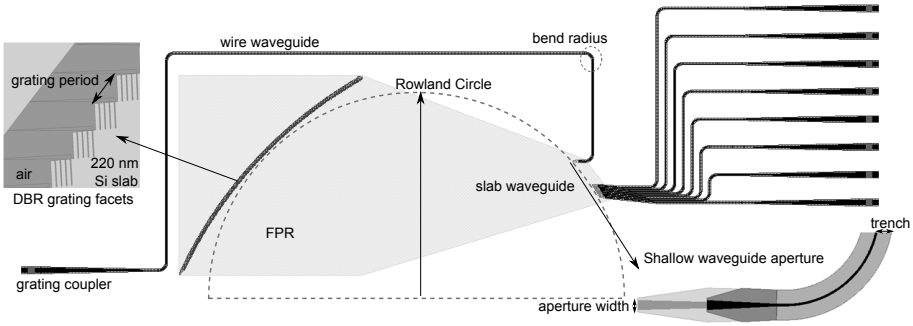

Figure 5.8: Important design features for a planar concave grating

Low-loss waveguides

The waveguide design considerations listed in this section are the result of a joint effort of multiple PhD students in the photonics research group at UGent. Firstly, the core and trench width of the routing waveguides was changed for operation in the combination band (CB). To determine the maximal width for single-mode behavior, we simulated the effective index at a wavelength of 2.1 μm for water clad wire waveguides with different widths. The result is shown in figure 5.9(a). Wire waveguides with a core width between 800 and 900 nm and 3 μm wide trenches were measured to be low-loss (< 2 dB/cm, air cladding). A waveguide width of 800 nm was chosen for the PCG designs, this matches the width for an evanescent spiral for the CB that has a good confinement factor and low losses. The standard bend radius is increased to 15 μm to avoid bending losses. We also investigated rib waveguides to serve as the input and output aperture of the PCG. In this case, a 110 μm long linear taper (see 4.2.5) is used to convert

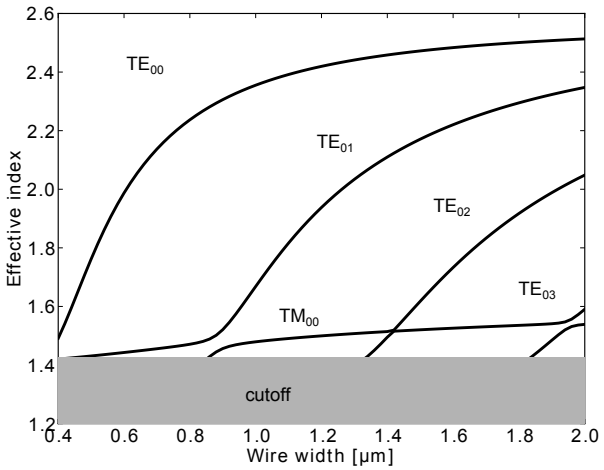

Figure 5.9: Effective index in function of width for a water clad wire at $\lambda = 2.11\mu m$

between 800 nm wide wire waveguides and a 3 μm wide rib waveguide. Simulations with the software FimmWave® show that this length allows an adiabatic mode size conversion. The loss measurement of rib waveguides with a core width of 1.2 μm, an oxide cladding and bend radius of 20 μm, is shown in figure 5.10(a). High losses are present for wavelengths between 2.2 and 2.3 μm. These originate in the strong absorption features of the top oxide, which was deposited using plasma enhanced chemical vapor deposition (PE-CVD). This means that the top cladding should be optimized when these rib waveguides are to be used in the combination band. This absorption loss is not present in the first overtone band. Another loss factor that grows with wavelength, is the substrate leakage. Because of the limited thickness of 220 nm and larger mode expansion for longer wavelengths, the light can more easily leak to the Silicon substrate. This substrate leakage was simulated using CAMFR for wire waveguides with a width of 800 nm and 900 nm. The simulation results are shown in figure 5.10(b). It is clear that the silicon thickness should be increased for wavelengths beyond 2.7 μm.

Distributed Bragg Reflector grating facets

To create high reflectivity grating facets, distributed Bragg reflector (DBR) gratings are used as shown in figure 5.8 [4]. These DBRs comprise four periods of deeply etched grating lines. First order DBRs were simulated and used in the $> 2\mu$m PCG designs. These first order gratings offer a

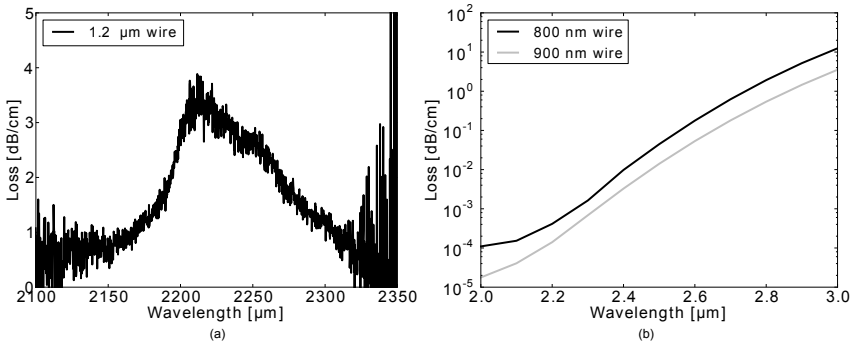

Figure 5.10: (a) propagation loss of a 1.2 μm wide rib waveguide with top oxide (b) propagation loss due to substrate leakage

very wide reflection band of 300 nm with $R > 90\%$. Two center wavelengths were targeted: 2.11 μm, 2.32μm. These are the main absorption wavelengths of glucose in the combination band. The reflection from the DBRs, is calculated using CAMFR as if the facet width is infinite (2D simulation). The result is shown in figure 5.11.

Polarization dependent performance: TE vs. TM

The free propagating region (FPR) of the PCG is a slab waveguide that can only support the fundamental quasi-TE and quasi-TM mode for the wavelengths that we use. The effective index of both modes differs strongly: 2.59 versus 1.59 for respectively the quasi-TE and quasi-TM mode at 2110 nm. Therefore, if both modes would be excited at the input aperture, their image would focus onto different locations on the Rowland circle. In the literature a few methods were developed to overcome this polarization dependence, such as a polarization diversity approach[1] or compensation regions[34]. Nonetheless, if one can choose the excited slab mode, the PCG design can be optimized for one of both. If the quasi-TM mode is chosen, an oxide top cladding is needed to prevent mode conversion losses in the aperture tapering [35]. The advantage of the quasi-TM mode is the higher ratio of $\frac{n_g}{n_{eff}}$. Based on equation 5.2, this means that the size of the PCG can be reduced for a given LD. Still, in comparison to the quasi-TE mode, the quasi-TM mode is much more sensitive to small deviations in the thickness of the 220 nm high slab waveguide. The quasi-TM mode will thus accumulate more phase errors due to small thickness variations that result from fabrication imperfections. In [36], it was found that, although the same PCG was measured, the crosstalk level is 6 dB lower for the quasi-TE mode (-27 dB) due to stronger sidelobes in the spectral response of the

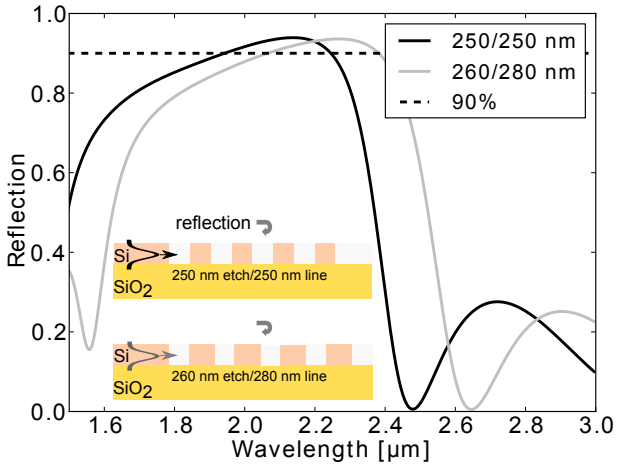

Figure 5.11: Reflection of the DBR facet in function of wavelength for two first order gratings

quasi-TM mode (-21 dB). We can conclude that the quasi-TE mode is preferred for better performance of PCGs.

Design strategy

As extensively studied and reported in the doctoral thesis of Joost Brouckaert, accumulated phase errors limit the performance of the PCG. These phase errors are caused by fabrication imperfections such as thickness variations in the FPR. Of course, for larger wavelengths, the size of the PCG increases for a given resolution, so that more phase errors result. Therefore, our PCG design always started from an upper limit on the Rowland radius R. Next, the minimal FSR and channel spacing $\Delta\lambda$ are fixed, as imposed by the targeted application. From the minimal FSR, the upper limit of the diffraction order m can be determined from equation 5.3. For smaller m-values, the FSR increases, but the period d for a given linear dispersion will decrease. This small period requires smaller facets that are more prone to fabrication imperfections. Still, smaller facets increase the channel uniformity, as the field at the output is the summation of the far-field profile of each of the facets. As mentioned before, the angles θ_i and θ_d should be chosen approximately equal to increase the diffraction efficiency. Their nominal value should not be too large, as in this case the facets further from the grating pole become illuminated and introduce aberrations. If the angles are too small, the small Rowland radius cannot be obtained. A choice

between 30° and 50° is advised [1]. Once all these parameters are fixed, the aperture width and aperture spacing come into play. When the apertures are small, the device can be smaller but again more facets far from the grating pole become illuminated. The aperture size can thus be increased until it doesn't interfere with the size limit. Still, this increase in width will also make the channel transmission broader. As equation 5.2 shows, the aperture spacing Δs is fixed as soon as $\Delta\lambda$, R and the angles θ_i and θ_d are chosen. Nonetheless, optimization of these parameters is needed to ensure that the Δs doesn't become too small. This can introduce optical coupling and shading between neighboring output apertures, which degrades the PCG performance.

5.2.3 Grating couplers

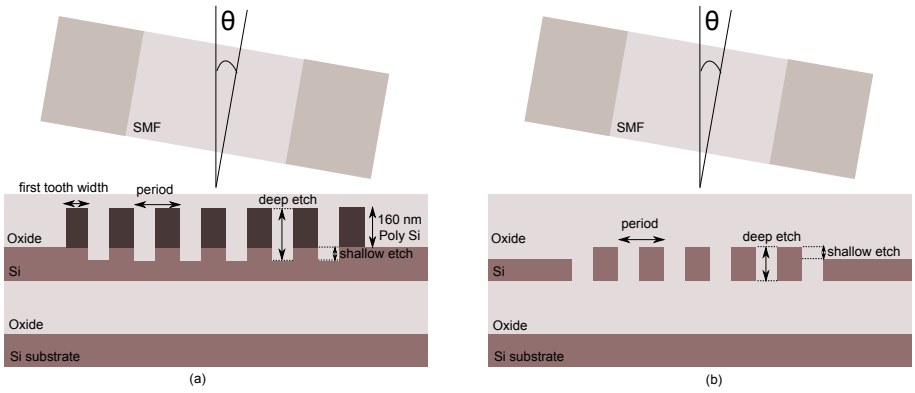

Figure 5.12: Straight gratings for (a) advanced passive and (b) standard passive fabrication runs at imec

Grating couplers are very useful components that can couple light from a near-vertically aligned optical fiber into the plane of the optical chip. At the start of the GlucoSens project, these grating couplers had to be developed for the combination band (CB). The grating coupler performance strongly depends on the available fabrication etch depths for the grating grooves. Imec offers two possible fabrication settings, denoted as standard passive and advanced passive runs. In the former case, the 220 nm silicon layer can be etched by 70 nm (shallow etch) or by 220 nm (deep etch). In the latter case, an additional 160 nm thick poly-silicon layer is deposited on top of the 220 nm silicon layer. In what follows, we shortly introduce the operating principle of grating couplers and discuss the developed designs and measurement results for both passive and advanced passive runs.

Theory of grating couplers

The operation of a grating coupler (GC) can be described by the Bragg condition that models the redirection of the k-vector of incident light due to the periodicity of a grating. For a straight 1D grating, an incidence angle of θ_{in} and grating period d, this Bragg condition becomes:

$$\frac{2\pi \cdot n_{GC}}{\lambda} = \frac{2\pi \cdot n_{env} \cdot sin(\theta_{in})}{\lambda} + \frac{2\pi}{d} \tag{5.4}$$

in which n_{GC} is the effective index of the excited grating mode and n_{env} the index of the grating cladding. The grating effective index n_{GC} can be calculated as the effective index of the slab mode with thickness $t = t_{non-etched} - ff * t_{etched}$, with ff the fill factor and $t_{non-etched}$ and t_{etched}, the thickness of respectively the grating line and the etch depth [37]. The fill factor of the grating is the width of the Si grating line divided by the period d. From the above relation we can derive that the coupling wavelength can be tuned with the grating period. The coupling efficiency depends on the directionality of the grating and the mode profile overlap between the fiber mode and upward diffracted mode. This overlap can be influenced by the width of the grating coupler and the coupling strength. When the grating has a low coupling strength, a larger number of periods N_p is needed and the upward diffracted mode profile becomes wider. The optimal upward diffracted mode width should match the mode field diameter (MFD) of the fiber mode. This becomes possible by matching the grating width to this MFD.
After the grating coupler, the light should be converted to the narrow single-mode routing waveguides. This can be done with a relatively long adiabatic taper. Another solution is to use focusing grating couplers[38], for which both the in/out-coupling and mode conversion is achieved simultaneously. Grating couplers can be designed for both the quasi-TE mode and quasi-TM mode. If one wants to excite the quasi-TM mode on an air-clad SOI chip, focusing grating couplers are a necessity. This is because a straight grating coupler in combination with an adiabatic taper suffers from mode conversion to higher order modes at certain taper widths [35]. In our work, we have only used TE-grating couplers.

Advanced passive design

The layer stack of advanced passive grating couplers is shown in figure 5.12(a). This type of grating couplers are also labeled raised gratings. As in the telecom range, raised gratings offer the highest coupling efficiency for the CB [39]. The simulation and characterization results of this type of grating were done by Nannicha Hattasan and can be found in [39]. The main results are shown in figure 5.13. For a fill factor of 0.3, the highest efficiency of -3.8 dB was obtained for $\lambda = 2.1\mu$m and $d = 0.98\mu$m. The typical

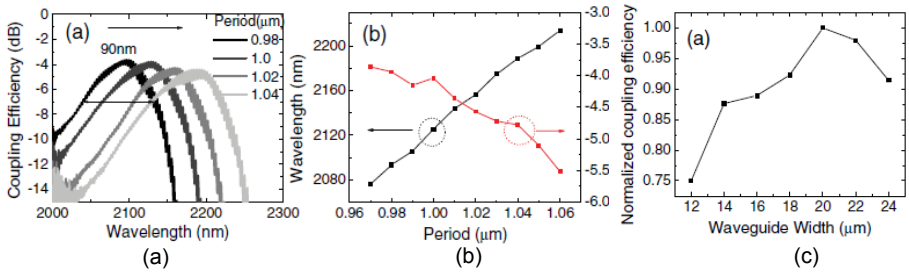

Figure 5.13: Experimental results on raised gratings: (a) coupling efficiency for different grating periods (b) dependency of the peak wavelength and peak efficiency on the grating period (c) normalized coupling efficiency in function of waveguide width (all graphs taken from [39])

3 dB bandwidth is 90 nm. We further investigated the relation between the grating width and the coupling efficiency. The grating width should be optimized such that the width of the upward diffracted mode approximately equals the mode field diameter (MFD) of the gaussian mode in the optical fiber. This will enhance the modal overlap, hence coupling efficiency. It was found experimentally [39] that for a wavelength of 2.2μm and a fiber angle of $10°$, the grating width optimum is 20 μm.

Standard passive design

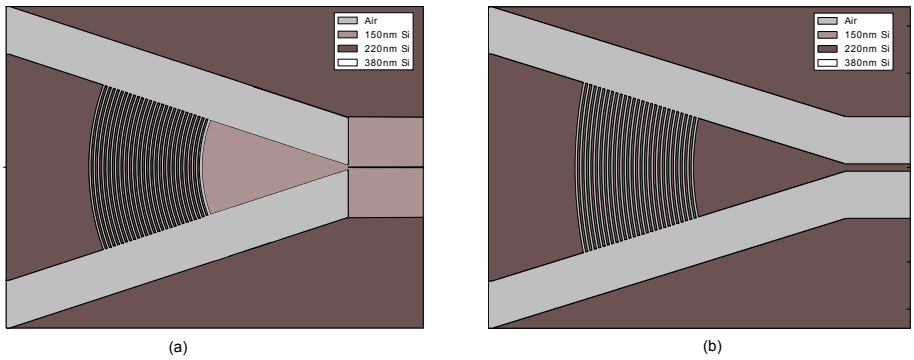

Figure 5.14: Curved grating design with (a) shallow aperture and (b) deep aperture.

As the advanced passive process is not available for every fabrication run and has a higher price, we investigated new grating coupler designs for the

standard passive fabrication runs. The straight grating design is shown in figure 5.12(b). It has deeply etched grating teeth but is coupled to a shallowly etched waveguide. This strongly differs from the standard grating coupler design that is used for the first overtone band. Those gratings have shallowly etched teeth in a 220 nm thick waveguide and a peak efficiency of -4.5 dB at 1550 nm for a 3 dB bandwidth of 50 nm. This design can, however, not work in the combination band, as the index change between a grating line and a grating etch is too small. This results in a too low (upward) coupling strength. This is confirmed by the measured peak efficiency value for this standard grating in the combination band [40]: -10.3 dB at a wavelength of 2.2μm for a period d=1.66μm.
In contrast, our straight grating coupler design offers reasonable peak efficiencies of -6.5 dB for a period d=1.65 μm and ff=0.35 at a peak $\lambda = 2.18\mu$m, while the 3 dB bandwidth increases to 160 nm. Similar to the raised gratings, we used the optimal grating width of 20 μm. This is very wide compared to the standard wire width of 800-900 nm. Hence a long taper (≈ 1 mm) is required to adiabatically convert the excited grating mode to the wire mode.

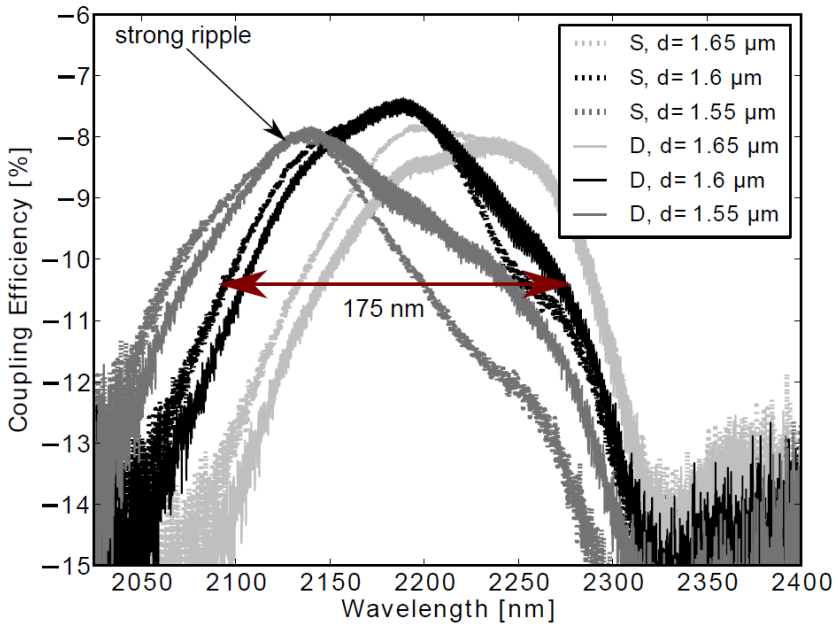

Figure 5.15: Measured coupling efficiency of the curved grating couplers in function of the grating period for both S (shallow) and D (deep) apertures.

To avoid the large footprint of this taper, two curved grating coupler de-

signs were tested. These are shown in figure 5.14. Either the grating couples to a 150 nm thick waveguide aperture or to a 220 nm thick waveguide aperture. Because of the effective index contrast between the grating mode and the 220 nm thick waveguide, Fresnel reflections will occur. These reflections are much lower in the case of coupling to a 150 nm thick waveguide. In figure 5.15 both designs are compared. The peak coupling efficiency for oxide clad grating couplers measured at 20° is, however, reduced to -7.5 dB.

5.2.4 Measurement results

Table 5.1: DESIGN PARAMETERS OF THE INDIVIDUAL DEMULTIPLEXERS

	PCG 0	PCG 1	PCG 2	PCG 3	PCG 4
center λ [nm]	1590	1550	1650	2125	2320
resolution [nm]	3.0	3.2	7	6	5
number of channels	30	8	14	16	8
wire width [μm]	0.45	0.45	0.5	0.8	0.8
aperture width [μm]	2	2	2	3	3
free spectral range [nm]	107	115	121	150	60
DBR period [nm]	340	600	340	500	540
DBR order	1	2	1	1	1
footprint [mm^2]	0.83	0.56	0.24	0.54	1.04
cladding	air	oxide	oxide	oxide	oxide

Here, we shortly list the design parameters and optical characterization results from the planar concave gratings that were fabricated during the GlucoSens project (see table 5.1). Both first overtone band and combination band PCGs for the quasi-TE mode were designed. PCG0 and PCG4 are focused on the glucose absorption peak wavelengths, whereas PCG2 and PCG3 are focused on biodiesel analysis. The latter two PCGs are preceeded by a spiral wire waveguide (for evanescent sensing) with a length of 1.7 cm and 1 cm for PCG2 and PCG3 respectively. For the experimental characterization, we used the semi-automatic set-up that automatically aligns the in- and output fibers above the PCG's grating couplers, based on their coordinates in the mask design gds-file. The output fiber is connected to an optical spectrum analyzer (Yokogawa AQ6375) and the input fiber is connected through a polarizer to a broadband light source. For the measurements in the first overtone band two SLEDs were used, one with a center wavelength λ=1.55 μm (PCG0, PCG1) and one with λ=1.65 μm (PCG2). The source light was coupled using standard passive shallowly etched grating couplers with ff=0.5, N_p=25 and a period of 650 nm, 630 nm and 690 nm for respectively PCG0, PCG1 and PCG2. For the combination band, a pulsed supercontinuum source was used and grating couplers

(see section 5.2.3) with ff=0.5, N_p=25 and a period of 1.45 μm, 1.61 μm, for respectively PCG3 and PCG4.

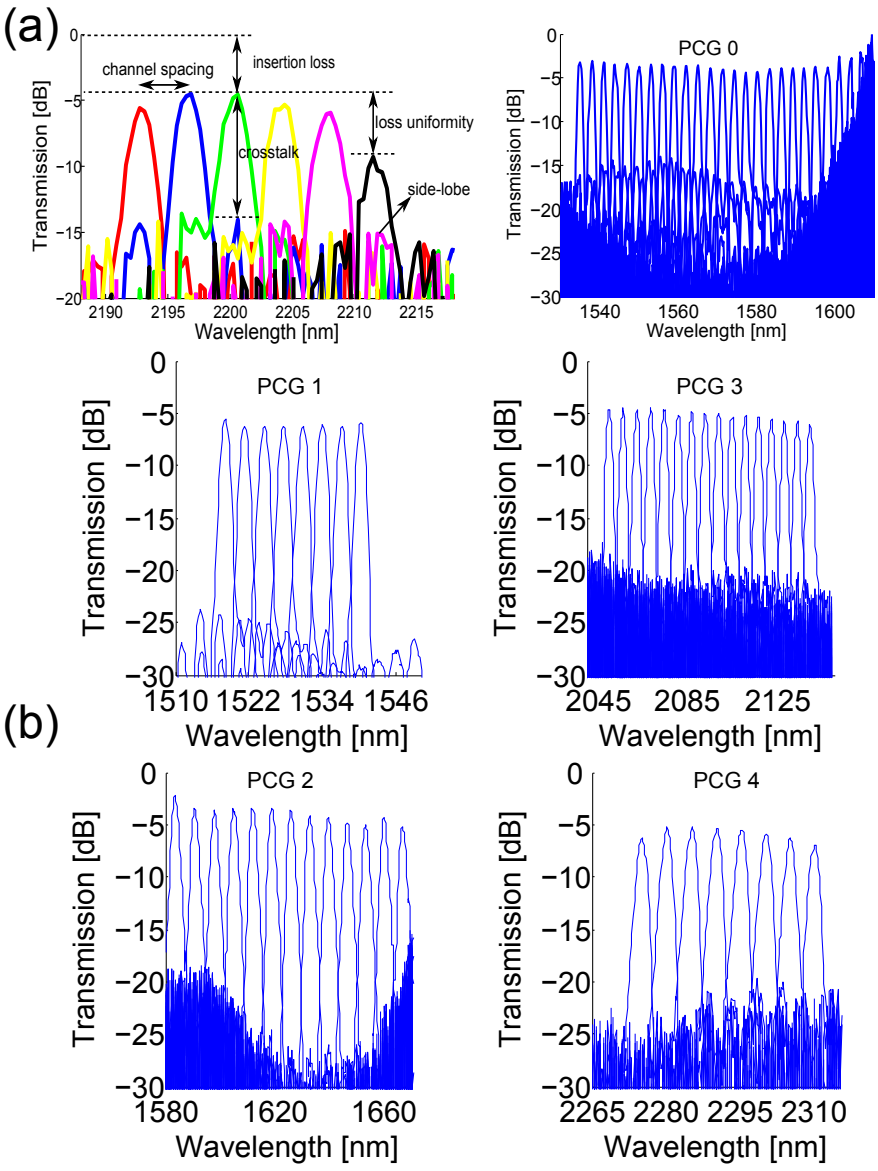

Figure 5.16: (a) Performance measures for spectrometers. (b) Optical characterization of PCG design listed in table 5.1

The performance metrics for a PCG are shown in figure 5.16(a) on a first generation PCG design. In the same figure, the measurement results of the above listed planar concave grating designs are shown. When we inspect the insertion losses, we notice that the insertion losses are much lower for PCG0 (-3 dB) than for the other PCGs (-5 to -7 dB). The latter were fabricated in the same run and after inspection of the DBR facets using SEM pictures, we found that the DBR facets are not fabricated properly (see figure 5.17). On the other hand, we find that PCG0 has the highest side-lobes with an extinction ratio of only -11 dB. This is due to the large size and air-cladding which increases phase errors. The crosstalk level of the combination band PCGs could not be properly measured due to the high noise floor, but at least -16 dB is obtained. As expected, the smallest PCG has the lowest crosstalk (-22.2 dB for PCG2). The best loss uniformity (0.6 dB) is found for PCG1 which has the smallest facets (3.1 μm wide).

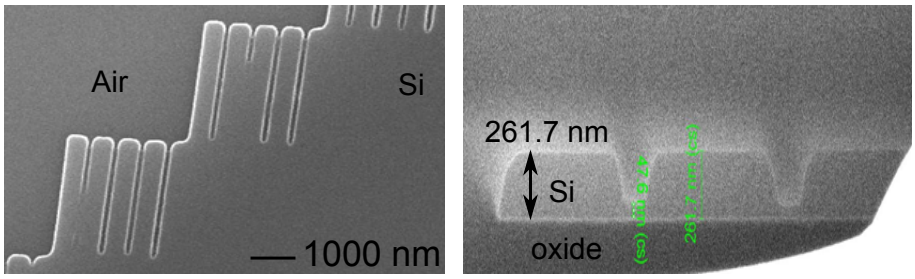

Figure 5.17: SEM pictures of the DBR facets (a) not fully etched second order DBR (b) silicon layer is thicker (260 nm) than expected (220 nm)

We used the same optical set-up to do a small detection test. We measured the spectral response of PCG2 on an air-clad sample in the case that the preceding waveguide spiral was empty and once when PEG was applied to this spiral. The result is shown in figure 5.18. The absorption due to PEG at 1620 nm is clearly visible. The drop in absolute transmission in all channels, is due to a change in fiber height in the case when PEG was applied. The height was increased to avoid immersion of the fibers in the liquid polymer, as this would lead to a spectral shift in grating coupler response.

5.3 Photodetector integration

In this section, we describe the photo-detector integration for on-chip readout of PCG1, PCG2, PCG3, PCG4 (see previous section). Two photo-detector

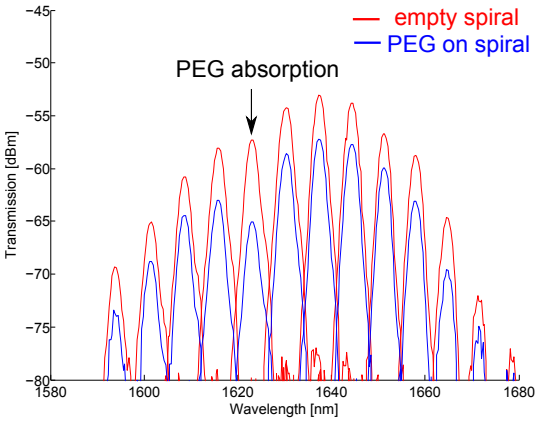

Figure 5.18: Transmission of PCG2 with preceding spiral immersed in (red) air and (blue) PEG. The absorption due to PEG at 1620 nm is clearly visible.

fabrication runs were organized. In the first run, GaInAsSb photodiodes were integrated and in the second run, InP-based photodiodes. The InP photodiode integration run was part of the work for the final demonstrator of the GlucoSens project (see further section A.2). Both will be discussed in terms of responsivity and dark current. Due to the large band gap of the used InP epitaxy, we could only use the InP photodiodes up to 1.65 μm. The GaSb-based photodiodes on the other hand, can be used up to 2.65 μm and thus work for both the first overtone band and combination band. The photodetector fabrication was done by Alban Gassenq and Steven Verstuyft from the photonics research group at UGent. Both series of fabricated chips with GaSb and InP photodiodes were used for evanescent detection experiments.

5.3.1 Photodiode operation

To convert the optical power at the different spectrometer channels into electrical current we use P-i-N photodiodes. This type of photodiode comprises a semi-conductor PN junction separated by an intrinsic, undoped layer. Photons that are incident onto the intrinsic region can be absorbed if the photon energy $h\nu$ is larger than the material bandgap. Upon absorption, an electron-hole pair is generated. This electron-hole pair becomes separated by the intrinsic electric field that exists across the PN junction and generates a photocurrent. This photocurrent I_p can be defined as:

$$I_p = q\frac{\#\text{collected electron-hole pairs}}{\delta t} = q\eta\frac{\#\text{incident photons}}{\delta t} = \eta\frac{q}{h\nu}P_{opt} \tag{5.5}$$

where q is the elementary electric charge, $h\nu$ the photon energy, δt the time frame, P_{opt} the incident power and η the quantum efficiency. The quantum efficiency depends both on the optical and electrical properties of the photodiode and should be maximized. It can be rewritten as:

$$\eta = \frac{I_p}{P_{opt}[mW]} \cdot \frac{1.24}{\lambda[\mu m]} \tag{5.6}$$

When an external bias voltage V_{bias} is applied across the photo-diode, the output current can be described by:

$$I = I_{diode} - I_p = I_0 \left[exp(\frac{qV_{bias}}{kT}) - 1 \right] - I_p \tag{5.7}$$

This yields the typical IV characteristic with two regimes: a forward bias and reverse bias regime. With a forward bias (larger than the built-in photodiode potential), the electrons and holes from the P and N regions are displaced and can recombine in the intrinsic region and generate a large (positive) current. In the reverse bias regime, a small (negative) current exists next to the photo-current I_p. This is called the dark current or leakage current and arises due to spontaneously generated electrons and holes in the intrinsic region that move apart due to the built-in potential. By applying a large reverse bias, one depletes the intrinsic region from carriers other than the photo-generated ones. This way, the detected current is less dependent on the reverse bias.

5.3.2 Performance metrics

Three figure-of-merit (FOM) are typically used for photodiodes: dark current, responsivity and speed or bandwidth. The bandwidth determines how fast an optical variation can be captured. As our integrated spectrometer doesn't require high-speed operation of the photodiodes for absorption spectroscopy, we are mainly interested in the dark current and responsivity of the photodiodes. The responsivity is related to the quantum efficiency and is defined as:

$$\Re = \frac{I_p}{P_{opt}} = \eta \frac{\lambda[um]}{1.24} [A/W] \tag{5.8}$$

The maximum responsivity $\Re$ is obtained for $\eta = 1$.
The dark current can limit the signal-to-noise ratio of the miniature spectrometer as it contributes to the noise-equivalent power (NEP). The NEP is the total noise current i_n divided by the responsivity ($NEP = \frac{i_n}{\Re}$) and represents the optical power that gives a signal-to-noise ratio of 1. The total photodiode noise current is typically dominated by Johnson noise and shot noise. Johnson noise i_j is the result of thermal motion of charge carriers in

resistive materials. The rms value of the Johnson noise is $i_{rms,j}$=$\sqrt{\frac{4kTB}{R}}$ with k the Boltzmann constant, T [K] the temperature of the photodiode, R[Ω] the resistance giving rise to the noise and B the detection bandwidth [Hz]. In the case of a photodiode, the shunt leakage resistor generates the Johnson noise. The shot noise is generated due to the quantum nature of the current, such that a current flow can be seen as the sum of many short and small current pulses. The shot noise associated with a current i is given by $i_{rms,s} = \sqrt{2qiB}$. Both the dark current and photo-current generate shot noise. The dark current should therefore be reduced. At room temperature, the Johnson noise typically dominates over shot noise. Naturally, by time-averaging the current signal, both the Johnson noise and shot noise can be reduced.

5.3.3 Grating-assisted photodiodes

There exist several ways to couple the light from the silicon waveguide to the integrated photodiode. One can use butt coupling [41, 42], evanescent coupling [43] or grating-assisted coupling [1]. They are depicted in figure 5.19. It is the last option that is implemented, as it offers the highest fabrication tolerance. This is important when a high number of spectrometer channels needs to be interrogated. To fabricate integrated photodiodes, heterogeneous integration based on DVS-BCB (Divinylsiloxane - bis - Benzocyclobutene) adhesive wafer bonding is used [41]. In this case, a layer of the polymer DVS-BCB is used as a glue to bond the III-V epi onto the processed silicon wafer. After the bonding, the III-V growth substrate is removed so that the remaining P-i-N stack can be further processed. When the BCB layer is thin, it becomes more difficult to obtain a uniform thickness distribution. This can interfere with the subsequent processing steps. Therefore, a thicker layer of BCB eases the fabrication.

In grating-assisted coupling, the photodiode is placed on top of a grating coupler that diffracts the light upwards. For this design, a thicker BCB layer poses no problem. In the case of evanescent coupling, the BCB layer needs to be thin ($< 0.6\mu m$), so that the waveguide mode can efficiently couple to the III-V stack. In addition, a long interaction length is needed to couple all of the light into the absorbing layer. For butt coupling, a short photodiode length is sufficient to obtain efficient detection, but the fabrication is more complex given the extra polymer taper and alignment requirements. The advantage of both butt coupling and evanescent coupling is the broadband operation. In the case of grating-assisted photodiodes, we are limited by the bandwidth of the grating coupler.

High fabrication uniformity can be achieved for photodiodes that are simultaneously processed within a limited area. Thus, to ensure high fab-

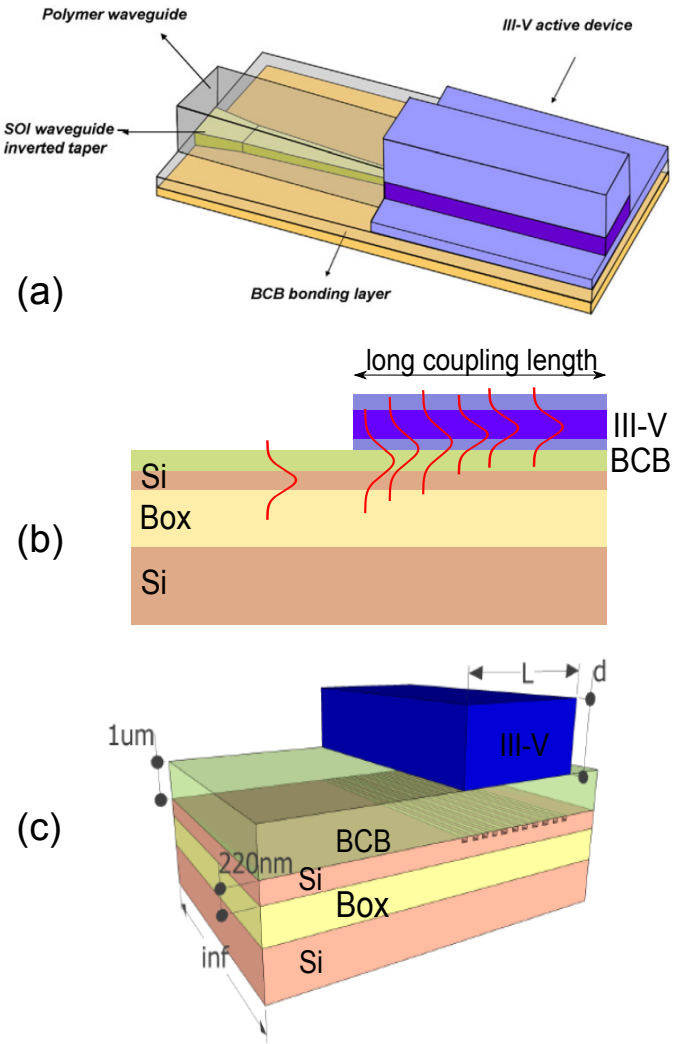

Figure 5.19: (a) Butt-coupled photodetectors (from [41]) (b) Schematic of the evanescent coupling mechanism (b) Schematic of the grating-assisted coupling mechanism (from [40]).

rication uniformity for our integrated spectrometers we should place the grating-assisted photodiodes closely together. However, a tight packing of the spectrometer's output grating couplers might lead to unwanted cross-talk due to stray light. Therefore, the grating coupler spacing was set to a safe 75 μm.

5.3.4 GaInAsSb photodiodes

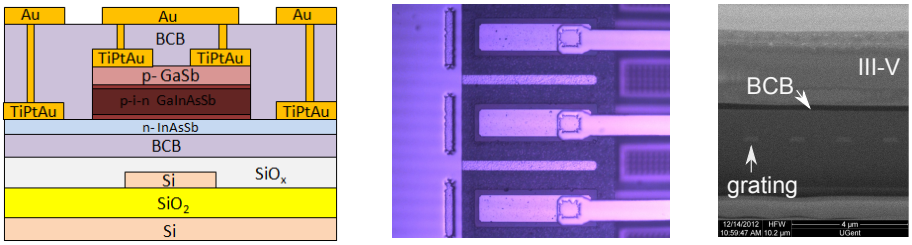

Figure 5.20: (a) Layer stack used for the integrated photodetectors. (b) microscope picture of the fabricated GaInAsSb photodiode array (c) SEM cross-section of the photodiode.

In the first fabrication run, GaSb-based photodiodes are bonded on top of the grating couplers of the four PCG designs that were discussed in section 5.2.4. The epi-design and fabrication of the integrated GaInAsSb photodiode array was done by respectively N. Hattasan and A. Gassenq. In the doctoral thesis of N. Hattassan[40], detailed information about the heterogenous integration of GaSb onto silicon wafers can be found.
The active photodetector material is a quaternary GaInAsSb epitaxial layer stack, grown by molecular beam epitaxy on a GaSb substrate [44]. This material, and GaSb compounds in general have proven to be excellent semiconductor materials for the short-wave infrared (SWIR, 2 - 3.5 μ m)[45, 46]. The used III-V epi-stack has a bandgap wavelength of 2.65 μm at room temperature and is shown in figure 5.20. The epitaxial stack is made using a reversed stack growth. It consists of a 50 nm thick p-doped (1.0x10^{18} cm^{-3}) GaSb and a 50 nm p-doped (1.0x10^{18} cm^{-3}) $Ga_{0.79}In_{0.21}As_{0.19}Sb_{0.81}$ layer as the p-zone of a p-i-n layer stack. A not intentionally doped 500 nm thick $Ga_{0.79}In_{0.21}As_{0.19}Sb_{0.81}$ layer is used for the intrinsic absorbing region. The n-type region consists of 80 nm $Ga_{0.79}In_{0.21}As_{0.19}Sb_{0.81}$ and 80 nm of $InAs_{0.91}Sb_{0.09}$. Both are doped to 1.0x10^{18} cm^{-3}. A grading layer of 40nm is used between $Ga_{0.79}In_{0.21}As_{0.19}Sb_{0.81}$ and $InAs_{0.91}Sb_{0.09}$. The fabrication details of both the epi-stack and bonding procedure can be found in [45].

Electro-optical characterization

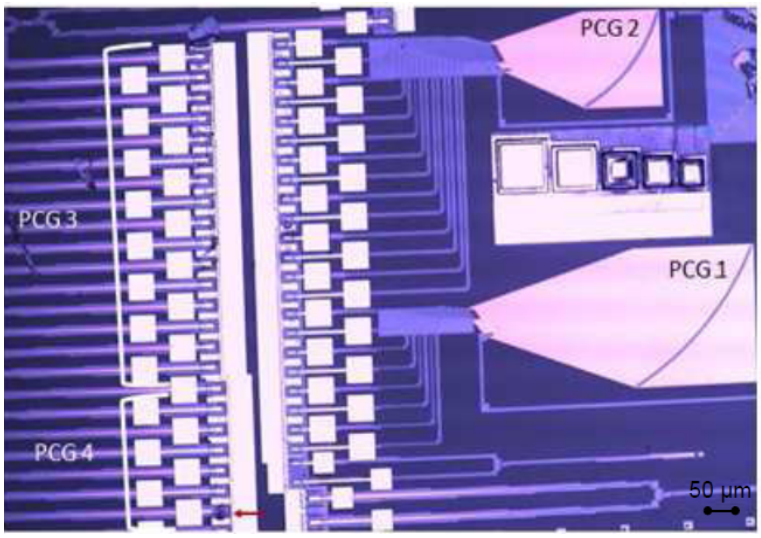

Figure 5.21: Microscope picture of the GaInAsSb photodiode array on top of the output grating couplers of four PCGs

Figure 5.21 is a microscope picture of the fabricated spectrometer chip. To characterize the spectrometers, we use a set-up as shown in figure 5.22. Light from a laser source with tunable wavelength is split into two paths. A first path, with 1 percent of the input power, leads directly to an optical spectrum analyzer. A spectrum is taken to obtain both a wavelength and power reference of the laser input. The second path, with 99 percent of the input power, leads to the SOI chip comprising all four spectrometers. The photodetectors are individually probed for biasing and photocurrent read-out using a Keithley SourceMeter.

In a first stage, we investigated the IV-curve of the photodiodes in both the first overtone and combination band. A total of 46 photodiodes were characterized with a failure of only 2 photodiodes. This proves the robustness of the fabrication process. The mean photodiode dark current at room temperature at a bias voltage of -1 V is around -2.5 μA for a mesa size of 17x50 μm^2 and -3 μA for a mesa size of 26x64 μm^2. The I-V curves for a photodiode for various input power levels at a wavelength of 1530 nm and 2324 nm are displayed in figure 5.23. The input power as set in the top X-axis, is calibrated for polarization and on-chip losses (grating efficiency, waveguide loss and PCG insertion loss), whereas the inset contains the laser power before entering the optical chip. We obtain an on-chip re-

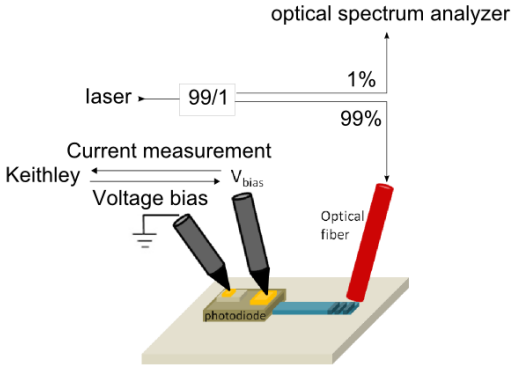

Figure 5.22: Schematic of the measurement set-up for the electro-optical characterization of the photodiodes.

sponsivity of 0.61 A/W at the bias voltage of -0.5 V for $\lambda = 1530$ nm. For $\lambda = 2324$ nm, we obtain an on-chip responsivity of 0.7 A/W at a bias voltage of -0.5 V.

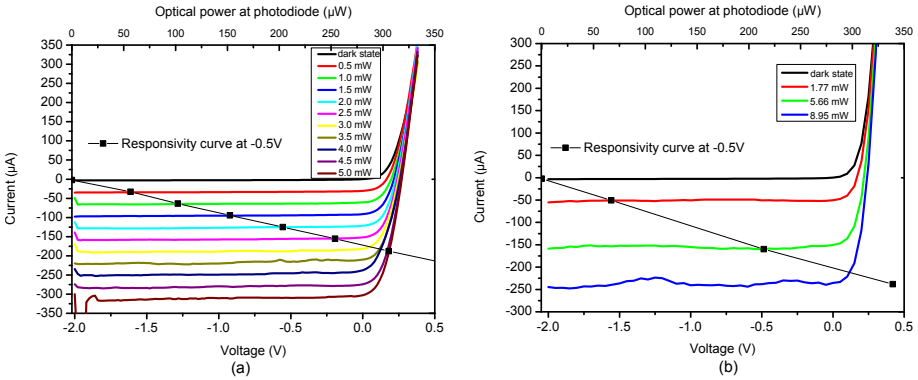

Figure 5.23: IV-curves for an integrated GaInAsSb photodiode at a wavelength of 1530 nm (a) and 2324 nm (b) at different input power levels. The inset contains the laser power before entering the optical chip. The top X-axis refers to the optical power at the input of the grating coupler with integrated photodiode.

We also studied the photodiode detectivity D* and NEP at zero bias and at room temperature. In this case, the photodiode noise is limited by Johnson noise, hence we can write the detectivity D* as [47]:

$$D^* = \Re\sqrt{\frac{R_0 A}{4kT}} \tag{5.9}$$

with R_0 the photodiode resistance at zero bias and A the mesa size of

the photodiode. For the photodiode in the first overtone band, we obtain a R_0A product of 0.40 Ωcm^2, a detectivity of D*= 3.04e^9 $cm\frac{\sqrt{Hz}}{W}$ and NEP=$\frac{1}{\Re}\sqrt{\frac{4kT}{R_0}}$=9.59e^{-13} $\frac{W}{\sqrt{Hz}}$. For the combination band photodiode, we obtain R_0A=0.52 Ωcm^2, D*= 3.98e^9 $cm\frac{\sqrt{Hz}}{W}$ and NEP=1.02e^{-12} $\frac{W}{\sqrt{Hz}}$. These detectivity values are slightly lower than for non-integrated p-i-n GaInAsSb-based photodiodes reported in literature e.g. D* =2.4 $\times$ 10^{10} [48] and D* =9.0 $\times$ 10^{10} [49]. In the doctoral thesis of N. Hattasan [40] it is discussed how the photodiode performance can be improved with optimization of the fabrication process.

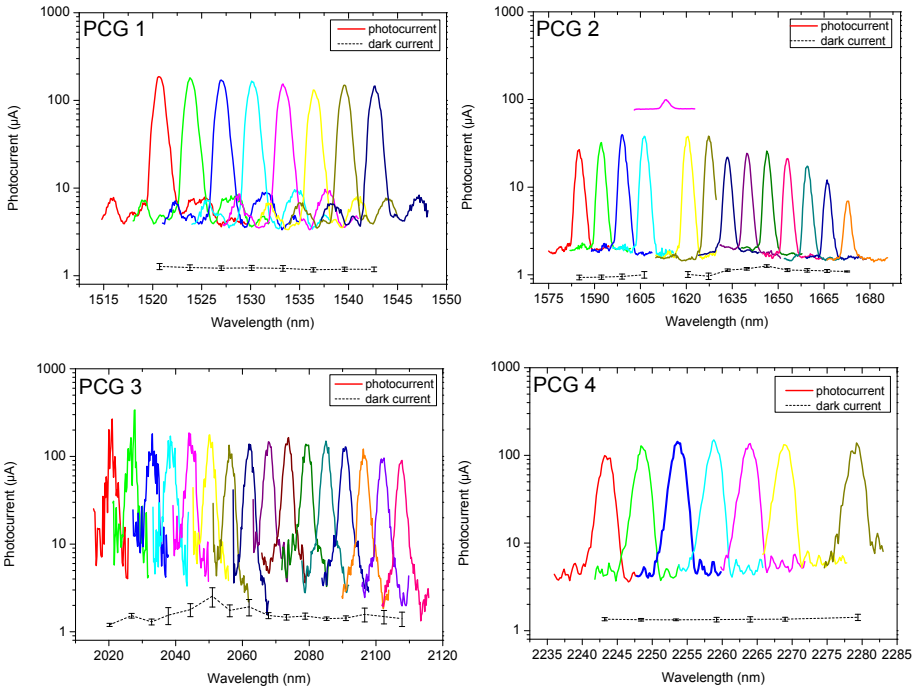

Figure 5.24: Photocurrent versus wavelength for the different PCG channels with integrated GaInAsSb photodiodes

In a second stage, we measured the photo-current for all spectrometer channels at a fixed bias of -0.1V. For every spectrometer channel, the laser is tuned with a wavelength step of 250 pm. A total of three different tunable lasers (TL) were needed to complete the measurement. For PCG1 and the first 7 channels of PCG2 a Santec TL(1510-1630nm) is used. The remaining 7 channels of PCG2 are measured with a Toptica DL100pro TL (1600-1750nm). Both PCG3 and PCG4 are measured with a SFTL-Cr-ZnS/Se-

2300-5000 TL from IPG Photonics (2000-2400nm). At the shorter wavelengths (2000-2050 nm), this laser is unstable on a time-scale shorter than the OSA spectrum acquisition time, therefore impacting the smoothness of the photocurrent measurement. In figure 5.24 the results of the electro-optical characterization is shown.
Remark that it is a different SOI chip than the one used for the passive demultiplexer characterization in section 5.2.4, therefore an exact comparison of the losses was not possible. The photo-current is corrected for the input grating coupler and calibrated for a constant injected power of 1 mW at all wavelengths. The losses in the spiral waveguide, that preceeds PCG2 and PCG3, are not corrected for. Thus, the resulting photo-current is the photo-current that is measured when a constant input power of 1 mW at the entrance waveguide goes through the spiral waveguide and PCG to the photodetector. The rms dark current of the respective photodetectors is indicated by the green line. We note two outliers. The first outlier is the fifth photodiode of PCG2. It has a very high dark current (>1000 μA) but is clearly responsive to light. It was added to the graph by reducing its photoresponse value by 1000 μA. The second outlier is the seventh photodiode from PCG4, which behaves as an open circuit. The performance of PCG1, 3, 4 is similar, whereas PCG2 has a lower photocurrent. We attribute this to the preceding spiral waveguide that was slightly damaged during fabrication. Although care was taken to provide a proper calibration, there is an amplitude discrepancy between the channels measured with the Santec TL and the Toptica TL. This is due to a slight deviation in the optical set-up between both measurements. The dark current at the low bias voltage of -0.1V is generally constant and below 2μA over the whole wavelength range. A maximum crosstalk level of -10 dB is obtained for all spectrometers.

Influence crosstalk level on the glucose spectrum

The crosstalk of the integrated spectrometer will impact the glucose detection limit. To show this, we simulated the 5.5 mM glucose absorption spectrum (1 cm path length, Γ=0.1, λ_{center}=1590 nm) that would be measured with a 30-channel, 3 nm resolution integrated spectrometer with various crosstalk levels. The spectrometer channel response is assumed identical for all channels and is set to the measured response of the first channel of PCG 1 with GaSb photodiodes. In figure 5.25, we show how the spectral shape $P(\lambda)/P(1590nm)$ changes for different crosstalk levels ranging from -10 dB to -40 dB. It is clear that the spectral features become stronger with lower crosstalk. Of course the impact of crosstalk also depends on the number of channels as the amount of power from neighbouring channels scales with the number of channels. When a large spectral range is probed it thus important to reduce the spectrometer crosstalk. As the dominant origin of crosstalk in our spectrometers is caused by phase errors due to a

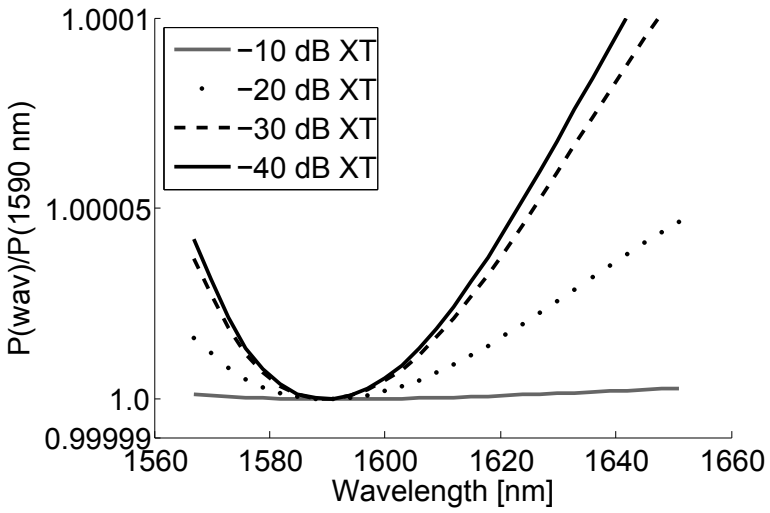

Figure 5.25: Simulated change in the glucose absorption spectrum due to change in the crosstalk level of the 30-channel, 3 nm resolution, integrated SOI spectrometer.

non-uniform slab thickness, an improved fabrication process is necessary to enhance the performance.

5.3.5 InP photodiodes

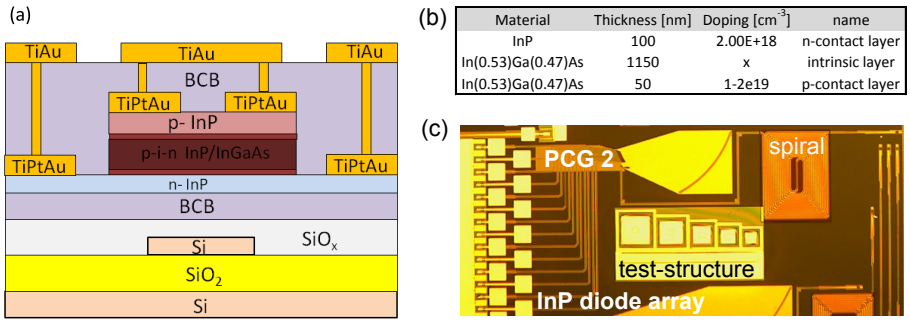

Material	Thickness [nm]	Doping [cm^{-3}]	name
InP	100	2.00E+18	n-contact layer
In(0.53)Ga(0.47)As	1150	x	intrinsic layer
In(0.53)Ga(0.47)As	50	1-2e19	p-contact layer

Figure 5.26: (a) Layer stack used for the integrated InP photodetectors.(b) P-i-N thickness and doping profile (c) Microscope picture of the InP photodiode array on top of PCG2. The preceding spiral is clearly visible.

In the second fabrication run, InP photodiodes were integrated by Steven Verstuyft on the same optical design with PCGs. The same contact mask was used for both fabrication runs, hence the photodiode dimensions were

identical. More information about the fabrication process can be found in [50]. The photodiode stack is shown in figure 5.26(a,b) and the fabrication result in figure 5.26(c). The average dark current of these photodiodes was relatively low, 3.4 nA at a bias voltage of -0.4V for a mesa size of 26x64 μm^2. The average responsivity of the photodiodes at a wavelength of 1610 nm was 0.44 A/W. In addition, we calculated the detectivity and NEP at zero bias for these photodiodes. We obtain an average R_0A of 141.93 Ωcm^2, D*= 4.12e^{10} $cm\frac{\sqrt{Hz}}{W}$ and NEP=1.37e^{-13} $\frac{W}{\sqrt{Hz}}$.

5.4 Sensing experiments

In this section, we discuss the detection experiments that we performed to test the miniature spectrometers with evanescent spiral, PCG wavelength demultiplexer and integrated photodiode array. To enable parallel read-out of the individual photodiodes, we designed an electrical read-out circuitry for a probe card. Two detection experiments were performed with this probe card: one with InP photodiodes in the first overtone band and one with GaInAsSb photodiodes in the combination band.

5.4.1 Probe card read-out

The probe card (from accuprobe®) contains a set of flexible probe needles with a tip diameter of 25.4 μm. These probes are mounted such that each probe fits onto the top contact pad (100 x 100 μm^2) of a single photodiode. Four additional probes are added to access the common bottom contact. A pin header is used for the electrical connections to the individual probes. To realize parallel read-out of the photodiodes, we designed (with the help of Jeroen Allaert) and soldered a custom PCB board with transimpedance amplifiers (TIA) to convert the photo-current from the probe needles into a 'photo-voltage'. These voltages can then be read in parallel by a data acquisition card (DAQ, National instruments). In addition, the DAQ can set the bias voltage across the photo-diodes. Using python code, we can automatically sweep the bias voltage and read-out the photo-voltages from the DAQ. The measurement set-up is shown in figure 5.27. The PCB board is mounted onto the probe card. The opamp ICs are fed by an external voltage supply (not shown).

To estimate the electrical noise of this set-up, we modulated the bias-voltage and did fourier analysis of the detected photodiode signal. A strong white noise contribution was found with an extinction ratio of only 18 dB compared to the modulated frequency component. To estimate the SNR ratio of the complete set-up, we measured the photo-current of the central PCG channel with InP photodiode ($\lambda = 1626nm$) during 10 minutes and calculated the SNR as the average current divided by the standard deviation.

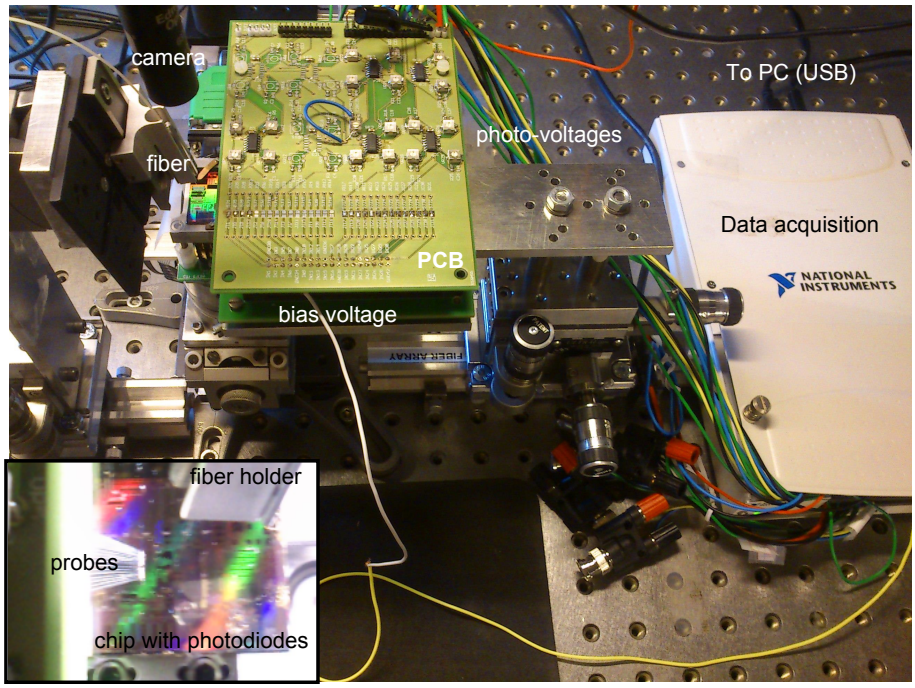

Figure 5.27: Measurement set-up for the parallel read-out of integrated photodiodes with a probe card

We obtain an SNR of 26.62 dB and 26.55 dB for respectively a SLED source and a tunable laser source. This SNR is obtained for an estimated optical power of 12 μW at the photodiode.

5.4.2 PEG detection

In the first experiment with the probe card read-out (at room temperature), we applied PEG to the 1.7 cm long 500 nm wide wire waveguide that precedes PCG2. The miniature spectrometer is illuminated with a broadband SLED source centered at 1650nm. The result is shown in figure 5.28. We calculated the PEG transmission as the ratio between the photovoltage at each InP photodiode with PEG and without (red dots). This gives a few points that we can interpolate with cubic splines (grey curve). We compare our measurement with the signal (black dots) that we expect based on the confinement factor of a 500 nm wire waveguide immersed in PEG (n=1.47), the length of the spiral and the absorptivity that we measured using an FTIR $\delta\lambda = 1nm$. We obtain a relatively good match. Because the PCG channels are not aligned to the PEG dip at 1620 nm, and the low PCG resolution ($\delta\lambda = 7nm$), the PEG feature is broadened and the power at 1620

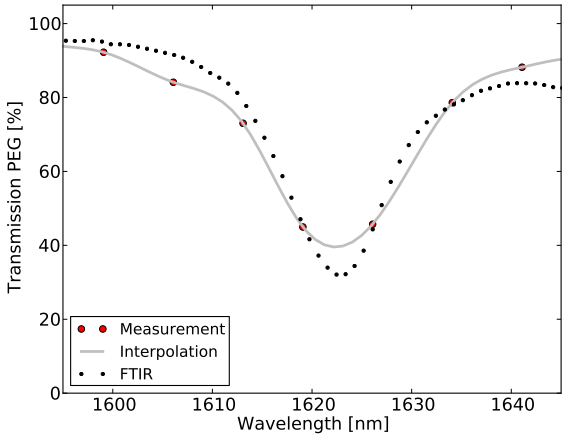

Figure 5.28: Evanescent PEG detection with a miniature SOI spectrometer with InP photodiode array

nm is not properly resolved.

5.4.3 Water detection

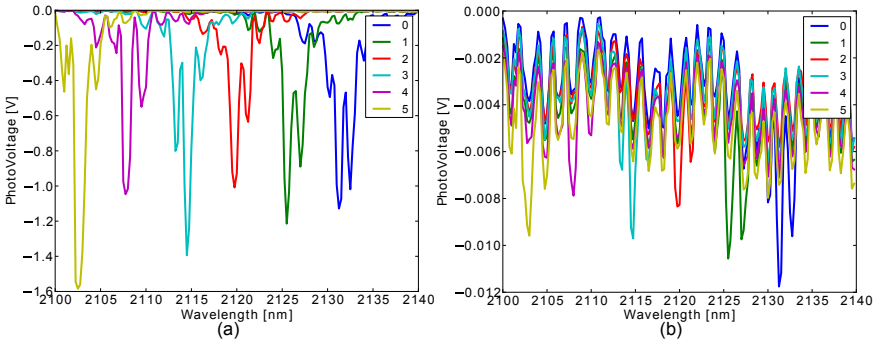

Figure 5.29: Evanescent water detection with a miniature SOI spectrometer with GaSb photodiode array. Photo-voltage in function of wavelength when the sensing spiral is (a) empty (b) immersed in water.

In a second experiment, also at room temperature, we applied water to the 1 cm long 800 nm wide wire waveguide that precedes PCG3. In this case, we measured the chip with a tunable laser with operating range from 2050 nm to 2350 nm onwards. At the shorter wavelengths, the laser source is

highly unstable, therefore we monitored only the spectrometer channels from 2100 nm onwards. The spectrally resolved photodiode photovoltage for both an air clad and water clad spiral is shown in figure 5.29(a,b). When we apply water, we find the expected strong attenuation given the long spiral length. Now, the impact of the spectral ripple due to the coherent source in combination with on-chip reflections, becomes very clear. To calculate the transmission, we simply took the average of the peak photovoltages and interpolated this with third order splines. To compare with the theorically expected water spectrum, we calculate the expected shape based on the simulated confinement factor Γ, spiral length and absorptivity of water that we measured using an spectrophotometer (Varian Cary 500) with $\delta\lambda = 1nm$. The result is shown in figure 5.30. Although there is a difference in absolute transmission, the upward trend of the water transmission with wavelength is clearly visible.

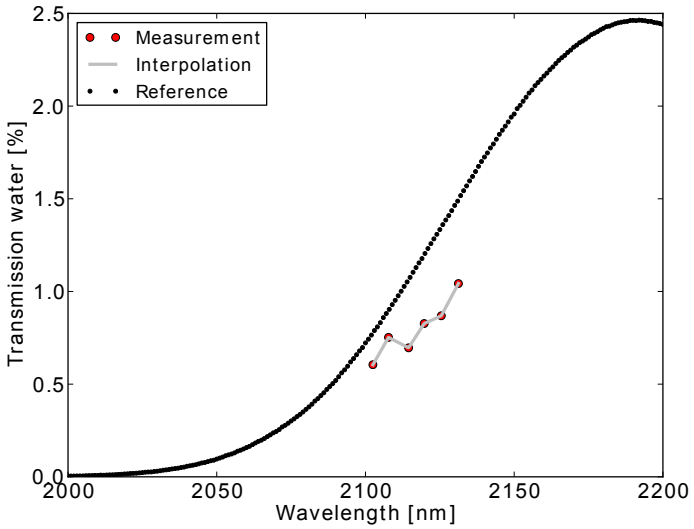

Figure 5.30: Measured water transmission with a miniature SOI spectrometer with GaSb photodiode array

5.5 Integration with CMOS electronics

The final stage of the miniature spectrometer development was to replace the probe card read-out with an electronic driver chip. This work was part of the final demonstrator for the GlucoSens project. As many people were involved in the development of this demonstrator, the results on this demonstrator are added to the appendix (see section A.2).

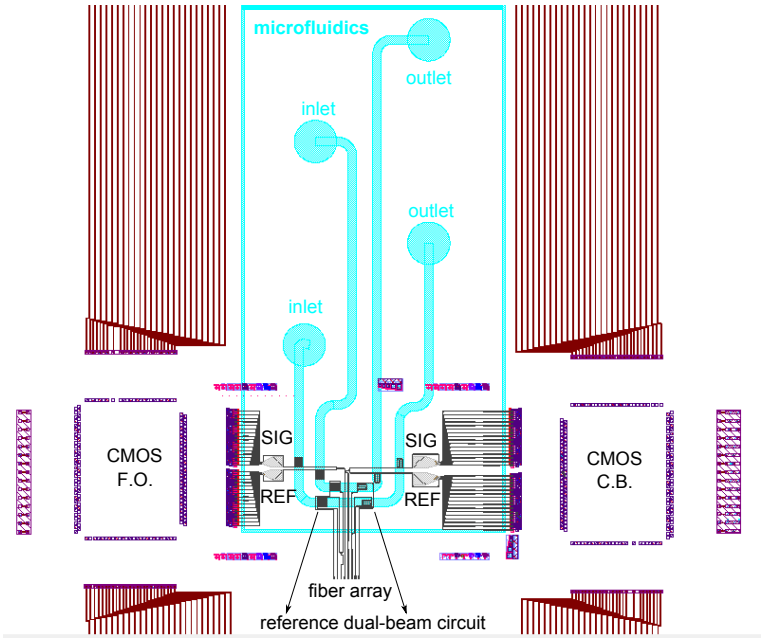

Figure 5.31: GlucoSens demo 4: Mask design for the passive SOI spectrometer, photodiode array, electrical wiring and microfluidics

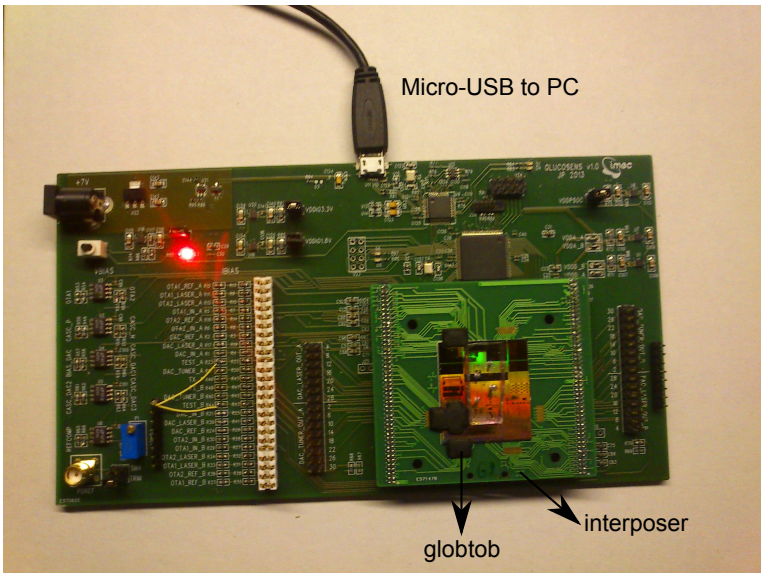

Figure 5.32: GlucoSens demo 4: micro-controller board with interposer containing the fabricated miniature spectrometer

The demonstrator combines an SOI chip with integrated photodiodes, microfluidics and a die-bonded CMOS (Complementary Metal Oxide Semiconductor) chip. The optical circuit comprises two dual-beam spectrometers with preceding evanescent sensor and photodiode array. The optical circuit is shown in figure 5.31. A microfluidics circuit in PDMS was designed and fabricated as well, to enable fast and easy switching of various sample fluids. The resulting demonstrator is shown in figure 5.32.

5.6 Conclusion

In this chapter we reported on the design and fabrication of miniature spectrometers on the silicon-on-insulator platform. Our efforts were focused on the implementation of planar concave gratings (PCG) as the wavelength demultiplexer. This component is well-known for telecom applications. However, for molecular detection, and glucose sensing in particular, it was necessary to extend the operating wavelength range to the combination band. This required a set of other components to be designed as well for these longer wavelengths. Next to the development of the passive components (grating couplers, evanescent spiral and wavelength demultiplexer), three active features were added to the SOI chip. Firstly, microfluidics in poly-dimethyl siloxane (PDMS) was bonded to the spectrometer chip, to allow easy sample handling. Secondly, heterogeneously integrated photodiodes were added to each of the different wavelength demultiplexer channels. By using GaSb-based epitaxial material, these photodiodes could be used for PCG designs with an operating range in both the first overtone band and combination band. Lastly, an electronic driver CMOS chip was die-bonded to the SOI with photodiode array. Although a new iteration is necessary, co-integration of an electronic CMOS chip with the spectrometer for photodiode read-out was shown to be technologically feasible. In the end, the investigation of this silicon-based spectrometer platform, led to a set of successful molecular sensing experiments in both the first overtone band and combination band.

References

[1] Joost Brouckaert. *Integration of Photodetectors on Silicon Photonic Integrated Circuits (PICs) for Spectroscopic Applications*. PhD thesis, Photonics Research Group, University of Ghent, 2010.

[2] Wenhui Wang, Yanzhe Tang, Yunxiang Wang, Hongchang Qu, Yaming Wu, Tie Li, Jianyi Yang, Yuelin Wang, and Ming Liu. *Etched-diffraction-grating-based planar waveguide demultiplexer on silicon-on-insulator*. Optical and quantum electronics, 36(6):559–566, 2004.

[3] Joost Brouckaert, Wim Bogaerts, Pieter Dumon, Dries Van Thourhout, and Roel Baets. *Planar concave grating demultiplexer fabricated on a nanophotonic silicon-on-insulator platform*. Lightwave Technology, Journal of, 25(5):1269–1275, 2007.

[4] Joost Brouckaert, Wim Bogaerts, S Selvaraja, P Dumon, Roel Baets, and D Van Thourhout. *Planar concave grating demultiplexer with high reflective Bragg reflector facets*. Photonics Technology Letters, IEEE, 20(4):309–311, 2008.

[5] Xiao Ma, Mingyu Li, and J He. *CMOS-Compatible Integrated Spectrometer Based on Echelle Diffraction Grating and MSM Photodetector Array*. 5(2), 2013.

[6] Jun Song and Ning Zhu. *Design and fabrication of compact etched diffraction grating demultiplexers based on α-Si nanowire technology*. Electronics Letters, 44(13):816–818, 2008.

[7] Jun Song, Xiang Zhou, Yuan-zhou Li, and Xuan Li. *On-chip spectrometer with a circular-hole defect for optical sensing applications*. Optics express, 20(17):19226–19231, 2012.

[8] GW Stroke. *Attainment of high efficiencies in blazed optical gratings by avoiding polarisation in the diffracted light*. Physics Letters, 5(1):45–48, 1963.

[9] Meint K Smit. *New focusing and dispersive planar component based on an optical phased array*. Electronics Letters, 24(7):385–386, 1988.

[10] Meint K Smit and Cor Van Dam. *PHASAR-based WDM-devices: Principles, design and applications*. IEEE Journal of Selected Topics in Quantum Electronics, 2(2):236–250, 1996.

[11] Tatsuhiko Fukazawa, Fumiaki Ohno, and Toshihiko Baba. *Very compact arrayed-waveguide-grating demultiplexer using Si photonic wire waveguides*. Japanese journal of applied physics, 43(5B):L673, 2004.

[12] Daoxin Dai and Sailing He. *Novel ultracompact Si-nanowire-based arrayed-waveguide grating with microbends*. Optics express, 14(12):5260–5265, 2006.

[13] Pieter Dumon, Walter Bogaerts, Dries Van Thourhout, Dirk Taillaert, Roel Baets, J Wouters, S Beckx, and P Jaenen. *Compact wavelength router based on a silicon-on-insulator arrayed waveguide grating pigtailed to a fiber array*. Optics express, 14(2):664–669, 2006.

[14] Stanley Cheung, Tiehui Su, Katsunari Okamoto, and SJB Yoo. *Ultra-compact Silicon Photonic 512x512 25-GHz Arrayed Waveguide Grating Router*. PP(99):1–1, 2013.

[15] Shibnath Pathak, Dries Van Thourhout, and Wim Bogaerts. *Design trade-offs for silicon-on-insulator-based AWGs for (de) multiplexer applications*. Optics letters, 38(16):2961–2964, 2013.

[16] Wim Bogaerts, Shankar Kumar Selvaraja, Pieter Dumon, Joost Brouckaert, Katrien De Vos, Dries Van Thourhout, and Roel Baets. *Silicon-on-insulator spectral filters fabricated with CMOS technology*. IEEE Journal of Selected Topics in Quantum Electronics, 16(1):33–44, 2010.

[17] Shibnath Pathak, Michael Vanslembrouck, Pieter Dumon, Dries Van Thourhout, and Wim Bogaerts. *Optimized silicon AWG with flattened spectral response using an MMI aperture*. Lightwave Technology, Journal of, 31(1):87–93, 2013.

[18] Zhimin Shi and Robert W Boyd. *Fundamental limits to slow-light arrayed-waveguide-grating spectrometers*. Optics express, 21(6):7793–7798, 2013.

[19] Zhimin Shi, Robert W Boyd, Daniel J Gauthier, and CC Dudley. *Enhancing the spectral sensitivity of interferometers using slow-light media*. Optics letters, 32(8):915–917, 2007.

[20] Zhimin Shi and Robert W Boyd. *Slow-light interferometry: practical limitations to spectroscopic performance*. JOSA B, 25(12):C136–C143, 2008.

[21] Miroslaw Florjanczyk, Pavel Cheben, Siegfried Janz, Alan Scott, Brian Solheim, and Dan-Xia Xu. *Multiaperture planar waveguide spectrometer formed by arrayed Mach-Zehnder interferometers*. Optics express, 15(26):18176–18189, 2007.

[22] Miroslaw Florjanczyk, Pavel Cheben, Siegfried Janz, Boris Lamontagne, Jean Lapointe, Alan Scott, Kenneth Sinclair, Brian Solheim, and Dan-Xia Xu. *Multi-aperture Fourier spectrometers in planar waveguides*. In SPIE OPTO: Integrated Optoelectronic Devices, pages 721816–721816. International Society for Optics and Photonics, 2009.

[23] Aitor V Velasco, Pavel Cheben, Przemek J Bock, André Delâge, Jens H Schmid, Jean Lapointe, Siegfried Janz, María L Calvo, Dan-Xia Xu, Mirosław Florjańczyk, et al. *High-resolution Fourier-transform spectrometer chip with microphotonic silicon spiral waveguides*. Optics letters, 38(5):706–708, 2013.

[24] Zhixuan Xia, Ali Asghar Eftekhar, Mohammad Soltani, Babak Momeni, Qing Li, Maysamreza Chamanzar, Siva Yegnanarayanan, and Ali Adibi. *High resolution on-chip spectroscopy based on miniaturized microdonut resonators*. Optics express, 19(13):12356–12364, 2011.

[25] Günay Yurtsever and Roel Baets. *Integrated spectrometer on Silicon on Insulator*. In 16th Annual symposium of the IEEE Photonics Benelux Chapter, pages 273–276. IEEE Photonics Society, 2011.

[26] Bernardo BC Kyotoku, Long Chen, and Michal Lipson. *Sub-nm resolution cavity enhanced microspectrometer*. Optics express, 18(1):102–107, 2010.

[27] BI Akca, CR Doerr, G Sengo, K Wörhoff, M Pollnau, and RM de Ridder. *Broad-spectral-range synchronized flat-top arrayed-waveguide grating applied in a 225-channel cascaded spectrometer*. Optics express, 20(16):18313–18318, 2012.

[28] Dipak Chowdhury. *Design of low-loss and polarization-insensitive reflection grating-based planar demultiplexers*. Selected Topics in Quantum Electronics, IEEE Journal of, 6(2):233–239, 2000.

[29] Qing Ding, Gary W Small, and Mark A Arnold. *Genetic algorithm-based wavelength selection for the near-infrared determination of glucose in biological matrixes: initialization strategies and effects of spectral resolution*. Analytical chemistry, 70(21):4472–4479, 1998.

[30] Gerhard Knothe. *Rapid monitoring of transesterification and assessing biodiesel fuel quality by near-infrared spectroscopy using a fiber-optic probe*. Journal of the American Oil Chemists' Society, 76(7):795–800, 1999.

[31] Alvaro Casas Bedoya. *Design and fabrication of a miniature spectrometer-on-a-chip for Biodiesel sensing applications*. PhD thesis, Masters thesis, University of Ghent, 2009.

[32] Henry A Rowland. *On concave gratings for optical purposes*. The London, Edinburgh, and Dublin Philosophical Magazine and Journal of Science, 16(99):197–210, 1883.

[33] Albert Eagle. *On a new mounting for a concave grating*. The Astrophysical Journal, 31:120, 1910.

[34] JJ He, Emil S Koteles, B Lamontagne, L Erickson, A Delâge, and M Davies. *Polarization insensitive waveguide DEMUXes with integrated slab polarization compensator*. In Optical Fiber Communication Conference, page TuO3. Optical Society of America, 1999.

[35] Diedrik Vermeulen, Karel Van Acoleyen, Samir Ghosh, Wout De Cort, Nebiyu Adello Yebo, Elewout Hallynck, Katrien De Vos, Peter Debackere, Pieter Dumon, Wim Bogaerts, et al. *Efficient tapering to the fundamental quasi-TM mode in asymmetrical waveguides*. In 15th European conference on Integrated Optics (ECIO 2010), 2010.

[36] Aditya Malik, Muhammad Muneeb, Yosuke Shimura, Joris Van Campenhout, Roger Loo, and Gunther Roelkens. *Germanium-on-silicon planar concave grating wavelength (de) multiplexers in the mid-infrared*. Applied Physics Letters, 103(16):161119, 2013.

[37] Diedrik Vermeulen. *Ontwerp en Fabricage van een Geintegreerde Zender voor Fiber-To-The-Home (FTTH) Optische Netwerken, 6/2008*. Master's thesis, Photonics Research Group, University of Ghent, 2008.

[38] Frederik Van Laere, Tom Claes, Jonathan Schrauwen, Stijn Scheerlinck, Wim Bogaerts, Dirk Taillaert, Liam O'Faolain, Dries Van Thourhout, and Roel Baets. *Compact focusing grating couplers for silicon-on-insulator integrated circuits*. Photonics Technology Letters, IEEE, 19(23):1919–1921, 2007.

[39] Nannicha Hattasan, Bart Kuyken, Francois Leo, Eva Ryckeboer, Diedrik Vermeulen, and Günther Roelkens. *High-efficiency SOI fiber-to-chip grating couplers and low-loss waveguides for the short-wave infrared*. IEEE Photonics Technology Letters, 24(17):1536–1538, 2012.

[40] Nannicha Hattasan. *GaSb/Silicon-on-Insulator Heterogeneous Photonic Integrated Circuits for the Short-Wave Infrared*. PhD thesis, Photonics Research Group, University of Ghent, 2014.

[41] Gunther Roelkens. *Heterogeneous III-V/Silicon Photonics: Bonding Technology and Integrated Devices*. PhD thesis, Photonics Research Group, University of Ghent, 2007.

[42] Günther Roelkens, Dries Van Thourhout, Roel Baets, M Smit, et al. *Laser emission and photodetection in an InP/InGaAsP layer integrated on and coupled to a Silicon-on-Insulator waveguide circuit*. Optics Express, 14(18):8154–8159, 2006.

[43] Gunther Roelkens, Joost Brouckaert, Dirk Taillaert, Pieter Dumon, Wim Bogaerts, Dries Van Thourhout, Roel Baets, Richard Nötzel, and Meint Smit. *Integration of InP/InGaAsP photodetectors onto silicon-on-insulator waveguide circuits*. Optics Express, 13(25):10102–10108, 2005.

[44] Nannicha Hattasan, Alban Gassenq, Laurent Cerutti, Jean-Baptiste Rodriguez, Eric Tournié, and Günther Roelkens. *Heterogeneous integration of GaInAsSb pin photodiodes on a silicon-on-insulator waveguide circuit*. IEEE Photonics Technology Letters, 23(23):1760–1762, 2011.

[45] Alban Gassenq, Nannicha Hattasan, Laurent Cerutti, Jean Batiste Rodriguez, Eric Tournié, and Gunther Roelkens. *Study of evanescently-coupled and grating-assisted GaInAsSb photodiodes integrated on a silicon photonic chip*. Optics Express, 20(11):11665–11672, 2012.

[46] Nannicha Hattasan, Alban Gassenq, L Cerutti, JB Rodriguez, E Tournié, and Günther Roelkens. *GaSb-based integrated lasers and photodetectors on a Silicon-On-Insulator waveguide circuit for sensing applications in the shortwave infrared*. In Photonics Global Conference (PGC), 2012, pages 1–4. IEEE, 2012.

[47] Mohamed Henini and Manijeh Razeghi. *Handbook of infra-red detection technologies*. 2002.

[48] AP Astakhova, BE Zhurtanov, AN Imenkov, MP Mikhailova, MA Sipovskaya, ND Stoyanov, and Yu P Yakovlev. *Long-wavelength photodiodes based on n-GaSb/n-GaInAsSb/p-AlGaAsSb heterostructures*. Technical Physics Letters, 33(1):11–13, 2007.

[49] H. Shao, A. Torfi, W. Li, D. Moscicka, and W.I. Wang. *High detectivity AlGaAsSb/InGaAsSb photodetectors grown by molecular beam epitaxy with cutoff wavelength up to 2.6xa0;m*. Journal of Crystal Growth, 311(7):1893 – 1896, 2009. International Conference on Molecular Beam Epitaxy (MBE-XV) The 15th International Conference on Molecular Beam Epitaxy (MBE-XV).

[50] Zhen Sheng, Liu Liu, Joost Brouckaert, Sailing He, and Dries Van Thourhout. *InGaAs PIN photodetectors integrated on silicon-on-insulator waveguides*. Optics express, 18(2):1756–1761, 2010.

6

Glucose sensing with an integrated evanescent sensor

It always seems impossible .. until it's done.

– Nelson Mandela

As evident from previous chapters, the detection of glucose in vivo using near-infrared light is challenging. Here, in this chapter, we focus on one essential aspect: how to detect physiologically relevant glucose concentrations with an evanescent absorption sensor integrated onto a silicon chip? The physiological concentration of glucose in the interstitial fluid (ISF) is very small in comparison with the water content. Therefore, any absorption spectrum of ISF is in essence the water spectrum with all other molecular spectral signatures being at least three orders of magnitude smaller. Thus, in a first stage, we have to develop a measurement configuration that can eliminate the large water background to reveal the glucose features. This requires a measurement set-up with a high signal-to-noise ratio (SNR). Secondly, we have to show that we can measure these glucose features reliably over long periods of time. Only then, a one-to-one correspondence between the measured spectrum and the glucose concentration can be established.

A threat to the SNR and stability of the sensor is its susceptibility to noise. We define noise in this work as any physical mechanism that has a time-variable influence on the measured signal that is not related to the absorption of the measured sample. It is thus used in a broad sense: it can be a

change in temperature, a mechanical vibration, a flickering lamp etc. To minimize the impact of noise, we needed to take all aspects of the set-up into account: the mechanical, the optical, the electrical and the fluidics part. This investigation led to an optimized set-up that will be discussed in this chapter. With this optimized and fully automated set-up, we demonstrate glucose detection in aqueous solutions with an error-of-fitting of 1.14 mM, which is on par with the clinical requirement for continuous glucose monitors. In vivo, however, the sample under test is much more complex. Therefore, we also investigated glucose detection in human serum.

The chapter is structured as follows: Firstly, we explain the optical circuit and micro-fluidics layout of the opto-fluidic chip that was used for glucose detection. Secondly, we introduce the optical detection instrumentation. Thirdly, we detail on the fluidics path-way. After this introduction to the complete set-up, we continue with the experimental results section. The performance of the set-up in terms of its short- and long-term SNR is investigated and the evanescent sensing results are given. We performed evanescent sensing experiments with both aqueous solutions, salt solutions and human serum. Finally, we end this chapter with a conclusion.

6.1 Integrated opto-fluidic chip for evanescent glucose detection

In this section we discuss in detail the design and fabrication of the opto-fluidic chip that was used for the sensitive glucose detection experiments.

6.1.1 Silicon-on-insulator design

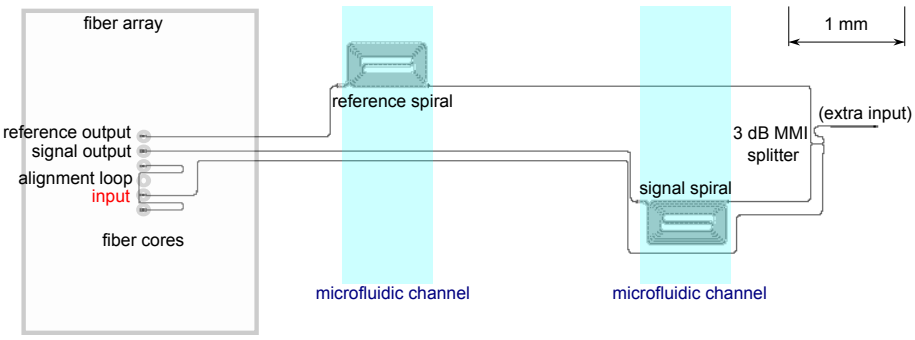

Figure 6.1: Silicon-on-insulator chip design (on-scale)

The designed and fabricated opto-fluidic chip is shown in figure 6.1. We chose for a dual-beam design to monitor any optical input fluctuations and to remove the large water background (see section 3.1.2). As in this case two outputs need to be measured in parallel, a fiber array is needed. We used a fiber array with a 127 μm pitch and a facet angle of 8°. Due to this facet angle, the fiber array can be positioned parallel with the surface of the optical chip, while a good grating coupler efficiency is preserved. In addition to the input and two output (signal and reference) grating couplers, two grating couplers are added and connected with an alignment loop for the fiber array. Proper alignment of the fiber array ensures a balanced dual-beam circuit, next to the circuit design with identical spiral sensors, equal path lengths and 3 dB splitting ratio. The fiber array is glued to the chip with UV-curable glue to enable a stable in- and out-coupling of the opto-fluidic chip.

The optical circuit is designed for a wavelength of 1.59μm, the peak absorption wavelength of glucose in the first overtone band. The straight grating couplers are designed for the quasi-TE mode and have a fill factor of 0.5, a period of 670 nm and 25 shallowly etched (70 nm) grating lines. For the evanescent sample interface, we use shallowly etched, 450 nm wide rib waveguides that are routed into a spiral with a footprint of 0.28 mm^2. The spiral is 1 cm long and has bends with a 20 μm bend radius. This length was calculated based on a simulated confinement factor of 0.07 and a waveguide loss figure of 2 dB/cm. This loss figure was estimated, as we did not have the measured loss data for this rib waveguide at the time of the mask design.

The choice for rib waveguides was based on extensive previous evanescent glucose measurements using a similar dual-beam design, but with wire waveguide spirals. Due to the sidewall roughness of the wires, distributed reflections occur all along the spiral waveguide and routing waveguides. When a coherent source is used, these reflections translate into a very dense interference pattern in the transmission spectrum. The specific pattern is very sensitive to the environment and it would require very complex digital filtering techniques to remove the unwanted frequencies. In addition, due to the 'sharp' nature of the pattern, it should be measured very precisely in both wavelength and amplitude. Small deviations in the sampling points, result in distortions of the transmission spectrum on the scale of the glucose variations (1e^{-4}). Rib waveguides are much less sensitive to these spurious reflections and are therefore preferred.

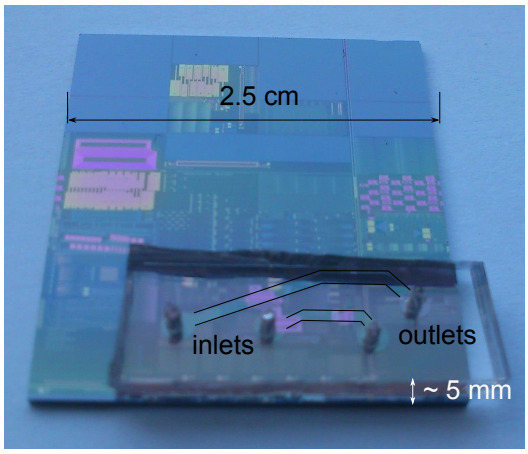

(a)

Figure 6.2: Photograph of the fabricated opto-fluidic chip. The microfluidic channels are highlighted with the black lines (the soft bends are not shown)

6.1.2 Micro-fluidics design

The micro-fluidics are fabricated in poly(dimethylsiloxane)(PDMS) (Sylgard ®184, Dow Corning Corporation) using soft lithography [1]. Both the SOI-chip and PDMS are given a short oxygen plasma treatment before applying direct bonding with a flip-chip machine [2]. The PDMS is kept relatively thin (5 mm) such that its shade doesn't block the camera's view on the alignment loop for the fiber array. The rectangular fluidic channels are 50 μm high and 780 μm wide with a bend radius of 800 μm. This large bend radius makes sure that small air-bubbles in the sample fluids cannot get trapped in the bends. The fabricated opto-fluidic chip is shown in figure 6.2.

6.1.3 Cover layer

To ensure that we exactly know the interaction length of the evanescent sensor with the sample fluids, we use SOI chips with a 1.35 μm thick top oxide cladding. To remove the oxide locally above the spirals, we first thin down the top oxide to a thickness of about 400 nm, using wet etching with a 40% b-HF (buffered Hydrogen Fluoride) solution. Then, two rectangular openings are lithographically defined (with AZ5214 photo-resist) above the two spiral sensors. Finally, the remaining oxide layer above the spirals is carefully removed with the b-HF and the remaining photo-resist is removed. For our rib waveguides with wide shallowly etch, there is no risk for under-etch of the buried oxide (see figure 6.3).

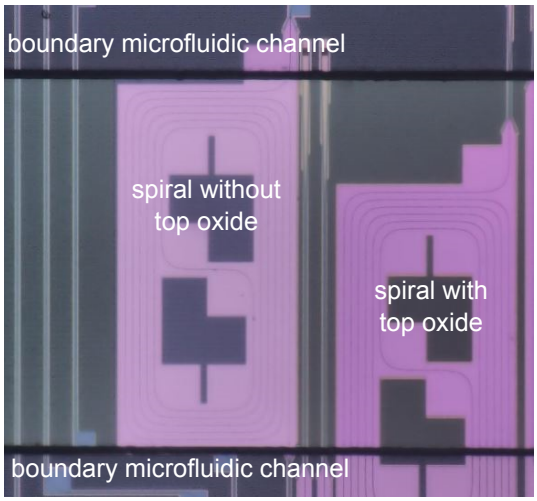

Figure 6.3: Microscope picture of a sensing spiral with and without top oxide in a microfluidic channel (green= uniform tiling region with squares of 220 nm high Si, pink=150 nm high Si)

6.2 Optical measurement configuration

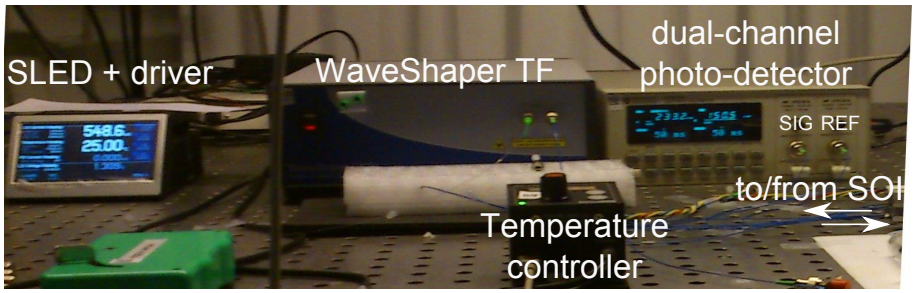

Figure 6.4: Photograph of the optical instrumentation used for the evanescent sensor read-out

In this section we discuss the optimized optical configuration for dual-beam evanescent glucose absorption spectroscopy. In figure 6.4 the optical instrumentation is shown. A broadband superluminescent light emitting diode (SLED) with a polarization maintaining output fiber (PMF) is followed by a polarization maintaining tunable filter (TF) with a gaussian pass-band. After the TF, the light is coupled in and out of the SOI chip through a fiber array with PMF. The output fibers from the signal and ref-

erence spirals are then connected to a dual-channel photodetector. To avoid any background light during experiments, a thick curtain completely encloses the optical table and all lights are switched off (including the PC screen and the lamp that is used for camera images of the opto-fluidic chip).

6.2.1 Source

Although laser sources have the advantage of higher power, we have chosen to use a broadband SLED instead of a laser source, due to its reduced coherence length. Even though we use rib waveguide spirals, the on-chip spurious reflections cannot be completely eliminated. As explained before, the impact of these reflections is larger in the case of a coherent light source. In addition, any wavelength instability of the laser between consecutive wavelength sweeps, translates into noise. To clarify this, we start from the observation that the fringe pattern from both the signal and reference arm can never be identical (due to unique side-wall roughness). For a fixed input power but a drift in lasing wavelength, it can be that the signal transmission spectrum changes shape because other points are sampled in the fringe pattern. The reference arm, however, will see a different change in transmission spectrum because the fringes look differently. The ratio of both is thus strongly dependent on the exact wavelength sampling. This will strongly limit the efficiency of the dual-beam configuration.
The total output power of the SLED that we used (SLD1005-SP, Thorlabs), is 17 mW over a 3 dB bandwidth of 50 nm with a center emission wavelength of 1570 nm.

6.2.2 Dispersive element

As we want a dual-beam configuration in combination with a broadband light source, we can either use a pre-dispersive system with a tunable filter or a post-dispersive system with two spectrum analyzers. Whereas the latter is feasible with on-chip spectrometers, it is not practical when using bulk equipment. Therefore, we opted for a tunable filter. The tunable filter that we use (Custom WaveShaper 1000s from Finisar®) is programmed (with Python) to yield a Gaussian pass band with high extinction ratio ($>$ 50 dB) and with a tunable center wavelength and bandwidth. The center wavelength can be tuned from 1535 nm to 1612 nm and the bandwidth is set to 5 nm. The tunable filter operation is based on a Liquid Crystal on Silicon (LCoS) display that can change both the phase and amplitude for each wavelength. This allows fast (settling time of 500 ms) switching between two distant wavelengths compared to grating based filters. In addition, this custom tunable filter is designed to transmit only one polarization state, while blocking the orthogonal state.

6.2.3 Photo-detectors

A dual-channel mainframe (HP 8153A) with two fiber-coupled sensitive InGaAs photodiodes is used to detect the power from both the signal and reference spiral sensor. Both channels can be measured at the same time. The photodiodes operate from 800-1700 nm and are set to an averaging time of 50 ms. In section 6.4.2, we will discuss the associated the detector noise.

6.2.4 Optical fibers

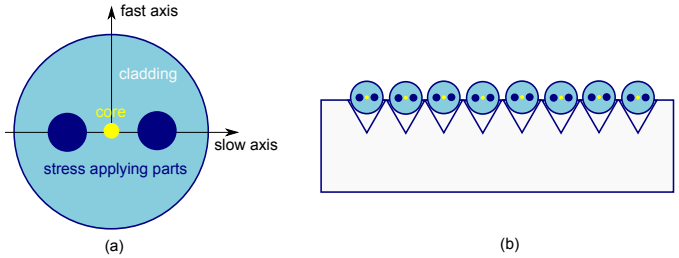

Figure 6.5: (a) Structure of the PANDA polarization maintaining fiber (b) positioning of the fibers in the fiber array

Throughout the complete optical set-up, single-mode polarization maintaining fibers (PMF) are used. This type of fiber exhibits very high birefringence such that the two orthogonal polarization states are not likely to couple, even when external stress (e.g. fiber bending) is applied. Integrated optical wires also show this high birefringence. This ensures that the incident polarization state is preserved throughout the complete optical path. We found that this significantly improves the stability of the set-up. The used PMF are PANDA fibers, see 6.5(a). The SLED output polarization is aligned with the slow axis and the WaveShaper TF only transmits light polarized along this slow axis. This polarization state should be aligned with the TE-mode of the grating coupler, therefore the PMF are positioned in the fiber array as shown in 6.5(b). In figure 6.6 we show how the fiber array is positioned above the fiber array.

6.2.5 Temperature control

The opto-fluidic chip is mounted onto a temperature controller with remote (programmable) control and kept at a fixed temperature of 25 degrees. The room where the measurements took place was, unfortunately, not temperature controlled. All sample solutions, are kept at room temperature to avoid large thermal variations in the micro-fluidic channels.

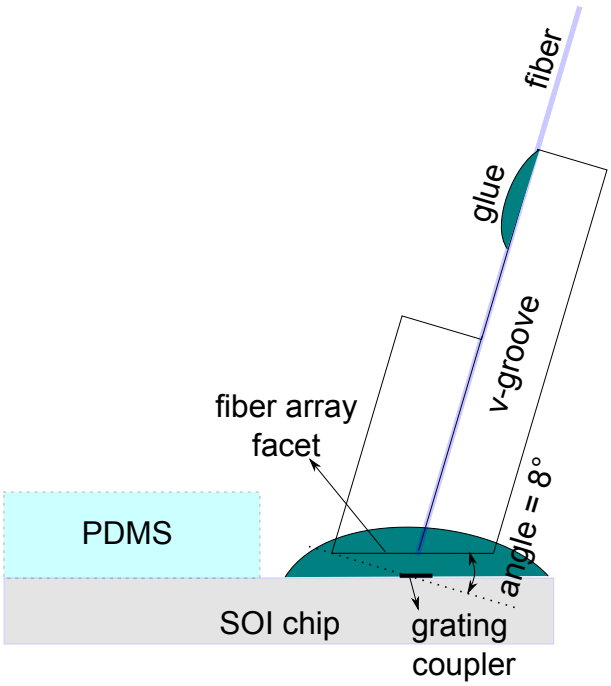

Figure 6.6: Positioning of the fiber array above the optical chip

6.3 Glucose solution preparation and handling

The fluidics pathway is shown in figure 6.7. A microfluidics pump (TSE systems) is used to pump up to 6 different syringes simultaneously. The syringe volume is 10 mL. One syringe contains the reference fluid and is connected to the reference channel of the opto-fluidic chip. This is typically the pure solvent water. The other syringes are connected to the input ports of a selection valve (C5C, Vici). This valve selects one input port and connects it internally to the single output port, whereas the other inputs are connected to a common waste port. Both the microfluidics pump and selection valve are programmable through a serial port and python code.

When the selection valve is switched, it generates a strong mechanical shock. To avoid that this mechanical vibration impacts the optical measurement, the valve is mounted onto small rubber shock absorbers. The valve output is connected to a T-connector that has one connection to the signal channel of the opto-fluidic chip and another connection to a closed valve. The latter fluidic pathway is used to translate any change in flow speed between the valve and the opto-fluidic chip, into a movement of

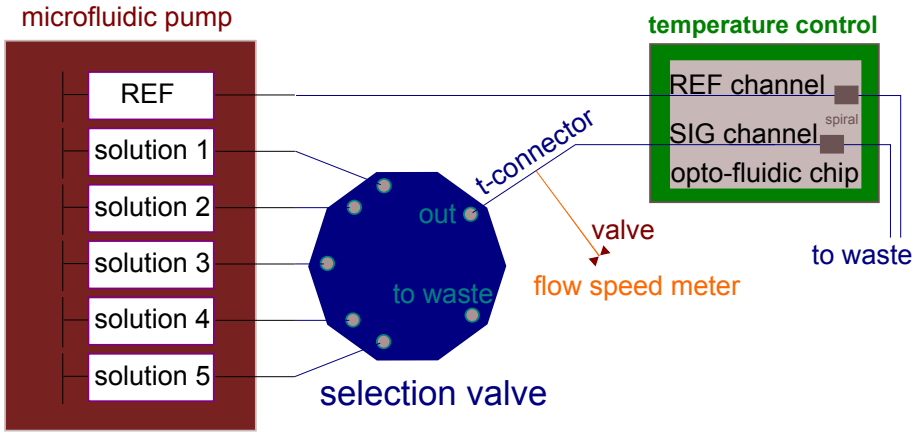

Figure 6.7: Schematic of the fluidic pathway

the fluid/air boundary in front of the closed valve. This way, we have an elementary pressure sensor. All fluidic connections are made with teflon (PTFE) tubing with a small inner diameter of 0.56 mm. This tubing fits into the inlets and outlets of the PDMS microfluidics. Care was taken to avoid any mechanical stress on these inlets and outlets of the PDMS, as this generates leaks. A picture of the set-up with fluidic connections is shown in figure 6.8.

The tubing length between the valve and the opto-fluidic chip should be minimized as mixing between consecutive solutions can occur. In addition, it creates a time delay between the moment of valve switching and the change in optical transmission.

The aqueous glucose solutions are prepared in the UGent clean room in Zwijnaarde, where D-glucose powder (Sigma-Aldrich) is added to de-ionized (DI) water to yield the wanted concentration. Similarly, salt solutions (NaCl) were prepared. Next to these aqueous solutions, we also measured in human serum. Serum solutions with different glucose concentrations were prepared by spiking it with extra glucose powder (0.18016 g/mol). The serum solutions were prepared in the UGent histology group of prof. Ria Cornelissen.

6.4 Noise analysis of the optical set-up

In this section, we report on the performance of our optical set-up in terms of signal-to-noise ratio and its sensitivity to changes in the flow speed, am-

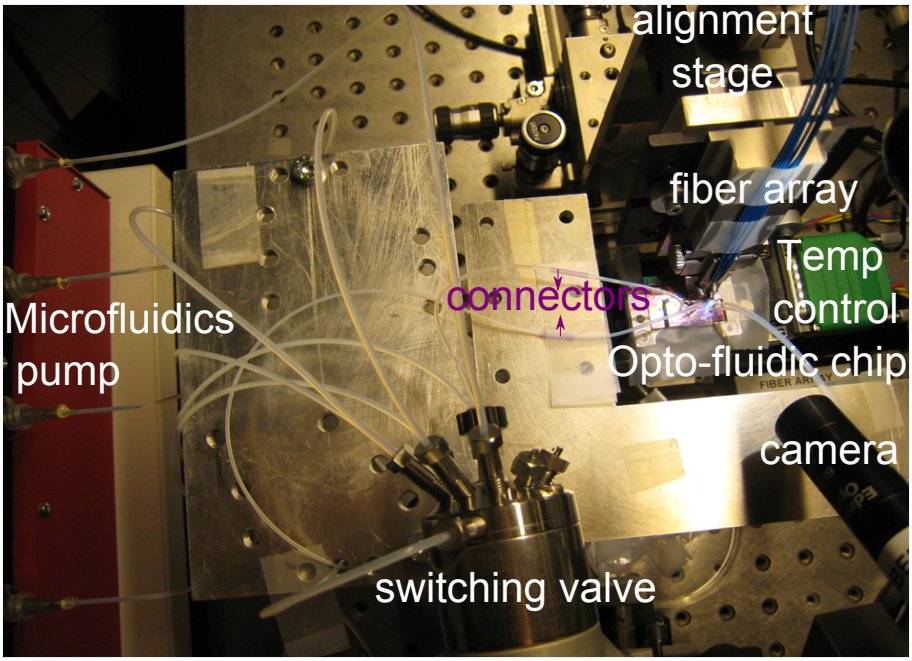

Figure 6.8: Photograph of the measurement set-up

bient temperature and optical cross-talk.

6.4.1 SNR evaluation

We calculate the signal-to-noise ratio of a set of N spectral measurements $P(\lambda)$ as:

$$SNR(\lambda) = \frac{< P(\lambda) >}{\sigma_p(\lambda)} \tag{6.1}$$

with $< P(\lambda) >$ the average detected power and $\sigma_p(\lambda)$ the standard deviation. The set-up SNR is then calculated as the average across all wavelengths SNR = $< SNR(\lambda) >$. To enable glucose detection up to the minimum level of 1 mM, the set-up should have a SNR on the order of 40 dB (see section 2.3.4). This high SNR should last for at least the time it takes to switch between two fluids (short-term SNR). On the other hand, if we want to relate the measured transmission spectrum to a glucose concentration, a large set of glucose samples needs to be measured. From these we can then derive a model. This type of measurement takes longer and slow drift effects become important. The long-term SNR is a measure for this slow-drift.

Short-term and long-term SNR

We calculate the short-term SNR for a set of transmission spectra that were acquired within 5 minutes. Within 5 minutes, we can acquire 20 spectra with a resolution of 5 nm. The long-term SNR is calculated for a total measurement time of 2 hours (480 spectra). This is our practical upper duration to measure a set of different glucose solutions with appropriate flow-speed, given the limited volume of the syringes. In table 6.1, the setup SNR is listed for both the signal channel, reference channel and the ratio (=$\frac{SIG}{REF}$) for an empty opto-fluidic chip that was measured during the night. The SNR for the ratio is calculated according to equation 6.1 in which $P(\lambda)$ is replaced by $\frac{SIG}{REF}$.

	SIG	REF	Ratio
5-min SNR [dB]	40.21	40.22	39.4
2-hour SNR [dB]	33.87	36.29	34.17

Table 6.1: SHORT-TERM AND LONG-TERM SNR

We obtain a high SNR in all cases, but two important observations can be made. Firstly, the short-term SNR is approximately equal for both single-beam and dual-beam measurements. Secondly, the long-term SNR is different for the SIG and REF channel. This points to a different slow-drift behavior in both channels.

Slow drift

To investigate the different drift in both channels, we spectrally analyzed the transmitted power drift of the opto-fluidic chip. We compare different transmission spectra that are acquired every 2.5 minutes. The result is shown in figure 6.9 and depicts the ratio of a measured transmission spectrum divided by the firstly acquired spectrum. It shows that the drift pattern of the signal and reference channel exhibits a quasi-periodic spectral behavior, but the envelope is quite different. This limits the effectiveness of our dual-beam design. We also measured the slow-drift of the fiber array alignment loop, to investigate whether this slow-drift is caused by the micro-fluidics or not (see figure 6.9(c)). The alignment loop is fully covered with oxide and is not in contact with the PDMS, but still shows a similar drift-pattern. Lastly, also the spectral slow drift of the tunable source (SLD+TF) was monitored (see figure 6.9(d)). We can see that the source pattern doesn't show the gradual change over time, but is more random. Although some peaks are visible in figure 6.9(d), they shift in location and strength when we compare source spectra at other time intervals (not shown). Based on these measurements, our current hypothesis is

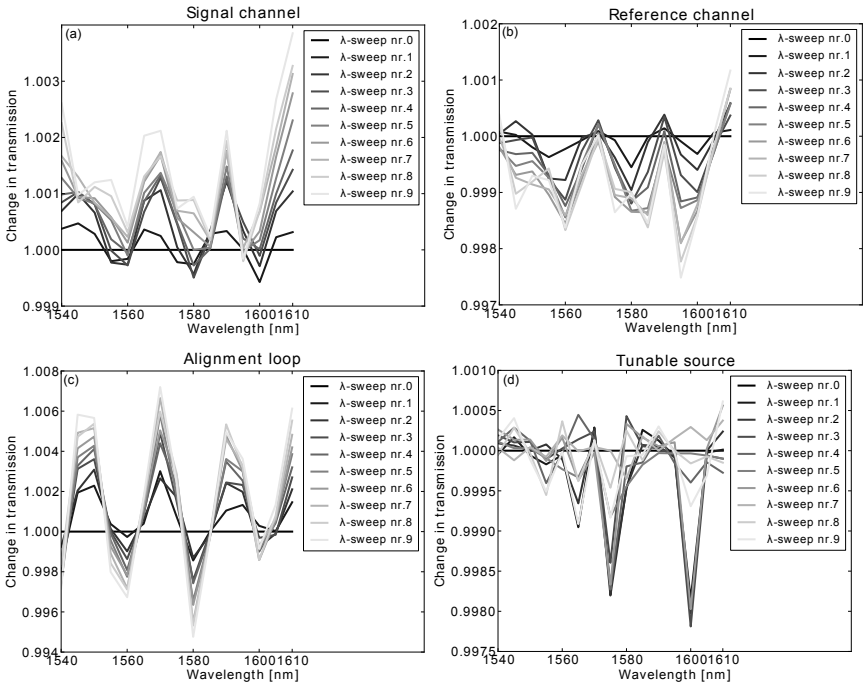

Figure 6.9: Change over time of the transmission spectrum, normalized to the firstly acquired spectrum of (a) signal channel immersed with water (b) reference channel immersed with water (c) alignment loop covered with oxide and (d) tunable source

that the slow drift doesn't originate from source fluctuations, but is related to the fiber-array to chip coupling section.

6.4.2 Noise sources

Here, we investigate the noise contributions from the source, detectors and environmental parameters.

Detector noise

The average detector signal in dark state is 1.33 pW (-88.76 dBm) with a peak-to-peak variation of 0.11 pW (-99.58 dBm). This noise-level of 0.11 pW, is the result of both the photodiode and electronics read-out noise. The averaging time of the detectors is set to 50 ms. This setting yields a low photodetector noise, while it allows fast wavelength sweeps. The

average optical power that is coupled out of the opto-fluidic chip in a wet state is 0.65μW (-31.87 dBm).

Source noise

The source of our measurement system is the SLD followed by the tunable filter. To assess the noise contribution of optical input power variations, we connected the output of the tunable filter directly to the photo-detector. The SNR is calculated to be 40.63 dB for source spectra that are acquired during 5 minutes and 38.89 dB for a 1 hour measurement. This indicates that the long-term set-up SNR is not yet limited by source intensity fluctuations.

Influence flow speed

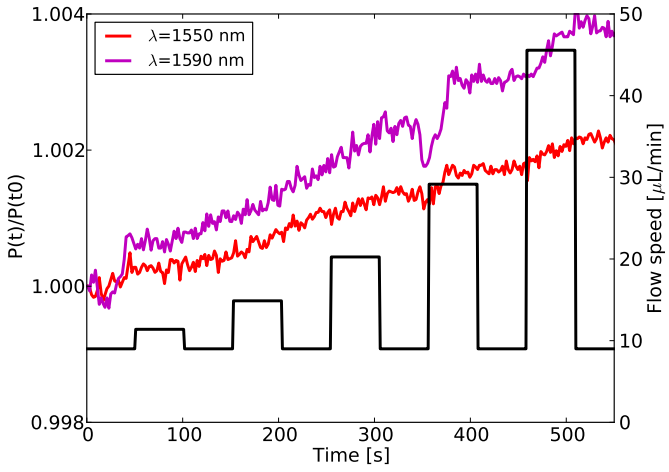

Figure 6.10: Change in optical power in function of flow speed

To assess the influence of the flow speed on our measurement, we monitored the signal channel transmission continuously, while the flow speed in the micro-fluidic channels is changed in discrete steps. The flow speed cannot be changed continuously because the pump needs to be stopped shortly before the pump speed can be altered. Two wavelengths were monitored: 1550 nm and 1590 nm. The result is shown in figure 6.10. Besides a steady upward drift, it shows that the optical transmission doesn't correlate with the flow speed. The reason for the sudden change in transmission at 350 s is unknown.

Influence temperature

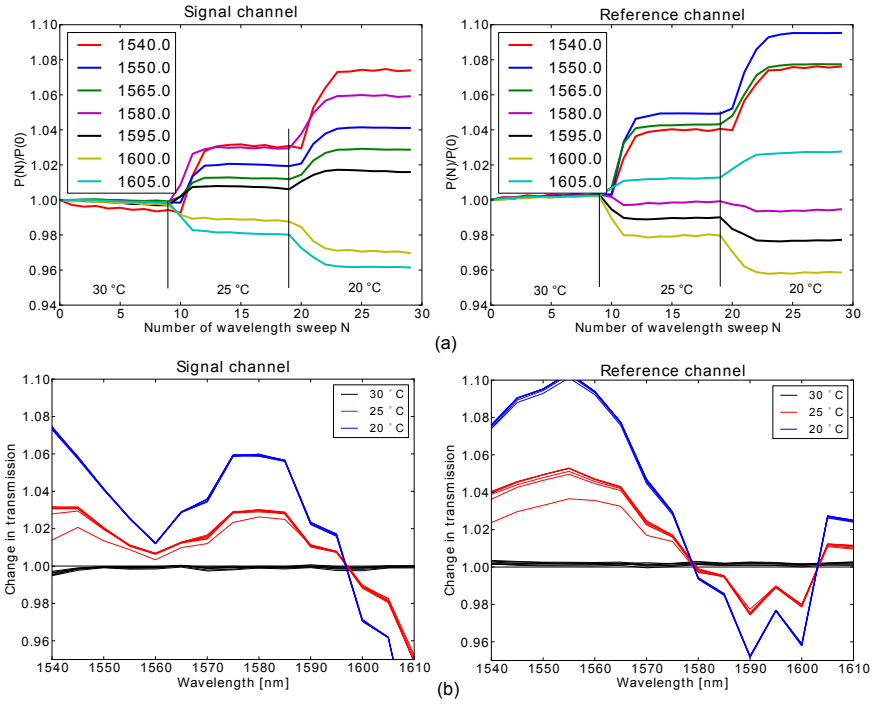

Figure 6.11: (top) Change in optical power, normalized to the initial temperature, due to a change in temperature. (bottom) Change in spectrum, normalized to the first spectrum at 20 °C, due to a change in temperature

To test the stability of the set-up for temperature changes, we monitor both the signal and reference channel of an empty optofluidic chip, while we change the temperature controller settings. The temperature is changed to three discrete values: 30 °C, 25 °C and 20 °C. The result is shown in figure 6.11(a) and is reproducible. Two observations can be made. Firstly, different wavelengths show a different response to a temperature change. Secondly, this spectral response is different for the signal and reference channel. The spectral response of both channels is plotted in figure 6.11(b). As derived in chapter 4, a change in temperature of 10°C shouldn't significantly alter the transmission through a change in effective index of the spiral waveguide mode. In addition, if the effective index would change with temperature, a linear dependency on wavelength is expected. What we measure here is clearly different. Our current hypothesis is that the fiber array alignment alters through temperature. To mechanically stabilize the fiber array, we use an UV-curable epoxy glue which is known to

be sensitive to both temperature and humidity changes. The glue can both change in shape (expansion/contraction) and change in refractive index. Small changes in the fiber array angle due to e.g. expansion of the glue can generate the measured wavelength-dependency.

Optical cross-talk

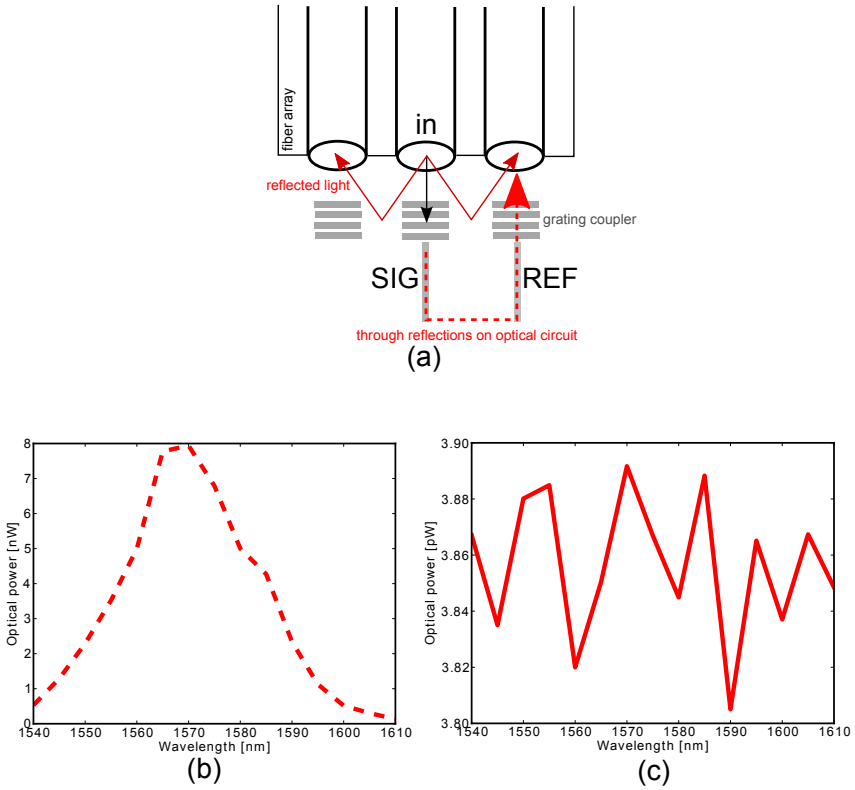

Figure 6.12: (a) Experimental layout to assess cross-talk from (b) on-chip reflections (measured at the fiber on the right of the input) and (c) reflections at the fiber array-chip interface(measured at the fiber on the left of the input)

A final noise source is optical cross-talk. Any light that is incident onto the detector that did not follow the foreseen optical path, generates noise. As we measure in complete darkness, the largest component of the optical cross-talk is light that leaks into the signal and reference output fibers at the fiber array/chip interface. We have evaluated this optical cross-talk by inserting light in the output grating coupler of the signal channel and by measuring the power in the neighboring fibers. The microfluidic channels

were filled with water. The schematic of the experiment is shown in figure 6.12(a). We find that an inserted input power (at λ=1570 nm) of -2.3 dBm generates -51.02 dBm (7.9 nW) of optical power into the reference channel output fiber and -29.1 dBm at the wanted output (not shown in figure). The spectral response of the reference channel output is shown in figure 6.12(b). As the spectral response has the shape of a grating coupler spectrum, it originates in unwanted reflections in the optical circuit. A much smaller fraction of -84.1 dBm (3.86 pW) leaks into the left neighboring fiber due to reflections at the fiber-array chip interface (see figure 6.12(c)). The relatively low extinction ratio of 21.9 dB, between the wanted signal (-29.1 dBm) and the unwanted reflections (-51.02 dBm), should be improved in future designs by using splitters and grating couplers that are optimized for low reflections [3].

6.5 Experimental results

Given the achieved high long-term SNR, we could do very sensitive evanescent absorption spectroscopy experiments of aqueous glucose, NaCl and human serum solutions. The performed experiments are listed in this section. These measurements are all dual-beam experiments, but in most cases the data analysis is performed as if the measurement was single-beam. This is due to the slow drift that is different for the signal and reference channel. This effect often results in a higher SNR for a single-beam configuration, which is also evident from table 6.1. All experimental settings and results will be discussed, in addition to the data processing algorithm.

6.5.1 Water detection

In a first experiment at room temperature, we measure the transmission spectrum of pure DI water with a resolution of 5 nm. We start from a dry opto-fluidic chip and measure the transmission spectrum of the signal and reference channel $P_{sig,air}$ and $P_{ref,air}$. Afterwards, DI water is applied to the microfluidic channel above the signal spiral to yield $P_{sig,water}$. The reference channel stays in a dry state and yields the reference spectrum $P_{ref,air2}$. The absorption due to water is then easily calculated as:

$$T_{measurement} = \frac{\frac{P_{sig,water}}{P_{ref,air2}}}{\frac{P_{sig,air}}{P_{ref,air}}} \tag{6.2}$$

In figure 6.13, we compare the obtained $T_{measurement}$ with the theoretically expected shape T_{theory}. This theoretical curve is calculated as $T_{theory} = 10^{-A_w L\Gamma}$ with the water absorbance A_w [mm^{-1}], confinement factor Γ and L= 10 mm, the length of our signal spiral. The water absorbance A_w is

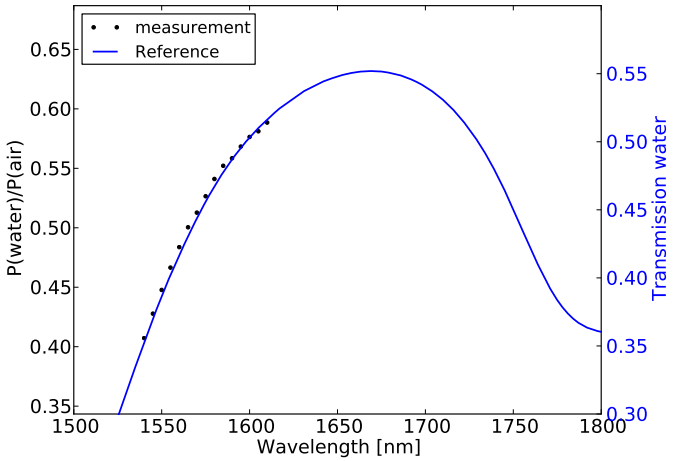

Figure 6.13: Measurement of the evanescent water absorption spectrum in comparison with the theoretically expected shape.

obtained from a reference measurement with a spectrophotometer (Varian Cary 500) at 20°C. The confinement factor Γ is simulated in function of wavelength for our rib waveguide design with a water top cladding (n_{clad}=1.31) using the software CAMFR (CAvity Modelling FRamework) as in chapter 4. Note that the y-axis scale is different for $T_{measurement}$(left y-axis) and T_{theory}(right y-axis). This shows that although the shape is similar, we have a difference in absolute transmission. This difference arises from the change in confinement factor and waveguide losses when changing between an air and water cladding and the small uncertainty about the absolute accuracy of our reference measurement.

6.5.2 Switching experiment with 70 mM glucose

In this experiment, we monitor the signal spiral and switch three times between pure DI water and a glucose solution with a high concentration of 70 mM at a steady pump speed of 9 μL/min. This way, we can estimate if we can resolve the glucose spectrum and if our measurements are reproducible. After every 14 spectral sweeps with a wavelength step of 3 nm, the selection valve is switched. It takes 30 seconds to acquire one spectral sweep. The result from the signal spiral is shown in figure 6.14(a). It shows for every spectral sweep N the transmitted power P(N) from the signal spiral, referenced to its initial value P(N=0). It is clear that the transmission drops when glucose is present, indicating the absorption due to

glucose. The small delay δN between the moment of switching and the drop in transmission is due to the finite flow-time between the valve and sensing spiral.

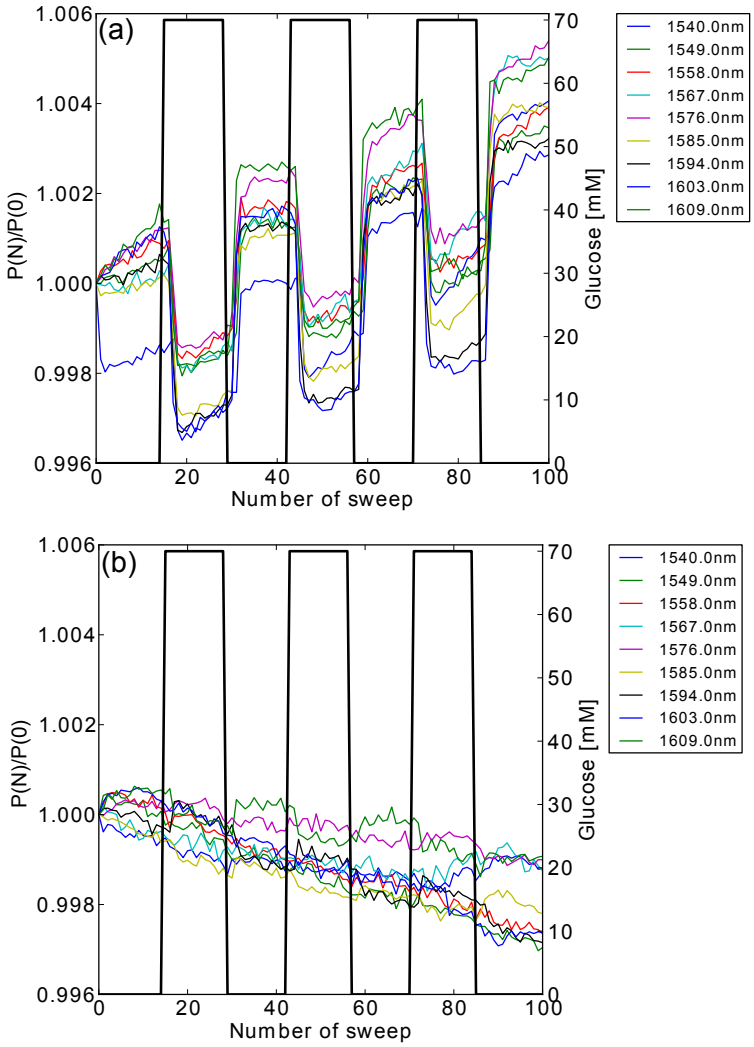

Figure 6.14: Evolution of the detected power of (a) the signal spiral and (b) the reference spiral at different wavelengths when a 70mM glucose solution is applied three times. The switching moments are indicated by the black line and the height refers to the applied glucose concentration.

Next to the absorption dips, all wavelengths experience a slow upward drift. A different drift was measured in the reference spiral transmission as shown in figure 6.14(b). This indicates that, although our set-up aims at maximizing the common path, the non-common noise is still larger than the common noise. Therefore, we opt to consider only the signal spiral for data analysis. To eliminate the slow drift, we developed a straightforward procedure that will be explained in the following section 6.5.3. After this procedure, the glucose absorption spectrum can easily be retrieved.

6.5.3 Virtual water absorption extraction procedure

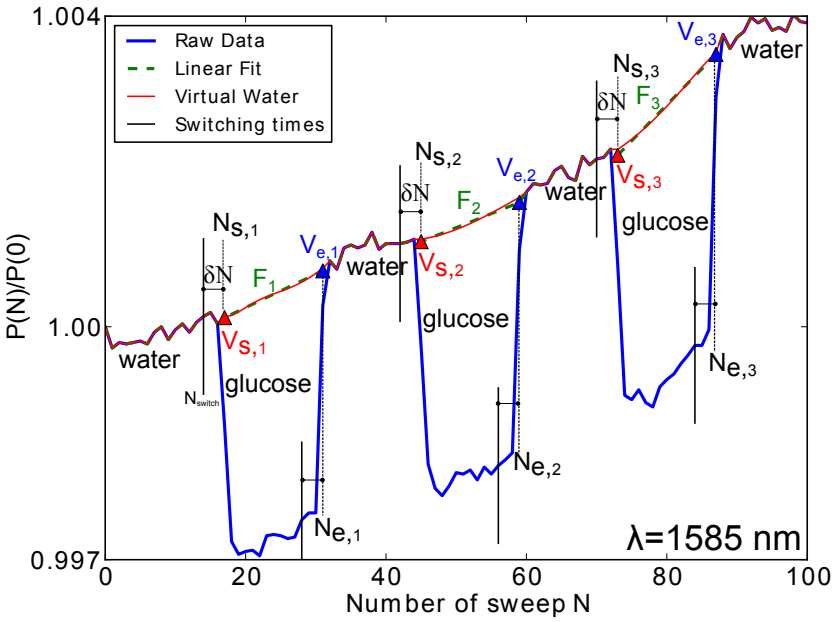

Figure 6.15: Procedure to create the virtual water reference spectrum for a single wavelength (in this case λ=1585 nm)

The strong water absorption dominates the absorption spectrum of an aqueous glucose solution. The water absorption thus has to be eliminated from our measured spectra to yield the glucose signature. We have access to the water absorption spectrum just before and after applying glucose. But, due to the wavelength dependent slow drift, as shown in figure 6.14, these measured water absorption spectra are not the same. Therefore, we need to create a 'virtual' water absorption spectrum based on the interpolation

of the water absorption spectra as measured before and after applying the glucose solution. The glucose absorption features are then revealed by dividing the measured aqueous glucose solution spectrum by the virtual water absorption spectrum.

The algorithm to create the virtual water spectrum is performed for each wavelength individually and is graphically explained in figure 6.15. Firstly, we determine the delay δN and add it to the switching times N_{switch} to yield the start and end times $N_{s,e}$ of the virtual water curve. The start point V_s of the virtual water curve is then calculated as the average of N_{avg} data points $\frac{P(N)}{P(0)}$ with N from $N_s - N_{avg}$ to N_s. The end point V_e of the virtual water is similarly calculated as $\frac{P(N)}{P(0)}$ with N from N_e to $N_e + N_{avg}$. Secondly, we fit a straight line F between V_s and V_e. We then append to this straight line a number M of data points $\frac{P(N)}{P(0)}$ from the water measurements before and after the glucose dip. Thirdly, this newly constructed curve is now interpolated with a polynomial of the appropriate order O to yield the virtual water curve. This virtual water curve thus accounts for the slow drift effects as evident in the measured water data points.

We extract the glucose absorption spectra for the experiment with the aqueous 70 mM glucose solution by dividing the measured glucose solution spectra with the virtual water curve. The virtual water curve was extracted for δN=3 (wavelength sweeps), N_{avg}=4, M=14 and O=7. For each of the three glucose dips we have about 7 glucose absorption spectra which can be averaged to yield one high SNR glucose absorption spectrum. The resulting three curves are plotted in figure 6.16 together with the theoretically expected absorption spectrum of a 70 mM glucose solution on top of a 1 cm long spiral, based on reference data from [4] as in 6.5.1.

Although our measured spectra have a strong, but repeatable, periodic variation in wavelength, we obtain a good match with the theoretically expected glucose absorption. The periodic variations are caused by unwanted on-chip cavities due to small reflections at e.g. grating couplers, MMI coupler[3, 5]. The repeatability SNR, calculated as the average of the three absorption curves divided by their standard deviation followed by wavelength-averaging, amounts to 41.95 dB.

6.5.4 Experiment with different glucose concentrations

In this experiment, we switch between five different glucose concentrations (1 mM, 5.5 mM, 16 mM, 24 mM and 36 mM) and pure DI water. The lowest concentration of 1 mM was chosen to show the detection limit. The

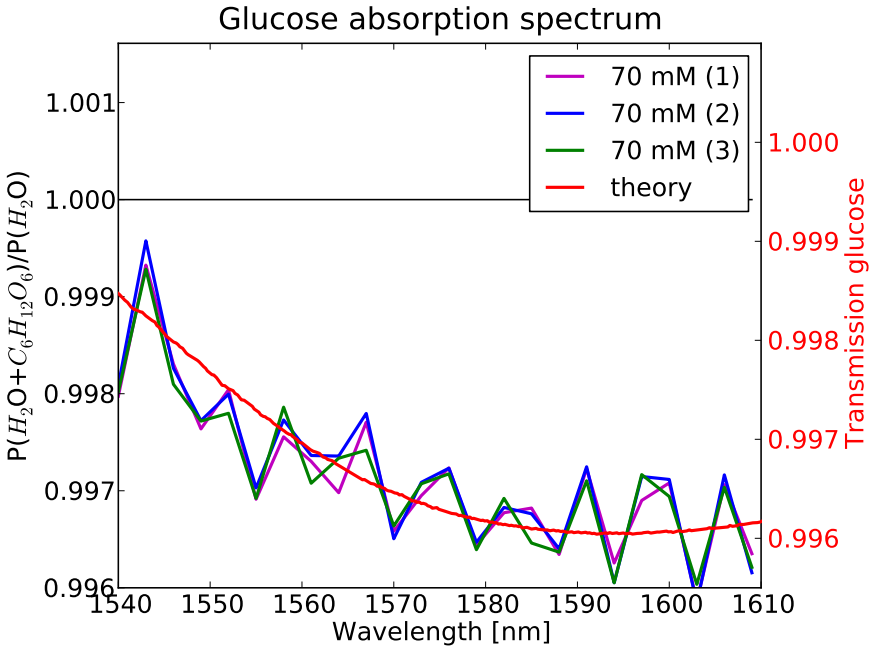

Figure 6.16: Extracted absorption spectrum (left y-axis) for the three 70 mM solution measurements with the theoretical expected shape (right y-axis).

concentration of 5.5 mM and 16 mM are respectively the mean and high extreme physiological blood glucose levels. The signal spiral transmission spectra are continuously acquired with a wavelength step of 3 nm and after every 16 spectral sweeps, the valve is switched between DI water and a glucose solution. The two lowest concentrations (1 mM, 5.5 mM) were measured twice. The measurement result is shown in figure 6.17(a,b).

A clear correlation between the change in power and the applied glucose concentration is present for the various wavelengths in the signal channel whereas the reference channels shows no correlation. When a higher concentration of glucose is applied, the power loss in the signal channel is larger due to the glucose absorption. This behavior is not visible in the reference channel.For the low glucose concentrations ($< 16mM$) the power loss in the signal channel is difficult to discriminate visually. Still, we will show in the next paragraph that by using the virtual water procedure, we can reliably extract the glucose concentration.

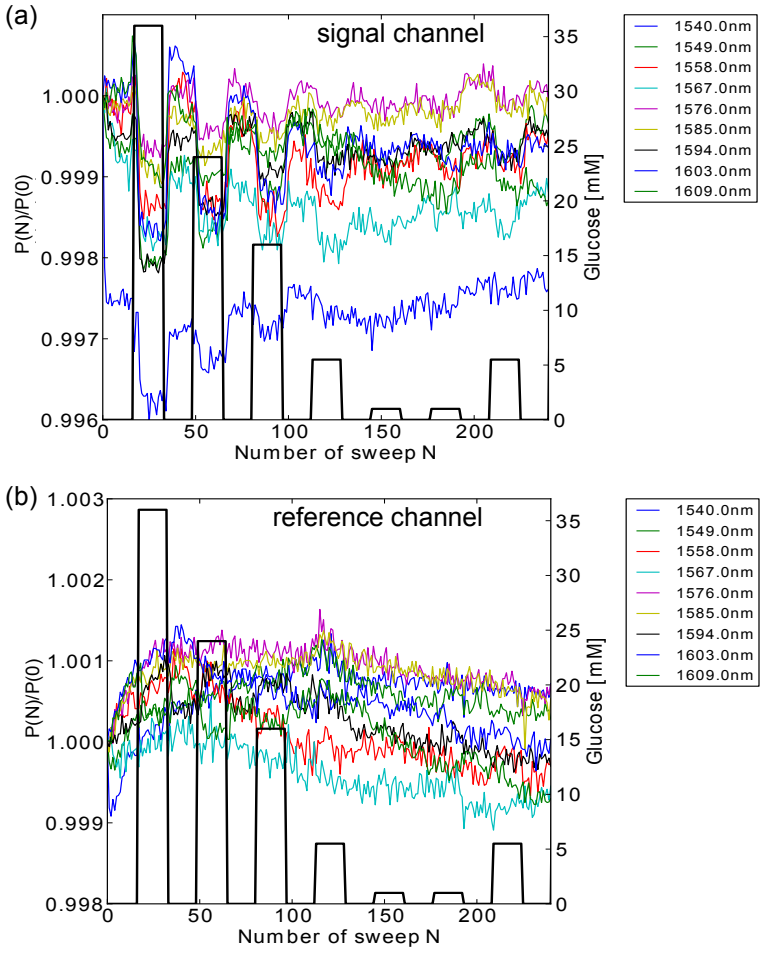

Figure 6.17: Evolution of the detected power of (a) the signal spiral and (b) the reference spiral at different wavelengths when five different glucose solutions are applied. The switching moments are indicated by the black line and the height refers to the applied glucose concentration.

We obtain the glucose absorption spectra for the experiment with different glucose concentrations, by dividing the measured glucose solution spectra with the virtual water curves. The latter are calculated for the signal channel (single-beam analysis) with δN=4 (wavelength sweeps), N_{avg}=4, M=14 and O=7. In addition, we have averaged the various glucose absorption spectra to one high SNR absorption spectrum and this for all of the different applied glucose solutions. The result is plotted in figure 6.18.

The y-scale in figure 6.18 shows that we can measure very small (0.01%) changes in transmission. Again, the obtained glucose absorption spectra exhibit a strong periodic ripple. The glucose absorption dip increases as expected with increasing glucose concentration. The replicate measurements (1 mM, 5.5 mM) are clearly grouped with the preceding measurements of the 1 mM and 5.5 mM solutions. Although the absorption dips caused by the 1 mM solution are very difficult to discriminate visually on figure 6.17(a), the straightforward data processing allows us to reliably extract the absorption spectrum.

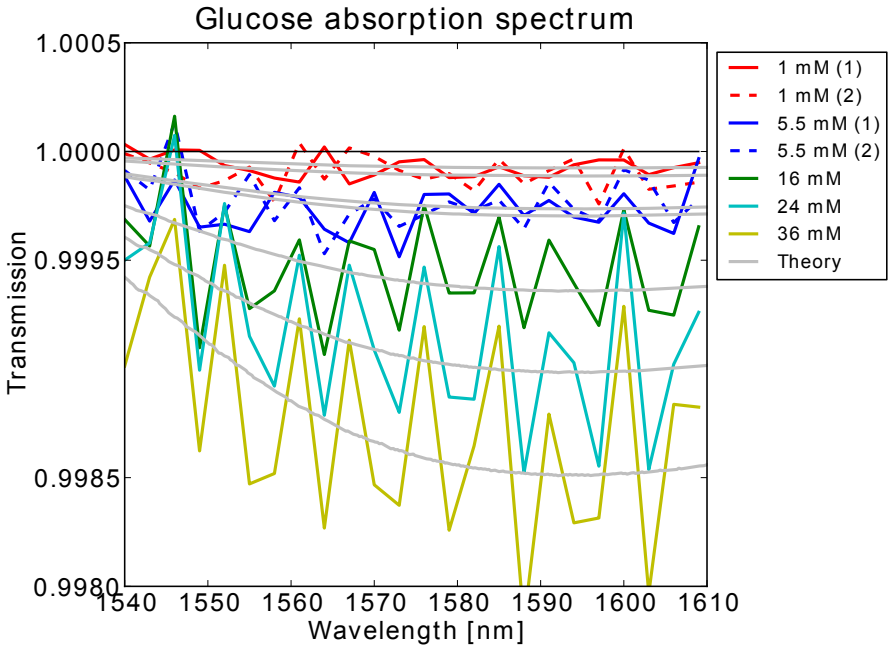

Figure 6.18: Extracted absorption spectrum for the different glucose solutions, compared to the theoretical fit that is obtained when using a linear regression model as derived in section 6.5.4

Linear regression model

Now that we have a set of transmission spectra for different glucose concentrations, we can derive a (sensor-specific) calibration model to correlate the two. Given the weak absorption due to glucose, the transmission is linearly dependent on the glucose concentration:

$$T = exp(-\alpha C_{gluc}) \approx 1 + \alpha C_{gluc} \tag{6.3}$$

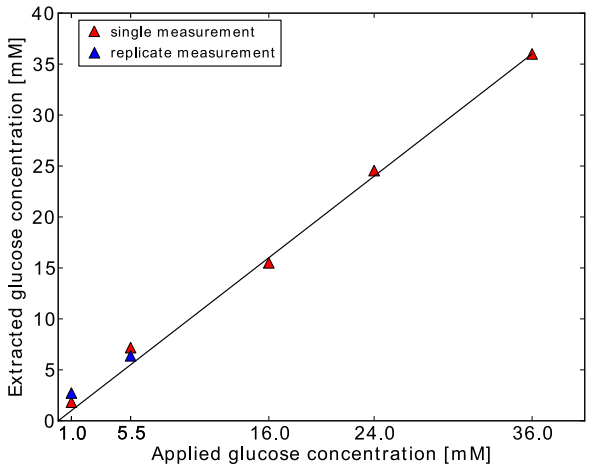

Figure 6.19: Linear regression model for glucose prediction when the virtual water procedure is applied

Therefore, we derive a linear regression model in which we use the absorbance $A_r = \log_{10}(T_{36mM})$ of the 36 mM glucose solution as the regression vector $V_r = A_r/36$. We do a least-squares fitting between the measured absorption spectra for every applied concentration and $10^{V_r \cdot C_p}$, for a range of possible glucose concentrations C_p between 0 and 50 mM. The predicted glucose concentration C_{pr} is the value of C_p for which the least-squares sum is minimal. The predicted glucose concentrations for every applied glucose solution is plotted in figure 6.19. The linear trend is clearly shown. We calculate the error-of-fitting $\hat{E}$ of our model using the predictions C_{pr} of all seven measurements except for 36 mM:

$$\hat{E} = \sqrt{\sum_{C_{pr} \neq 36mM} \frac{(C_{ref} - C_{pr})^2}{6}} = 1.14mM \tag{6.4}$$

The reference values C_{ref} are the prepared glucose concentrations.
Based on the predicted glucose concentrations, we also calculated the theoretically expected absorption spectra based on the reference data from [4]. These are plotted as grey curves in figure 6.18. We can see that our measurements are in good agreement with the theoretically expected shape. A dual-beam analysis gave a slightly worse error-of-fitting ($\hat{E}$=1.76 mM) than a single-beam analysis ($\hat{E}$=1.14 mM) with the same settings. This indicates that the slightly opposite drift (reference decreases over time), again limits our dual-beam design.

The performance of glucose sensors is often compared based on the 95% confidence interval (CI) [6]. If we consider the difference $(C_{ref} - C_{pr})$ as a normally distributed variable x, then the 95% confidence interval for the mean μ_x can be calculated as [7]:

$$\mu_x \in [\bar{x} \pm t_{n-1,\alpha/2} \frac{s}{\sqrt{n}}] \tag{6.5}$$

with $\bar{x}$ the sample mean, s the sample standard deviation, n the number of samples and $t_{n-1=5,\alpha/2=0.025}$ calculated from the t-distribution with 5 degrees of freedom. The 95% confidence interval for the mean difference between the measured and applied glucose value is $\mu_X \in 0.86 \pm 0.86$ mM and is currently limited by the small size of our sample set of aqueous glucose solutions.

6.5.5 Real-time glucose monitoring

Whereas we have shown with the above experiments that we can reliably extract the glucose concentration from the transmission spectra, we still needed the virtual water curve to remove the water background. Essentially, the technique that we applied was to provide a regular time-reference instead of a spatial reference. In vivo, however, we only have a proper time-reference at the moment a reference blood measurement is performed to calibrate the sensor. To aid in the glucose estimation, we can also directly track the change of the signal transmission with respect to the preceding measurements. We tested this approach in a new glucose sensing experiment, in which we switch between different glucose concentrations without returning to DI water. The measured power of the signal channel P_{sig} for different wavelength sweeps is shown in figure 6.20(a). The power changes almost immediately after the selection valve is switched, as we used a higher pump speed in this measurement. With this data, we do not have the possibility to use the virtual water elimination procedure, but we can create a new variable $V_g(N)$ that incorporates the change in P_{sig} due to a change in glucose concentration ΔC after n additional sweeps:

$$V_g(N) = 1 - \left| 1 - \frac{P_{sig}(N)}{P_{sig}(N-n)} \right| \approx 1 - \alpha \left| \Delta C \right| \tag{6.6}$$

This time-dependent variable $V_g(N)$ is plotted in figure 6.20(b) for $n = 2$. It shows distinct peaks, common to all wavelengths, at the switching times. The other peaks are caused by sudden changes in the signal and do not occur at all wavelength simultaneously (noise!). When we spectrally analyze this parameter at the switching times, we obtain 7 different spectra for the 7 different steps in glucose concentration (36 mM, 28 mM, 8 mM, 10.5 mM, 64.5 mM, 62 mM and 8 mM).

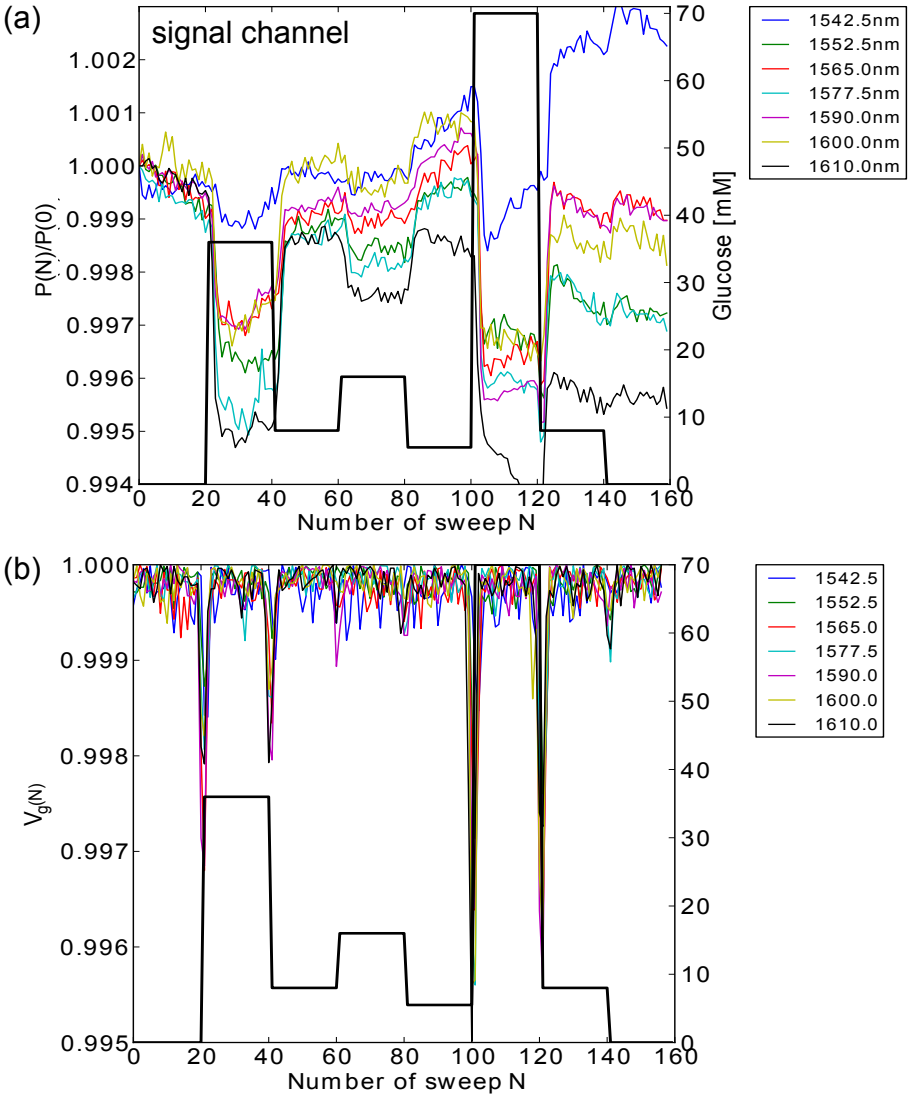

Figure 6.20: (a) Evolution of the detected power of the signal spiral at different wavelengths when six different glucose solutions are applied. The switching moments are indicated by the black line and the height refers to the applied glucose concentration. (b) Plot of variable V_g which indicates the rate of change in detected power due to a step in glucose concentration.

When we take the spectrum of the largest step in glucose concentration

(64.5 mM) and derive a linear regression model as in section 6.5.4, we can again calculate the root mean squared error of calibration. The result of this regression model is shown in figure 6.21. The error-of-fitting amounts to $\hat{E}$=1.63 mM for a single-beam analysis. Likewise, we can perform a dual-beam analysis in which we replace P_{sig} in the expression of V_g to $\frac{P_{sig}}{P_{ref}}$. This dual-beam analysis yields a slightly worse error-of-fitting of $\hat{E}$= 1.99 mM.

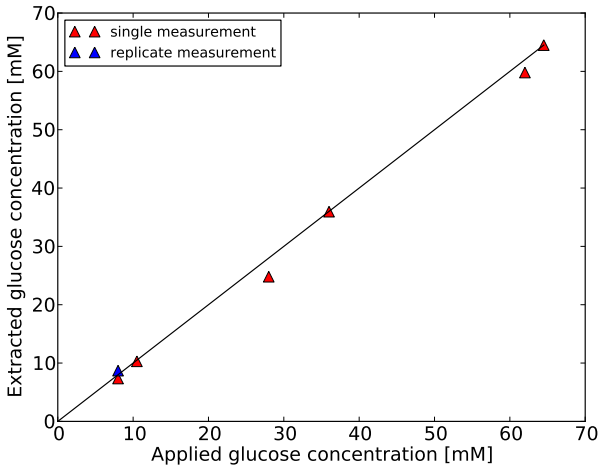

Figure 6.21: Linear regression model for glucose prediction when we track direct changes in transmission.

6.5.6 Experiments with NaCl solutions

To test the response of the evanescent sensor to non-absorbing molecules, we measured aqueous NaCl solutions. In addition NaCl is a good test molecule, as the human body fluids contain a high concentration of salts (154 mM). To monitor the transition to the NaCl solution in real-time, we did not acquire a transmission spectrum, but measured (single-beam) the power at (alternated) λ=1550 nm and λ=1590 nm with a sampling rate of 1 Hz. Firstly, we flow DI water through the signal micro-fluidic channel and after 200 s we switch to a 20 mM salt solution. After 400 s, we switch again to DI water and finally we apply a 70 mM glucose solution during the period from 600 to 800s. The measurement configuration is slightly different from previous measurements, as the evanescent sensor did not reside in the flow channel, but in a side-branch.

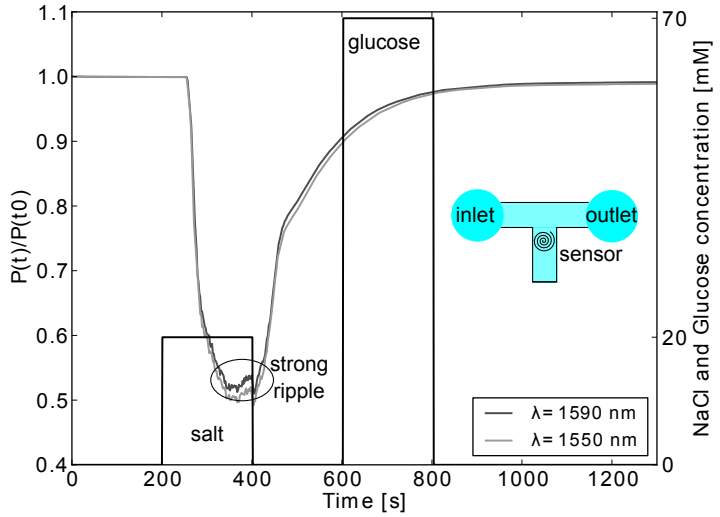

Figure 6.22: Evolution of the detected power of an evanescent spiral in the presence of 20 mM salt and 70 mM glucose. The switching moments are indicated by the black line and the height refers to the applied salt and glucose concentration.

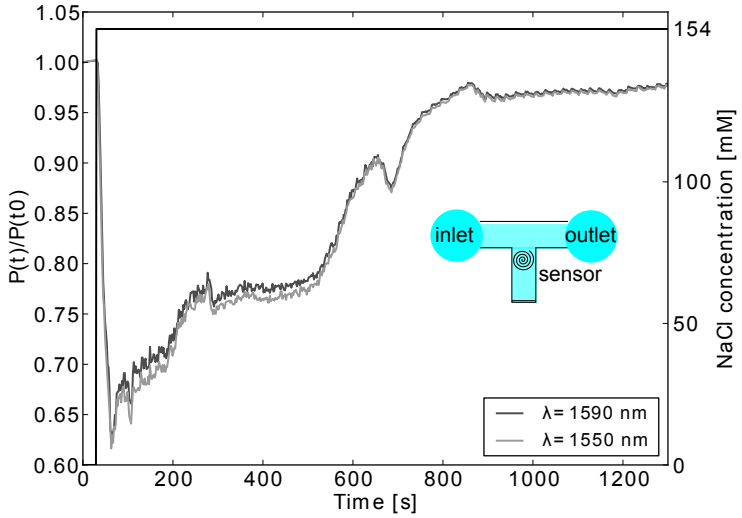

Figure 6.23: Evolution of the detected power of an evanescent spiral in a side-branch of the flow channel when a 154 mM salt solution is continuously applied to this sensor.

The result is shown in figure 6.22. Although we expected to find minor influence of NaCl on our sensor, the sensor shows a very strong ($\Delta T > 50\%$) and nonlinear response, whereas it reacts normal to the large glucose concentration of 70 mM (too small to see on this y-scale).

In a second experiment, we switch to a 154 mM salt solution and do not switch back to DI water. This time, a similar response to salt with a sharp decrease and slower return to the initial power value is visible (see figure 6.23). Thus, even though we do not switch back to DI water, the optical power is restored over time. Still, a power ripple remains visible which has a period of about 20 s and an amplitude of 0.0037 (normalized to 1).

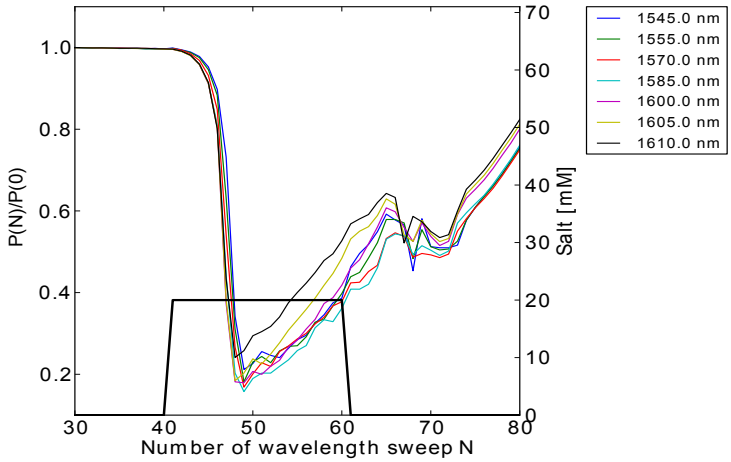

Figure 6.24: Evolution of the detected power for different wavelength sweeps when a 20 mM salt solution is applied. The switching moments are indicated by the black line and the height refers to the applied salt concentration.

In a third set of experiments we investigated spectrally how the sensor responds to salt and if we can still measure glucose in the presence of salt. To measure the spectral response to salt, we continuously acquire the transmission spectra of the spiral sensor when we switch from DI water to a 20 mM salt solution and back. The result is shown in figure 6.24 and reveals a spectrally flat but strong transient behavior of the sensor. The small deviations between wavelengths are mostly due to the slow sampling speed (1 wavelength sweep takes about 25 seconds), while the sensor response to

NaCl fluctuates faster. It should be investigated further what causes this strong interaction of the sensor with a NaCl solution and if this interaction happens with other salts as well. Nonetheless, we can still measure glucose in the presence of a high 154 mM NaCl solution after the initial strong transient has faded.

A sensing experiment with a 154 mM salt solution spiked with glucose (36 mM and 70 mM) is shown in 6.25. We can clearly see the correspondence between the applied glucose concentration and the change in transmission.

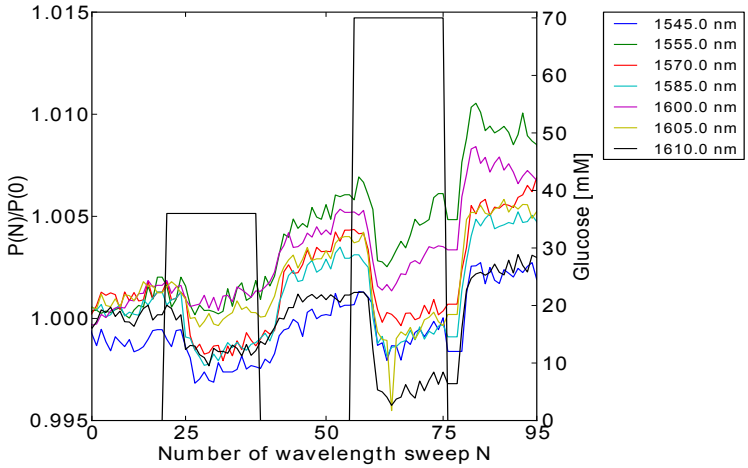

Figure 6.25: Detection of 36 mM and 70 mM of glucose in the background of a 154 mM salt solution.

6.5.7 Serum experiments

After the positive evaluation of our sensor for the detection of glucose in aqueous solutions, we wanted to measure glucose in human serum. This biological medium contains a large number of different molecules and proteins. The latter make pure serum very viscous, so that we could not pump it through the thin tubing nor through the micro-fluidic channels. Therefore, the serum solutions were first centrifuged to lower the protein concentration so that the serum was less viscous. Due to the high salt concentration in serum, we first waited till the transient behavior was almost saturated (about 2 hours). After this, a serum solution spiked with 10 mM

and 20 mM was applied to the sensor. The raw measurement data is shown in figure 6.26. The extracted glucose spectra using a single-beam analysis with virtual serum extraction yields figure 6.27.

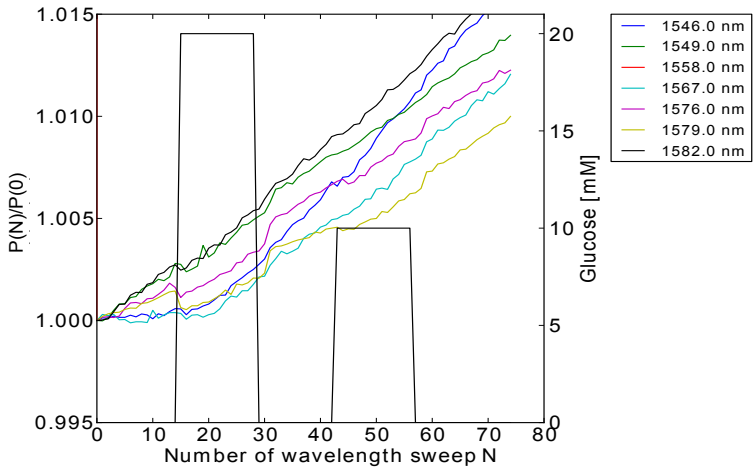

Figure 6.26: Evolution of the detected power for different wavelength sweeps when a serum solution with 10 mM and 20 mM glucose is applied. The switching moments are indicated by the black line and the height refers to the applied glucose concentration.

Although slow drift is still present on the signal, the glucose dips can be extracted. The theoretically expected shape is calculated based on the simulated confinement factor. If we inspect figure 6.27, we can see that that there is an amplitude mismatch between the measurements and the theory. To match the measurements, the confinement factor should be higher. We found, however, on camera images that the serum proteins form small slimy structures on top of our sensor (see figure 6.28) and reduce the evanescent sensitivity of our waveguides. If this protein layer varies over time, we cannot rely on a single confinement factor and it becomes difficult to extract a glucose model.
It is clear that in an implantable sensor, this adhesion of proteins should be avoided by the use of a membrane. Furthermore, it can be necessary to surface-functionalize the waveguide itself with a very thin layer (preferably monolayer) to avoid adhesion from molecules that do make it through the membrane. This will increase the sensor lifetime.

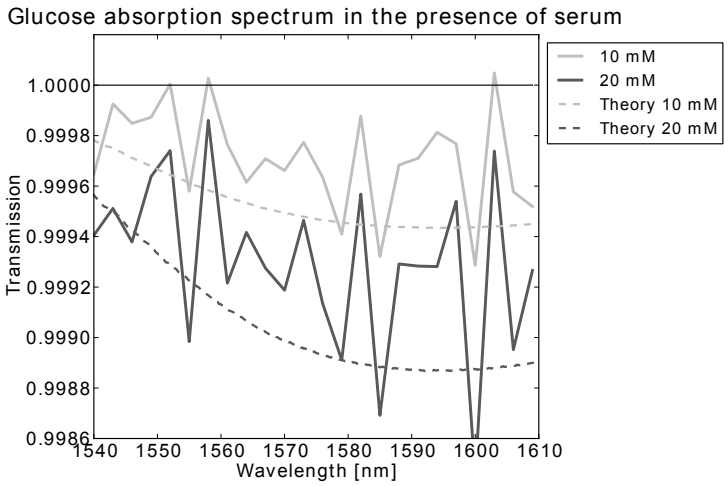

Figure 6.27: Extracted glucose absorption spectrum together with the theoretically expected shape.

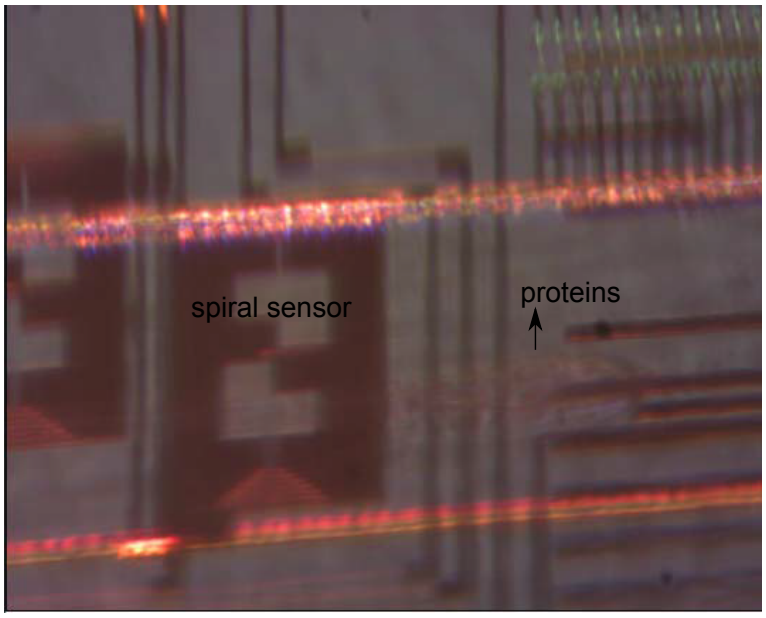

Figure 6.28: Camera image of the sensor in the presence of proteins

6.6 Conclusion

Here, we have presented the optimized optical configuration to measure small power variations due to glucose on a large background spectrum of water. This optimized set-up was fully automated, such that the measurements need not be disturbed by manual handling steps. It comprised a pre-dispersive spectrometer, a microfluidic pump and a selection valve to select different glucose solutions. The pre-dispersive spectrometer consists of a broadband source (SLD) followed by a tunable filter and a dual-channel photodetector for the signal and reference measurements of an opto-fluidic chip. This opto-fluidic chip is a silicon-on-insulator chip with a dual-beam circuit layout, combined with micro-fluidics in PDMS. The sensor chip comprises two evanescent sensors that are 1 cm long, 450 nm wide rib waveguides that reside in a signal and reference microfluidic channel.

Next to the introduction to the used optical measurement configuration, we elaborated on the signal-to-noise ratio of our set-up. It was found that although the set-up aims at maximizing the common path, non-common noise limits our dual-beam design. Still, a high long-term SNR of 36.29 dB for 2 hours is achieved. In addition, we have investigated the sensitivity of our set-up to noise and identified slow drift and temperature variations as the limiting factors.

In the measurement results section of this chapter, we have shown that we can reliably measure the transmission spectrum of glucose in physiological concentrations. Thanks to these reliable measurements, we could establish a linear regression model that relates the measured spectra to a glucose concentration. A good error-of-fitting of 1.14 mM was found, when we could make use of the virtual water extraction procedure. This is on par with the requirements for in vivo continuous glucose monitoring. A slightly higher value of 1.63 mM was measured when we do not have access to regular water reference measurements.

Whereas we focused on glucose detection in aqueous solutions, we have raised the sample complexity in two steps. Firstly, a high concentration of NaCl (154 mM) was added to the glucose solutions. This is relevant as the human body contains this high concentration of salts. Secondly, we measured glucose in human serum.
In the measurements with NaCl we found a strong initial transient when switching from pure DI water to NaCl solutions. More research is needed to investigate the cause of this behavior and if it occurs for other salts as well. Still, we were able to detect glucose, albeit only for a higher concentration.
In the serum measurements, again a strong transient was found when switching between water and serum. Nonetheless, we could extract the

glucose transmission spectra using a virtual serum analysis. Camera images showed that the serum proteins adhere to the sensor surface and limit the confinement factor determination. This in turn, creates a missing link to estimate the glucose concentration from a transmission spectrum. For an implantable sensor, this protein adherence should thus be avoided.

To conclude this chapter, we can state that we have successfully measured physiologically relevant glucose concentrations using evanescent absorption spectroscopy on a silicon chip. To enhance the glucose detection limit, the long-term stability of our set-up should be improved. This can be achieved by optimizing the fiber array/chip interface, which will reduce the slow-drift effects due to small changes in the fiber array alignment above the output grating couplers. Another straightforward solution to limit the non-common drift, is the use of integrated photodiodes with a very low-noise electronic read-out unit.

References

[1] Janelle R Anderson, Daniel T Chiu, Hongkai Wu, Olivier JA Schueller, and George M Whitesides. *Fabrication of microfluidic systems in poly (dimethylsiloxane)*. Electrophoresis, 21:27–40, 2000.

[2] KC Tang, E Liao, WL Ong, JDS Wong, A Agarwal, R Nagarajan, and L Yobas. *Evaluation of bonding between oxygen plasma treated polydimethyl siloxane and passivated silicon*. In Journal of Physics: Conference Series, volume 34, page 155. IOP Publishing, 2006.

[3] Diedrik Vermeulen, Yannick De Koninck, Yanlu Li, Emmanuel Lambert, Wim Bogaerts, Roel Baets, and Günther Roelkens. *Reflectionless grating couplers for Silicon-on-Insulator photonic integrated circuits*. Optics express, 20(20):22278–22283, 2012.

[4] Airat K Amerov, Jun Chen, and Mark A Arnold. *Molar absorptivities of glucose and other biological molecules in aqueous solutions over the first overtone and combination regions of the near-infrared spectrum*. Applied spectroscopy, 58(10):1195–1204, 2004.

[5] Yanlu Li and Roel Baets. *Improved multi-mode interferometers (MMIs) on silicon-on-insulator with the optimized return loss and isolation*. In 16th Annual Symposium of the IEEE Photononics Benelux Chapter, Belgium, 2011.

[6] L. Hooft J. DeVries A. Mudde M. Langendam, Y. Luijf and R. Scholten. *Investigation of experimental errors in the quantitative analysis of glucose in human blood plasma by ATR-IR spectroscopy*. The Cochrane Library, 2, 2012.

[7] Richard Martin Feldman and Ciriaco Valdez-Flores. *Applied probability and stochastic processes*. Springer, 2010.

7

Diffusion-assisted glucose sensing experiments

Thus far, we assumed that we can use a dual-beam evanescent sensor, with a signal and reference arm, to measure glucose *in vivo*. However, we never defined how the reference arm should look like. To maximize the efficiency of a dual-beam system, the reference arm should be exactly the same as the signal arm, apart from the glucose content. We know that the signal arm of our implantable evanescent sensor will be in contact with interstitial fluid (ISF). This fluid consists mainly of water, but has a high degree of complexity due to the large variety of small molecules and proteins that are present. So now we should ask ourselves, how can we approach this situation, where the reference arm sees the same ISF, apart from the glucose molecules? We cannot simply put a physical barrier that passes glucose but withholds all other molecules or vice versa.

In this chapter, we will show that the gradient in glucose concentration, naturally created by diffusion, enables a dual-beam design for *in vivo* measurements. By exploiting this diffusion-induced concentration gradient, we can design an implant for which the signal sensor sees the relevant glucose level, whereas the reference sensor is set to see a quasi monotonous (low) glucose value. Nonetheless, the water content will be the same at both sensors, so that we can still eliminate the dominant water absorption from the transmission spectrum. The conceptual idea is shown in figure 7.1. This idea was implemented in a new opto-fluidic chip design. By using this chip for evanescent glucose sensing experiments, we could demon-

strate the potential of our proposed solution.

This chapter is structured as follows: firstly, we derive a theoretical model to give insight in our proposed solution for *in vivo* dual-beam spectroscopy. Secondly, we detail on the opto-fluidic chip design. Next, we discuss the measurement results that were obtained with this optofluidic chip. Finally, we end with a conclusion.

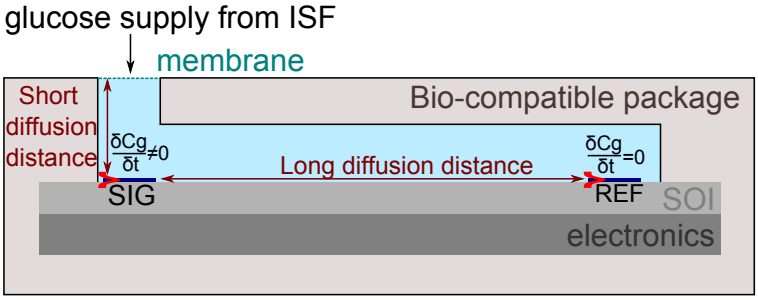

Figure 7.1: Implantable dual-beam evanescent sensor

7.1 Theoretical model

In this section, we discuss our approach in more detail using straightforward simulations based on the 1D diffusion equation. In addition, we derive the transfer function for diffusion in a half-open (1D) channel. Lastly, we list a few design considerations that are relevant for the *in vivo* sensing application.

7.1.1 Diffusion-assisted dual-beam configuration

To illustrate the main idea, we simulate a 4 cm long, but narrow microfluidic channel, that is open on one side but closed on the other. At the entrance of this diffusion channel, we apply 5 different glucose concentrations as listed in table 7.1.

Time of the day	breakfast	morning	lunch	afternoon	dinner	night
Glucose [mM]	7.0	5.0	10.0	6.0	9.0	4.0

Table 7.1: APPLIED GLUCOSE CONCENTRATION

Glucose has a diffusion coefficient D of $6.75\text{x}10^{-10} m^2/s$ at a temperature of $25°\text{C}$ and is initially uniformly distributed (5.5 mM) in the 4 cm long mi-

crofluidic channel. By solving the 1D diffusion equation with these boundary conditions, we can monitor the glucose distribution along the diffusion channel over time. The 1D diffusion equation is given by:

$$\frac{\delta C}{\delta t} = D\frac{\delta^2 C}{\delta x^2} \tag{7.1}$$

with D the diffusion coefficient. The result is plotted in figure 7.2. We

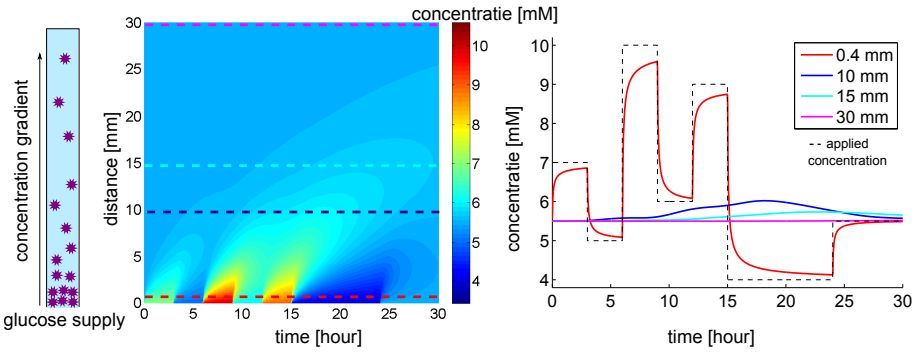

Figure 7.2: Simulation example of 1D diffusion in a half-open diffusion channel with a varying input glucose concentration.

can easily see that a sensor, residing in approximately the first 500 μm, would quickly respond to the applied concentration at the entrance of the diffusion channel. In contrast, a sensor at the end of the diffusion channel remains constant. For a sensor in the first cm of the diffusion channel, we can see small (<1 mM) variations over time. Generally we can say that, as long as the average applied glucose concentration is constant, we can make the diffusion channel long enough to avoid any substantial variation at the end. Still, all other environmental parameters (e.g. temperature, water content) can be uniform along the diffusion channel. This way, a sensor located at the end of the diffusion channel is a good reference for a signal sensor that resides at the entrance.

7.1.2 Transfer function model

Diffusion can be modeled as a linear time invariant (LTI) system. Therefore, we can use a transfer function to yield the frequency response at every position in the diffusion channel. Here, we derive the 1D transfer function for a diffusion channel of length L, that is closed on one side. In order to find the transfer function, we first need to derive the step response. The step response is the solution to the diffusion equation for the following

boundary conditions:

$$C = 0, \quad t < 0 \quad ; \qquad C(x = 0) = C_0, \quad t \geq 0 \tag{7.2}$$

$$\frac{\delta C}{\delta x} = 0, \quad x = L \tag{7.3}$$

By following a similar derivation as in [1], we obtain the step response:

$$S(x,t) = C_0 \sum_{n=0}^{\infty} (-1)^n erfc \frac{(2n+2)L - x}{2\sqrt{Dt}} + C_0 \sum_{n=0}^{\infty} (-1)^n erfc \frac{2nL + x}{2\sqrt{Dt}} \tag{7.4}$$

with $erfc$ the complimentary error function. Once we have this step response $S(x,t)$, we can derive the impulse response $h(x,t)$, through the following relation:

$$\frac{\delta S(x,t)}{\delta t} = h(x,t) \tag{7.5}$$

Next, we introduce the Laplace transform $L(p)$ of a function f(t):

$$L(p) = \int_0^{\infty} e^{pt} f(t) \tag{7.6}$$

with p a complex number such that this integral converges. Then, by taking the Laplace transform of both sides of equation 7.5, we obtain:

$$L(h(x,t)) = H(x,p) = p.L(S(x,t)) - S(x, t = 0_+) \tag{7.7}$$

The last term reduces to zero as the $erfc(\infty) = 0$. The transfer function that we are looking for is the Fourier transform of the impulse response $h(x,t)$. But as the impulse response is only known for $t > 0$, the Fourier transform reduces to the Laplace transform with $p = i\omega$. Thus by using equation 7.7, if we know the Laplace transform of the step response $S(x,p)$, we can calculate the transfer function $H(x,\omega)$. Using Laplace transform pairs we can immediately write down S(x,p):

$$S(x,p) = \frac{C_0}{p} [e^{\sqrt{\frac{p}{D}}(x-2L)} + e^{-\sqrt{\frac{p}{D}}x}] \sum_{n=0}^{\infty} (-1)^n e^{-2nL\sqrt{\frac{p}{D}}} \tag{7.8}$$

The transfer function is then known as:

$$H(x,\omega) = C_0 [e^{\sqrt{\frac{i\omega}{D}}(x-2L)} + e^{-\sqrt{\frac{i\omega}{D}}x}] \sum_{n=0}^{\infty} (-1)^n e^{-2nL\sqrt{\frac{i\omega}{D}}} \tag{7.9}$$

We have evaluated this transfer function for a set of frequencies in function of distance along the microfluidic channel. The result is shown in figure 7.3. As expected, fast glucose variations are damped by the diffusion process and this damping is more effective with increasing distance.

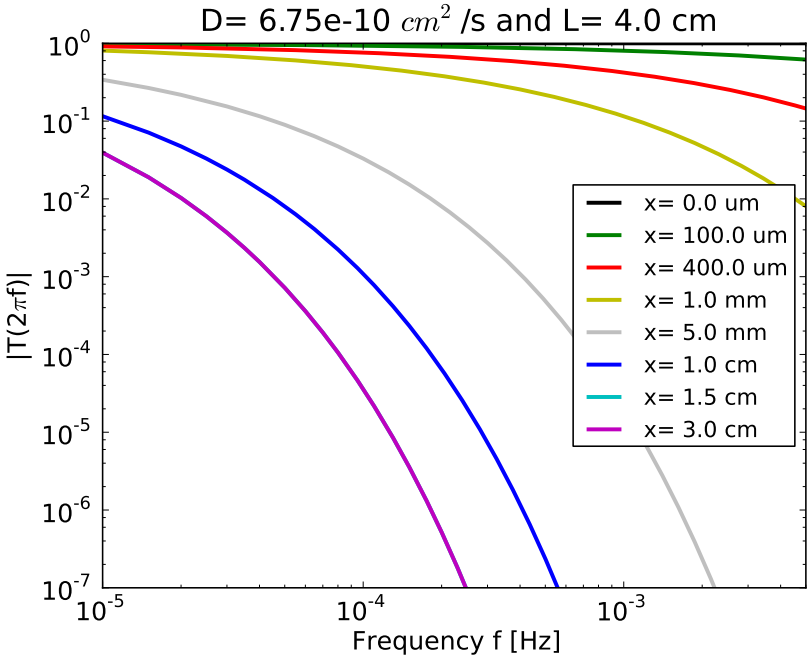

Figure 7.3: Transfer function of 1D glucose diffusion in a half-open 4 cm long diffusion channel.

In general, the concentration measured at the reference sensor C_{ref} is related to the concentration measured at the signal sensor C_{sig} through the impulse response h(x,t): $C_{ref} = (h * C_{sig})(t)$. If we take the ratio of the transmission spectrum at both sensors we thus obtain:

$$R = \frac{T_{sig}P_{in}}{T_{ref}P_{in}} \approx \frac{1 - \alpha C_{sig}}{1 - \alpha(h * C_{sig})} \approx 1 - \alpha[(1 - h) * C_{sig}] \tag{7.10}$$

To calculate the concentration C_{sig} from this equation, we need a deconvolution step in the data processing.

7.1.3 Design considerations

In the ideal case, the reference sensor varies only by an amount smaller than the accuracy of our sensor, such that the reference sensor can be considered constant. This can be achieved if the reference sensor is placed at a large distance (as glucose only varies in a limited concentration range).

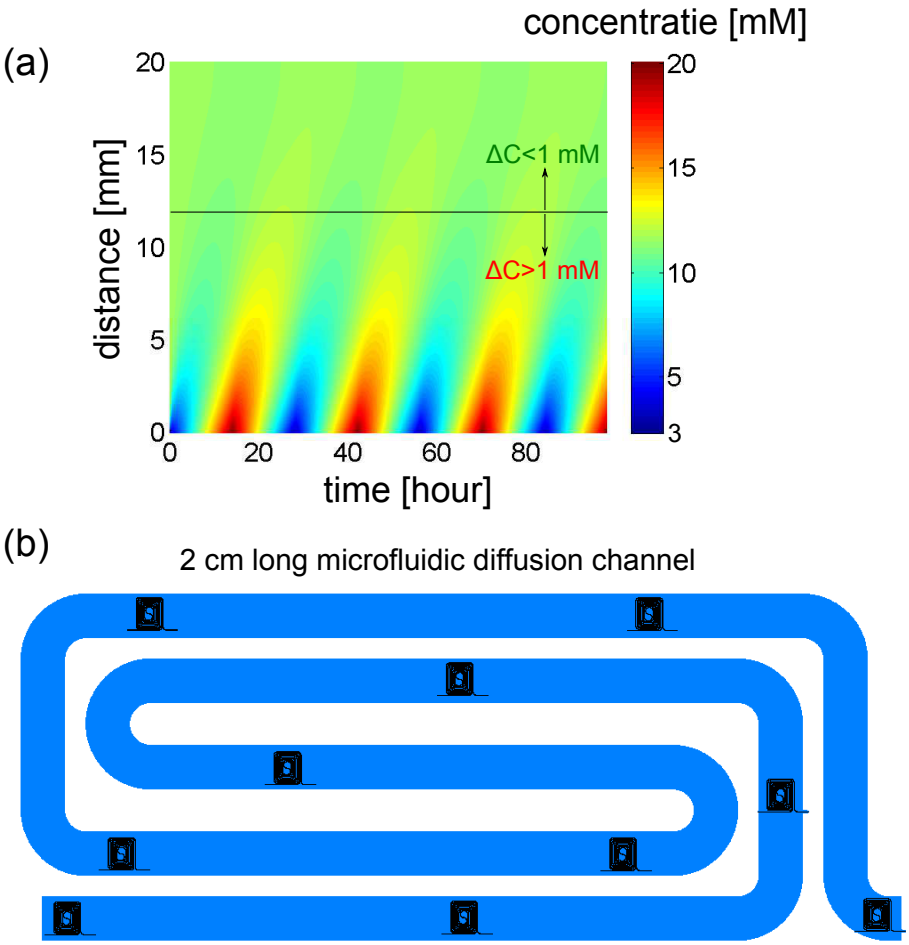

Figure 7.4: (a) Simulation result of diffusion in a 2 cm long channel to see at which distance the glucose variations are reduced to 1 mM (b) 2 cm long microfluidic channel illustrating the possibility for sensor multiplexing.

Here, we will do a simple calculation of the diffusion length that is necessary to obtain a reference reading that varies maximally with 1 mM, whereas the signal reading varies over the full physiological glucose range (3 to 20 mM). We let the glucose supply vary up and down at the typical rate of glucose change. The mean rate of blood glucose change in 111 diabetic patients was measured in [2] to be -0.36$\pm$0.95 mg dL^{-1} min^{-1} before lunch and 0.36$\pm$0.99 mg dL^{-1} min^{-1} after lunch. This boils down to a change of 1.2 mM per hour. The result of this calculation is shown in figure 7.4(a). At a distance of 1.2 cm the variations are reduced to 1 mM. By

increasing the length of diffusion channel beyond this 1.2 cm, we can add some safety margin for slower variations.

However, there is a trade-off between the length of the diffusion channel and the size of our implant. Similar to our evanescent sensors, it makes sense to design a spiral-shaped diffusion channel to reduce the footprint. The width of the microfluidic channel is determined by the spiral sensor dimensions. If we consider a ridge waveguide spiral sensor with optimal length for the first overtone band with square dimensions of 160x160 μm^2, then the footprint of a 2 cm long microfluidic channel, with a 200 μm width, is 4 mm x 1.6 mm. An example of such a microfluidic channel is shown in figure 7.4(b). We can see that there is plenty of space to add additional spiral sensors. These sensors can provide extra means to differ glucose from other components in the ISF. Nonetheless, it is a topic of further research to see how these extra sensors should be placed to increase the detection limit.

7.2 Opto-fluidic chip design

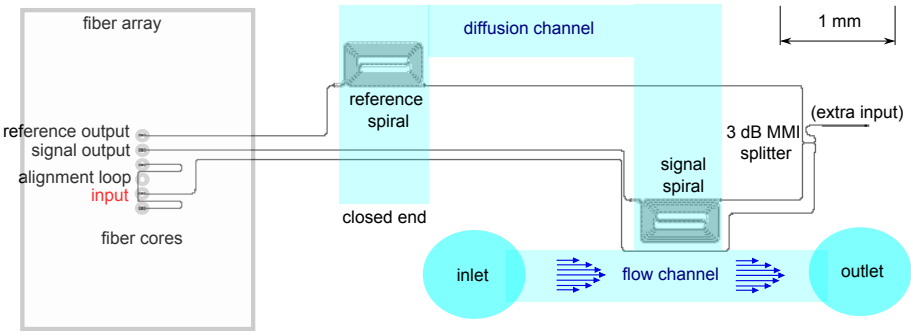

Figure 7.5: Opto-fluidic chip design

As in chapter 6, we fabricated a new opto-fluidic chip for dual-beam evanescent glucose sensing. The silicon-on-insulator chip design is the same as in section 6.1.1. Contrary, the microfluidics design of the opto-fluidic chip is substantially different and is schematically shown in figure 7.5. We use a flow channel to supply glucose to a diffusion channel. This diffusion channel has a small outlet at the end that can be sealed. This small outlet is necessary to fill this diffusion channel with pure DI water at the start of an experiment. The signal spiral resides at a small distance of 100 μm from the entrance of the diffusion channel and the reference spiral at a distance of 6.5 mm.

Variations of the glucose supply in the flow channel are quickly sensed by the signal spiral. In contrast, the reference spiral is not affected by these glucose variations given the distance and our experimental settings (see next section). The main difference of this *in vitro* implementation compared to the *in vivo* setting, is the flow at the entrance of the diffusion channel. In the next chapter (chapter 8), we shortly discuss how this flow induces small convective currents at the entrance of the diffusion channel. This way, glucose molecules travel down the beginning of the diffusion channel faster than expected based on pure diffusion alone. The magnitude of these convective currents depends on the flow speed in the flow channel and decreases exponentially with distance. Given the flow-speed and distance to the reference sensor in our opto-fluidic chip, the impact of these convective currents is negligible.

7.3 Measurement results

As the measurement configuration is the same as described in chapter 6, we immediately start by describing the experimental results of the diffusion-assisted dual-beam glucose measurements.

7.3.1 Glucose experiment with different concentrations

In this experiment, we flow different glucose solutions, alternated with pure DI water, through the flow-channel at a steady rate of 9 μm/L. Five different glucose concentrations are used: 8 mM, 16 mM, 24 mM, 36 mM and 70 mM. These are somewhat higher values than in previous glucose experiments, but the actual glucose concentration at the sensor is lower than the glucose concentration in the flow channel. This is due to the mixing of glucose with water in the beginning of the diffusion channel.

The signal spiral transmission spectra are continuously acquired with a wavelength step of 5 nm and after every 20 spectral sweeps, the valve is switched between DI water and a glucose solution. The measurement result is shown in figure 7.6(a,b). A clear correlation between the change in power and the applied glucose concentration is present for the various wavelengths for the signal sensor, whereas the reference sensor shows no correlation. This means that the diffusion approach works well. Still, a very strong slow drift is present for both sensors (5 $\%$ drift over a 1.5 hour measurement). The reason for the large drift in this experiment is unkown.

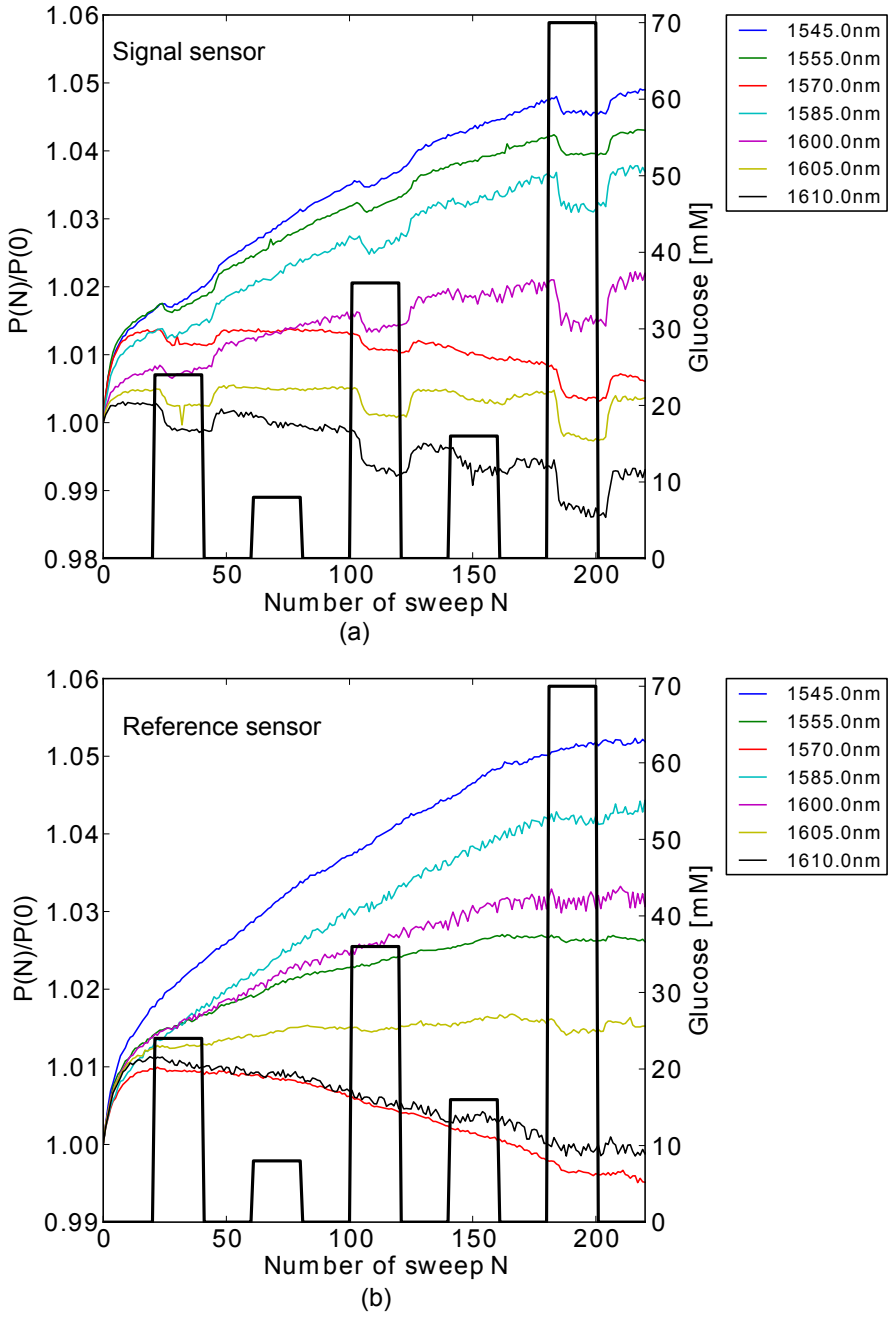

Figure 7.6: Evolution of the detected power of (a) the signal spiral and (b) the reference spiral at different wavelengths when five different glucose solutions are applied. The switching moments are indicated by the black line and the height refers to the applied glucose concentration.

The evolution of the ratio of the signal power over the reference power for the different wavelength sweeps is shown in figure 7.7. The glucose dips are clearly visible and the strong drift from the signal and reference arm is partially eliminated. The virtual water elimination procedure (see section 6.5.3) was used to extract the glucose spectra from the ratio. The following settings were used: δN=4 (wavelength sweeps), N_{avg}=1, M=3 and O=6. In addition, we have averaged the first five glucose absorption spectra to one high SNR absorption spectrum and this for all of the different applied glucose solutions.

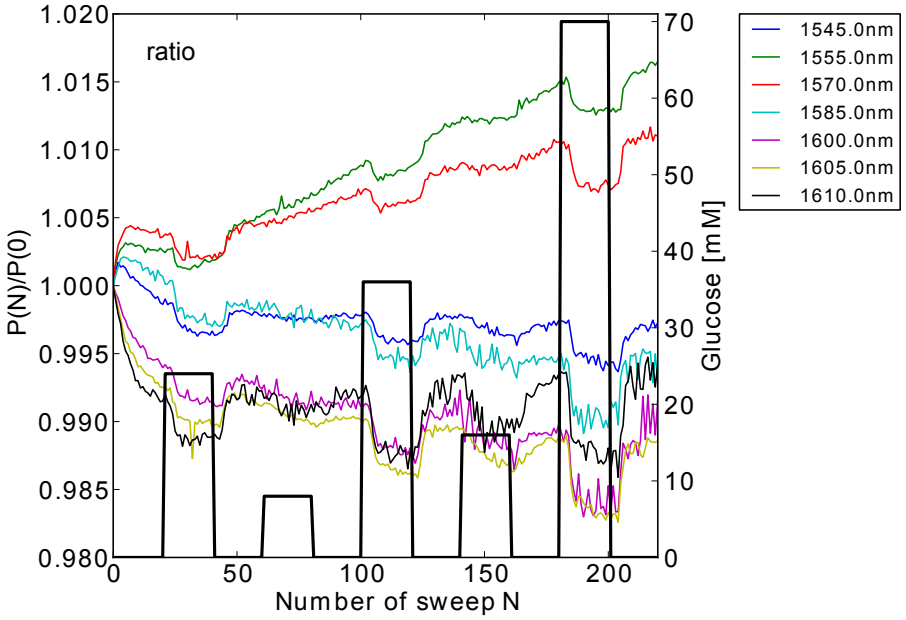

Figure 7.7: Evolution of the ratio at different wavelengths when five different glucose solutions are applied. The switching moments are indicated by the black line and the height refers to the applied glucose concentration.

Based on the retrieved five glucose spectra, we made a linear regression model, in which we used the absorbance $A_r = \log_{10}(T_{70mM})$ of the 70 mM glucose solution as the regression vector $V_r = A_r/70$ (see section 6.5.4). The result of this linear regression model is shown in figure 7.8. As expected, we have a slight under-estimation of the glucose concentration. The error-of-fitting of this measurement was calculated to be $\hat{E}$=1.41 mM (using the predictions C_{pr} of all glucose measurements except for the 70 mM glucose

prediction). Although higher glucose concentrations were applied in these experiments, this low error-of-fitting demonstrates the potential of this approach for an in vivo sensor.

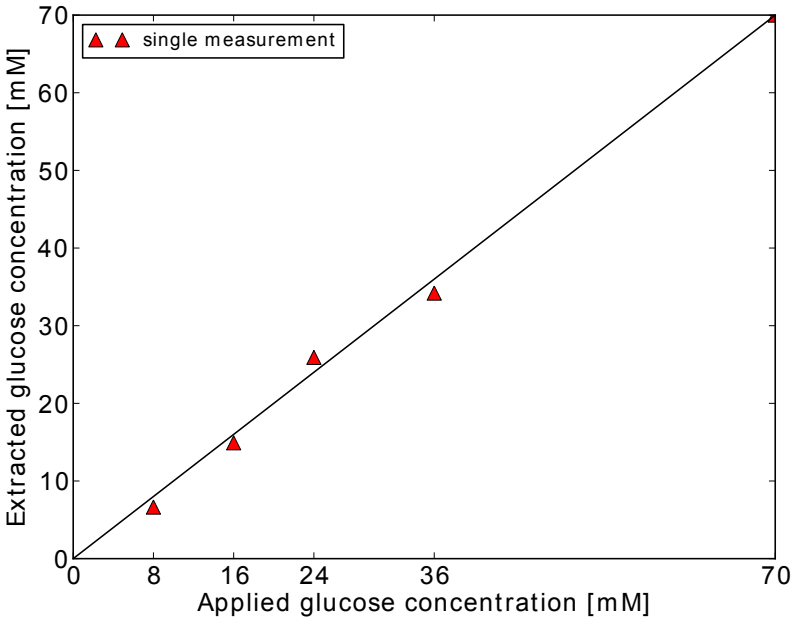

Figure 7.8: Linear regression model for glucose prediction when the virtual water procedure is applied

7.4 Conclusion

We investigated a new dual-beam configuration that is suitable for *in vivo* measurements. In this configuration, we use a long half-open microfluidic channel in which the signal sensor is placed at the entrance and the reference sensor at the end. The entrance of this channel serves as the glucose supply and glucose molecules travel down the microfluidic channel through diffusion. This slow diffusion process effectively filters fast and strong glucose variations. Thus, the signal sensor sees the fast variations and the reference sensor sees a quasi monotonous value.

In this short chapter, we have presented the theoretical basics and a proof-of-concept experiment with a good error-of-fitting of $\hat{E}$=1.41 mM. Still, we

believe that there is still a lot of interesting research to be done. Interesting research questions include:

- Can we use differences in diffusion speed to distinguish glucose from other small molecules in the interstitial fluid?
- What is the optimal sensor multiplexing strategy?
- How can we calibrate this sensor for slow changes in the average glucose concentration?
- What is the best way to analyze the obtained spectra to retrieve the glucose concentration?

References

[1] John Crank. *The mathematics of diffusion*. Oxford university press, 1979.

[2] Timothy C Dunn, Richard C Eastman, and Janet A Tamada. *Rates of glucose change measured by blood glucose meter and the GlucoWatch Biographer during day, night, and around mealtimes*. Diabetes Care, 27(9):2161–2165, 2004.

8

Measurement of small molecule diffusion with an optofluidic silicon chip

Whereas the diagnostic measures for diabetes are based on the blood glucose level, our implantable sensor is set to measure glucose in the interstitial fluid (ISF). Generally, the glucose concentration in ISF has a close relation with the blood glucose level thanks to the omnipresent blood capillaries. Glucose molecules are transferred from these capillaries into the ISF and then travel through the process of diffusion to the cells that take up the glucose. This diffusion process is slow, as on average it takes a glucose molecule about 1 day to travel 1 cm in ISF. This slow movement is, however, not a problem for our body, as the mean distance between the blood capillaries and the cells that need glucose is very small. Nonetheless, for our sensor this slow diffusion can become problematic. If the distance between the closest blood capillary and our sensor surface is large, we will measure the glucose concentration with a large delay. This can cause the sensor to signal a hyper- or hypoglycemia too late, leading to health complications.

To avoid this slow response time, we should design the sensor such that the glucose supply to the sensor surface is guaranteed. Therefore, we study in this chapter the diffusion of glucose molecules in aqueous solutions. To enable accurate measurements of the diffusion speed, we devised a new opto-

fluidic chip with ring resonator sensors. These small sensors are very sensitive to glucose-induced refractive index changes and can be placed along a microfluidic channel to measure the glucose concentration gradient over time. The measurement of diffusion speed can also can be achieved with a multiple of other methods, e.g. interferometry [1, 2] or fluorescence microscopy [3, 4]. Typical limitations involve the stability requirements for an interferometric set-up and a need for labeling and a limited field-of-view of the microscope for the latter method. It is, however, true that there is no diffusion-measurement technique that outperforms all other techniques. Therefore, the preferred method is often a choice based on the availability of equipment, cost and microfluidic chip layout.

This chapter is structured as follows: Firstly, we derive theoretically the impact of glucose on the refractive index of an aqueous solution. Secondly, we shortly discuss the operation principle of ring resonators sensors that are sensitive to this glucose-induced refractive index change. Thirdly, we will show how an array of these ring resonators can be used to measure the diffusion speed of glucose molecules in microfluidic channels. Next, we discuss our method in terms of accuracy and robustness to noise. Finally we end with a conclusion.

8.1 Refractive index change due to glucose

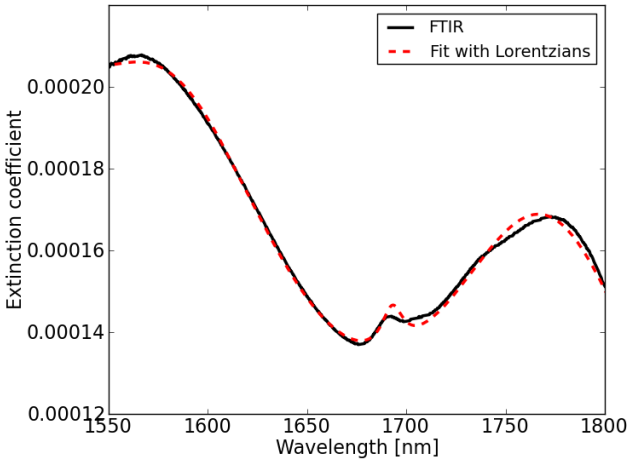

Figure 8.1: Comparison of the fitted extinction ratio of glucose calculated through the Lorentz classical oscillator model to a reference FTIR measurement.

In this section, we will show a general approach to obtain $\frac{\delta n_{mix}}{\delta C}$, the change in refractive index of a diluted aqueous solution n_{mix} due to a change in solute concentration C.

Based on the theory of electrostatics of dielectrics by L. Landau [5], the dielectric permittivity ϵ_{mix} of a diluted solution can be written as:

$$\epsilon_{mix} = \epsilon_{solvent}(1 + 3C\frac{\epsilon_{solute} - \epsilon_{solvent}}{\epsilon_{solute} + 2\epsilon_{solvent}}) \tag{8.1}$$

in which $\epsilon_{solvent}$ and ϵ_{solute} are the dielectric permittivity of respectively the solvent and solute molecules. This expression is correct to the first order of C, with C the concentration of the solute.
The dielectric permittivity ϵ is a wavelength-dependent complex quantity that can be written as: ϵ=ϵ_r-jϵ_i with $\epsilon_r = n^2 - \kappa^2$ and $\epsilon_i = 2\kappa n$ in which n represents the (real) refractive index of the material and κ the extinction coefficient of the material due to absorption losses ($\kappa = \frac{\alpha\lambda}{4\pi}$). To solve equation 8.1 for a given concentration C, we need to know the complex valued $\epsilon_{solvent}$ and ϵ_{solute}. In the case of aqueous glucose solutions in the near-infrared, we can easily find both n_{H_2O} and κ_{H_2O} in literature such that ϵ_{H_2O} is known. But for glucose only κ_{gluc} is known. Luckily, due to Kramers-Kronig relations, the real part of the permittivity can be calculated when κ_{gluc} is known.
To find ϵ_{gluc}, we make use of the following formulas, derived originally by nobel laureate H.A. Lorentz:

$$\epsilon(\nu) = \epsilon_r - j\epsilon_i = \epsilon_e + \sum_s \frac{f_s\nu_s^2}{\nu_s^2 - \nu^2 - jg_s\nu} \tag{8.2}$$

and

$$\kappa = \sqrt{\frac{\sqrt{\epsilon_r^2 + \epsilon_i^2} - \epsilon_r}{2}}, n = \sqrt{\frac{\sqrt{\epsilon_r^2 + \epsilon_i^2} + \epsilon_r}{2}} \tag{8.3}$$

The first equation writes the complex permittivity as a sum of lorentzian oscillators with center frequency ν_s, oscillator strength f_s and damping factor g_s. The value of ϵ_e is the value of the permittivity at frequencies much higher compared to the considered ν. For glucose, we know the peak absorption features, such that the ν_s are approximately known. We perform least-square fitting of the remaining parameters f_s and g_s to yield the correct ϵ_r and ϵ_i that matches the known κ_{gluc} from a reference FTIR measurement ([6]), through equation 8.3. The result of this fitting procedure in the first overtone band, is shown in figure 8.1. Now that ϵ_{gluc} is known, we can calculate ϵ_{mix} for different concentrations and derive n_{mix} through equation 8.3. Finally, we find that for aqueous glucose solutions $\frac{\delta n_{mix}}{\delta C}$ = 2.16e-5 RIU/mM at a wavelength of 1550 nm, with RIU =refractive index unit.

Although this derivative seems small ($\approx 1e^{-5}$), we will present in the next section a small sensor that is very sensitive to these small variations in the refractive index. This sensor can thus be implemented to monitor the glucose concentration.

8.2 Silicon-on-insulator micro-ring resonator sensing

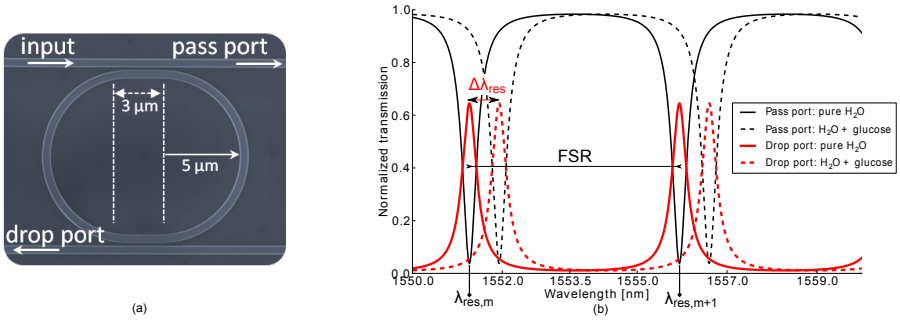

Figure 8.2: (a) Microscope picture of a micro-ring resonator in add-drop configuration. (b) Simulation of the transmission spectrum of this ring resonator. The red and black curves show respectively the drop- and pass ports. The resonant wavelengths shift due to the presence of glucose with a concentration of 50 mMol.

A silicon-on-insulator (SOI) ring resonator (see figure 8.2(a)) supports optical modes with wavelength λ that satisfy the resonance condition

$$\frac{2\pi}{\lambda} n_{eff}(\lambda) L = m \cdot 2\pi \tag{8.4}$$

with n_{eff} the effective refractive index of the circulating mode, L the circumference of the ring and m is an integer representing the order of resonance. From this relation and in the absence of dispersion, it follows that a change in the effective refractive index leads to a shift in the resonant wavelengths:

$$\Delta\lambda = \frac{\Delta n_{eff} L}{m} \tag{8.5}$$

By taking the transmission spectrum of a ring resonator and by subsequently identifying the wavelength shift of the resonances, one can thus detect a change in the surrounding fluid. As shown in the previous section 8.1, the refractive index changes linearly with the solute concentration in

an aqueous solution. For glucose the proportionality constant $\frac{\delta n}{\delta C}$ is 2.16e-5 change in refractive index unit (RIU) per mMol. A micro-ring is thus readily implemented as a glucose sensor. Figure 8.2(b) demonstrates how the transmission spectrum of a micro-ring changes when glucose is present.

It is useful to rewrite equation (8.5) to take into account dispersion, which is large for the high-index contrast SOI material system. Due to dispersion, the resonance wavelength change will also have an effect on n_{eff}. The resulting equation given first order dispersion is [7]:

$$\Delta\lambda_{res} = \frac{\Delta_{env} n_{eff} \cdot \lambda_{res}}{n_g} \tag{8.6}$$

in which $\Delta_{env} n_{eff} = (\frac{\delta n_{eff}}{\delta n_{env}})_{\lambda=\lambda_{res}} \Delta n_{env}$ with Δn_{env} the change in refractive index in the environment and n_g is the group index, defined as $n_g = n_{eff} - \lambda \frac{\delta n_{eff}}{\delta \lambda}$.

8.3 Opto-fluidic chip for diffusion monitoring

Here, we introduce a new opto-fluidic chip for evanescent refractive index sensing, as opposed to evanescent absorption spectroscopy. The opto-fluidic chip consists of a silicon-on-insulator chip with integrated ring resonator structures and microfluidics in PDMS. The developed opto-fluidic chip can monitor the diffusion of glucose along a microfluidic channel. This microfluidic channel encloses a set of equally spaced ring resonators. The channel is open on one side for the solutes to enter, but is closed on the other side. We apply a step function in solute concentration at the entrance of this channel and observe how the concentration evolves along the channel. As the channel is long but narrow, we essentially study the longitudinal diffusion.

The first demonstration of this glucose diffusion measurement was performed by master thesis student Agnes Lee [8]. Additional experiments with aqueous NaCl solutions were then performed to demonstrate that this diffusion measurement set-up yields an accurate measurement of the diffusion coefficient for different types of small molecules and at different temperatures. To get a better understanding of the flow and mass transfer in our opto-fluidic chip and to optimize the data processing strategy, we collaborated with professor Jan Vierendeels from the Department of Flow, Heat and Combustion Mechanics at Ghent University, who performed simulations of our opto-fluidic chip and with whom we had regular discussions.

8.3.1 Opto-fluidic chip design

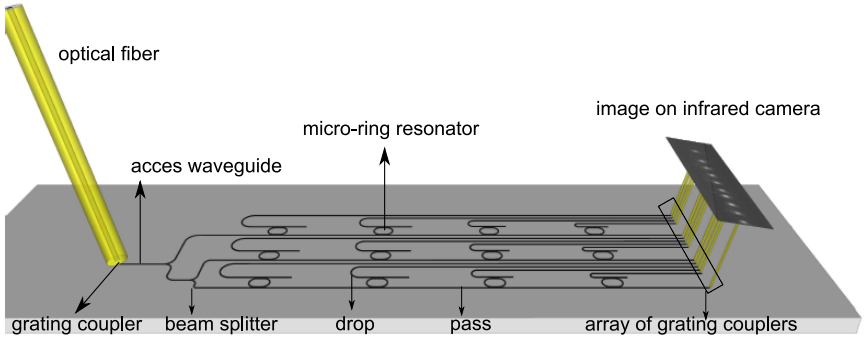

Figure 8.3: Schematic of the silicon-on-insulator chip design with illustration of the read-out principle. An optical fiber is used as the input and camera images are taken from the light coupled out from a grating coupler array. (figure adopted from [9])

As mentioned before, the opto-fluidic chip consists of a SOI photonic chip with ring resonators and microfluidics in PDMS. The photonic chip was originally designed by a former PhD student Katrien De Vos, for another refractive index sensing experiment. An input grating coupler is used to excite the quasi-TE mode of the ring resonators which consist out of 500 nm wide and 220 nm high wire waveguides. The ring resonators have a footprint of 12x12 μm^2 and are grouped in sets of four rings with slightly increasing circumference. These four rings are in the add-drop configuration and spaced equally with a distance of 1.8 mm (see figure 8.3). At the operating wavelength of 1550 nm, the free spectral range of the rings with water cladding is around $FSR = \frac{\lambda^2}{n_g L} = 16.4$ nm.

The microfluidic design has one main channel connecting the inlet with the outlet and one perpendicular branch which we call the diffusion channel. All the fluidic channels are 200 μm wide and 50 μm high. The diffusion channel must be closed at one side to avoid flow in this branch. Two slightly different designs were fabricated, differing mainly in the number of ring resonators that are enclosed. The first design is shown in figure 8.4(a) and was used for the glucose diffusion experiments. The small number of bends in this design is interesting to study the effect of flow in the main channel, but limits the number of micro-rings that are sampled. The second design (figure 8.4(b)) encloses four sets of micro-rings with a spacing of 1.8 mm. Each set has three vertically spaced ring resonators separated by a short distance of 0.1 mm. This design was used for NaCl diffu-

sion experiments ($\frac{\delta n}{\delta C}$ = 1e-5 RIU/mM [10]).

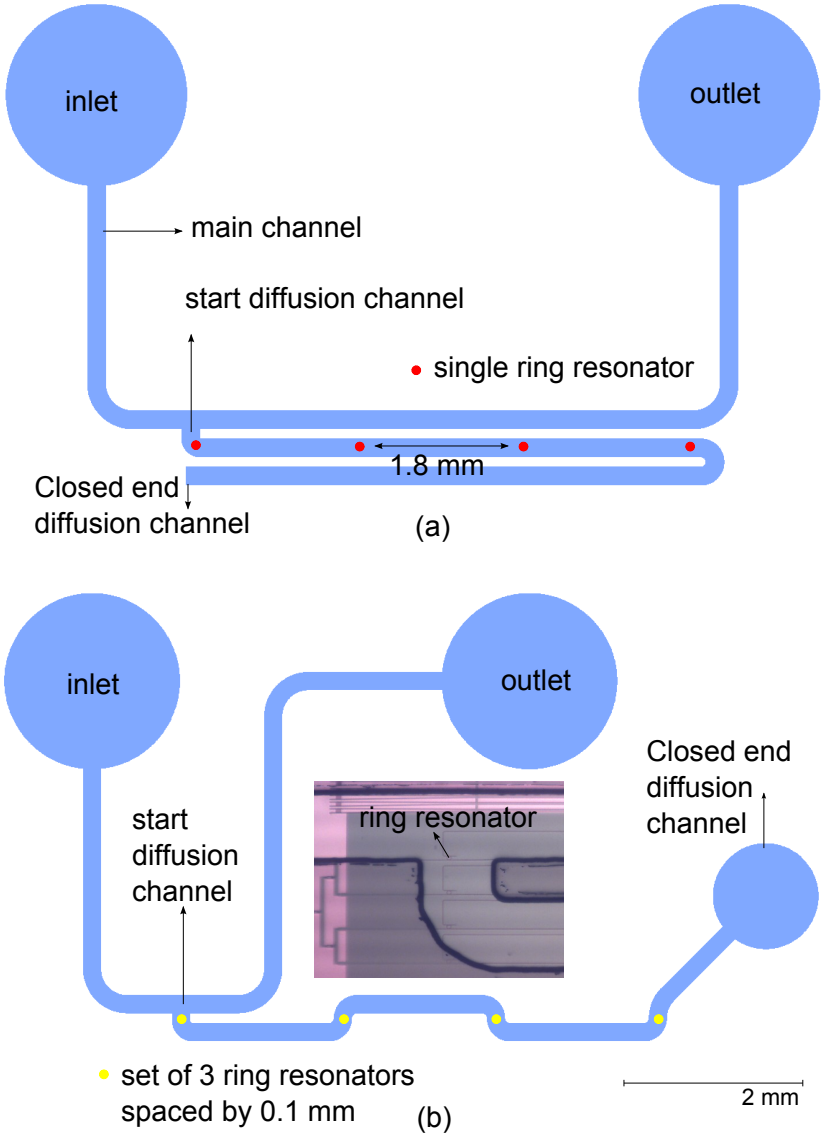

Figure 8.4: (a) Microfluidics design showing the main channel, from inlet to outlet, and the perpendicular diffusion channel, that encloses the ring resonator glucose sensors. (b) Microfluidics design that is used for NaCl experiments. The diffusion channel contains four times a set of three closely spaced micro-rings.

8.3.2 Measurement configuration

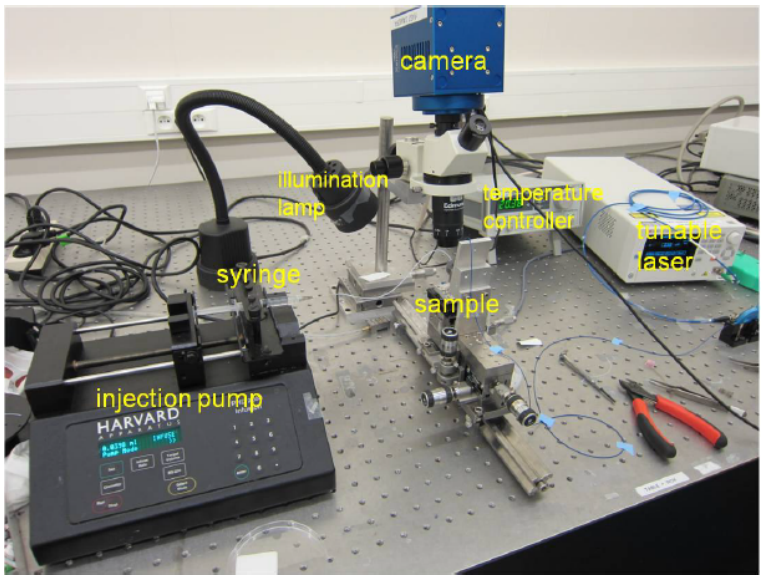

(a)

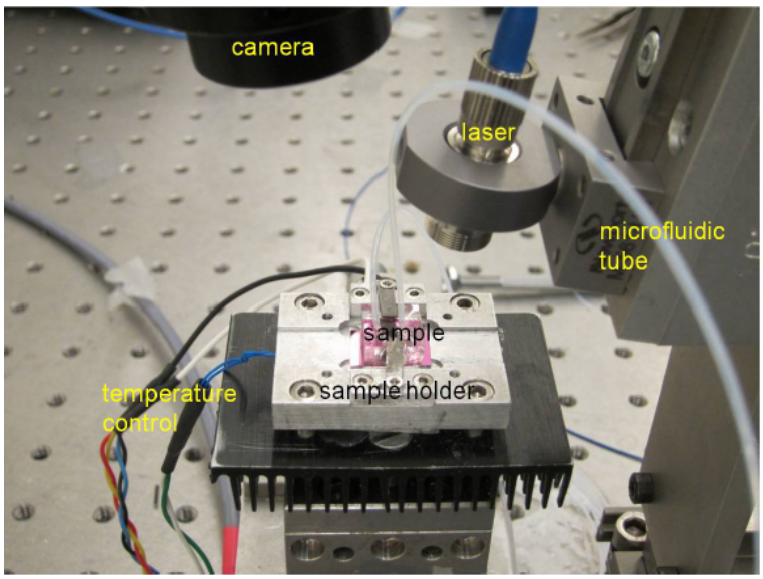

(b)

Figure 8.5: (a) Overview of the measurement set-up (b) close-up picture of the opto-fluidic chip (taken from [8])

Optical read-out system

All micro-rings are fed by one tunable laser source. The laser light is coupled from an optical fiber into the SOI chip using grating couplers [11]. Identical grating couplers are used to image the signal from both the pass and drop ports of all the ring resonators simultaneously onto a fast infrared camera. By tuning the laser wavelength, the output spots from the drop ports will vary in intensity with peaks at the ring resonances. Conversely, the pass ports will show a dip in intensity at the ring resonances.

The opto-fluidic chip is mounted on a temperature controller and the experiments took place in a cleanroom environment. The data acquisition rate to measure consecutive transmission spectra depends on the FSR of the set of micro-rings and the chosen wavelength resolution to resolve the various resonances. It takes e.g. 16 seconds to measure the transmission spectrum over a wavelength range of 16 nm with a stepped resolution of 10 pm. The transmission spectra are continuously acquired. For every transmission spectrum, we first fit a lorentzian to the resonance to determine the peak wavelength. This way, we can accurately determine the wavelength shift of the resonances between consecutive measurements.

In our set-up, the smallest detectable wavelength is 0.6 pm, which corresponds to a glucose concentration of 0.079 g/L and to a NaCl concentration of 0.066 g/L. This optical set-up was developed by the bio-sensing team from the photonics research group. Additional information can be found in [12].

Fluid handling

Deionized (DI) water solutions with a glucose concentration of respectively 70 g/L, 90 g/L and 300 g/L (D-glucose from Sigma-Aldrich) were prepared as well as a NaCl solution with a concentration of 300 g/L. To avoid air bubbles in the solutions, they are degassed in an ultrasonic bath with a vacuum pump. This step is very important as the large change in refractive index between water and air gives a huge shift in resonance wavelengths and distorts the measurement results heavily. To switch between two solutions without generating an air bubble, we use a manual selection valve (not shown in figure 8.5).
The output of the valve is connected to the inlet of the PDMS microfluidics with a flexible PTFE micro-tube. The outlet is connected with a similar tube to a petri-dish to collect the waste fluids. A syringe injection pump (Harvard apparatus) is used to pump the samples.

8.4 Diffusion measurements

8.4.1 Glucose diffusion experiments

We first experimentally verified the expected wavelength shift for a glucose concentration of 300 g/L. We then performed two experiments, one with flow and one with stopped flow in the main microfluidic channel. This way, we can study the effect of the flow in the flow channel on the speed of mass transport in the diffusion channel at the set temperature of $25°C$.

Measurement of the glucose induced resonance shift

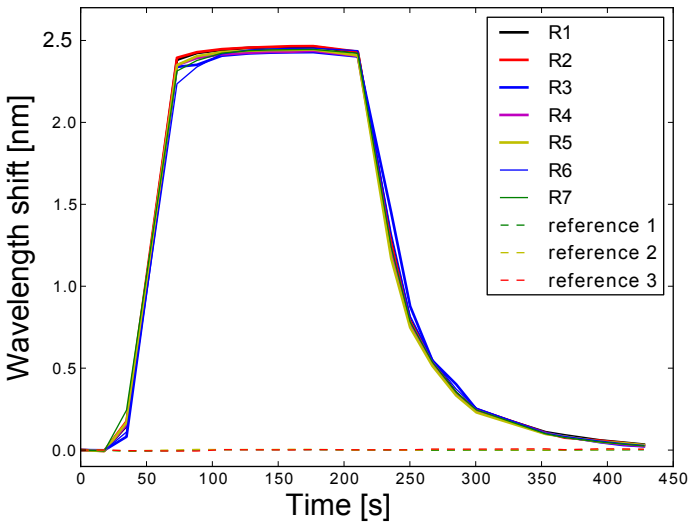

Figure 8.6: Shift in resonance wavelength due to a glucose concentration of 300 g/L.

To measure the sensitivity of the ring resonators for glucose, we evaluate the shift in resonance of the ring resonators due to a glucose concentration of 300 g/L. A straight microfluidic channel is placed above a set of 7 ring resonators and a set of three ring resonators is positioned just outside this microfluidic channel to serve as a reference. First, pure DI water is applied, followed by a glucose solution of 300 g/L. After about 3 minutes, the valve is switched back to pure DI water. The result is shown in figure 8.6. The ring resonators inside the microfluidic channel experience a mean wavelength shift of 2.44 nm after 150 seconds, whereas the reference resonators show the expected flat response. Although the ring resonators are identical in design, the fabrication process leads to small differences in the physical dimensions of the ring resonators. This causes each of them

to have a slightly different sensitivity, hence resonance shift, for glucose. The standard deviation on the mean shift is 12.7 pm which corresponds to a 0.5% variation between the different micro-rings.

Experiment with stopped flow

Initially we flow pure DI water through the main channel of the optofluidic chip. The pump speed is set to 10 μL/min. The flow is laminar given the dimensions of the microfluidic channels. There is no flow in the diffusion channel, as it is completely sealed at the end. We then switch the valve to the glucose solution of 90 g/L and inspect the transmission spectrum of the first ring which is at the entrance of the diffusion channel. As soon as the resonances of this ring start to shift, the pump is switched off. This makes sure that the main channel now serves as a still glucose reservoir (but with a slowly time-varying concentration). During the fluid transfer from valve to optofluidic chip, a parabolic flow profile in the 25-cm long PTFE micro-tube leads to a strong radial concentration gradient. This leads to a large diffusion component in the radial direction and reduces the mean axial concentration gradient in the downstream flow direction. Thus, given that diffusion also occurs in the 25-cm long PTFE micro-tube, there is no sharp transition between the water and glucose solution. Therefore, when the first ring starts to shift, the concentration in the main channel is not immediately 90 g/L. In our experiment, the concentration in the main channel is 60 g/L when the pump is stopped. The glucose concentration at each ring is monitored for about two hours to observe the diffusion process. The measurement results are presented in figure 8.7(a).

It shows the expected outcome that the first ring, at a distance of 145 μm of the main channel, reacts fast to the sudden concentration gradient and soon reaches saturation. The rings at distances 1945 μm and 3745 μm show a delayed and slower rise. In the later section 8.5.1, we calculate the glucose diffusion coefficient based on these measurements.

Experiment with flow

Throughout the complete second experiment, we pump the fluids with a steady flow of 10 μL/min. Again, we verify that there is no flow in the diffusion channel. At first, the channels are filled with pure DI water, then the valve is switched to a glucose solution of 70 g/L. After 50 minutes the valve is switched back to the pure DI solution. As the pump is running continuously, there is a constant supply of glucose molecules with a fixed concentration to the entrance of the diffusion channel. The ring resonator responses to this applied block function are shown in figure 8.7(b).

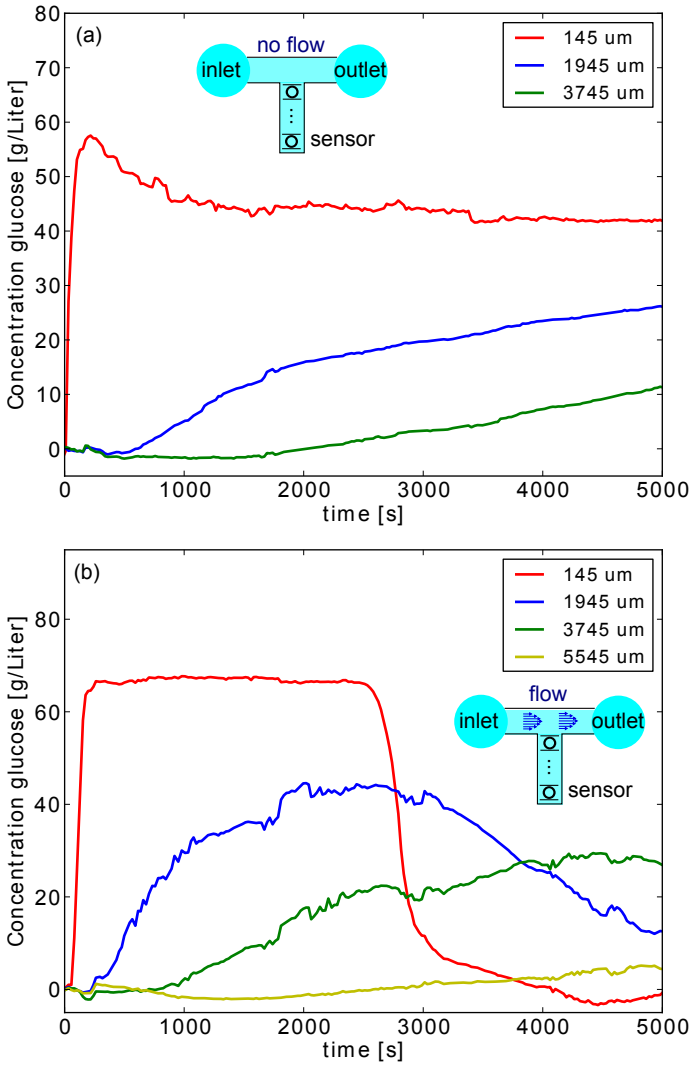

Figure 8.7: Glucose concentration as calculated from the wavelength shift of the micro-ring resonances in function of time at the discrete positions of the ring resonators for (a) a stopped flow and (b) a continuous flow at the entrance of the diffusion channel. The wavelength shifts are a direct measure for the position and time-dependent glucose concentration in the diffusion channel.

The signal from the first ring corresponds well with the applied glucose concentration profile. The second and third ring both show the increase and decrease in glucose concentration, whereas the decrease still has to set in for the last ring. When we compare the time scale of the experiment with

and without stopped flow, we immediately note the faster mass transport of the latter. If we look e.g. at the response of the ring resonator at a distance of 1945 um from the entrance of the diffusion channel, we note that it has reached a glucose concentration of 43.7 g/L after 2500 seconds in the case of continuous flow at the entrance whereas it only reaches 17.7 g/L when the flow was stopped. The applied input concentration, however, was respectively 70 g/L and 60 g/L.

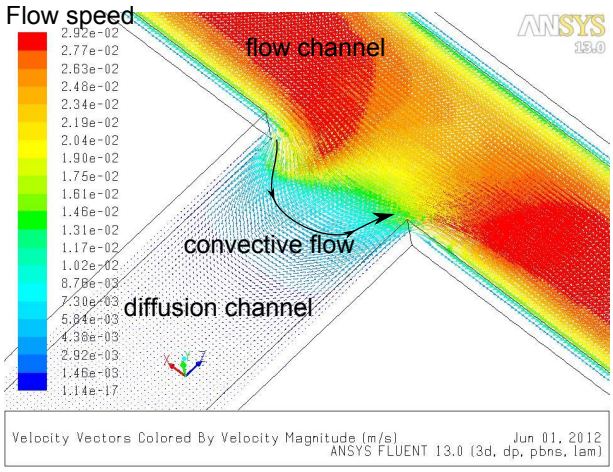

Figure 8.8: Plot of the velocity vectors at the entrance of the diffusion channel. This shows the driven cavity effect (simulation by prof. Jan Vierendeels)

This faster mass transport can be explained by two effects. Firstly, the main channel serves as a reservoir with constant concentration and secondly, the presence of a convective flow that carries the glucose molecules down the diffusion channel. Although the diffusion channel is closed, the flow in the main channel induces convective currents. This is an example of a driven cavity which is a well-known phenomenon in viscous incompressible fluids.[13],[14] The velocity of the convective flows decreases exponentially along the diffusion channel. In figure 8.8 we show a simulation result of this driven cavity effect with the software Fluent ®, for the dimensions of our microfluidic channels for a flow speed of 50 μL/min. In figure 8.9 the exponential decay of the convective flow along the diffusion channel is shown. These simulation were performed by Prof. Jan Vierendeels.

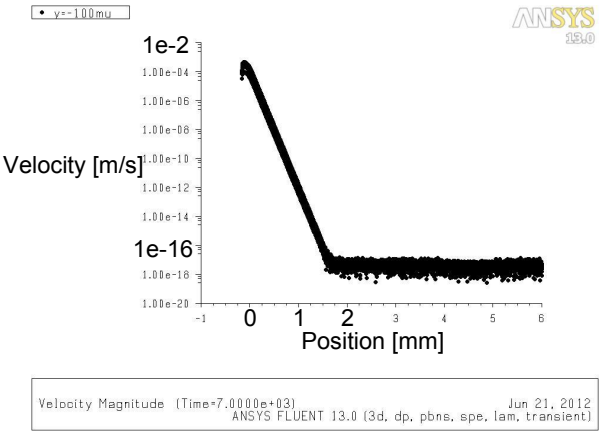

Figure 8.9: Exponential decay of the flow speed of the convective currents with distance in the diffusion channel. (simulation by prof. Jan Vierendeels)

8.4.2 NaCl diffusion experiments

Three experiments with NaCl were performed. In the first experiment we measure the sensitivity of the ring resonators to NaCl. In the second and third experiment we perform a diffusion experiment with stopped flow at both $20°C$ and $30°C$. This allows us to confirm the faster diffusion rate with increasing temperature.

Sensitivity to NaCl

In the first experiment we determine the sensitivity of the micro-ring resonators to a 300 g/L NaCl aqueous solution. The pump speed is set to 25 μL/min. First pure DI water is applied, followed by the NaCl solution after which we switch the valve again to pure DI water. The resulting evolution of the resonance shift for a set of seven ring resonators is measured. The three reference ring resonators that are outside the microfluidic channel show a flat response. The micro ring resonators exhibit a mean shift of 2.71 nm after 500 seconds with a standard deviation of 46 pm. This corresponds to a 1.7% variation between the different rings with an identical design. This is a rather high value, but poses no problem to accurately study the evolution of concentration profiles in micro-fluidic channels. Indeed, the information from this type of measurement can be used to our advantage to calibrate the response from the individual micro-ring resonators.
First a sensitivity factor $\frac{\Delta\lambda_{ring}}{\Delta\lambda_{mean}}$ is calculated for each ring with $\Delta\lambda$ the wavelength shift due to 300 g/L of NaCl. This sensitivity factor is then used to linearly scale the measured resonance shift during the diffusion

experiments. In addition, the mean shift is used to calculate the conversion factor between wavelength shift [nm] and NaCl concentration [g/L].

Experiment at 20°C

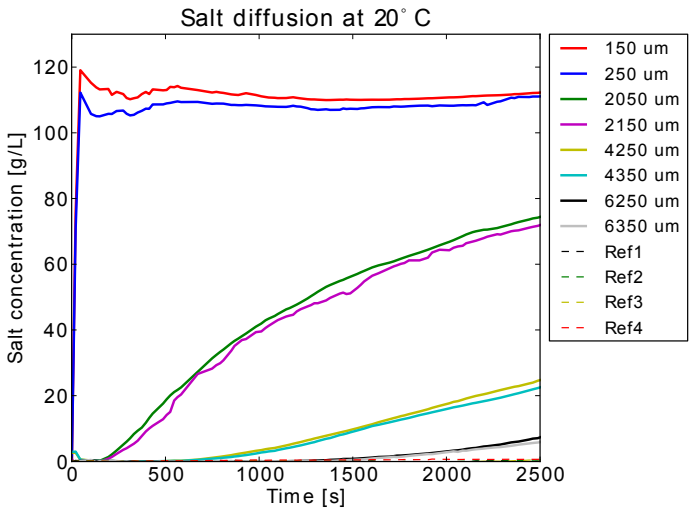

Figure 8.10: NaCl concentration as calculated from the wavelength shift of the micro-ring resonances in function of time at the discrete positions of the ring resonators at a temperature of 20°C. The dotted lines show the flat responses of the reference ring resonators.

Initially we flow the pure DI solution through the main channel of the optofluidic chip. The pump speed is set to 5 μL/min and the temperature controller is fixed at 20°C. We then switch to the NaCl solution and as soon as the first ring resonator starts to shift the pump is stopped. The shift of the ring resonators is then recorded during 2500 seconds. The results are shown in figure 8.10. The time axis starts at the transition from pure DI water to the Nacl solution. The stated position of the various ring resonators is the distance from the entrance of the diffusion channel to the ring resonator (as designed), with straight lines and 90 degree bends, along the center line of the microfluidic channel.

Experiment at 30°C

For this experiment, a new optofluidic chip was fabricated. The temperature controller was set to 30°C and the flow speed to 5 μL/min. After switching to the NaCl solution from a pure DI solution, the pump was stopped when the first ring resonator is shifting in resonance. The results

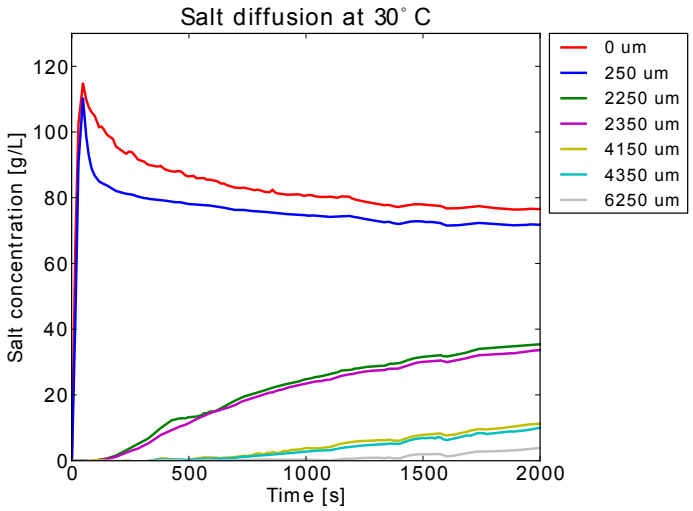

Figure 8.11: NaCl concentration as calculated from the wavelength shift of the micro-ring resonances in function of time at the discrete positions of the ring resonators at a temperature of 30°C. The dotted lines show the flat responses of the reference ring resonators.

of this measurement are shown in figure 8.11. Again a clear diffusion profile is found.

8.5 Discussion of the results

8.5.1 Extraction of the diffusion coefficient

To calculate the diffusion coefficient D, we use the explicit finite difference expression of the 1D diffusion equation:

$$\frac{C_{i+1,j} - C_{i,j}}{\Delta t} = \frac{D}{(\Delta x)^2}(C_{i,j+1} - 2C_{i,j} + C_{i,j-1}) \tag{8.7}$$

In the above equation, $C_{i,j}$ represents the solute concentration at time $t = i \cdot \Delta t$ and position $x = j \cdot \Delta x$. The microfluidic channel is approximated by a straight line of length 1 cm. The left boundary condition is a measured concentration profile C_{input}, whereas the right boundary condition is the impermeable wall condition. First, we set the step size along the microfluidic channel to Δx. We then perform a spline interpolation of the measured C_{input} to a fixed temporal grid with a time step Δt. To obey the stability condition for the explicit finite difference expression, this Δt must obey $\Delta t \leq \frac{\Delta x^2}{2D}$. Secondly, the evolution of solute concentration, during

the experimental time of T_{exp}, is determined for a large set of diffusion coefficients along the microfluidic channel with step Δx. These theoretical curves $C_{i,j}(D)$ are then evaluated at the position of the ring that we want to predict. Finally, the sum of least squares $S(D)$ is calculated (8.8) between these theoretically predicted $C_p(t, D)$ curves and the experimental results $C_{exp}(t)$ of the ring at a distance L.

$$S(D) = \sum_{t=0}^{t_{exp}} (C_{exp}(t) - C_p(t, D))^2 \tag{8.8}$$

We can then extract the measured diffusion coefficient as the minimum in the least squares curve $S(D)$. Important to note is that we use the raw concentration data from the measurements, without any post-processing such as noise filtering, as an input for the diffusion extraction procedure.

The distance L, the shortest distance between the two rings, is determined by the microscope images from the fabricated sample. This is necessary as the fabricated sample can have a misalignment between the microfluidics and SOI design. The choice about which ring resonator serves as the input for the simulation C_{input} and which ring as the predicted curve C_{exp}, can be optimized. Firstly, the input ring has to be closer to the entrance of the diffusion channel than the predicted ring. Secondly, the ring resonators close to the entrance of the diffusion channel can be influenced by the initial flow conditions whereas the ring resonators at the end of the diffusion channel have a weaker signal.

In the NaCl experiment at 20°C, we used the middle ring of set 2 to predict the middle ring of set 3. The distance to the predicted ring is discretized into 100 parts, leading to $\Delta x = 19.45\mu$m. The other parameters for the data analysis were Δt=0.1 s, T_{exp}=2500 s and L=1945 μm. The minimum in the least squares curve is found for a diffusion coefficient of $13.74\text{x}10^{-10} m^2/s$. For the NaCl experiment at 30°C, the first ring of set 2 and the first ring of set 3 is used. They are horizontally aligned, therefore the distance L is 1800 μm. The position step is $\Delta x = 18\mu$m, the time step Δt=0.09 s and the total experimental time T_{exp}=1999.98 s. From the least squares fitting, we can extract a diffusion coefficient of $16.31\text{x}10^{-10} m^2/s$.

Finally, we also extracted the glucose diffusion coefficient from the stopped flow experiment in section 8.4.1 using the ring at 1945 and 3745 μm with parameters $\Delta x = 18\mu$m, Δt=0.2 s, T_{exp}=5000 s and L=1800 μm. A value of $6.55\text{x}10^{-10} m^2/s$ is obtained.

We also investigated if a smaller Δx and Δt had an effect on the resulting diffusion coefficient. Hereto, we followed the same diffusion extraction procedure for the NaCl experiment at 30°C with $\Delta x = 5\mu$m, Δt=0.007 s

and $\Delta x = 10\mu$m, Δt=0.025 s. We found that the diffusion coefficient equals $16.311\text{x}10^{-10} m^2/s$ for both $\Delta x = 5\mu m$, $\Delta x = 10\mu m$ and $\Delta x = 18\mu m$, showing that the extracted diffusion coefficient varies less than 0.1%, hence, the numerical solution is converged.

A clear advantage of this analysis method is that the exact concentration at the entrance of the diffusion channels doesn't have to be known. This entrance concentration is hard to predict and depends strongly on the exact experimental settings such as the length of the tubing, flow speed, connection between tubing and the microfluidics etc.

8.5.2 Comparison with literature

The measured concentration profiles are impacted by errors in the resonance fitting procedure, non homogeneities in the sample fluid, and a limited acquisition rate. It is therefore interesting to evaluate how tight a diffusion estimate can be obtained. From literature we find a NaCl diffusion coefficient of $13.08\text{x}10^{-10}\ m^2/s$ at $20°\text{C}$. This diffusion coefficient D was calculated from the literature value at $25°\text{C}$ ($T_0 = 298.15K$) by using the formula (8.9) with μ the dynamic viscosity and T the temperature in kelvin.[15, 16]

$$D(T) = \frac{T \cdot \mu(T_0)}{T_0 \cdot \mu(T)} \cdot D(T_0) \tag{8.9}$$

Similarly, we find a NaCl diffusion coefficient of $16.79\text{x}10^{-10}\ m^2/s$ at $30°\text{C}$. The literature value of the glucose diffusion coefficient is $6.75\text{x}10^{-10}\ m^2/s$ at $25°\text{C}$. [13] When we compare the diffusion coefficients obtained by the experiments and the literature values we find a discrepancy of -2.96%, $+5.04\%$ and -2.86% for glucose, NaCl at $20°\text{C}$ and $30°\text{C}$ respectively.

8.5.3 Robustness to noise

To estimate the robustness of our method, we take a closer look at the NaCl experiment at $30°\text{C}$. First, the concentration profiles of both ring resonators (C_A and C_B), that were used to calculate the diffusion coefficient, are smoothed with a third order Savitzky-Golay filter to yield $\tilde{C_A}$ and $\tilde{C_B}$.[17] Secondly, we add low-pass filtered gaussian noise ($N_A(\sigma)$ and $N_B(\sigma)$) to these smoothed curves with a zero mean and varying standard deviation σ. The cut-off frequency of the second order low-pass Butterworth filter was chosen to match the typical time-scale of the experimental noise. The diffusion extraction method is followed based on these smoothed curves with added noise $\tilde{C_A} + N_A(\sigma)$ and $\tilde{C_B} + N_B(\sigma)$ for the different values of σ. The procedure is clarified in figure 8.12. We can then extract how the obtained diffusion coefficient is affected by an increase in experimental noise. The results are shown in figure 8.13. When the applied noise has a

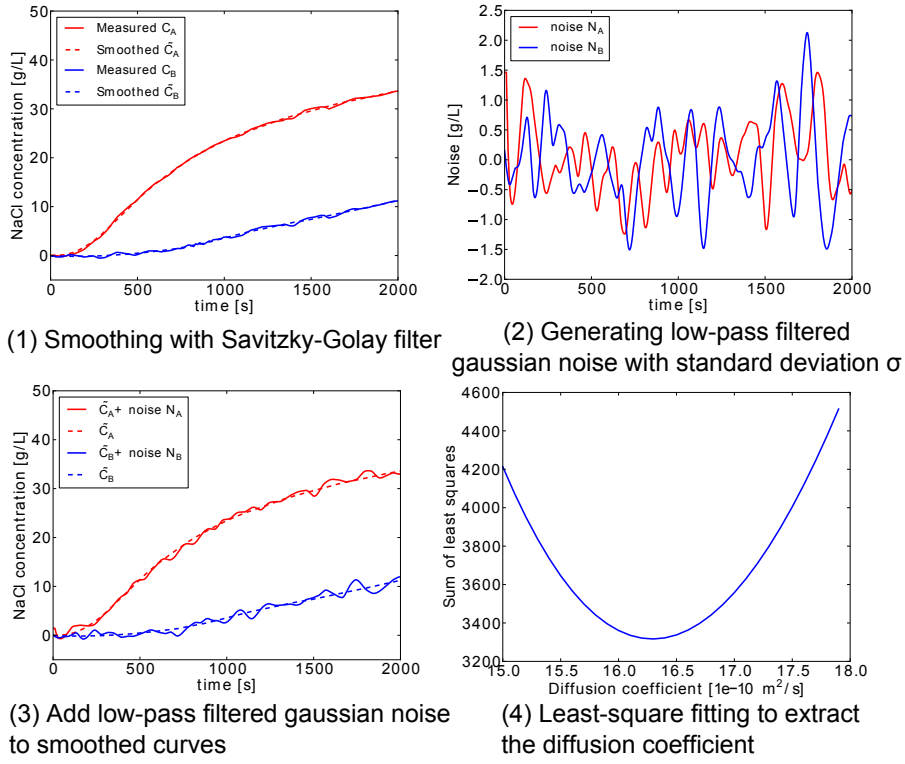

Figure 8.12: Step-by-step visualization of the procedure followed to obtain the diffusion coefficient for a given experimental noise with standard deviation σ.

standard deviation σ >0.5 g/L, the diffusion coefficient is varying rapidly up and down such that a reliable extraction of the diffusion coefficient is no longer possible.

8.5.4 Experimental noise

We also evaluated the experimental noise of the measured concentration profiles of the microring resonators. Hereto, we take the standard deviation of the difference between the Savitzky-Golay smoothed curve and the measured concentration curves of the ring resonators in set 2, 3 and 4 (the resonators that can be used for diffusion extraction). This way, we obtain an average standard deviation value of 0.081 g/L. This value is indicated in figure 8.13 by a green line. The diffusion coefficient that is found based on the smoothed curves ($\sigma = 0$), has a value $16.306\text{x}10^{-10}\ m^2/s$, which is 2.88% lower than the literature value.

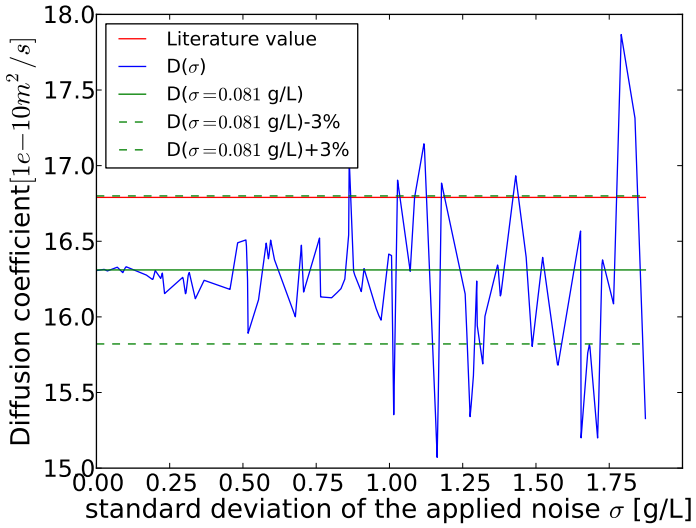

Figure 8.13: Extracted diffusion coefficient for a given experimental noise with standard deviation σ (blue). The red curve shows the literature value whereas the green curve shows the diffusion coefficient D for an experimental noise σ=0.081 g/L and the $D(\sigma = 0.081) \pm 3\%$ limits.

8.6 Conclusion

We presented a new method to study the diffusion process of small solutes in microfluidic channels with an integrated opto-fluidic chip. Both glucose and NaCl were used as example solutes to demonstrate the potential of this method. In the glucose diffusion measurements, we experimented with two distinct cases of mass transport: one where the glucose can enter the diffusion channel from a stopped flow and a second, where the glucose enters from a moving reservoir. In the first case, pure diffusion applies, whereas the latter serves as a text-book example of a driven cavity. In the NaCl diffusion measurements, we used two distinct temperature settings to confirm the increase in diffusion speed with temperature.

The robustness of the measurement procedure was investigated. It shows that when the concentration curves are measured with an experimental accuracy σ of up to 0.85 g/L, the error in diffusion coefficient remains lower than 3.0%. The presented method is also robust against temperature variations during the measurements, as reference sensors can be employed. It is furthermore versatile in the way the ring resonators are positioned along the microfluidic channels, such that mass transport can be observed over

a large chip area. It is important, however, that the distance between the consecutive ring resonators is known.

Future improvements include a new silicon-on-insulator chip design with more micro-ring resonators and a smaller ring spacing than 1.8 mm in the diffusion channel. This leads to more and faster acquired time-dependent concentration profiles that can be used in the determination of the diffusion coefficient. In a last step, the whole measurement procedure and data extraction can be automated. This will make way for a quick and accurate diffusion coefficient determination.

References

[1] D Ambrosini, D Paoletti, and Nasser Rashidnia. *Overview of diffusion measurements by optical techniques*. Optics and Lasers in Engineering, 46(12):852–864, 2008.

[2] Jeremy W Mares and Sharon M Weiss. *Diffusion dynamics of small molecules from mesoporous silicon films by real-time optical interferometry*. Applied optics, 50(27):5329–5337, 2011.

[3] Christopher T Culbertson, Stephen C Jacobson, and J Michael Ramsey. *Diffusion coefficient measurements in microfluidic devices*. Talanta, 56(2):365–373, 2002.

[4] Andrew Evan Kamholz, Eric A Schilling, and Paul Yager. *Optical measurement of transverse molecular diffusion in a microchannel*. Biophysical Journal, 80(4):1967–1972, 2001.

[5] Lev Davidovich Landau, Evgenij Mihajlovič Lifšic, John Bradbury Sykes, John Stewart Bell, MJ Kearsley, and Lev Petrovich Pitaevskii. *Electrodynamics of continuous media*, volume 364. Pergamon press Oxford, 1960.

[6] Airat K Amerov, Jun Chen, and Mark A Arnold. *Molar absorptivities of glucose and other biological molecules in aqueous solutions over the first overtone and combination regions of the near-infrared spectrum*. Applied spectroscopy, 58(10):1195–1204, 2004.

[7] Wim Bogaerts, Peter De Heyn, Thomas Van Vaerenbergh, Katrien De Vos, Shankar Kumar Selvaraja, Tom Claes, Pieter Dumon, Peter Bienstman, Dries Van Thourhout, and Roel Baets. *Silicon microring resonators*. Laser & Photonics Reviews, 6(1):47–73, 2012.

[8] Agnes Lee. *Glucose Sensing on an Optofluidic Silicon Chip*. Master's thesis, Photonics Research Group, University of Ghent, 2013.

[9] Katrien De Vos. *Label-Free Silicon Photonics Biosensor Platform with Microring Resonators*. PhD thesis, Photonics Research Group, University of Ghent, 2010.

[10] Hui Su and Xu Guang Huang. *Fresnel-reflection-based fiber sensor for on-line measurement of solute concentration in solutions*. Sensors and Actuators B: Chemical, 126(2):579–582, 2007.

[11] Dirk Taillaert, Wim Bogaerts, Peter Bienstman, Thomas F Krauss, Peter Van Daele, Ingrid Moerman, Steven Verstuyft, Kurt De Mesel, and Roel Baets. *An out-of-plane grating coupler for efficient butt-coupling between compact planar waveguides and single-mode fibers*. Quantum Electronics, IEEE Journal of, 38(7):949–955, 2002.

[12] Katrien De Vos, Jordi Girones, Tom Claes, Yannick De Koninck, Stepan Popelka, Etienne Schacht, Roel Baets, and Peter Bienstman. *Multiplexed antibody detection with an array of silicon-on-insulator microring resonators*. Photonics Journal, IEEE, 1(4):225–235, 2009.

[13] William BJ Zimmerman. *Microfluidics: history, theory and applications*, volume 466. Springer, 2006.

[14] TP Chiang, WH Sheu, and Robert R Hwang. *Effect of Reynolds number on the eddy structure in a lid-driven cavity*. International journal for numerical methods in fluids, 26(5):557–579, 1998.

[15] Jacob H Dane, Clarke Topp, Gaylon S Campbell, Robert Horton, William A Jury, Donald R Nielsen, Harold M van Es, Peter J Wierenga, and G Clarke Topp. *Part 4-Physical methods*. Methods of Soil Analysis, 2002.

[16] Joseph Kestin, H Ezzat Khalifa, and Robert J Correia. *Tables of the dynamic and kinematic viscosity of aqueous NaCl solutions in the temperature range 20–150 C and the pressure range 0.1–35 MPa*. Journal of physical and chemical reference data, 10(1):71–88, 1981.

[17] Abraham Savitzky and Marcel JE Golay. *Smoothing and differentiation of data by simplified least squares procedures.* Analytical chemistry, 36(8):1627–1639, 1964.

9 Conclusions and perspectives

9.1 Conclusions

Numerous research initiatives are geared towards the development of a continuous glucose monitor (CGM). This device can offer to millions of diabetes patients worldwide the chance to optimize their medical treatment. Although numerous transducers can be imagined to detect glucose, we investigated near infrared (NIR) absorption spectroscopy of the interstitial fluid. More specifically, we analyzed whether a miniature NIR absorption spectrometer integrated onto a silicon chip can be used in an implantable CGM. This involved the study of both the sensing principle itself (NIR absorption spectroscopy) and the various constraints imposed by the *in vivo* setting.

We started with a discussion on the sensing principle (see chapter 2). Two main conclusions were drawn: to accurately detect glucose in ISF, we need both multivariate analysis and a spectrometer with a very high signal-to-noise ratio (SNR) on the order of 40 dB. The latter demand originates from the low physiological glucose concentration compared to the water content in interstitial fluid. Only a spectrometer with a very high SNR can distinguish the glucose signal from the dominant water absorption. To also distinguish glucose from other absorbing bio-molecules, multivariate analysis is needed. Furthermore, this multivariate analysis points to a large set of wavelengths, across a wide wavelength range, to be used to increase the specificity for glucose.

The investigation of the *in vivo* setting led to the conclusion that we need an evanescent sample interface, instead of a free space interface (see chapter 3). Hereto, we first derived that the strong tissue scattering and the low glucose content in cells, imposes the use of a membrane, such that only fluids are sampled. When this membrane is present, the risk for a sensor delay due to slow glucose diffusion into the fluid cavity is smaller in the case of an evanescent sensor. In addition, the sturdy alignment of an evanescent sensor, compared to the free space configuration, will improve the sensor stability and allows the straightforward integration of additional sensors. The latter is important as the high SNR requirement of the spectrometer strongly favors a dual-beam configuration with at least one signal and one reference sensor.
We theoretically investigated evanescent absorption spectroscopy using silicon waveguides and concluded that the optimal evanescent sensor is a low-loss rib waveguide of appropriate (computable) length, that is routed into a spiral to minimize the sensor footprint (see chapter 4).
The performance of these evanescent spirals for glucose sensing was also experimentally verified (see chapter 6). For these experiments we firstly optimized the instrumentation to read-out the evanescent sample interface. We found that a pre-dispersive dual-beam system with a broadband source and tunable filter allows accurate glucose measurements with an error-of-fitting down to 1.14 mM and 95% confidence interval of 0.86 ± 0.86 mM. These values are limited by slow, thermal drift effects in our optical set-up. The potential impact of the *in vivo* setting on the evanescent sensors was also studied. We found that the sensor transmission is severely impacted by the high content of salt (154 mM) that is present in bodily fluids. In addition, we need to ensure that molecules do not adsorb to the waveguide surface. A thin layer of 40 nm already reduces the confinement factor of rib waveguides (hence sensitivity) by 50 %.

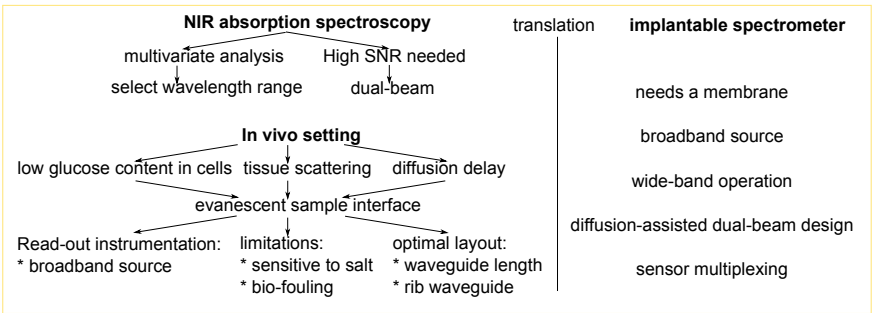

Figure 9.1

All of the above considerations can be translated into the general design of an implantable spectrometer with an evanescent sample interface (see figure 9.1). From the *in vivo* setting, we could derive that the implant needs a membrane and from the measurements with evanescent spirals we know that the spectrometer needs a broadband source. The implementation of these features were however not studied in detail in this work. In contrast, we did investigate the three additional features of the implantable silicon chip: wide-band operation, dual-beam design and sensor multiplexing.

The spectrometer should cover a wide wavelength range to enable high glucose-specificity. We showed that integrated SOI spectrometers with GaSb-based photodiodes can be designed to operate with wavelengths from 1510 to 2300 nm (see chapter 5). This covers both the first overtone and combination band features in the glucose absorption spectrum. The developed spectrometers have a channel spacing ranging from 3 to 7 nm and a number of channels ranging between 8 and 30. A minimum insertion loss of -3 dB and a moderate cross-talk level of -10 dB was obtained, which is currently limited by the fabrication process. We showed experimentally that they are suitable for molecular detection of strongly absorbing molecules.

The integrated spectrometer should have a dual-beam configuration suitable for *in vivo* operation. We showed with a proof-of-principle experiment that this can be realized with a so-called diffusion-assisted dual-beam design. In this design, the signal sensor is located close to the glucose supply and glucose molecules can only reach the reference sensor by diffusing down a long channel (see chapter 7). A good error-of-fitting of 1.41 mM was obtained. More research, however, is needed to elaborate on the glucose concentration extraction procedure, calibration strategies and limitations of this approach.

The final feature, sensor multiplexing, was indirectly investigated in chapter 8. We showed that ring resonators can be used to accurately measure the diffusion of small molecules such as glucose. Because ring resonators are sensitive to refractive index changes, they can be implemented as a (non-specific) glucose sensor, temperature sensor, sensor for molecular adherence etc. By monitoring all of these environmental parameters in the implant, we can monitor what happens at the sensing site and use this information to correctly interpret the measured ISF transmission spectrum.

9.2 Perspectives

Is it possible to measure glucose *in vivo* with an implantable Si photonics optical chip? That is the ultimate question. Unfortunately, we cannot answer this question positively yet. Fortunately, what we can say is that our sensor has good potential. However, at least the two following issues have to be solved before we can positively answer the fundamental question.
The first problem relates to the strong response of our sensor to NaCl. It should be studied what the exact cause is of this behavior and if this happens for other salts as well. Still, the human body requires a minimum amount of Na^+ ions of 135 mM, which is 25 times larger than the average glucose concentration. Thus, we must make sure that we can make our sensor insensitive to NaCl as it has a large and time-varying concentration in the interstitial fluid. A strategy to avoid the interaction between salt and our semi-conductor surface must be identified before further sensor development (for *in vivo* glucose detection) is sensible.
The second problem that should be solved, concerns the integration of a suitable source into the implant. Which source configuration gives the lowest glucose detection limit, highest technological feasibility (high fabrication yield/tolerance) and has a low power-consumption? In this work, we conclude that a coherent light source will introduce a strong time-varying ripple in the spectral response of the sensor. This ripple is very sensitive to environmental parameters and is considered to be a dominant source of noise. Therefore, a broadband source is strongly advised. A broadband source (SLED or LED) is, however, not elegant in terms of required energy. The spectrally interesting regions for glucose are typically smaller than the emission bandwidth of an SLED/LED and spread across a wide wavelength range. Therefore, a large part of the emission bandwidth is often not needed for the glucose determination but still constitutes emitted energy. As energy consumption is an important parameter for a wirelessly powered implant, this is a drawback for broadband source integration. In addition, at this point it is not yet clear what the technological arguments in this discussion are. What is the fabrication yield for both a laser array and a SLED/LED for example?
Another concern with respect to the selection of a suitable source is the wavelength range that is needed to detect glucose. There seems to be a chicken-or-egg problem with respect to the selection of operation wavelengths of the integrated spectrometer. How can we find the optimal wavelengths (through multivariate analysis) using measurements of a spectrometer, who's performance depends on the wavelengths for which it is designed?

Next to the above more fundamental problems, there are two aspects that should be looked into to confirm that an integrated evanescent sensor can

achieve the required performance. Firstly, during the evanescent glucose absorption experiments, we identified slow drift as the main limitation of our set-up. Small thermal changes that impact the fiber array/chip interface, induce a slow drift that is different for the signal and reference arm. This imbalance renders the dual-beam system ineffective. It should thus be investigated if a better balanced on-chip read-out with integrated photodiodes and low-power wire-bonded CMOS electronics can outperform a fiber array-based set-up with highly sensitive external photo-detectors.
Secondly, the long-term performance of the diffusion-assisted dual-beam design with a membrane should be looked into. Is it possible that small molecules that enter the membrane adhere permanently to the silicon surface? Can this adhesion be avoided? As mentioned before, any thin layer reduces the sensitivity of an evanescent sensor. This is especially true for SOI waveguides which have a high refractive index contrast and small dimensions.

On a last note, during this doctoral thesis an interesting optical circuit was fabricated, but was not used due to priority- and time issues. The fabricated silicon-on-insulator chip contains a dual-beam circuit with wire waveguide spirals that is diced in such a way that it can be integrated on top of a 8-channel fiber array facet. This fiber array probe can enable quick and easy absorption measurements without the need for microfluidics.

A

GlucoSens project

A.1 GlucoSens

Diabetes is a serious chronic disease that affects 347 million people worldwide. It is related to the malfunction of the pancreas to produce enough insulin or when the body doesn't effectively uses the produced insulin. These effects limit the glucose uptake by cells, causing a myriad of health problems. Major clinical trials have demonstrated that tight control of the blood glucose level reduces the health complications and reduces the overall cost of treatment. Continuous glucose monitoring (CGM) is crucial for this glycemic control. CGM is the regular measurement of the glucose concentration in either blood or the interstitial fluid (ISF). The research presented in this doctoral thesis is part of GlucoSens, a large research project for the development of an implant for continuous glucose monitoring in diabetes patients (www.glucosens.be). This multidisciplinary project was funded by the IWT for four years as a strategic basic research project, meaning that a considerable amount of the research results can be leveraged to other applications as well. The envisioned implant comprises an optical sensor that detects glucose based on its absorption spectrum. The implant would measure the glucose in the interstitial fluid. The optical sensor is integrated onto a photonic chip, meaning that it is a collection of miniature optical components that are aligned onto a planar base substrate. In figure A.1 the envisioned implant is shown. Each of the GlucoSens researchers worked intensively towards overcoming the challenges imposed by the requirements for an implantable device based on absorption spec-

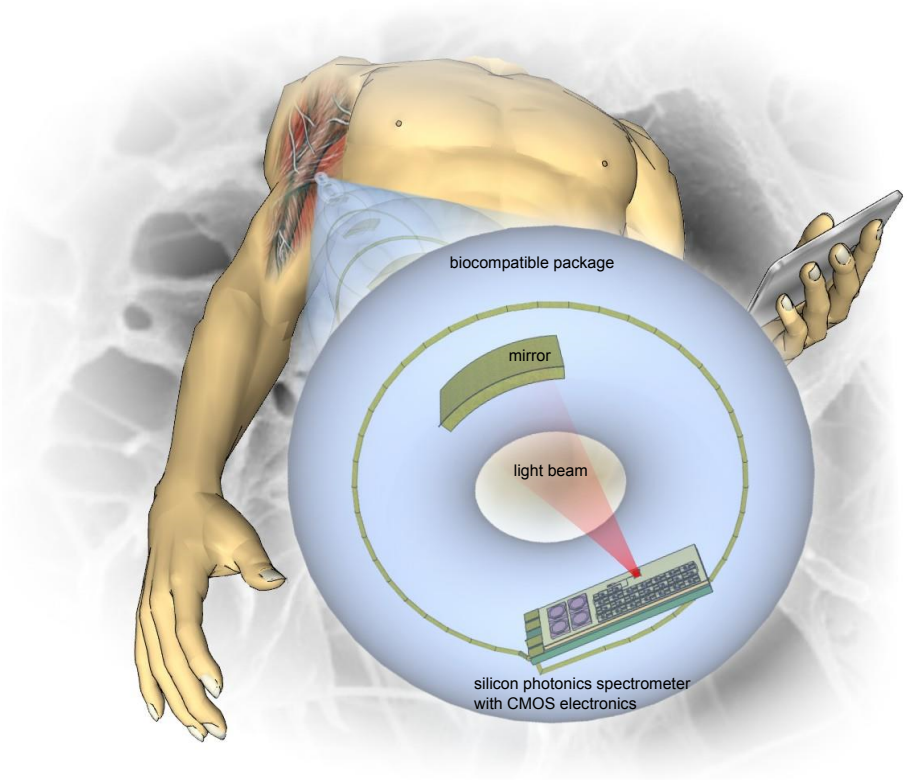

Figure A.1: GlucoSens: development of an implantable glucose sensor (drawing by Wim Bogaerts)

troscopy. These requirements are long-term stability, high performance, small size, low weight and last but definitely not least bio-compatibility. The following research groups were involved:

1. Photonics research group, UGent, responsible for the development of a miniature spectrometer
2. Polymer chemistry and biomaterials research group, UGent, responsible for the development of biocompatible coating materials based on PDMS and PMMA
3. Tissue engineering group, UGent, responsible for in vitro evaluation of the developed implant
4. Surgery & anesthesiology of domestic animals, UGent, responsible for in vivo testing of the developed implant

5. Mechatronics, Biostatistics and Sensors group (MeBioS), KULeuven, responsible for tissue modeling and multivariate analysis of absorption spectra

6. Imec, responsible for electronic drivers and sensor read-out

A short introduction to the goals of each of the involved teams is given below:

A.1.1 Photonics research group

To tackle the size and weight limitations of a human implant, the miniature spectrometer is a silicon-based photonic integrated circuit (PIC). To create this miniature spectrometer we needed to combine both passive (light-routing) and active (light generating and detecting) components on a single silicon chip. At the start of the project, the photonics research group (PRG) had already demonstrated first generation devices of these necessary individual components. It was, however, key to the project to extend this expertise to both a new wavelength range and new materials, next to analyzing and developing the optimal spectrometer configuration.

A.1.2 Polymer chemistry and biomaterials research group

The bio-compatibility is an important factor for the long-term stability of the implant. Heavy body reactions to the implant can lead to biofouling of the sensor, leading to a cut-off from the glucose supply to the sensor. The glucose supply can be stimulated by an increased number of blood vessels in the surrounding of the sensor. By working with soft polymers with a surface treatment, these blood vessels can be attracted. The appropriate surface treatment also reduces the body reactions. The polymer chemistry group (PBM) focused on the surface functionalisation of two synthetic materials namely, (poly)dimethylsiloxane (PDMS) and (poly)methylmethacrylate (PMMA). In addition, they optimized the fabrication process to reduce the roughness of the materials which also improves the biocompatibility of the implant.

A.1.3 Tissue engineering group

The tissue engineering group worked closely together with the PBM team and focused on the in vitro characterization of the developed polymer materials by studying the cell growth and the density of blood vessels around the materials. In addition, they were involved in the analysis of the samples that were implanted during the various in vivo animal test-rounds that were organized during the project.

A.1.4 Surgery & anesthesiology of domestic animals

This research team was responsible for the four implantation rounds that were organized during the project. This included the care for and health monitoring of the animals, next to the implantation and explantation surgery itself. Given that live animal research is challenging, they also solved lots of practical issues such as the design and fabrication of special jackets and experimental cages. The test animals were goats and all in vivo tests were approved by the ethical committee.

A.1.5 Mechatronics, Biostatistics and Sensors group

The MeBioS research was targeted at the extraction of the glucose concentration given the measured ISF absorption spectra. This required multivariate analysis strategies in order to distinguish the glucose signature from other molecules that have similar absorption bands. In addition, they investigated the glucose detection limits when the additional complexity of light scattering due to cells was present in the optical measurement path.

A.1.6 Imec

As a world-renowned institute for nano-electronics research, imec was involved in the design and fabrication of a CMOS electronic chip that combined both the read-out functionality and driver-circuitry for the miniature spectrometer.

A.2 Demo 4

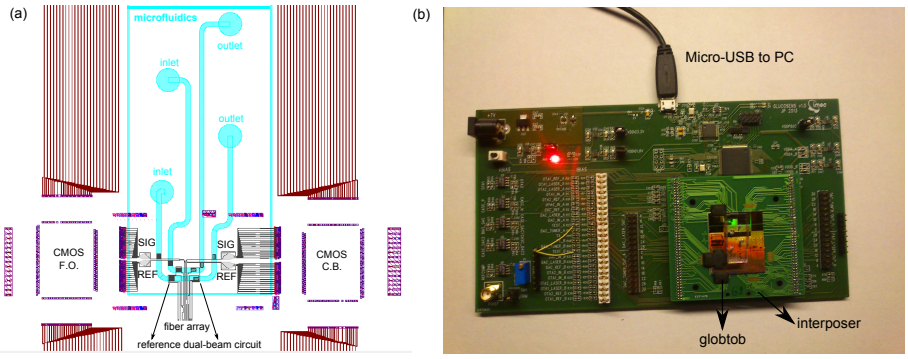

Figure A.2: GlucoSens demo 4: (a) Mask design for the passive SOI spectrometer, photodiode array, electrical wiring and microfluidics (b) micro-controller board with interposer containing the fabricated miniature spectrometer

Demo 4 was one of the final demonstrators for the GlucoSens project. The demonstrator combines an SOI chip with integrated photodiodes, microfluidics and a die-bonded CMOS (Complementary Metal Oxide Semiconductor) chip. The optical and microfluidics design was done in the photonics research group and the electronics was developed by imec. The optical circuit comprises two dual-beam spectrometers with preceding evanescent sensor and photodiode array. The optical circuit is shown in figure A.2(a). The spectrometers are 16-channel PCGs with 6 nm channel spacing and a center wavelength of 1.59 μm for the first overtone band (F.O.) and 2.11μm for the combination band (C.B.). The optical design is such that a fiber array can be used as an input to ensure a stable input signal. In addition, the remaining fiber array channels can be used to read-out two reference dual-beam optical circuits that contain the evanescent sensors without wavelength demultiplexer. A microfluidics circuit in PDMS was designed and fabricated as well, to enable fast and easy switching of various sample fluids.

The CMOS electronics chip was designed at imec in Leuven and had two functionalities. On the one hand, it can drive a 16-channel laser array and 16-channel heater array and on the other hand, it can process the photocurrent from 2 x 16 photodiodes. The CMOS chip contains a 16 bit analog-to-digital convertor that can analyze two photocurrents (1-10 μA) simultaneously. This is to measure both the signal photocurrent and reference photocurrent from the dual-beam spectrometer.

Although initially it was the plan to use GaSb photodiodes, InP photodiodes were processed due to lack of manpower. Therefore only the left side of the optical circuit (for the first overtone band) was used and a single CMOS chip was bonded onto the SOI. The SOI was fixed onto an interposer PCB and wire-bonds were used to connect the PCB to the CMOS chip. This interposer was then mounted onto a micro-controller board as shown in figure A.2(b). Through a GUI in matlab we could communicate with the CMOS chip. Both the CMOS chip and SOI chip with InP photodiodes were tested separately and found working properly. Unfortunately, the full demonstrator showed no photocurrent read-out. The reason is thus far unkown and because the CMOS chip, wire-bonds and photodiodes are covered with the protecting polymer globtob, we cannot properly test the electrical connections. We can conclude that the fabrication cycle is developed, but a new iteration (without globtob) is needed to find the failing process step.